DOE/ID/12940-1
(DE93002507)
Distribution Category UC-310

DOE/ID/12940--1

DE93 002507

PILOT DEMONSTRATION OF CERIUM OXIDE COATED ANODES

Final Report for the Period
April 1990 to October 1992

October 1992

Work Performed Under Contract No. DE-FC07-90ID12940

Prepared for the
U.S. Department of Energy
Under DOE Idaho Field Office
Sponsored by the Office of the Assistant Secretary
for Conservation and Renewable Energy
Office of Industrial Technologies
Washington, D.C.

Prepared by
ELTECH Research Corporation
Fairport Harbor, OH

ABSTRACT

Cu cermet anodes were tested for 213 to 614 hours with an in-situ deposited CEROX coating in a pilot cell operated by Reynolds Manufacturing Technology Laboratory. At high bath ratio (~1.5) and low current density (0.5 A/cm^2), a ≥1 mm thick dense CEROX coating was deposited on the anodes. At lower bath ratios and higher current density, the CEROX coating was thinner and less dense, but no change in corrosion rate was noted. Regions of low current density on the anodes and sides adjacent to the carbon anode sometimes had thin or absent CEROX coatings. Problems with cracking and oxidation of the cermet substrates led to higher corrosion rates in a pilot cell than would be anticipated from lab scale results.

CONTENTS

ABSTRACT
SUMMARY

FIGURES

TABLES

SUMMARY

Copper cermet anodes for aluminum electrowinning were evaluated in two tests sponsored by DOE, one directed by Battelle Pacific Northwest Laboratories (PNL) and one directed by ELTECH Research Corporation. Both tests were conducted at Reynolds Metals Manufacturing Technology Laboratory (Reynolds) in Sheffield, Alabama. The tests were conducted to determine the stability of a $Cu/NiO/NiFe_2O_4$ cermet in a pilot aluminum electrowinning cell. The stability of the material was evaluated by the amount of cermet components (Fe, Ni, and Cu) that accumulated in the Al metal produced and by examination of the anodes after testing. The performance of the anodes was studied at "optimum" conditions based on laboratory testing and at other bath ratios, current densities, and alumina concentrations. In addition, the stability of the Cu cermet material was evaluated both without (PNL) and with (ELTECH) a protective $Ce(O,F)_2$ layer (CEROX). This report includes the details, results, and conclusions of the ELTECH test, and compares the performance of the uncoated cermets (the PNL test) to the CEROX coated cermets.

The testing of PNL began with two carbon anodes until the operation of the pilot cell was stabilized. One of the carbon anodes was then exchanged for a 6-pack of Cu cermets manufactured by Ceramic Magnetics Inc. (CM). The Cu cermets operated for a 20 d period, with over 300 h of testing on some of the cermet anodes.

At the conclusion of the test for PNL, the second test began under the direction of ELTECH. The cell was again operated with two carbon anodes for 13 d in order to clean the cell of alumina muck and to return the cermet generated impurities in the metal to baseline levels. At the end of that period, another 6-pack of Cu cermet anodes manufactured by CM replaced one of the carbon anodes. The anodes were operated for 26 d with individual anodes tested for up to 614 h. During the test cerium fluoride was added to the cell to form a CEROX coating on the anodes.

The ELTECH test was conducted for ~16 d at "preferred conditions" that were based on the best conditions found in the previous ELTECH laboratory tests: a bath ratio (BR) of 1.5 to 1.6 and a current density (CD) of 0.5 A/cm^2. CD was then increased to 0.65 A/cm^2 for 7 d, and then BR was decreased to ~1.15 for the remaining 3 d. Bath and metal impurities were monitored throughout the testing to assess the corrosion of the cermet substrate.

During the ELTECH test, as in the PNL test, several problems were encountered. Anodes cracked during introduction to the cell, probably as a result of thermal stress due to temperature gradients and thermal expansion differences between the metal current collector rod and the cermet. Anodes generally remained together and continued operating in spite of the cracks.

A second problem during cell operation was mucking of the cell

because of high alumina content. The muck tended to accumulate on the bottom of the cell, raising the cathode and reducing cell volume. A third problem during the test was that current to individual cermet anodes was impossible to control, only total current to the 6-pack was controlled. This allowed fluctuations in CD depending on the position of the anode in the cell, and fluctuations in CD during the lifetime of each anode.

Corrosion rates were calculated by Reynolds based on the impurities in the metal. They found corrosion rates during the ELTECH test to be half that of those during the PNL test. The calculated rates are

	PNL	ELTECH
Iron Increase (lb/d)	(0.21) 0.31	(0.12) 0.30
Nickel increase (lb/d)	0.26	0.13
Copper increase (lb/d)	0.13	0.075
Surface area loss (mm/d)	0.2	0.1

In both tests the ratio of Fe:Cu:Ni was higher in the metal than that found in the untested cermet. Therefore, the number in parentheses indicates the amount of Fe that would be in the aluminum from the cermet (based on the Fe ratio in the cermet) and the remainder of the Fe is believed to be caused by contamination from cell maintenance tools.

Because of the presence of cracks in the anodes and the possibility of chips or pieces of the anode falling into the bath during testing, the corrosion values are probably not representative of those that would occur with an uncoated or CEROX-coated anode.

The CEROX coating was normally 0.5 to 3 mm in thickness. The thickness was greater on the sides of the anodes than on the bottoms. Bare areas (no CEROX coating) were found on some anodes on the sides adjacent to another cermet anode. The lack of CEROX coating in those areas appears to be a result of low CD in that region. No enhanced corrosion was macroscopically noted in those uncoated areas.

On the sides of some of the cermets adjacent to the carbon anodes there was an indentation in the cermet, which indicates higher corrosion on that side. The side facing the carbon anode sometimes had a CEROX coating and sometimes did not. No microstructural differences were noted in the indented area. The lack of a CEROX coating next to the carbon anode may be a result of either the decreased CD on that side of the cermet anode (the carbon anode draws most of the current) or the increased CO_2 and decreased O_2 content in that area.

The CEROX coating was densest on the anodes removed after about 200 to 300 h and operated under "preferred" conditions. The CEROX coating on an anode operated during the second half of testing, when CD was higher and BR was lower, was thinner and less continuous. The CEROX coating formed around the edge of some cracks in the anodes and a short distance into the widest cracks; however, much of the cracked surface area was not coated with CEROX.

The three cermet anodes on the side of the cell furthest from the carbon anode operated for over 600 h but became partially frozen into the crust during the last 300 h. The CEROX coating on that side of the anodes was porous and thick.

All anodes had some oxidation of the Cu within the outermost bottom layer of the anodes. The thickness of the oxidation ranged up to 10 mm thick on anodes operated for up to 300 h. On an anode operated for over 600 h, the oxidation thickness was up to 18 mm thick. Within the oxidized region, there were changes in the phase composition and distribution. Most of the tested anodes were more porous than the untested cermet but local dense regions occurred next to the CEROX coating. Cryolite rich in AlF_3 was found in the pores of the tested cermet and local layers of Ni fluoride were found within the anode operated for over 600 h.

Conclusions

The test demonstrated that a CEROX coating could be deposited on a Cu cermet anode in a pilot cell and that the coating could be maintained during 600 h of testing. The thickness of the CEROX coating was reduced in acidic baths and in low CD regions of the anodes. Corrosion rates of Fe, Ni, and Cu were calculated for both the uncoated Cu cermets and the CEROX-coated Cu cermets. However, because of the cracking of the cermets during both tests, the corrosion rates are not indicative of the corrosion of an intact anode and a comparison between the coated and uncoated cermets can not be made with confidence. Thus, the value of the CEROX coating on the Cu cermets can not be proven in these tests.

The Cu cermet anodes cracked because of thermal shock during introduction into the cell. In addition, the Cu cermets experienced microstructural changes that included increased porosity and the oxidation of the Cu metal phase. These changes show that the Cu cermet employed in these tests is not suitable for long term inert anode testing.

Recommendations

Research should be directed toward improving the thermal, oxidation, and corrosion resistance of the Cu cermet or toward developing an alternative cermet or ceramic as an inert anode. The design of the pilot cell for testing inert anodes could be improved by containing all cermet anodes (no carbon anodes) with individual current control. Careful design of the inert anode and cell should minimize the problem of mucking because of the high alumina concentration.

PILOT DEMONSTRATION
OF
CERIUM OXIDE COATED ANODES

1. INTRODUCTION

A great deal of research has been performed on inert anodes to replace carbon anodes for Al electrowinning. This report details the test conditions, results, and conclusions of a pilot cell test directed by ELTECH and conducted by Reynolds. The inert anode materials tested were Cu cermets fabricated by CM but coated with a CEROX coating developed and patented by ELTECH. Testing of CEROX coatings on Cu cermets in the Reynolds pilot cell followed Phase I and Phase II laboratory tests on CEROX coated anodes completed by ELTECH under cooperative agreements with DOE. Phase III laboratory experiments were being completed during the pilot cell testing.

1.1 Background

Inert anodes have long been sought to replace carbon anodes and thereby reduce the energy penalty of the carbon anodes and eliminate the costs associated with their production and use.[1,2] The key material requirements for an inert anode are:

- Low solubility in the molten cryolite bath
- Oxidation resistance
- Thermal shock resistance
- Electrical conductance greater or comparable to carbon
- Low oxygen overpotential
- Adequate mechanical strength.

The Aluminum Company of America (Alcoa) developed a $NiFe_2O_4/NiO/Cu$ cermet material that was promising in small scale tests.[3] The material achieved adequate electrical conductivity through the incorporation of 17 wt% Cu and had resistance to dissolution resulting from the use of oxides with very low solubilities in cryolite. Alcoa discontinued work on this material in 1985 but research on the Cu cermet was continued by PNL. They operated numerous laboratory experiments and achieved low dissolution rates.[4] In a larger scale test operated by Reynolds with a 15 cm anode, the cermet was tested for over 100 h but corrosion rate was unacceptable.[5]

In 1982, ELTECH developed the concept of a cerium oxyfluoride coating on an anode substrate for use in Hall-Heroult cells. DOE supported research in Phases I, II, and III to test the CEROX coating on SnO_2 and the Alcoa Cu cermet substrate at varying test conditions for up to 100 h. The tests defined the optimum testing conditions for CEROX on a Cu substrate and showed that corrosion was ~7 times higher with an uncoated Cu cermet than with a CEROX coated Cu cermet under identical test conditions.[6]

1.2 Objectives

The test at Reynolds was performed to determine the performance advantages of the CEROX coating on Cu cermet substrates on a pilot scale. A second objective was to gain experience with depositing and maintaining a CEROX coating in an industrial cell.

1.3 Scope

The ELTECH pilot cell testing followed pilot cell testing of uncoated Cu cermets by PNL at Reynolds. The ELTECH test consisted of four main parts. First, Reynolds operated the test cell with two carbon anodes until the Fe, Ni, and Cu corrosion from the PNL test reached a stable "baseline" level. During the second part of the test, 6 Cu cermets replaced one of the carbon anodes and were tested for up to 377 h under the ELTECH "optimum" conditions. Several anodes were exchanged and an increased CD was then applied during the third part of the test. Finally, the BR was reduced for the final phase of the testing.

The Cu cermets for the ELTECH test were supplied by DOE from CM and the operation of the pilot test cell was performed by Reynolds. Reynolds summarized their test cell operation in a report (see Appendix 1). ELTECH was responsible for setting the test conditions, overseeing the test and exchanges of anodes, and the analysis of the tested anodes. Reynolds analyzed the bath and metal throughout the testing and calculated corrosion rates from the impurities in the aluminum. The figures for bath and metal composition and for corrosion were taken from Appendix 1.

1.4 Accomplishments

CEROX-coated Cu cermet anodes were operated in a pilot scale test for 213 to 614 h. Corrosion rates were half that of the uncoated Cu cermets; however, with the cracking of the cermets during testing and with the mixture of carbon and cermet anodes in the cell, it is difficult to predict what industrial corrosion levels would be and exactly what protection factor the CEROX affords.

It was demonstrated that dense, adherent, 1 to 3 mm thick CEROX coatings could be deposited and maintained in a pilot cell under optimum conditions. Levels of Ce in the metal and bath could be maintained near the targeted levels if the cell was kept free from mucking. The influence of low CD on the presence of the CEROX coating was seen. Increased porosity and thickness of the CEROX coating was found where the cryolite crust froze around the edges of the anode. The CEROX coating was thinner and less continuous at lower BR, although no change in the corrosion rate was noted.

The Cu cermet substrate was found to undergo a number of changes during testing. The major changes were an increase in porosity throughout the anode and oxidation and loss of the Cu metal in the outer areas of the anode. In some areas a dense $NiFe_2O_4$ and NiO layer also was present next to the CEROX coating, and the composition of the ferrite and NiO were changed in that region. This dense layer was not reported by PNL and thus may be related to the presence of the CEROX coating.

2. TEST CELL AND ANODE DESIGN AND PROCEDURES

The test cell was designed and operated by Reynolds and was located in their facility in Alabama. Anodes were fabricated by CM.

2.1 Description of Pilot Cell

The self heated pilot cell had inside dimensions of 44 x 33 x 17 in., as shown in Figures 1 and 2. The sidewalls consisted of rammed carbon, prebake carbon blocks, and TR-19 vermiculite insulation. The cell normally operated with two industrial sized carbon anodes (15.5 x 21.5 in.), one of which was replaced with an inert anode cluster for this test. The cermet anode positions were labeled A through F (Figure 3). Each cermet anode could be individually removed.

Alumina was point fed hourly between the carbon anode and the inert anode cluster. The carbon anode and the inert anode cluster were fed by two separate power supplies so that the current to each could be independently controlled. Current to each of the individual cermet anodes could not be independently controlled, but was monitored throughout the test. Additions of CeF_3 were made hourly. Cryolite, NaF, and AlF_3 were added as needed to maintain the desired BR and bath levels. Aluminum was tapped frequently with a ladle in order to keep a fairly constant metal depth.

2.2 Description of the Anodes

The Cu cermet anodes were fabricated by CM under the guidance and specifications of PNL.[7] The cermet anodes for the PNL test and for the ELTECH's test were made in an identical manner. In brief, the anodes were prepared by mixing 51.7 wt% NiO with 48.3 wt% Fe_2O_3, calcining the mixture to form $NiFe_2O_4$ with excess NiO, and then mixing in 1% polyvinyl alcohol (PVA) binder and spray drying. 17 wt% Cu metal was then blended with the spray dried powder. The final composition of the anodes, based on starting components, was 17 wt% Cu, 42.9% NiO, and 40.1% Fe_2O_3. The powder mixture was then consolidated at 13,000 psi with an isopress. Anodes were sintered at 1200°C for 24 h in an $Ar-O_2$ atmosphere with an oxygen partial pressure of 150 ppm O_2 (1.5×10^{-4} atm).

PNL typically achieved densities of ~6.05 to 6.10 g/cm^3 with 0laboratory anodes that were consolidated at 20 kpsi (140 MPa). The density of anodes fabricated by CM ranged from ~5.74 to 5.85 g/cm^3.[7] The main reason attributed to this lower density is the lower isopress pressure, which was the maximum pressure that could be achieved with the CM isopress. Theoretical density has been estimated to be 6.28 g/cm^3 (Alcoa), 6.09 g/cm^3 (from the mixture of the $NiFe_2O_4$/NiO powder with 17 wt% Cu), or higher (see "Microstructure of the Cermet anodes" section). The maximum density of laboratory produced cermets is around 6.11 g/cm^3.

Pilot Cell Design
Plan View

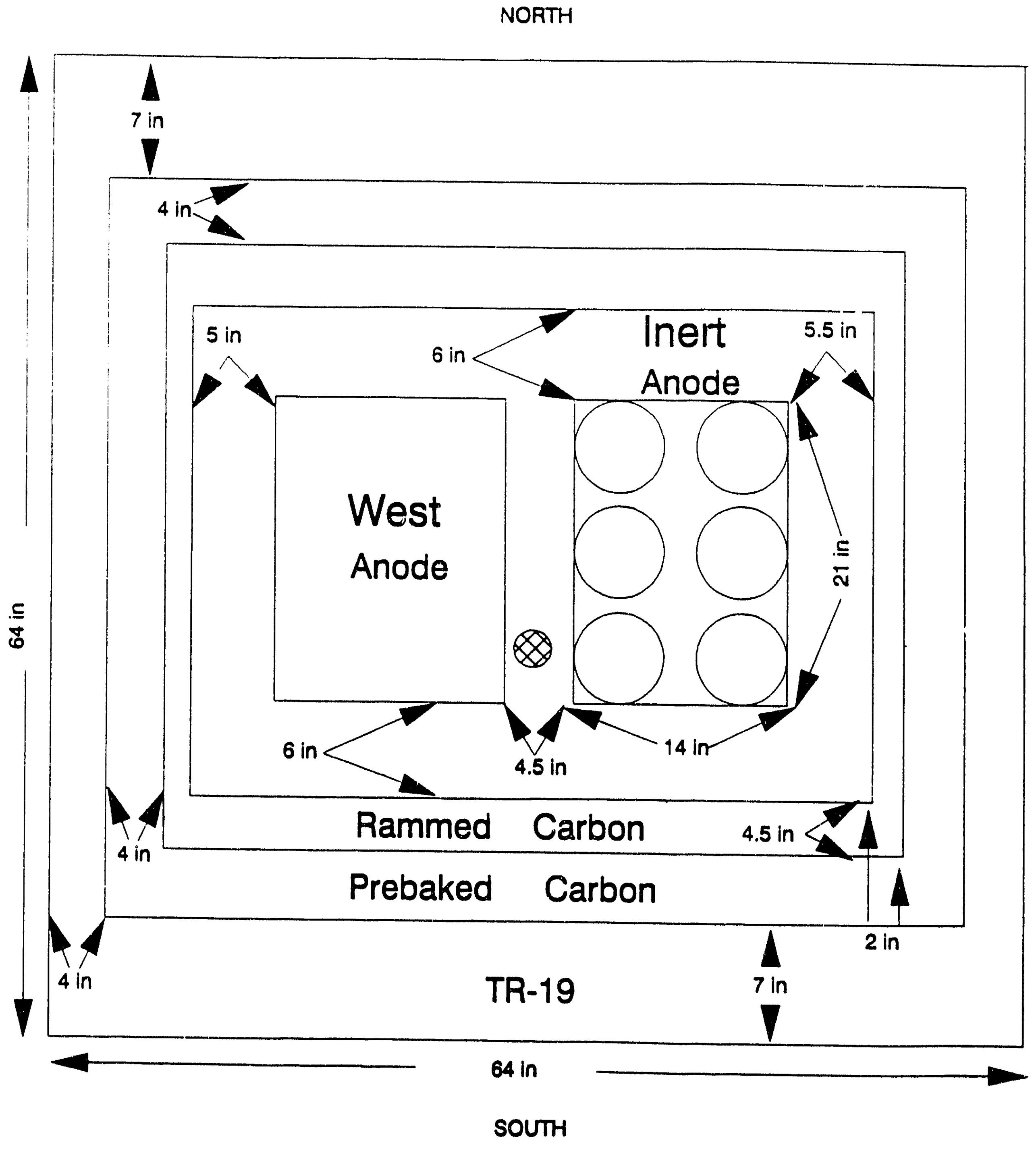

Figure 1.

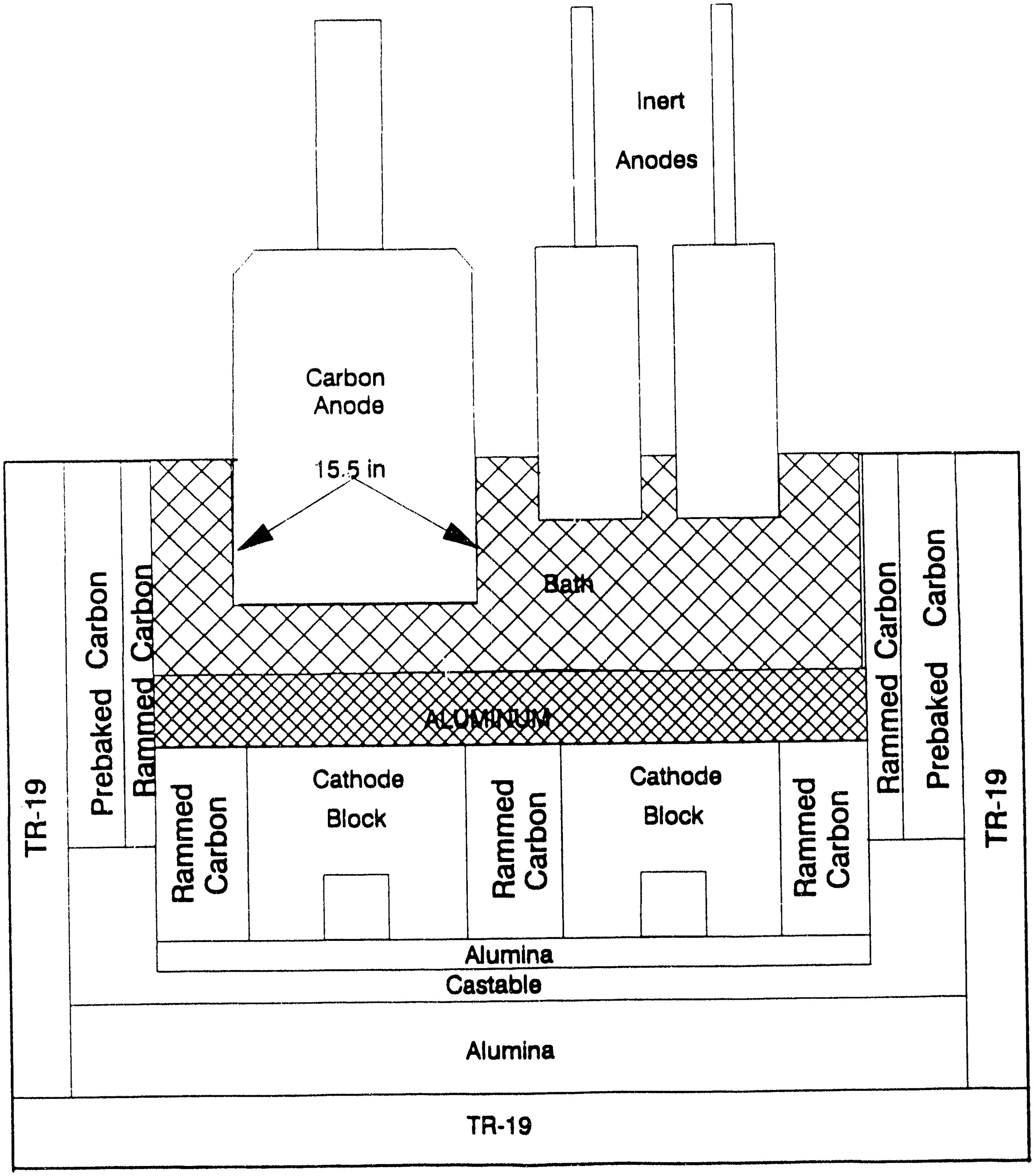

Figure 2. Pilot cell design, cross section.

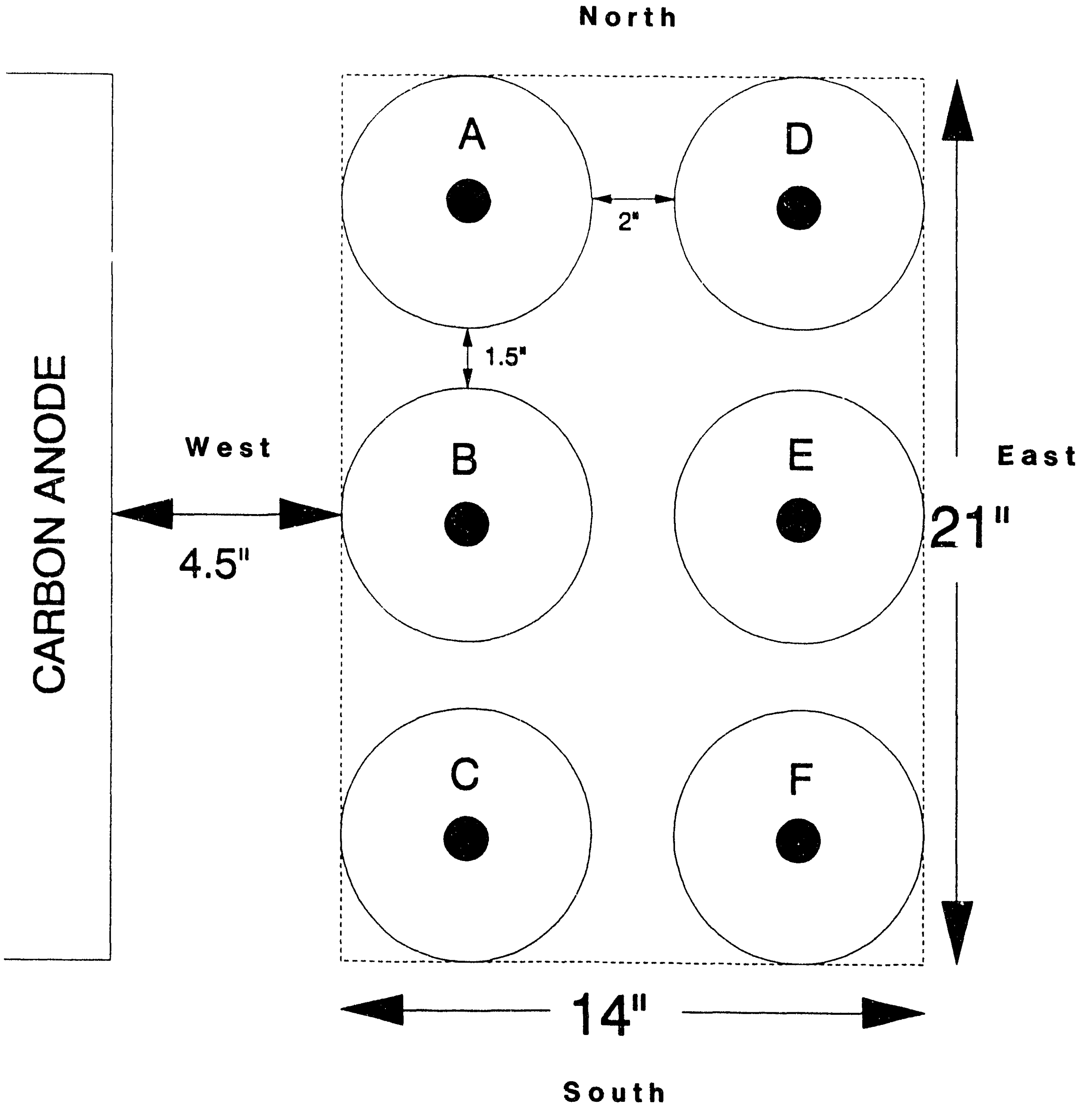

Figure 3. Position of inert anodes in the pilot cell.

Density on a sample from an untested anode was measured by Archimedes density method (ASTM C 373-72) and found to have a bulk density of 5.74 g/cm^3 and an apparent open porosity of ~0.76%.

The anodes were cylindrical with a diameter of 6 in., a thickness of 3 in., and an additional 1 in. lip on the top as shown in Figures 4 and 5. The bottom was rounded with a radius of 1.5 in. The current connector was an 18-in. long 1-in. diameter Inconel 601 threaded rod that was screwed into the threaded hole in the cermet. This rod was sheathed with a 3-in. long alumina sheath and alumina cement (Fisher C218 Alundum) covered the sheath; the top of the cermet, and the top of the sheath.

2.3 Data Collection

Routine data [collected and recorded hourly (detailed in Appendix 1)] consisted of cell voltages, anode currents, bath and metal depths, bath temperature and anode immersion. In addition, current to each cermet anode, voltage to the two anodes, total current to the carbon anode, and cluster were logged every 30 s with a data acquisition system. Bath and metal samples were taken every 4 h. The bath was analyzed for Cu, Ni, Fe, Ce, Al_2O_3, CaF_2, and the BR was determined. Metal was analyzed for Cu, Ni, Fe, and Ce.

Figure 4. Cu cermet anode prior to testing. Alumina cement coats the bottom of the Inconel connector rod next to the cermet.

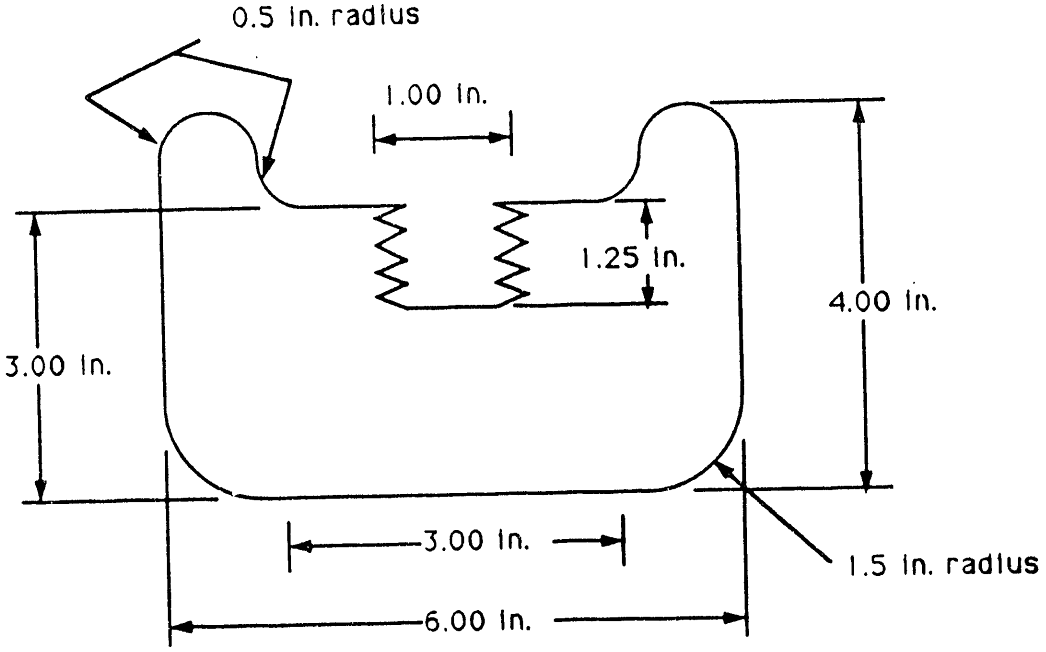

Figure 5. Cermet anode design.

3. TEST CELL OPERATION

The ELTECH test was divided into four main parts: operation with two carbon anodes, operation with a carbon anode and a 6-pack of cermets at our targeted "optimum" conditions, continued operation with the cermets but at a slightly higher CD, and continued operation of the cermets but at a lowered BR. Target "optimum" operating conditions were chosen based on the experiments conducted during the ELTECH Phase III laboratory test. During the pilot cell test these target conditions were not always achieved.

3.1 Target Operating Conditions

During the first part of the test (with the operation of the two carbon anodes) the goal of the testing was to reduce Fe, Ni, and Cu impurity levels in the metal to pre-PNL baseline levels. Reynolds proposed to accomplish this by siphoning out much of the metal and by adding additional Al to the cell to dilute the impurities. In addition, anode effects were planned to reduce the muck accumulated in the cell. Bath composition and Ce concentration would be brought up to the desired levels for the second phase of testing, which would take ~1 week or less.

The 6 cermet anodes were then to be introduced into the cell simultaneously (with current on) and operated at "optimum" conditions. In Phase III laboratory testing CEROX coatings were most dense and continuous, and corrosion was lowest at a BR of 1.5 to 1.6. Therefore, the target "optimum" BR for the second phase of the pilot cell testing was 1.5. In the Phase III laboratory tests there was also a slight decrease in corrosion with decreasing CD. At high CD extensive oxidation of the Cu and increased porosity led to an increase in cell voltage with time. Therefore, a CD of 0.5 A/cm^2 (equivalent to ~90 A per anode)[7] was chosen for the second phase of testing.

Most of the laboratory work was performed with baths saturated with alumina and research has shown that decreasing the alumina concentrations increases the dissolution of the oxide phases and corrosion of the Cu cermet.[3,6] Thus, maintaining the bath at 90 to 100% of alumina saturation (~8 to 10% Al_2O_3, depending on temperature) was targeted. Operating temperature was targeted at 990 to 1000°C.

Changes in operating conditions were implemented after 377 h of operation in order to assess the effect that the CD and BR have on inert anode performance. The CD was raised to a maximum target of 115 A on any anode (~0.65 A/cm^2); after ~160 additional hours, the BR was lowered to a target of 1.15 and ran for 77 h under the lower BR and higher CD conditions.

The target starting Ce concentration in the bath for coating the anodes was between 0.5 and 1.0 wt%. Laboratory testing demonstrated that the Ce concentration in the bath should remain above 0.175% to maintain a coating, once it is present on an anode. The target concentration for the pilot test for maintenance of the CEROX coating was set between 0.2 and 0.33%. With an expected Ce partition coefficient of between 5 and 12, the Ce concentration in the metal was expected to be around 1 to 4%.

3.2 Actual Test Conditions and Exchange of Anodes

Following the PNL test the cermets were removed and the cell was operated with two carbon anodes. Anode effects were forced to eliminate the muck. The impurities in the metal were monitored with a target impurity level of that before the PNL test (Table 1), 100 lb of aluminum were added to the cell to help reduce the impurities. After 13 d the impurities had leveled out as shown in Figure 6; but the ELTECH baseline was still higher than the PNL baseline level (Table 1) for Ni and Fe. CeF_3 was then added to the cell.

The inert anodes were preheated by placing them on the deck plate of the cell and covering them with kaowool. The electrodes remained there for ~5 d at which time they were placed into the anode holder over the crust until they reached between 130 and 230° C. The anodes were covered with kaowool and slowly lowered into the bath for over 26 h or until they had reached about 600 to 650°C (thermocouples were placed at the tops of the anodes). At 1:30 p.m. September 14, the inert anode cluster was immersed in the bath and the anodes were conducting current.

Upon introduction to the bath, it was observed that anode 2 in position B (Anode B1) was cracked and incapable of carrying any significant amount of current. This anode was removed from the cell after ~1 hour.

Analysis and observation of a small independently current controlled 4 cm diameter reference anode was used to determine that the Ce concentration in the bath was insufficient to form a CEROX coating. Therefore, current to the inert cluster was turned off and additional CeF_3 was added to the cell. At 1:00 p.m. September 15, the current was turned back on and anode coating began. Examination of the reference anode showed that a CEROX coating was forming and analysis of the bath showed that the Ce had reached ~0.85%.

On September 23, after 213 h of operation, a piece of anode 1 in position A (Anode A1) broke off and fell into the bath. The piece was recovered and the rest of A1 was removed. On September 26, anode 3 in position C (Anode C1) was removed from the cell as scheduled after 275 h of operation. The anode was cracked.

Table 1. Baseline impurity levels.

PNL	
Iron	0.380 wt%
Copper	0.050 wt%
Nickel	0.003 wt%
ELTECH	
Iron	0.440 wt%
Copper	0.020 wt%
Nickel	0.030 wt%

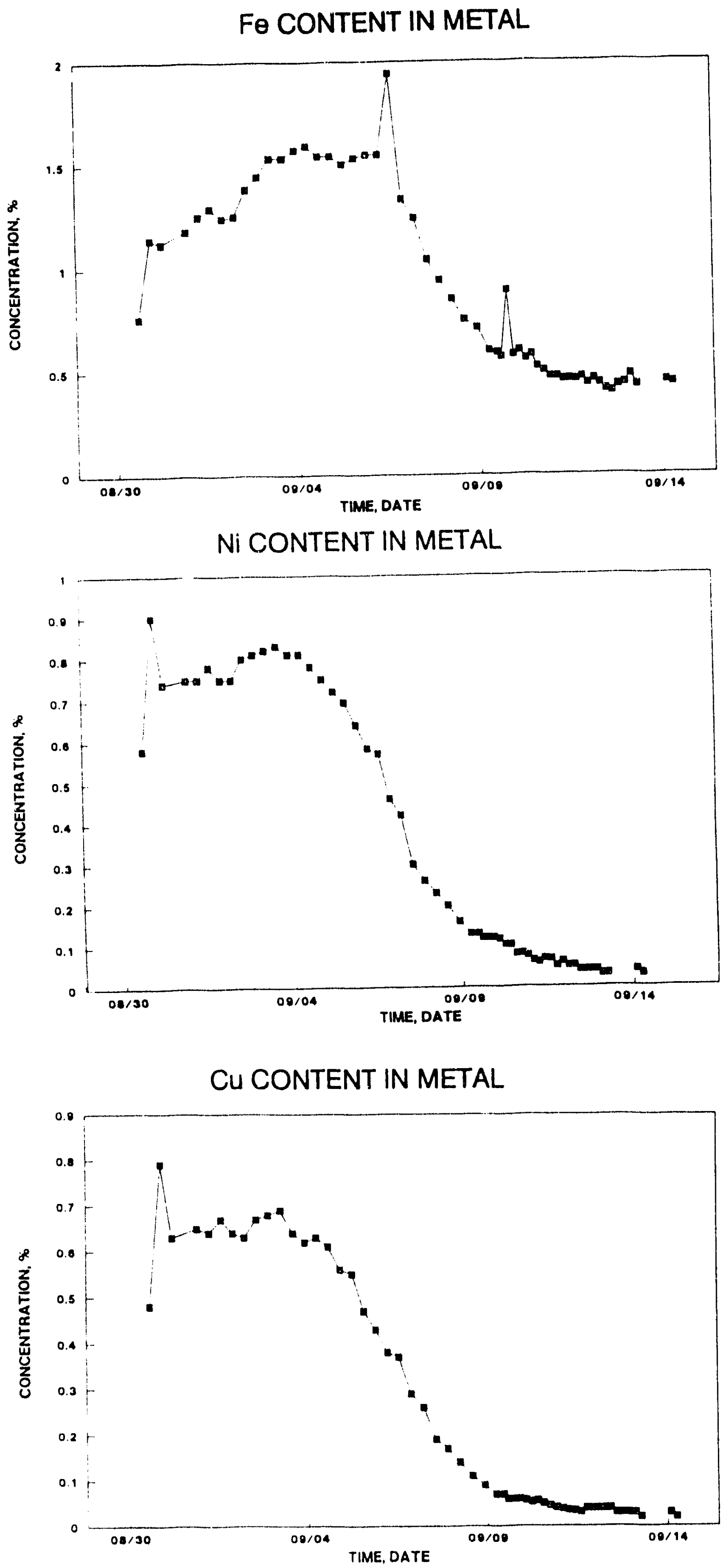

Fe CONTENT IN METAL

Ni CONTENT IN METAL

Cu CONTENT IN METAL

Figure 6. Impurity levels in the aluminum during operation of the pilot cell with two carbon anodes.

Anodes 7, 8, and 9 were preheated with the same procedure as described for anodes 1 through 6. Additional CeF_3 was added to the cell, and the anodes were lowered into the cell in positions A, B, C (Anodes A2, B2 and C2) September 27 and began conducting current. Because of the problems with cracking of the anodes, no other exchanges of anodes were made during the test.

On September 30, after A2, B2, and C2 had been in the cell for ~74 hours, the maximum current on any one anode was raised from 90 to 115 A to determine if the increased current would effect anode corrosion. After ~160 hours of the higher CD, the BR was reduced to 1.15 (while CD was maintained at 0.65 A/cm^2) to assess its effect on anode corrosion. After 77 h of further testing, the cermet 6-pack of anodes were removed and the cermet testing was completed. Table 2 summarizes the lifetime of each anode.

The bath level and metal inventory during the test is shown in Figures 7 and 8. The anode immersion (representative of anodes in position D, E, and F) is shown in Figure 9. Anodes A2, B2, and C2 were immersed 1 in. less than D, E, and F. Anode-cathode distance is shown in Figure 10 and reflects the build-up of muck on the bottom of the cell during the test.

3.3 Current and Cell Voltage

Because the current to the cermets could not be individually controlled, current to the cluster was controlled such that the highest current any individual anode would carry was the target current. For the first part of the cermet testing the maximum current to an anode was 90 A; the other anodes carried ≤90 A. The current maintained by the individual cermets varied during the length of the test and is shown in Figures 11 through 16. In general, at the beginning of the test the current carried by anodes in positions A, B, and C was lower than the current carried by anodes in positions D, E, and F. Because the carbon anode carried a larger current in order to maintain a molten electrolyte, the carbon anode was at a higher potential than the cermet anodes. The higher potential of the carbon anode resulted in reduced current through the inert cluster, resulting in anodes A, B, and C carrying less current than D, E, and F during the first half of the test.

As the experiment progressed, a layer of frozen bath formed under and around the top of the anodes in positions D, E, and F. This area was the coolest in the cell because most of the heat was generated by the carbon anode. In addition, a frozen ledge may have formed on the bottom of the cell inhibiting current flow at positions D, E, and F resulting in increased current to flow to anodes in positions A, B, and C. Thus, toward the end of the test, positions A, B, and C were carrying more current than positions D, E, and F.

Table 2. Anode summary.

Anode	Cell Position	Operation	Comments
1	A	9/15-23 213 h	Section of anode broke, removed
2	B	9/14 1 h	Cracked down center of anode at start-up
3	C	9/15-26 275 h	Removed on schedule
4	D	9/15-10/10 614 h	End of test
5	E	9/15-10/10 614 h	End of test
6	F	9/15-10/10 614 h	End of test
7	A	9/27-10/10 312 h	End of test
8	B	9/27-10/10 312 h	End of test
9	C	9/27-10/10 312 h	End of test

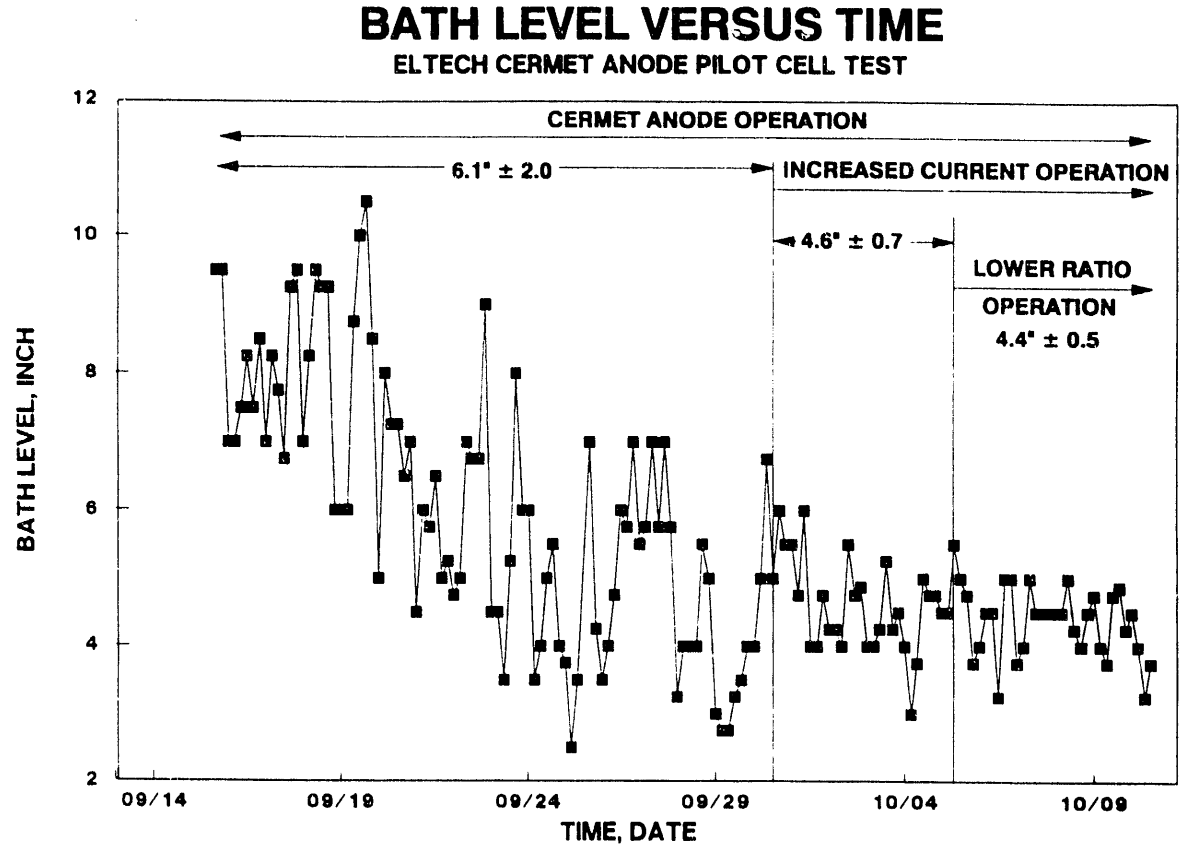

Figure 7.

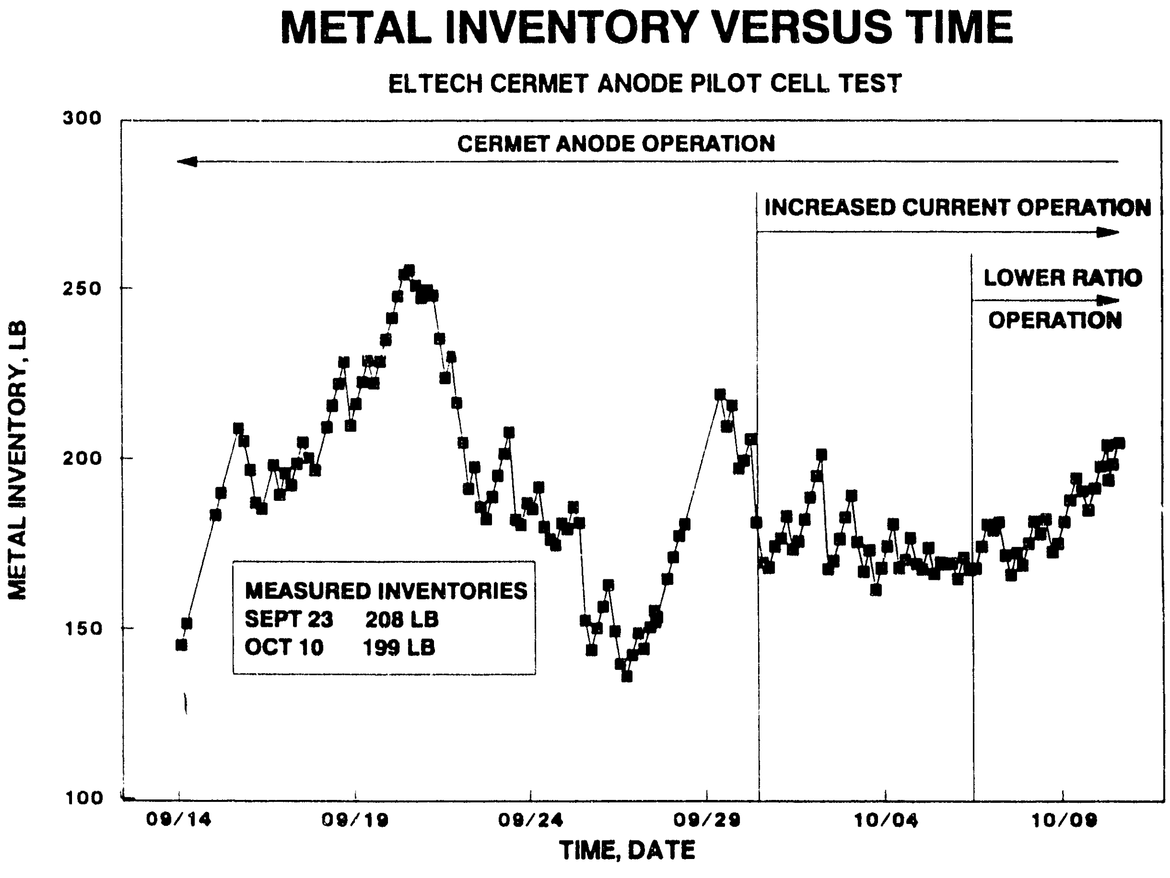

Figure 8.

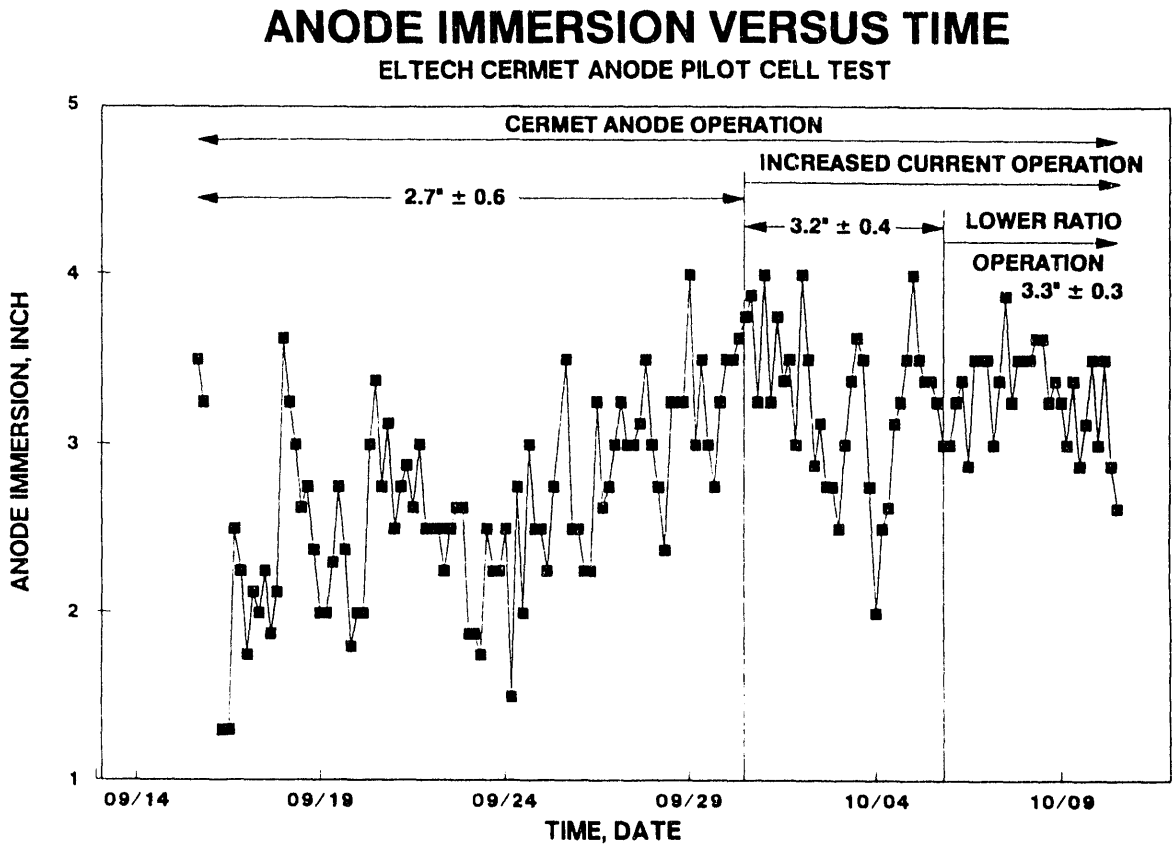

Figure 9.

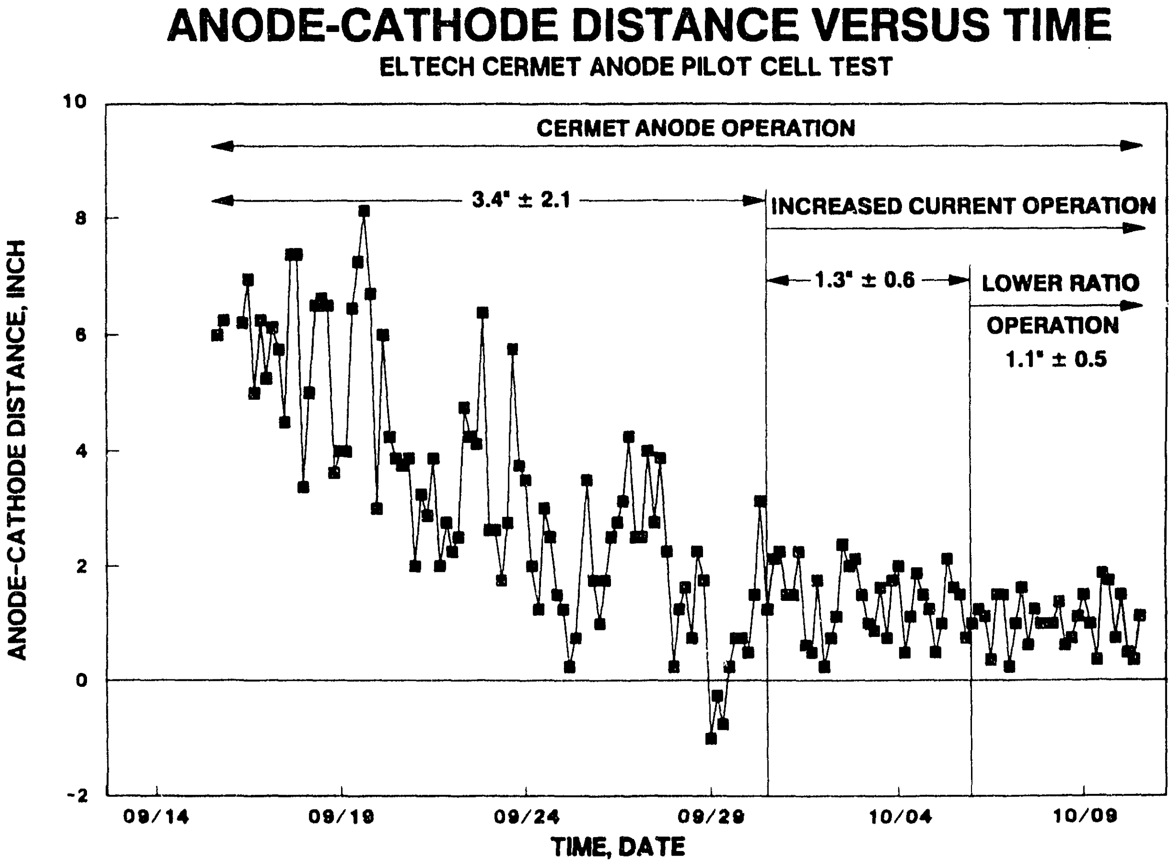

Figure 10.

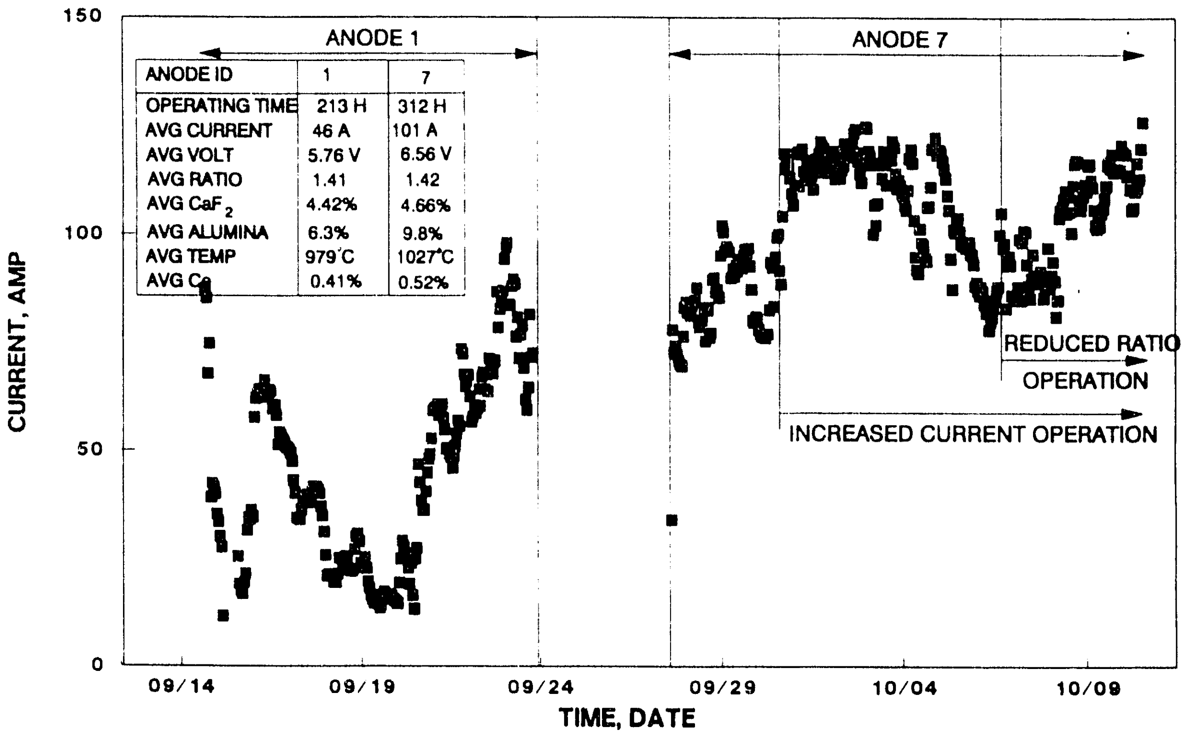

CURRENT VERSUS TIME

POSITION A

ANODE ID	1	7
OPERATING TIME	213 H	312 H
AVG CURRENT	46 A	101 A
AVG VOLT	5.76 V	6.56 V
AVG RATIO	1.41	1.42
AVG CaF_2	4.42%	4.66%
AVG ALUMINA	6.3%	9.8%
AVG TEMP	979°C	1027°C
AVG Ce	0.41%	0.52%

Figure 11.

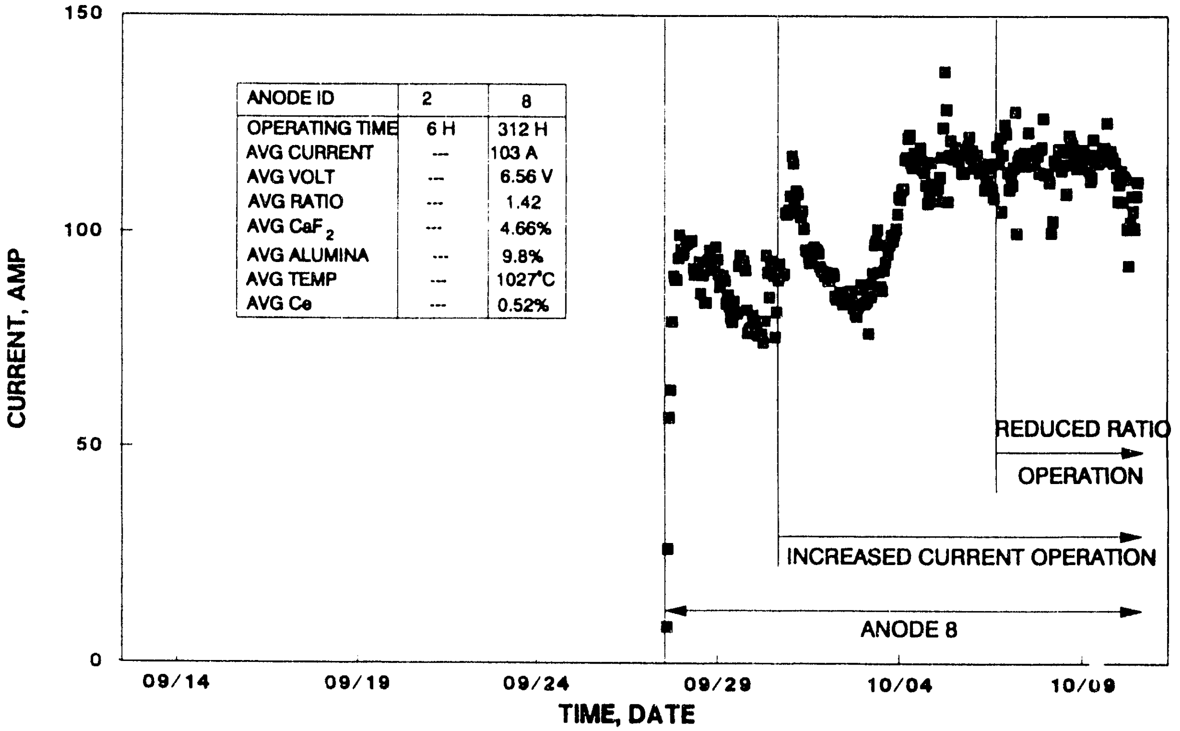

CURRENT VERSUS TIME

POSITION B

ANODE ID	2	8
OPERATING TIME	6 H	312 H
AVG CURRENT	---	103 A
AVG VOLT	---	6.56 V
AVG RATIO	---	1.42
AVG CaF_2	---	4.66%
AVG ALUMINA	---	9.8%
AVG TEMP	---	1027°C
AVG Ce	---	0.52%

Figure 12.

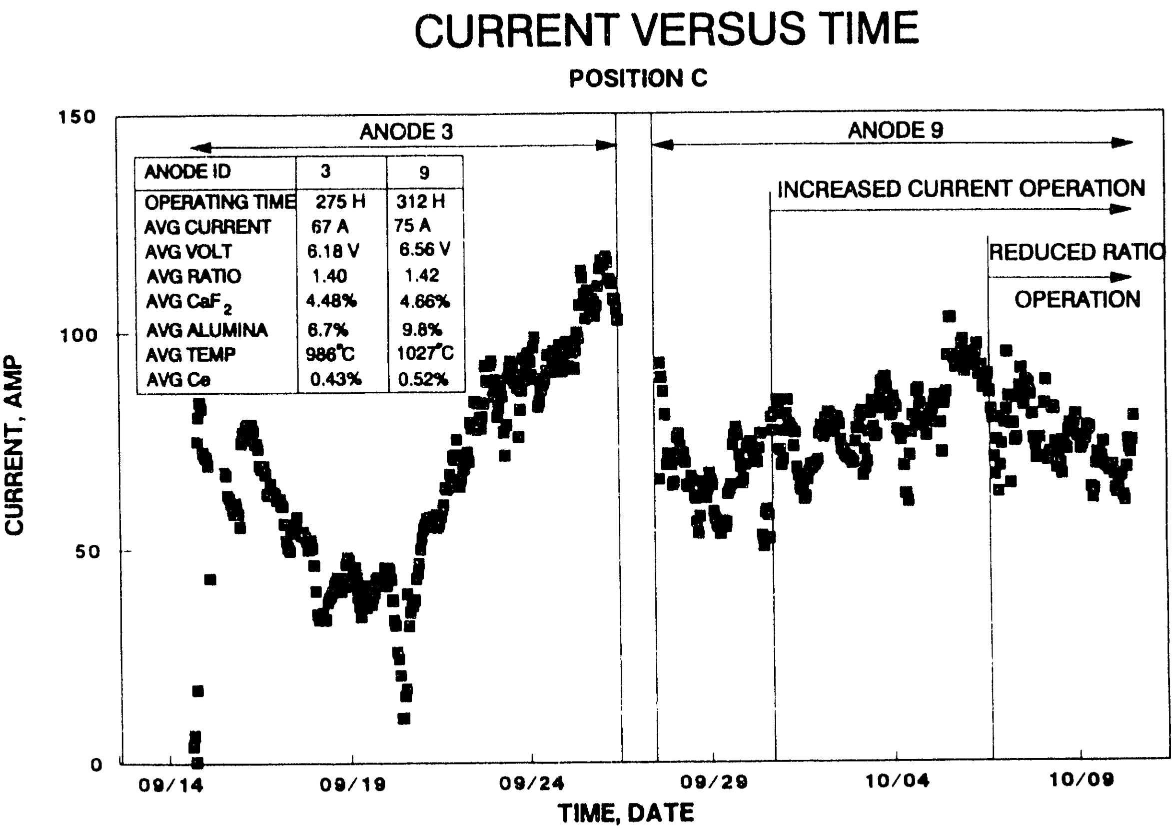

ANODE ID	3	9
OPERATING TIME	275 H	312 H
AVG CURRENT	67 A	75 A
AVG VOLT	6.18 V	6.56 V
AVG RATIO	1.40	1.42
AVG CaF_2	4.48%	4.66%
AVG ALUMINA	6.7%	9.8%
AVG TEMP	986°C	1027°C
AVG Ce	0.43%	0.52%

Figure 13.

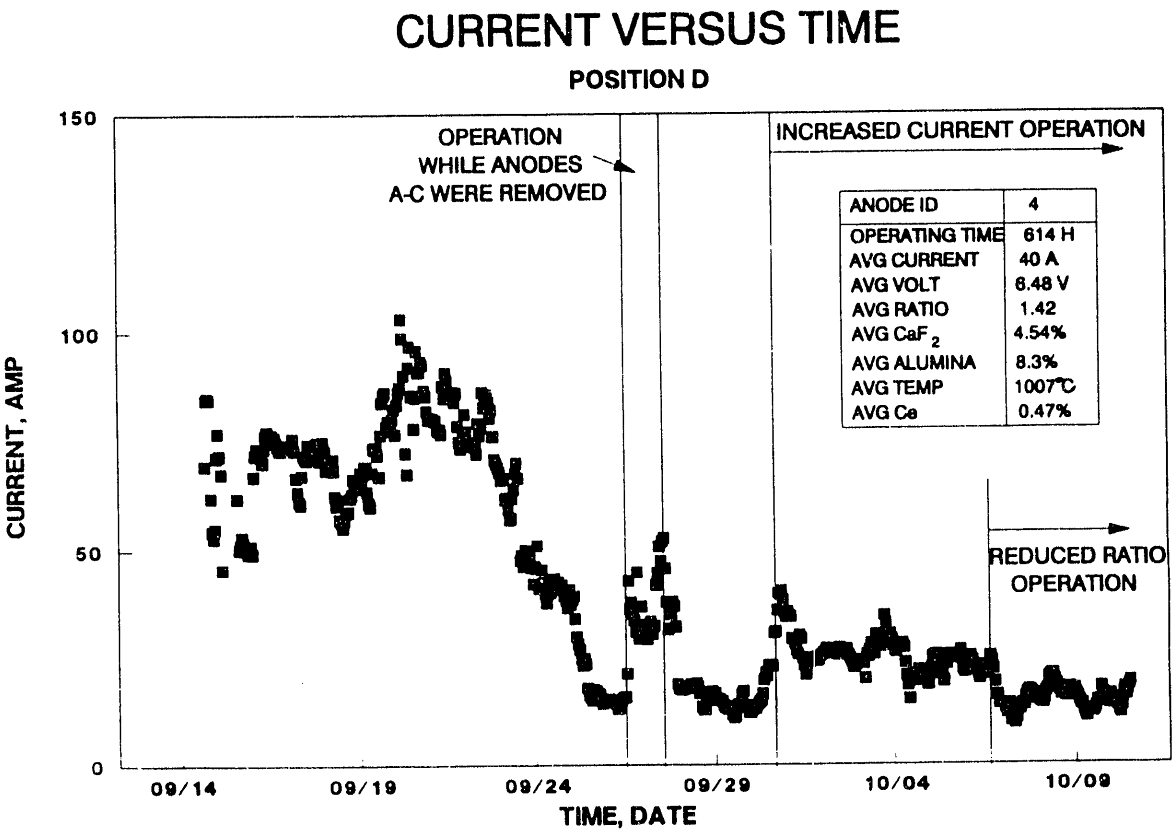

ANODE ID	4
OPERATING TIME	614 H
AVG CURRENT	40 A
AVG VOLT	6.48 V
AVG RATIO	1.42
AVG CaF_2	4.54%
AVG ALUMINA	8.3%
AVG TEMP	1007°C
AVG Ce	0.47%

Figure 14.

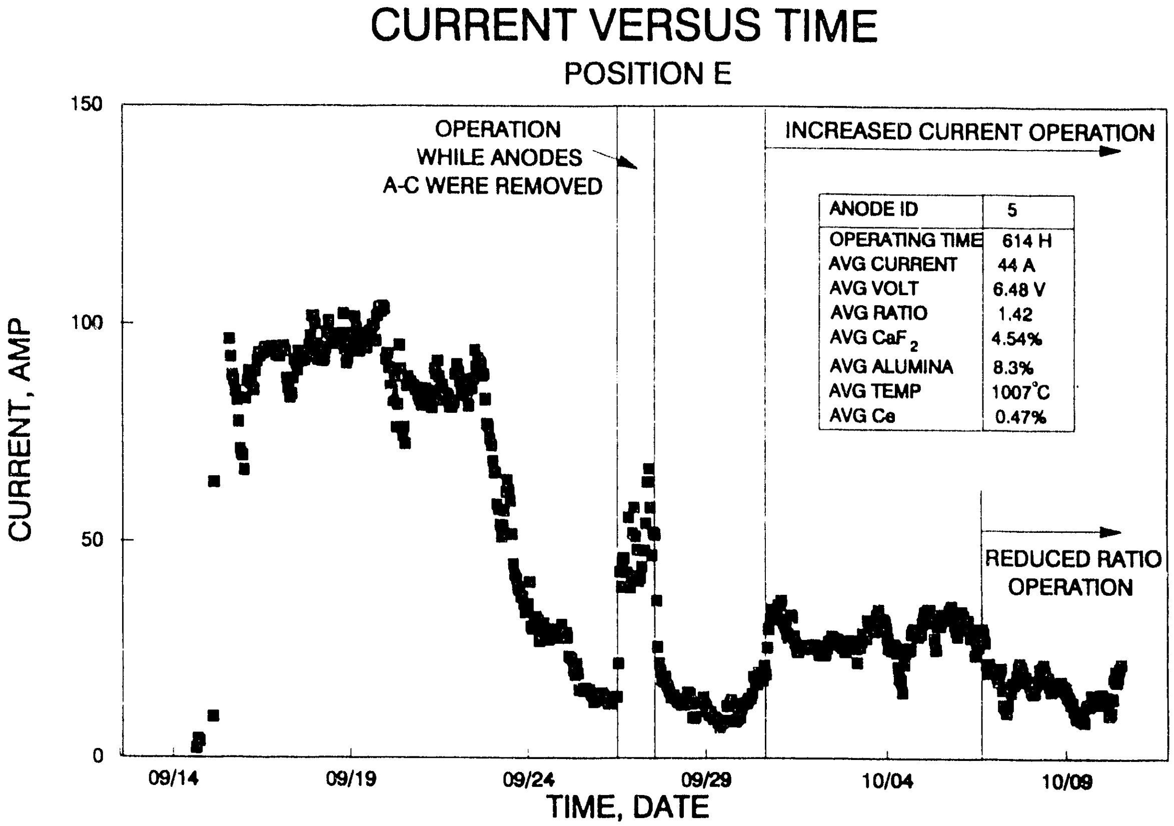

ANODE ID	5
OPERATING TIME	614 H
AVG CURRENT	44 A
AVG VOLT	6.48 V
AVG RATIO	1.42
AVG CaF_2	4.54%
AVG ALUMINA	8.3%
AVG TEMP	1007°C
AVG Ce	0.47%

Figure 15.

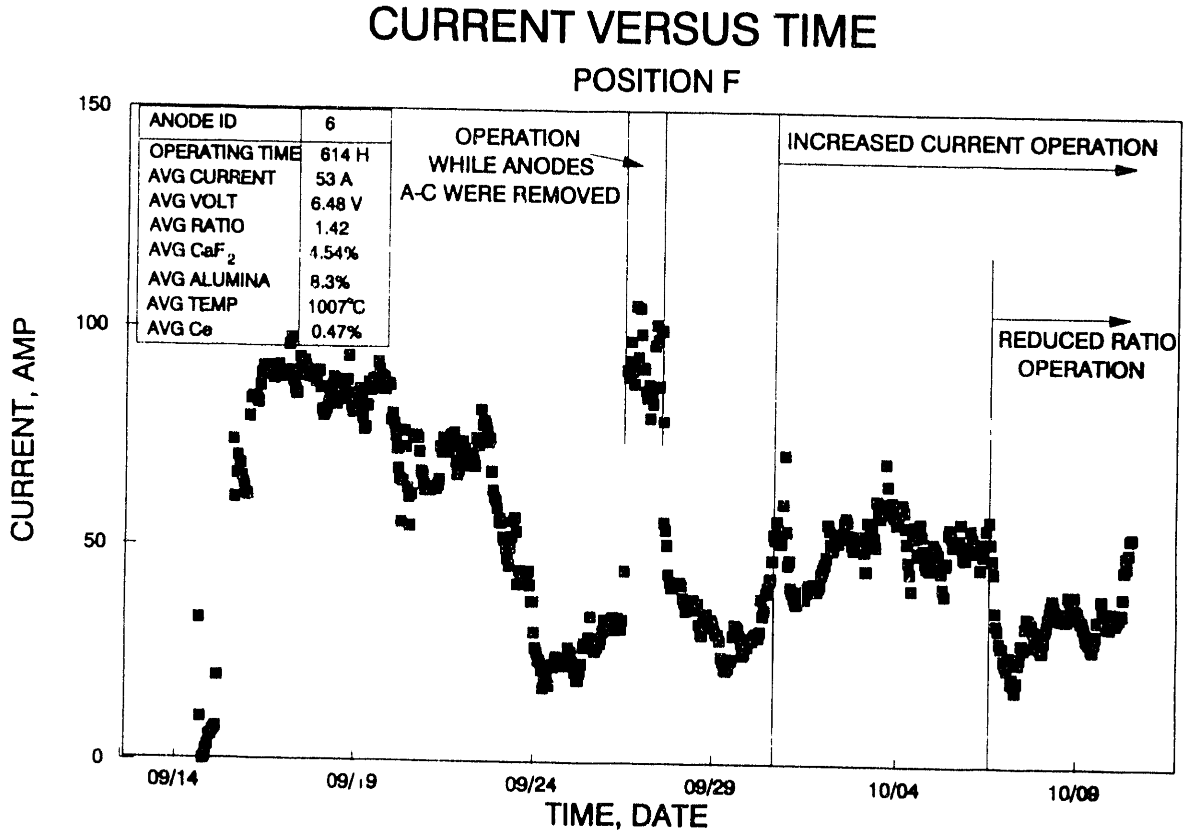

ANODE ID	6
OPERATING TIME	614 H
AVG CURRENT	53 A
AVG VOLT	6.48 V
AVG RATIO	1.42
AVG CaF_2	4.54%
AVG ALUMINA	8.3%
AVG TEMP	1007°C
AVG Ce	0.47%

Figure 16.

The carbon anode current ranged between 1.8 and 3 kA and was varied during the test in an effort to keep the cell molten and to reduce the effect on the current to the cermet anodes. The voltage on the carbon anode ranged between 7 and 11 V. The cell voltage on the cermet anodes is shown in Figure 17 and averaged around 7 V.

3.4 Bath Composition and Temperature

The BR variation during the test is shown in Figure 18. The BR was very irregular and averaged slightly less than the targeted BR of 1.5 during the first three parts of testing. During the low BR testing, the BR averaged 1.16. The temperature also varied considerably throughout the experiment as shown in Figure 19. The temperature averaged around 980°C during the first half of the testing. However, halfway through the second phase of the test, the temperature became more erratic and reached temperatures of higher than 1050°C. The temperature variations were forced by MTL to try to dissolve some of the muck on the bottom of the cell so there would be a more even current distribution to the anodes. The temperature variations resulted in bath freezing and melting throughout the latter part of the test.

During the first phase of the cermet testing, the Al_2O_3 content averaged ~7%, which was around 70% of saturation. During the later phases of the test (high CD, low BR), the alumina concentration rose to an average >10% and was between 88 to 96% of saturation as shown in Figures 20 and 21. It appears the problems with dissolution of Al_2O_3 and mucking began at 80% of alumina saturation. The percent of saturation is based on the formula of Skybakmoen.[8] CaF_2 content during the testing averaged 4.2 to 4.6% (Figure 22).

3.6 Ce Concentration

The Ce concentration in the bath was the key parameter to control in order to grow and maintain a CEROX coating. Ce content in both the bath and metal is shown in Figures 23 and 24. A level of about 0.9% Ce was needed in the bath to deposit the CEROX coatings on the first five cermet anodes (September 15, 1991). As the coating formed on the anodes, the Ce concentration in the bath rapidly dropped. After coating, the Ce concentration in the bath was then maintained at 0.3 to 0.4%. About halfway through the test (as the cell began to accumulate Al_2O_3 muck and cycles of freezing and thawing were experienced with the temperature changes) the Ce levels became more erratic and more difficult to control. It appeared that Ce was freezing out with some of the muck, giving lower concentrations in the bath, and then as temperature increased, the Ce would again dissolve into the bath, giving high bath concentrations. The fluctuating and higher Ce levels were compounded by the fact that additional CeF_3 was added to the cell when anodes A2, B2, and C2 were placed in the cell. Thus, Ce concentration was much more erratic and higher during the second

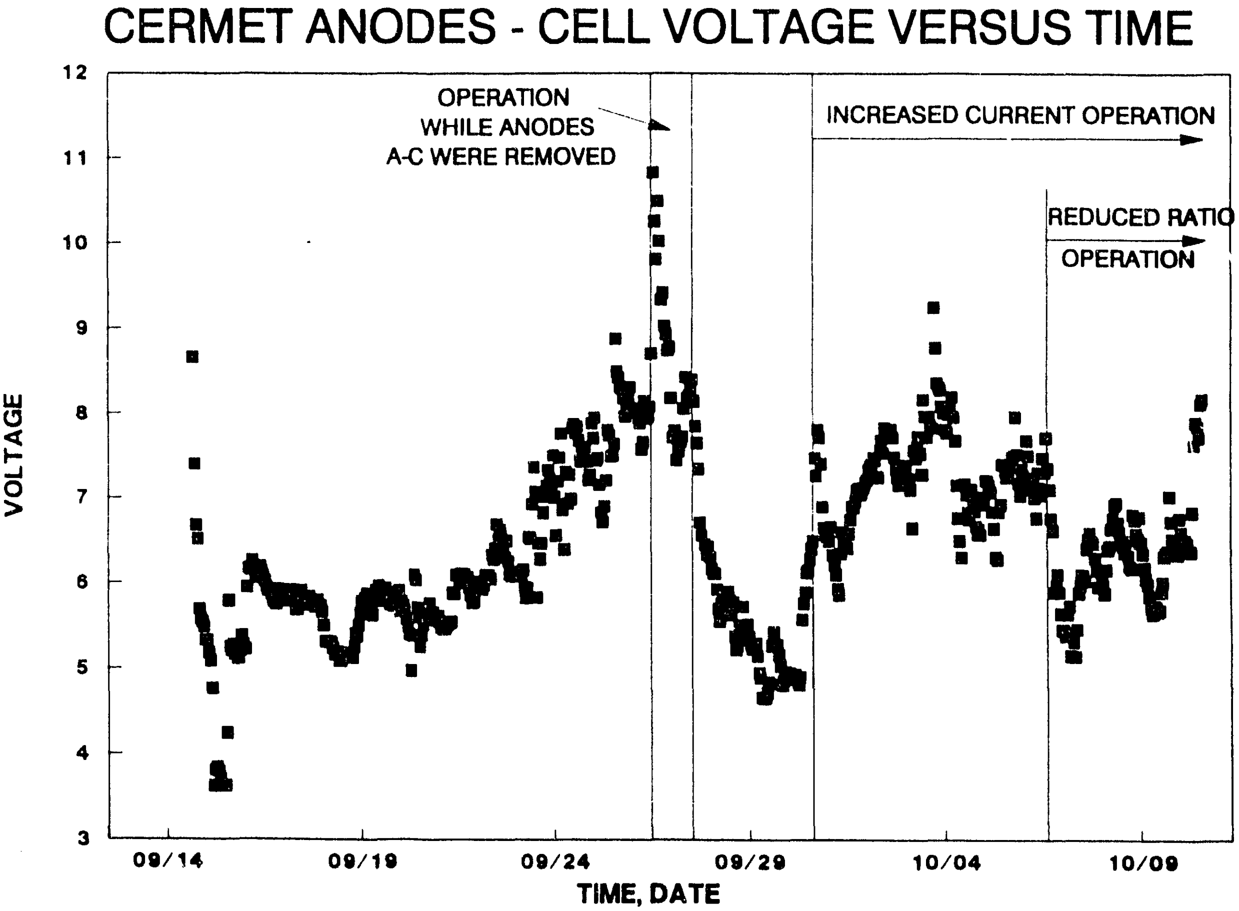
CERMET ANODES - CELL VOLTAGE VERSUS TIME
OPERATION WHILE ANODES A-C WERE REMOVED
INCREASED CURRENT OPERATION
REDUCED RATIO OPERATION
VOLTAGE
12
11
10
9
8
7
6
5
4
3
09/14
09/19
09/24
09/29
10/04
10/09
TIME, DATE

Figure 17.

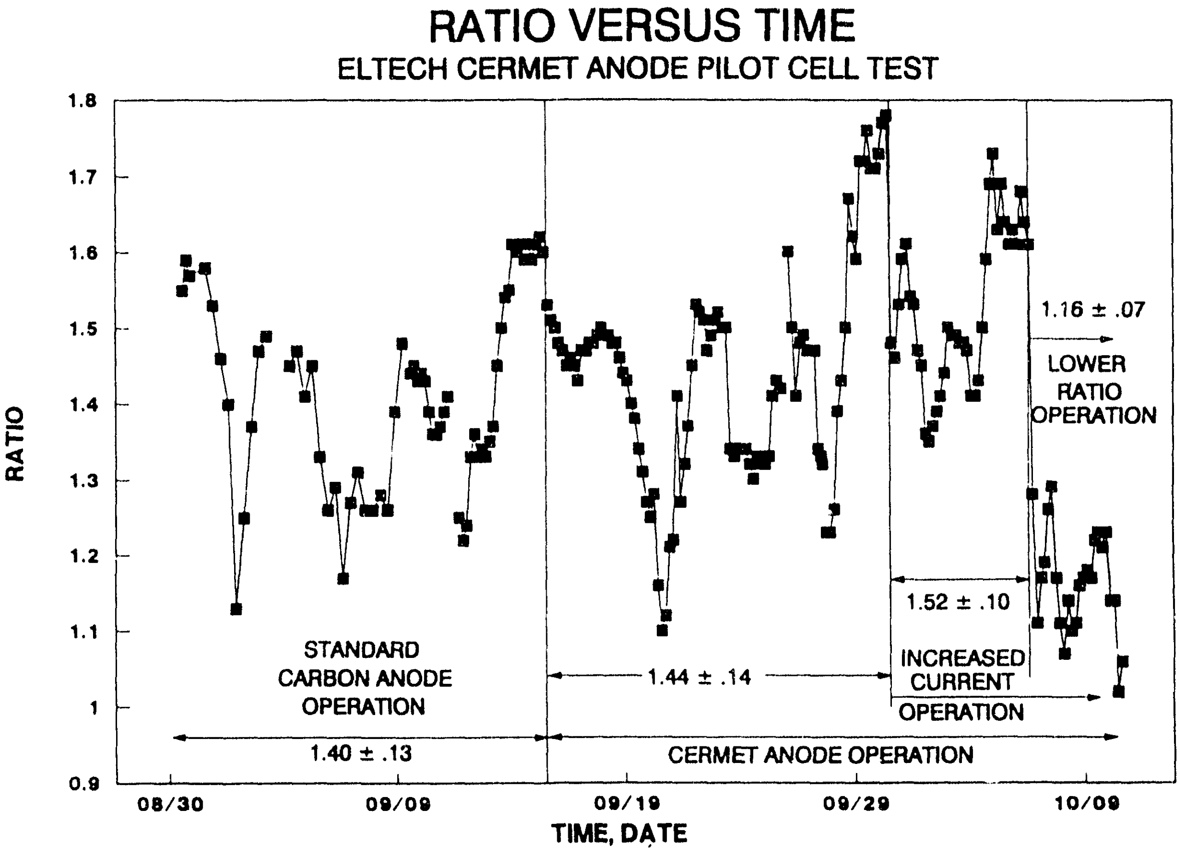

Figure 18.

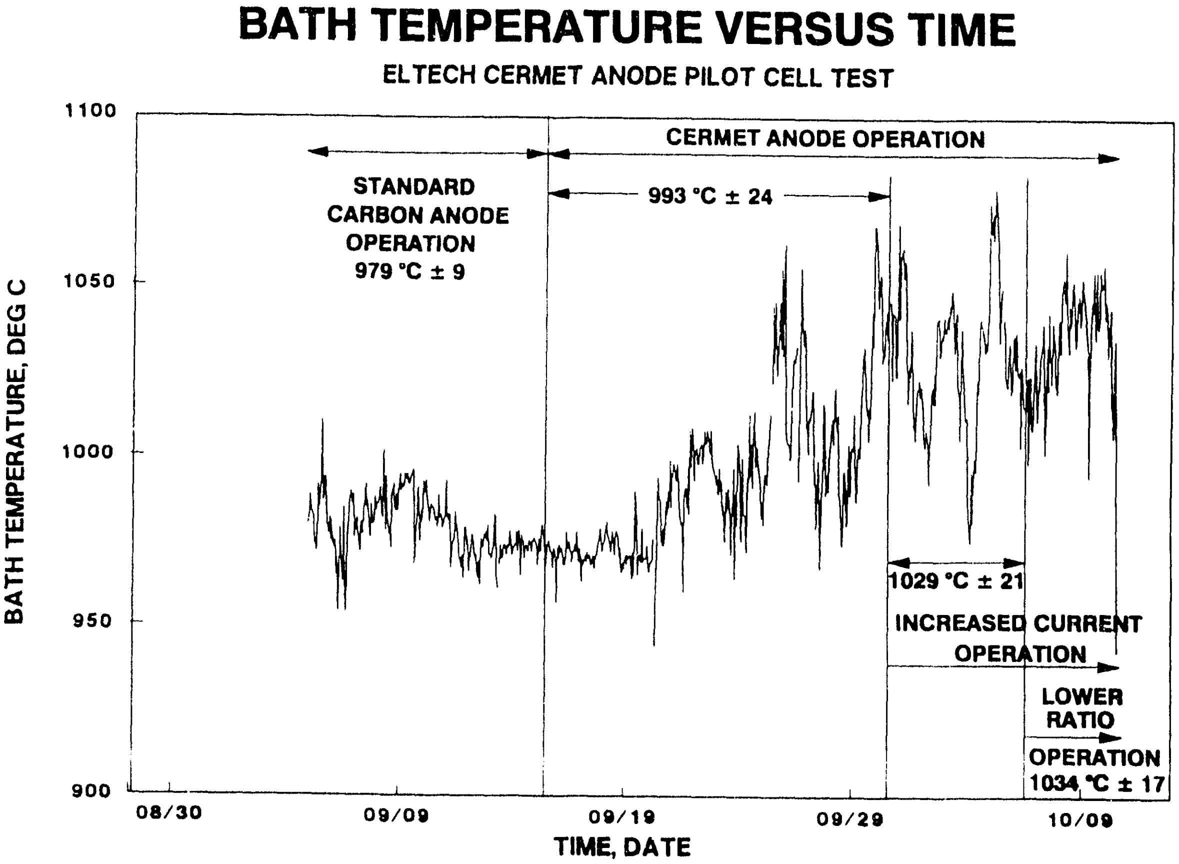

Figure 19.

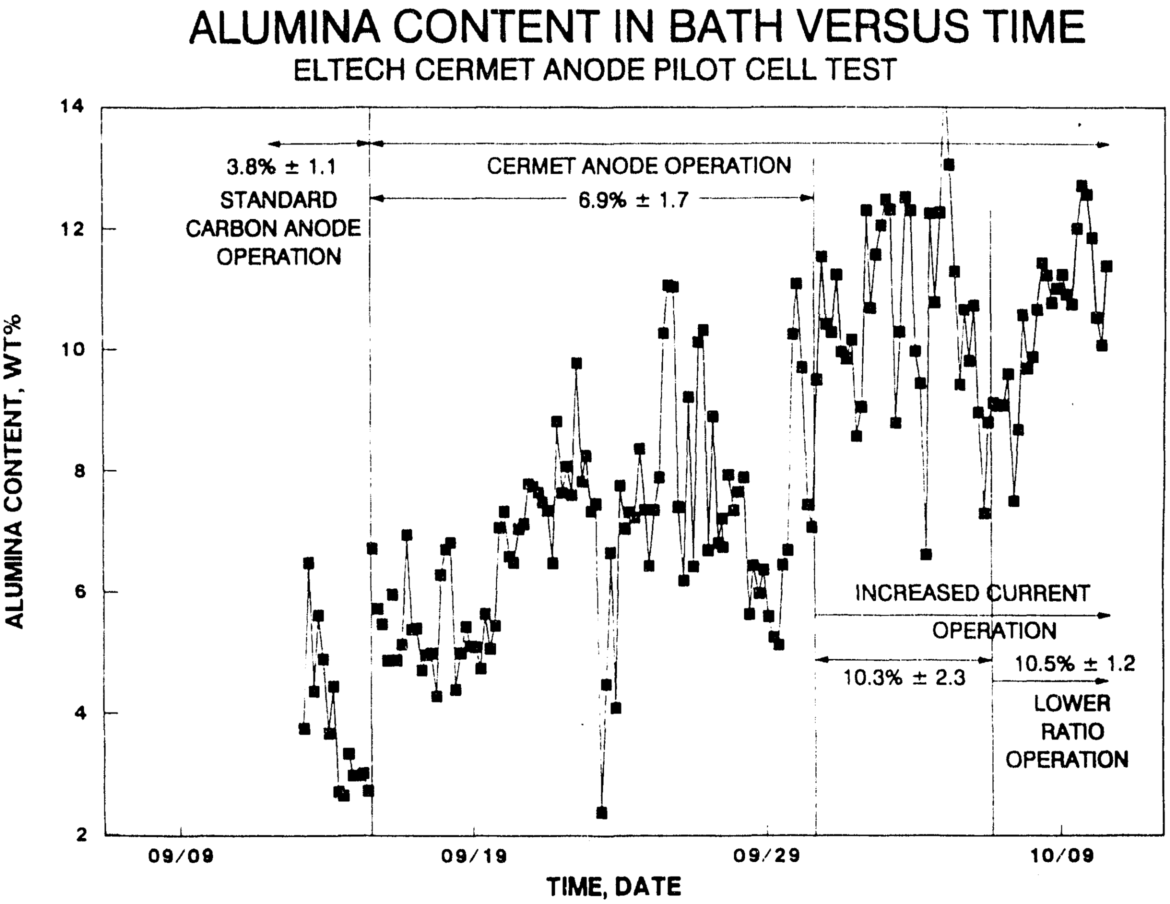

Figure 20.

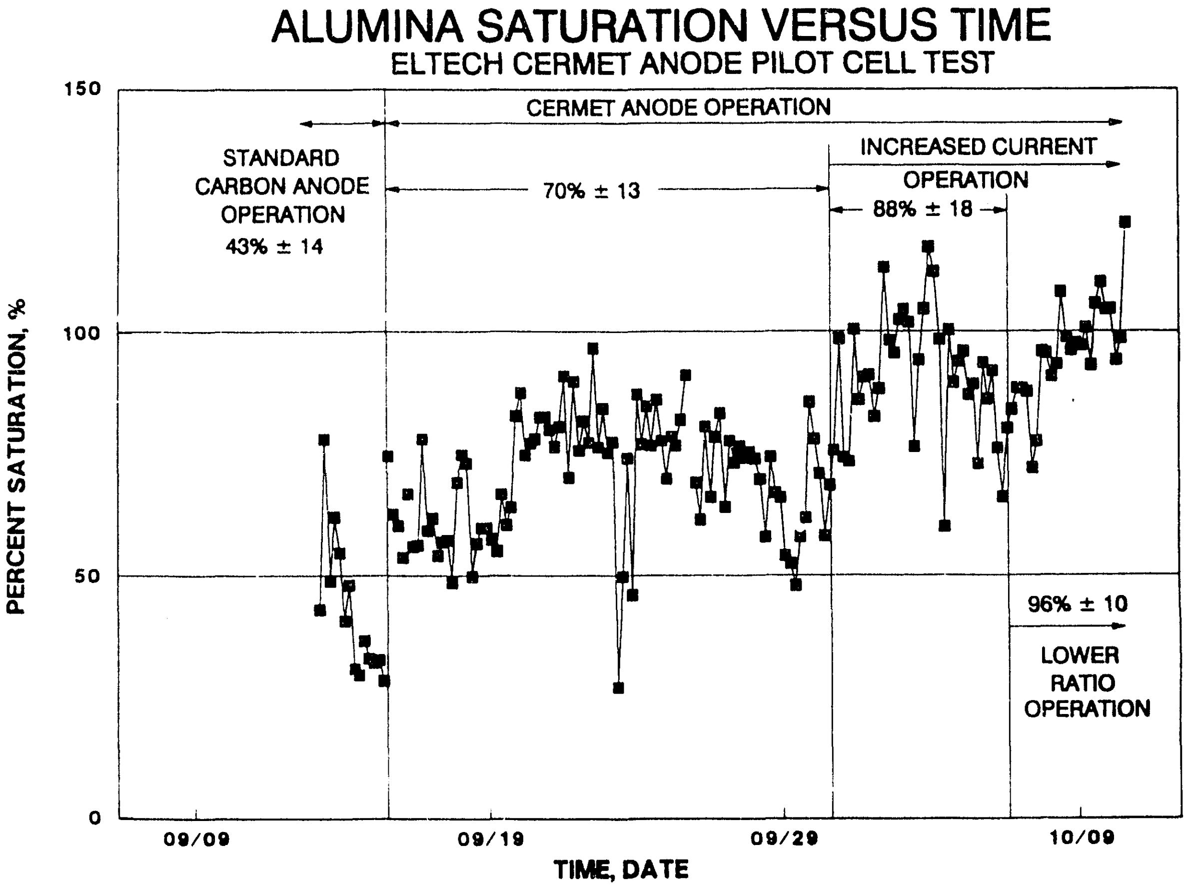

Figure 21.

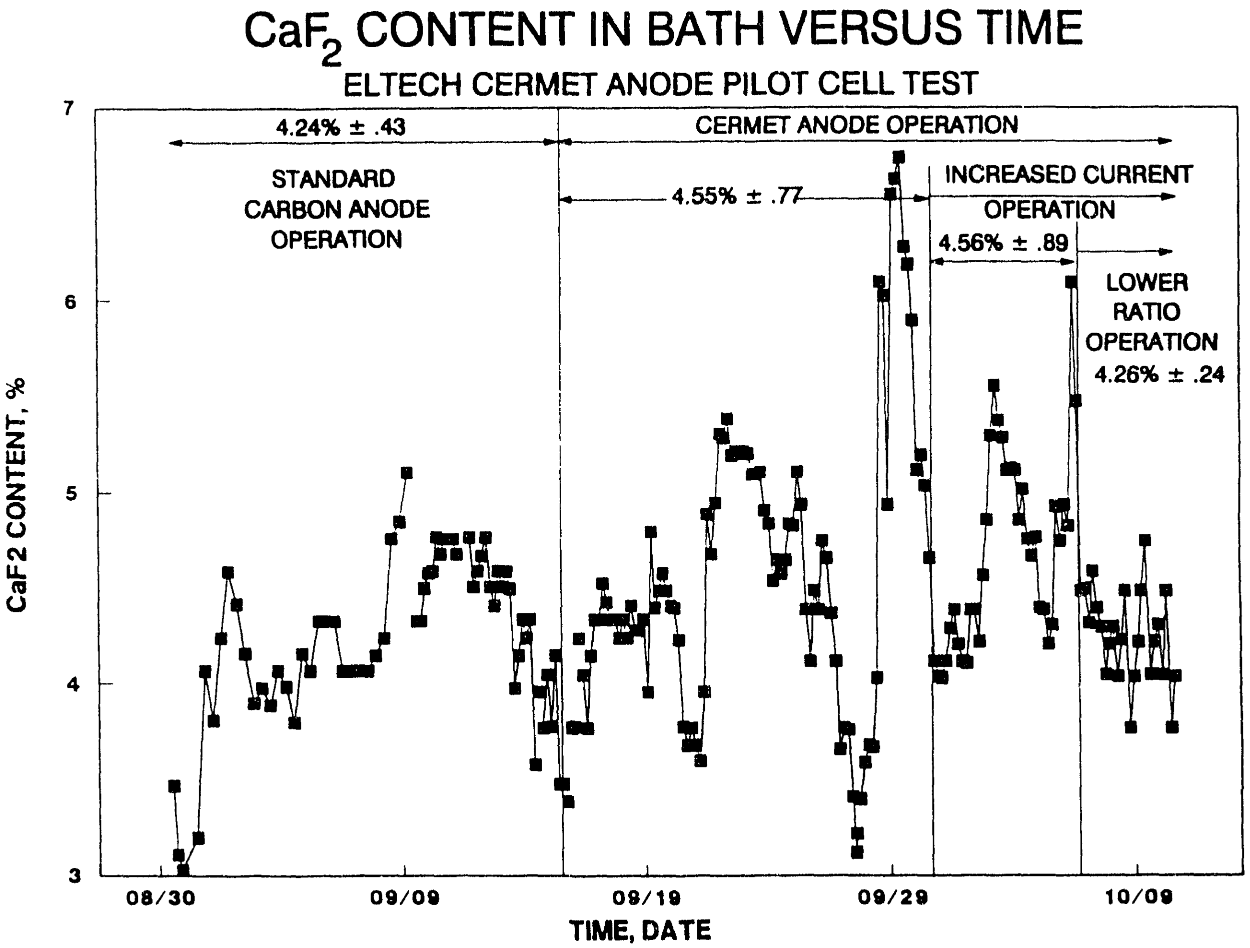
CaF_2 CONTENT IN BATH VERSUS TIME
ELTECH CERMET ANODE PILOT CELL TEST
4.24% ± .43
CERMET ANODE OPERATION
STANDARD
CARBON ANODE
OPERATION
4.55% ± .77
INCREASED CURRENT
OPERATION
4.56% ± .89
LOWER
RATIO
OPERATION
4.26% ± .24
7
6
5
4
3
CaF2 CONTENT, %
08/30
09/09
09/19
09/29
10/09
TIME, DATE

Figure 22.

Figure 23. Ce CONTENT IN THE METAL

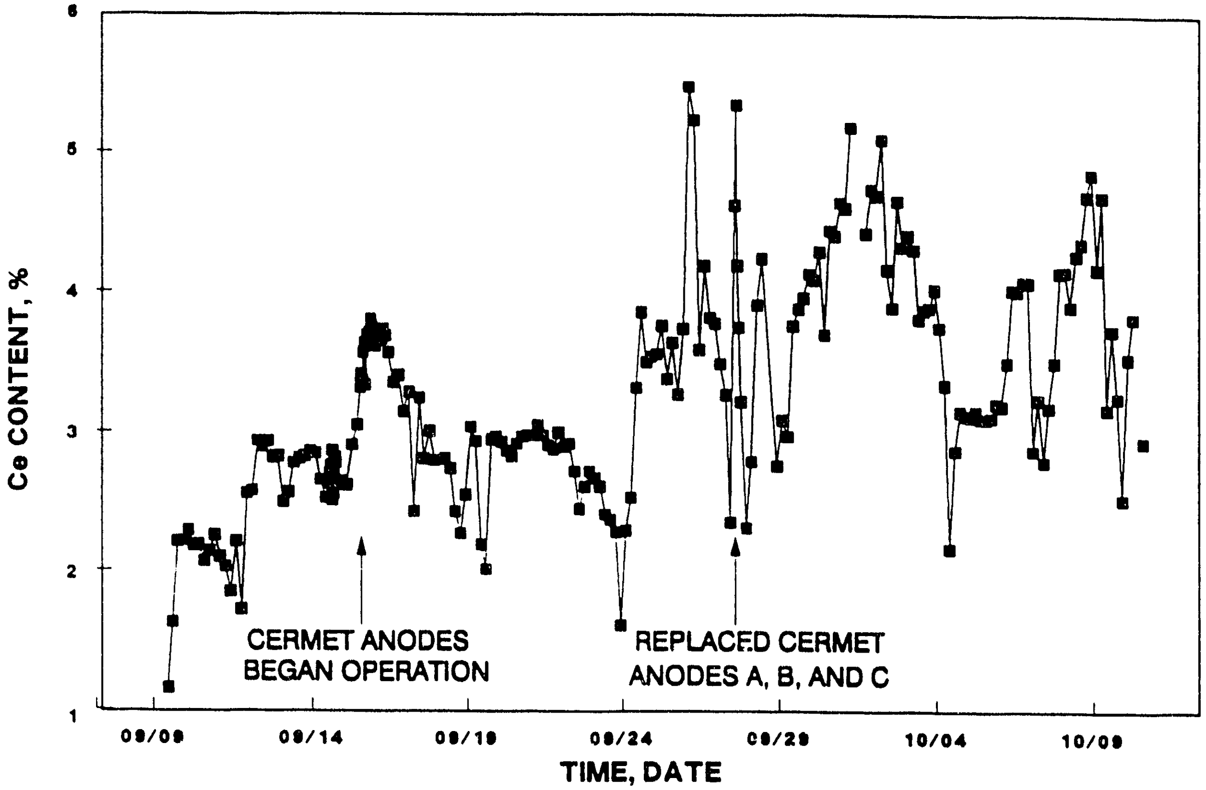

Figure 24. Ce CONTENT IN THE BATH

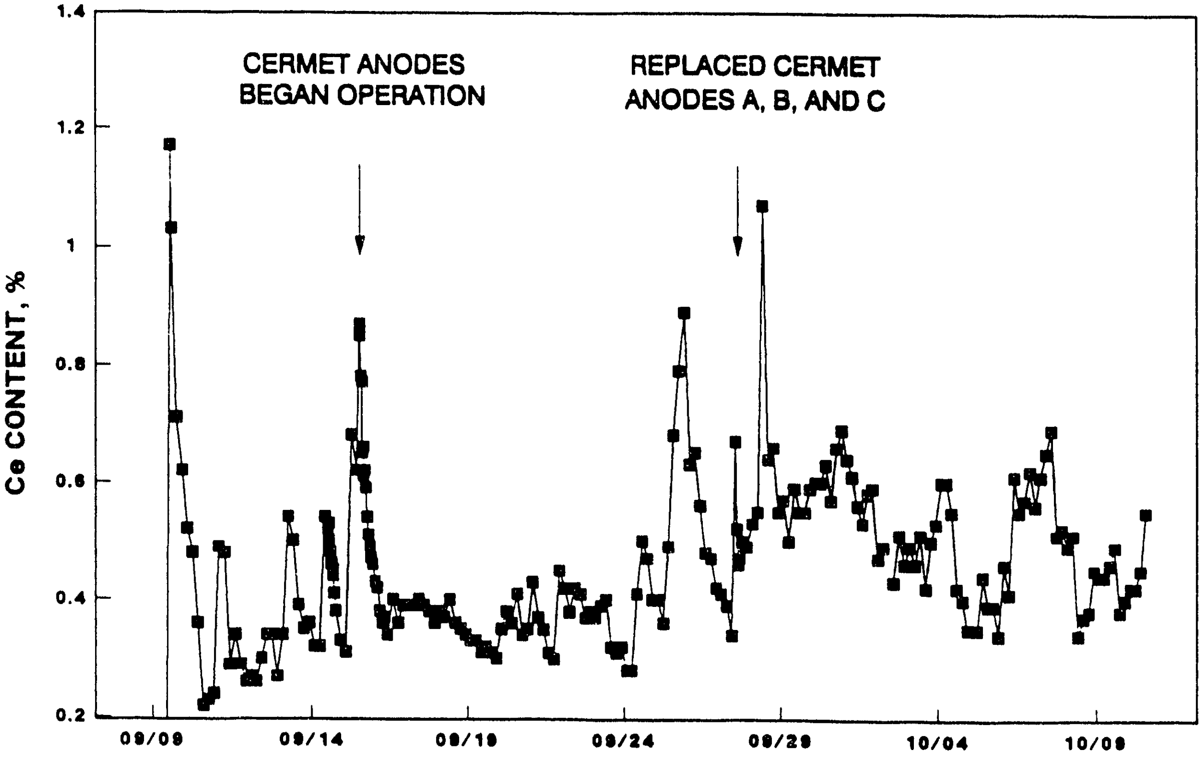

half of the testing than was originally targeted.

The Ce concentration in the metal followed the same trends as that in the bath. In addition (as the bottom of the cell mucked up) it was suspected that the metal pool became segregated into numerous pools, which caused a lack of equilibrium between the pools. As with the Ce bath concentration, the Ce in the metal was much more erratic and higher than was expected, particularly for the second half of the test.

Laboratory tests indicate that the partition coefficient for Ce in the metal and bath (wt% Ce_{metal}/wt% Ce_{bath}) ranges from 8 to 10 for BR between 1.2 and 1.6. The Ce wt% in the metal versus Ce wt% in the bath is shown in Figure 25. The partition coefficient ranged from ~3 to 10. The scatter in the data is probably partly because of measurements taken when the system was not at equilibrium. In addition, temperature, alumina content, and BR fluctuated during testing and could have lead to a range of distribution coefficients.

Table 3 summarizes the average bath composition and temperature for each phase of testing.

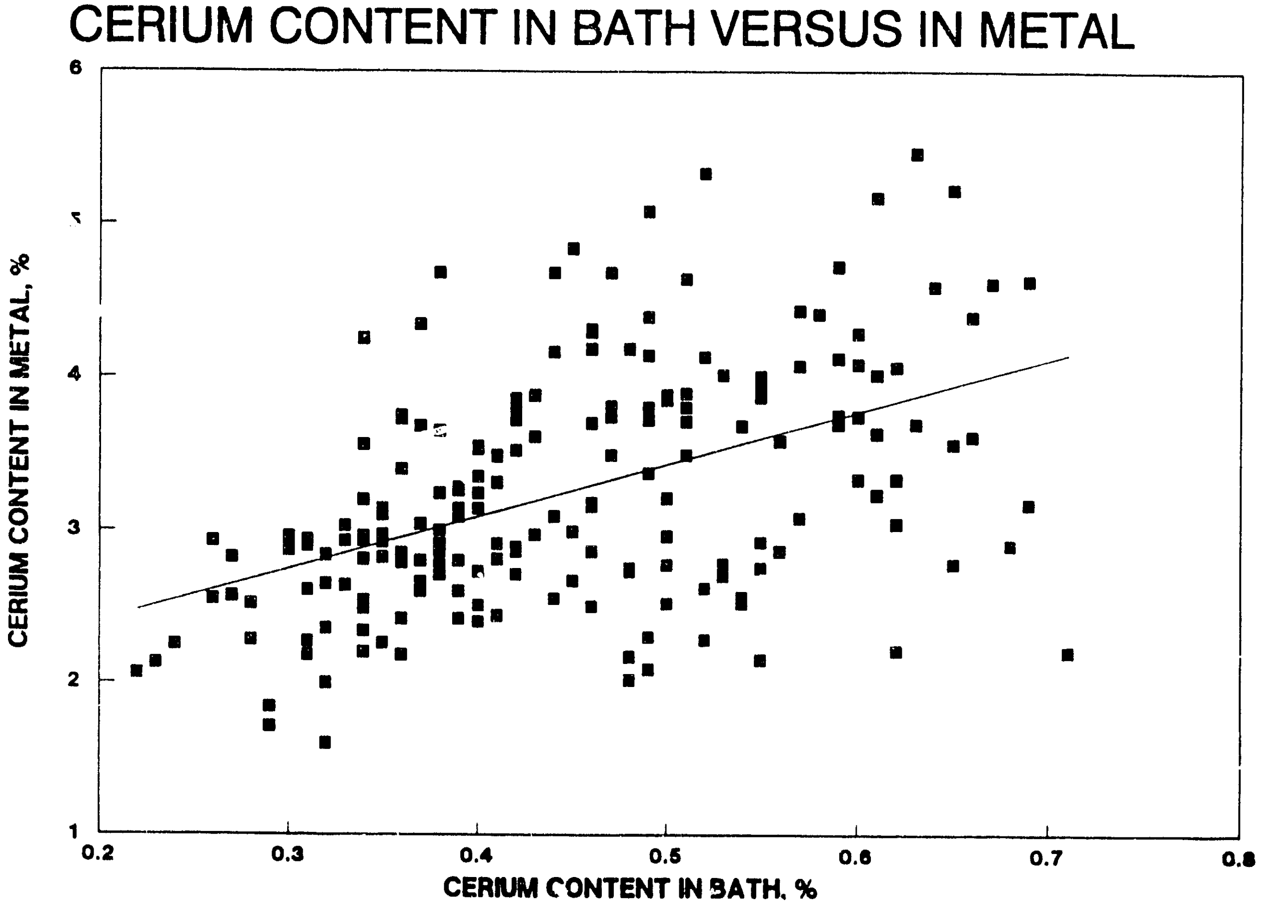
CERIUM CONTENT IN BATH VERSUS IN METAL
CERIUM CONTENT IN METAL, %
1
2
3
4
5
6
0.2
0.3
0.4
0.5
0.6
0.7
0.8
CERIUM CONTENT IN BATH, %

Figure 25.

Table 3. Average operating conditions during the four phases of testing.

Date	Sept 1-15	Sept 15-30	Sept 30-Oct 6	Oct 6-10
Current	Carbon anode	Max 90 A	Max 115 A	Max 115 A
Ratio	1.40	1.44	1.52	1.16
CaF_2	4.24%	4.55%	4.56%	4.26%
CeF_3	-----	0.47%	0.50%	0.49%
Temp.	979°C	993°C	1029°C	1034°C
Al_2O_3	3.8 wt%	6.9 wt%	10.3 wt%	10.5 wt%
% Sat.	43%	70%	88%	96%

4. RESULTS AND DISCUSSION

The anode corrosion and the protection of the CEROX coating were judged from the impurities in the Al pool and from macroscopic and microscopic examination of the anodes. Where data is available, a comparison was made to the uncoated cermets tested by PNL.

4.1 Impurities in the Al Pool

The Ni, Cu, and Fe impurities measured in the Al are shown in Figures 26, 27, and 28. The spikes in the data are probably caused by sampling (see Appendix 1) the small, and possibly segregated, metal pool that was present in the cell.

One way to quantify the deterioration of the inert anodes is to calculate a corrosion rate based on these changing impurity levels. By assuming a constant corrosion rate and considering the Al inventory, contamination of the Al can be calculated and compared to the actual impurities found in the bath. Corrosion rates of 0.075, 0.13, and 0.30 lb/d for Cu, Ni, and Fe respectively, fit the data best as shown in Figures 29, 30, and 31. Assuming the losses are actually Cu, NiO, and Fe_2O_3 and assuming a density of 6 g/cm^3, this amounts to ~0.1 mm surface area loss/d. There was a period between September 9,1991 and October 10,1991 where the data are substantially lower than the model. During this period there were only three or four cermets present in the bath instead of the usual five or six.

The Fe data show considerably more scatter than the other contaminants and a poorer fit to the model. It is assumed that the use of iron tools for cell maintenance and sampling was responsible. The ratio of Cu:Ni:Fe in the cermet anodes is 1:1.98:1.65. The ratio of the best fit corrosion rates is 1:1.74:4. The Cu and Ni contamination correspond fairly well with their relative amounts in the anode material, but the Fe contamination is much higher. Reynolds assumed that the Fe in the Al metal from the corrosion of the anodes should be in the correct ratio of the Fe in the anode; therefore, the Fe from the anode must be ~0.12 lb/d and the remainder must be from other sources.

The Ni, Cu, and Fe corrosion from the PNL test is shown in Figures 32, 33, and 34. Corrosion models were fit to the data for the time period of under their "optimum" conditions (BR ~1.3, CD ~0.5 A/cm^2 or less). For that time period, the corrosion data fit the model very well as shown in Figures 35, 36, and 37. The calculated corrosion during their test was 0.13, 0.26, and 0.31 lb/d Cu, Ni, and Fe, respectively. The calculated surface area loss was ~0.2 mm/d. The Fe in their test was also higher than would be expected from the anode. The calculated corrosion was in the ratio of 1:2:2.4 (Cu:Ni:Fe) as compared to the untested anode ratio of 1:1.98:1.65. Fe corrosion, recalculated based on the ratio of Fe in the cermets, was 0.21 lb/d. Corrosion in the PNL test is about

Ni Content in Metal

ELTECH Cermet Anode Pilot Cell Test

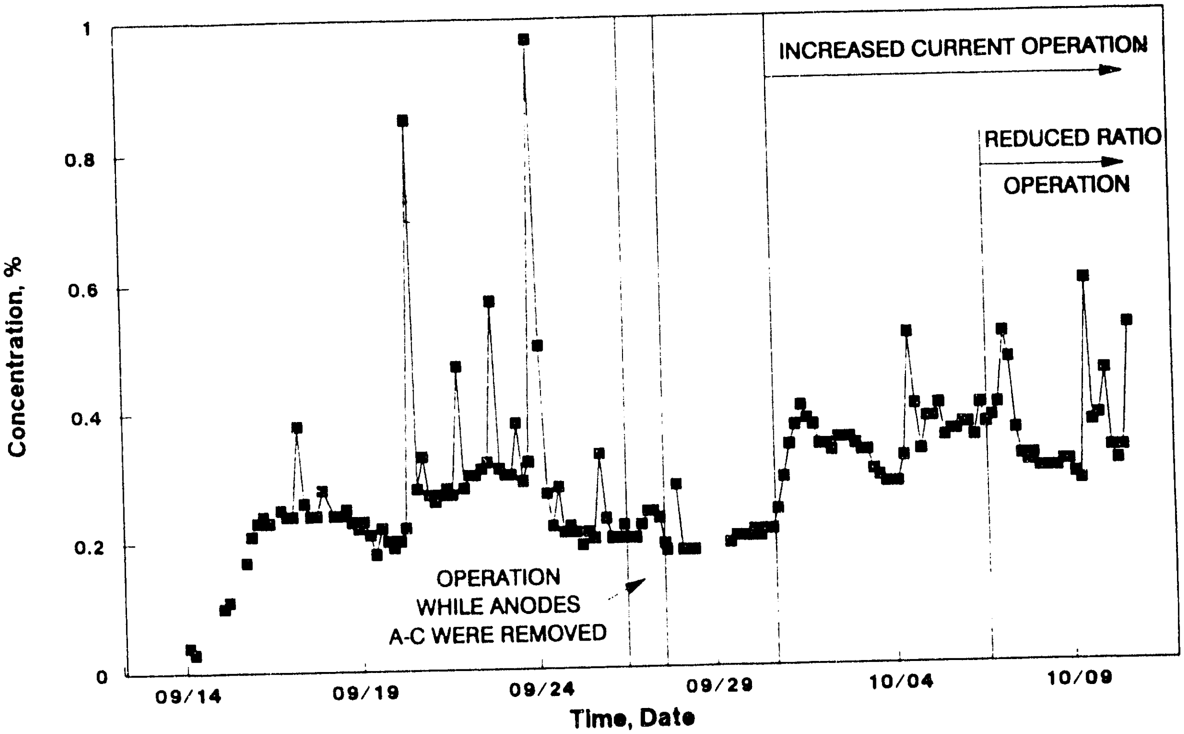

Figure 26.

Cu Content in Metal

ELTECH Cermet Anode Pilot Cell Test

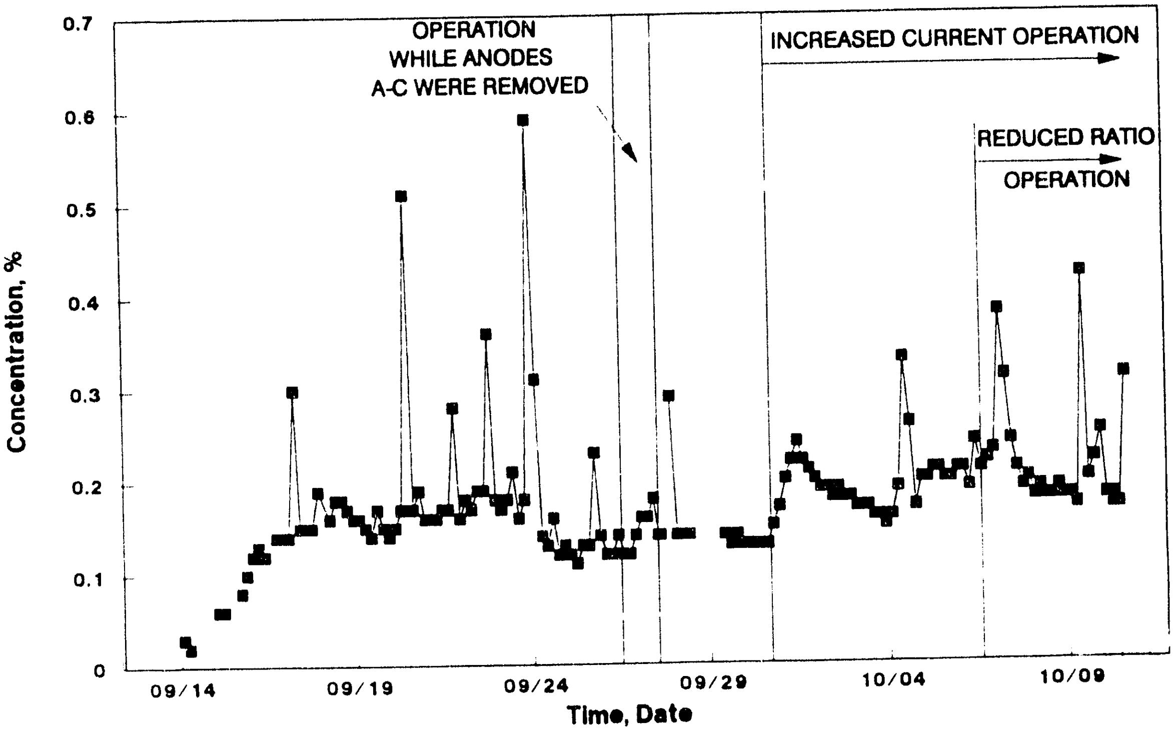

Figure 27.

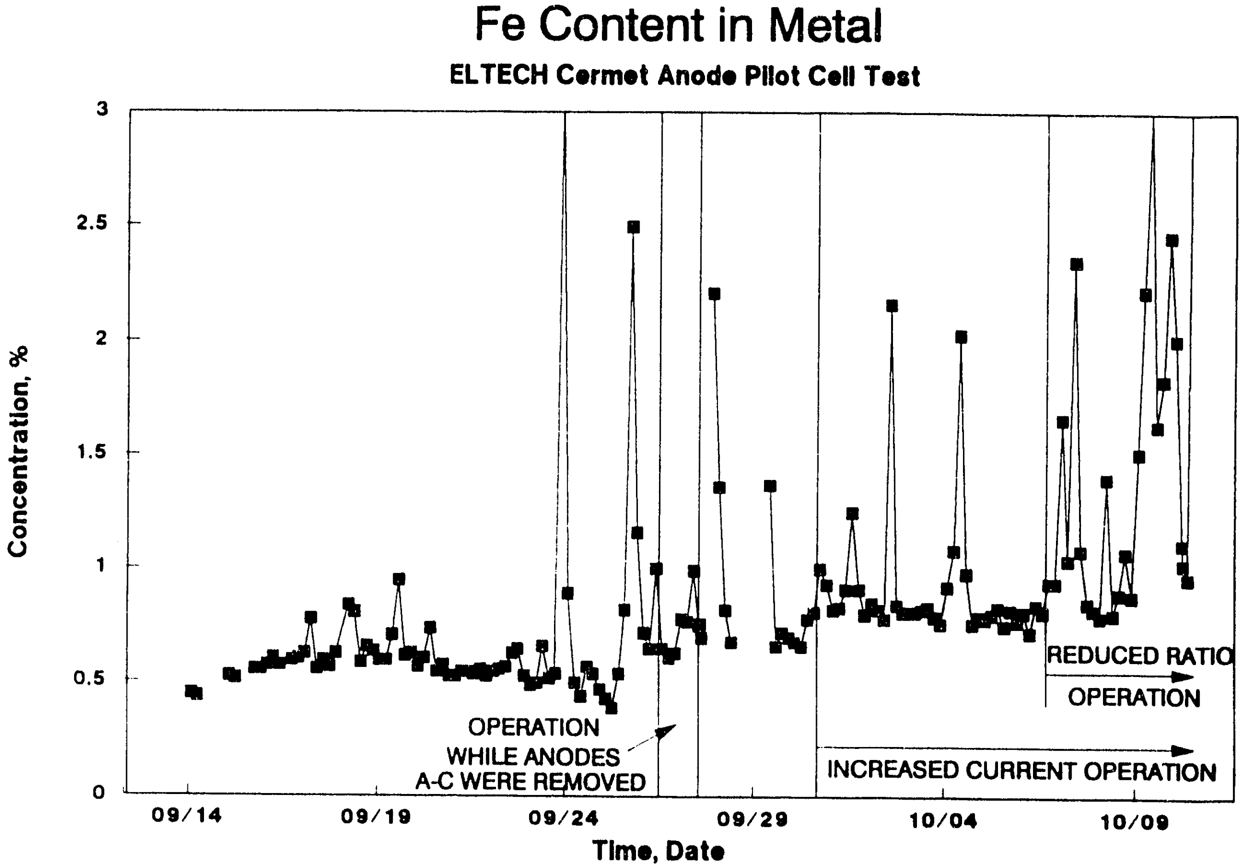
Fe Content in Metal
ELTECH Cermet Anode Pilot Cell Test
Concentration, %
3
2.5
2
1.5
1
0.5
0
09/14
09/19
09/24
09/29
10/04
10/09
Time, Date
OPERATION
WHILE ANODES
A-C WERE REMOVED
INCREASED CURRENT OPERATION
REDUCED RATIO
OPERATION

Figure 28.

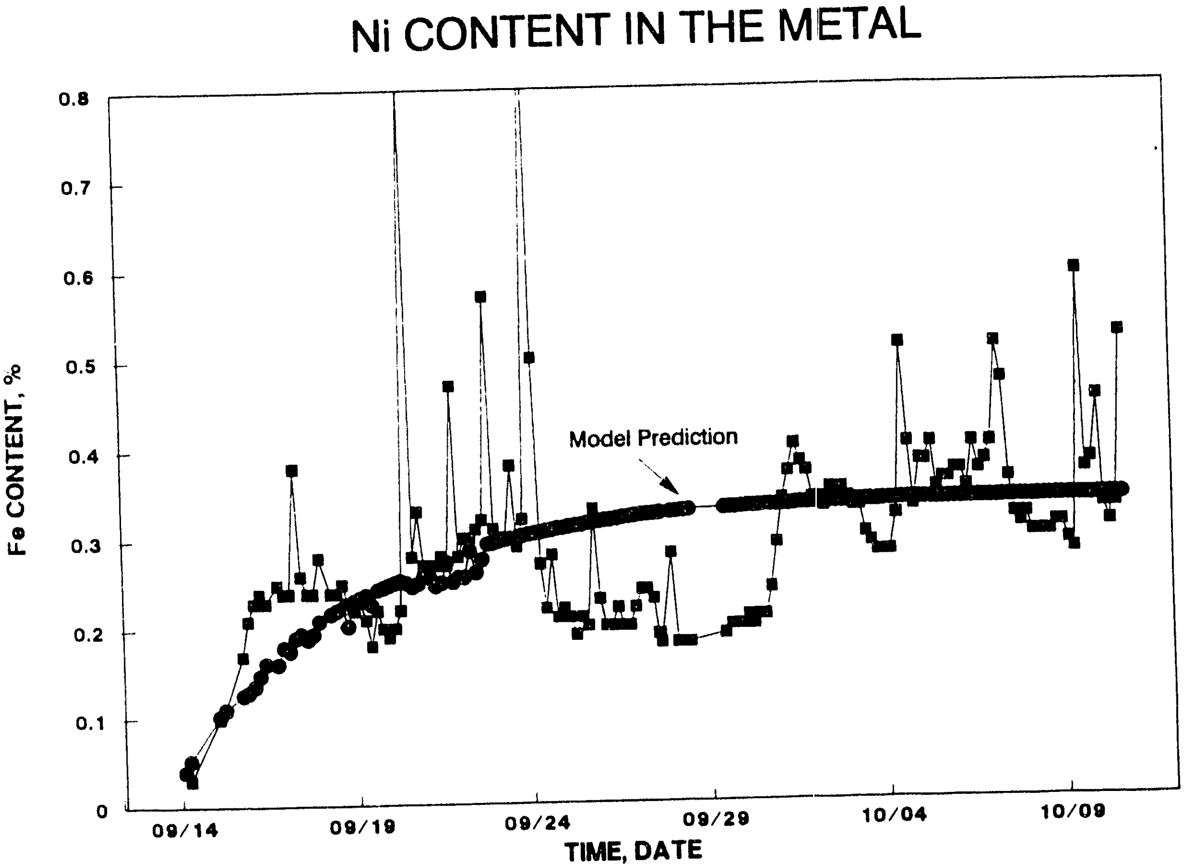

Figure 29.

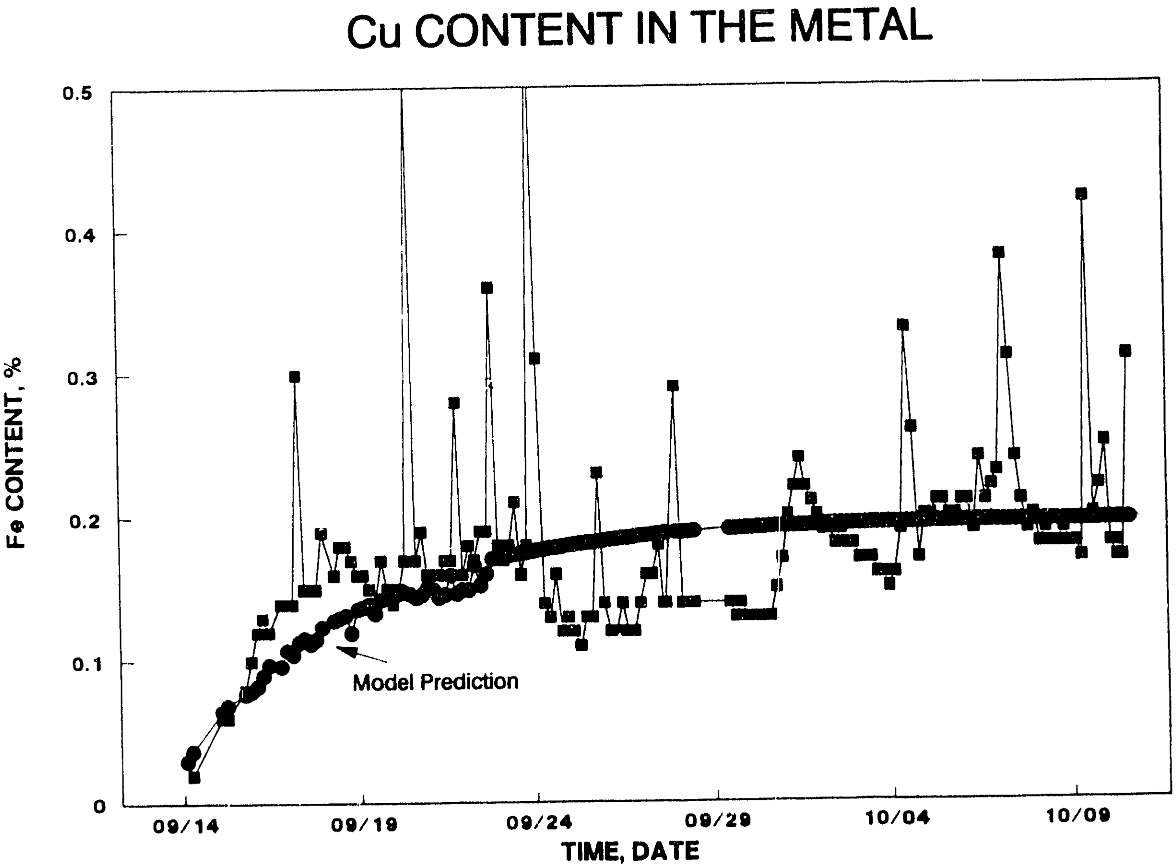

Figure 30.

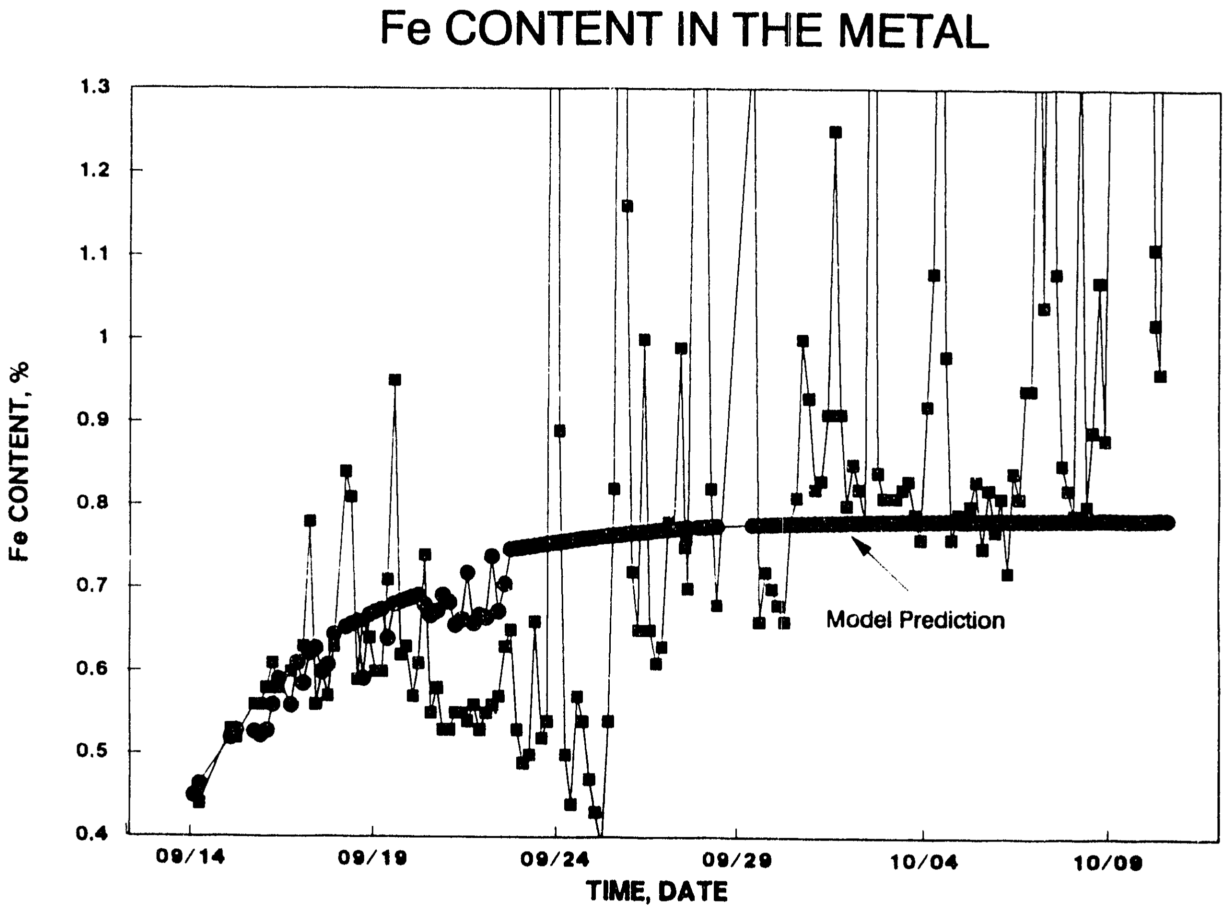
Fe CONTENT IN THE METAL
Fe CONTENT, %
1.3
1.2
1.1
1
0.9
0.8
0.7
0.6
0.5
0.4
09/14
09/19
09/24
09/29
10/04
10/09
TIME, DATE
Model Prediction

Figure 31.

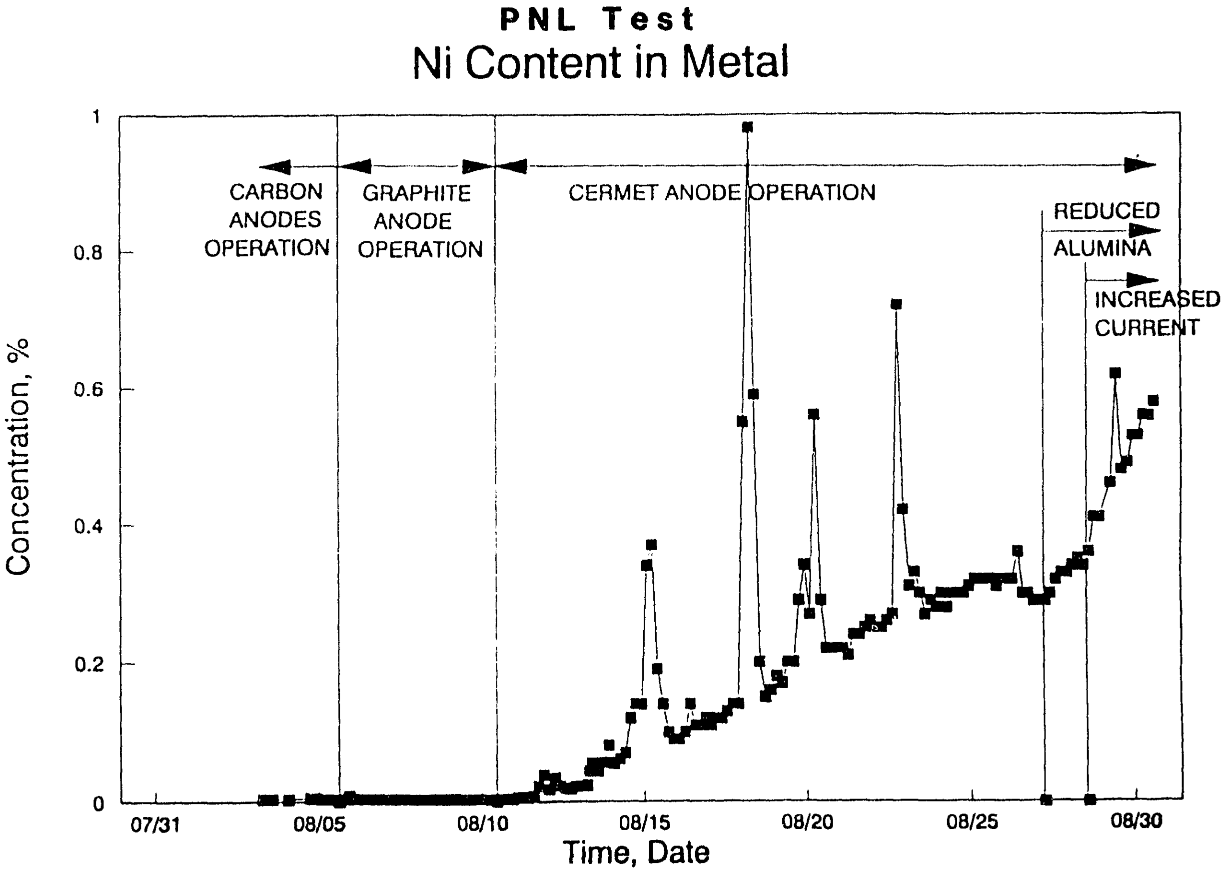

Figure 32.

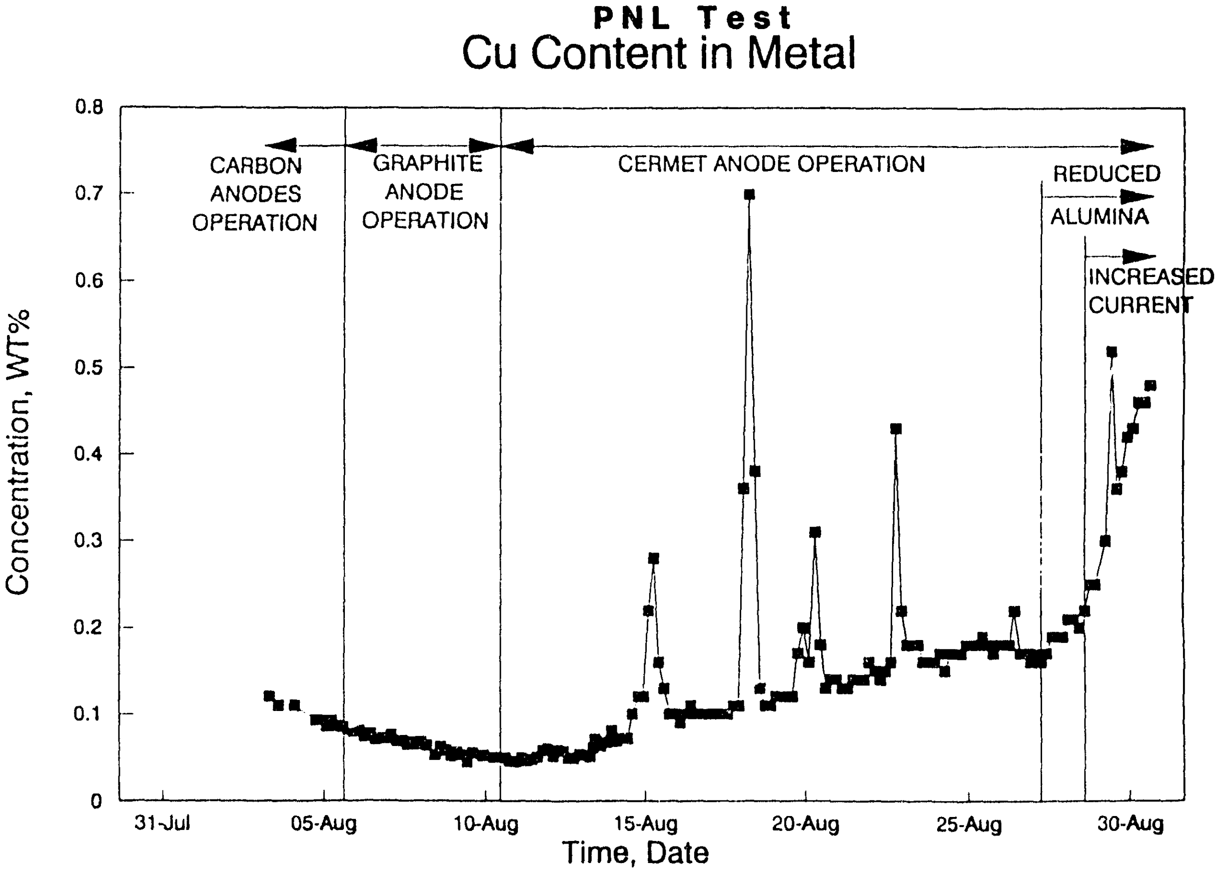

Figure 33.

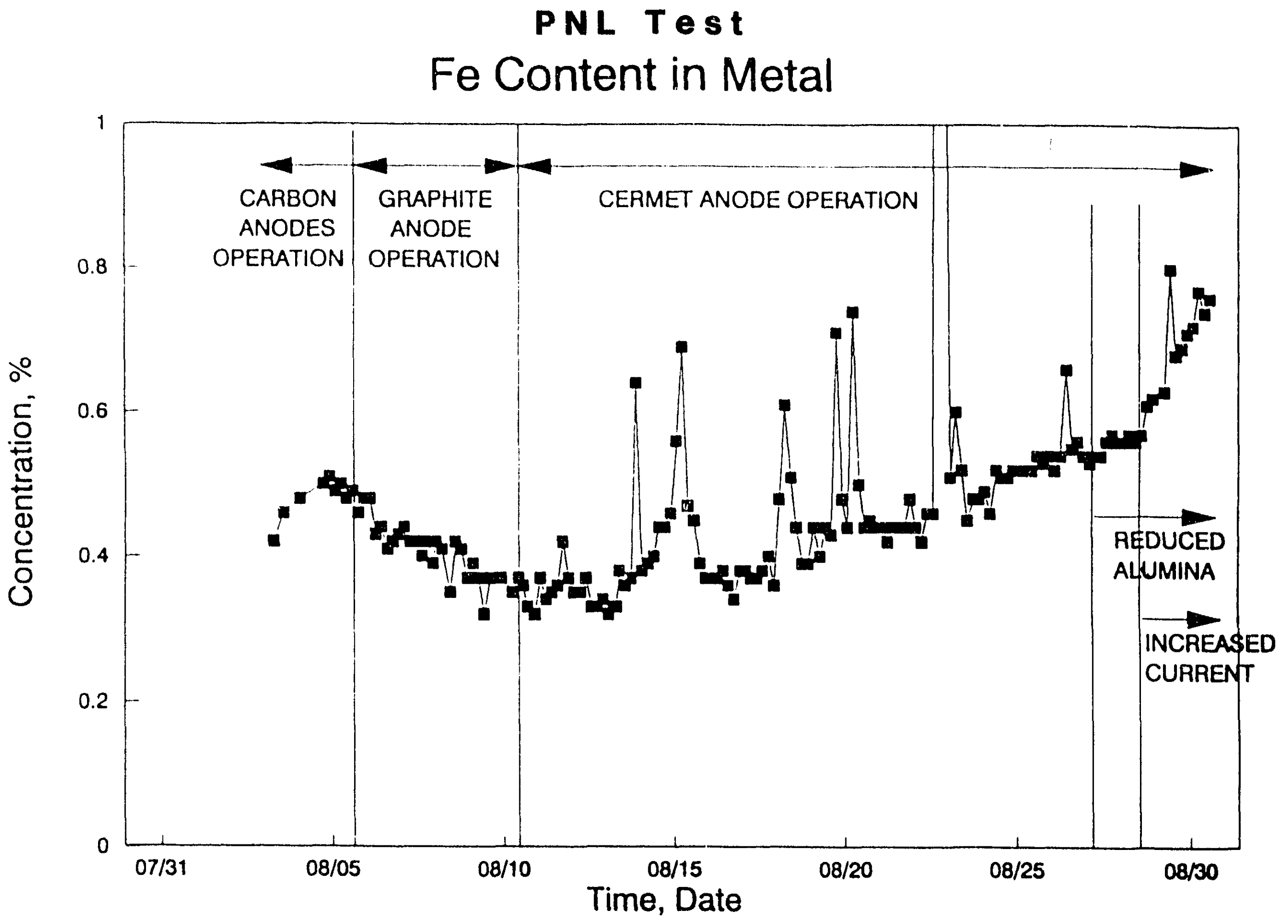
PNL Test
Fe Content in Metal
CARBON ANODES OPERATION
GRAPHITE ANODE OPERATION
CERMET ANODE OPERATION
REDUCED ALUMINA
INCREASED CURRENT
Concentration, %
1
0.8
0.6
0.4
0.2
0
07/31
08/05
08/10
08/15
08/20
08/25
08/30
Time, Date

Figure 34.

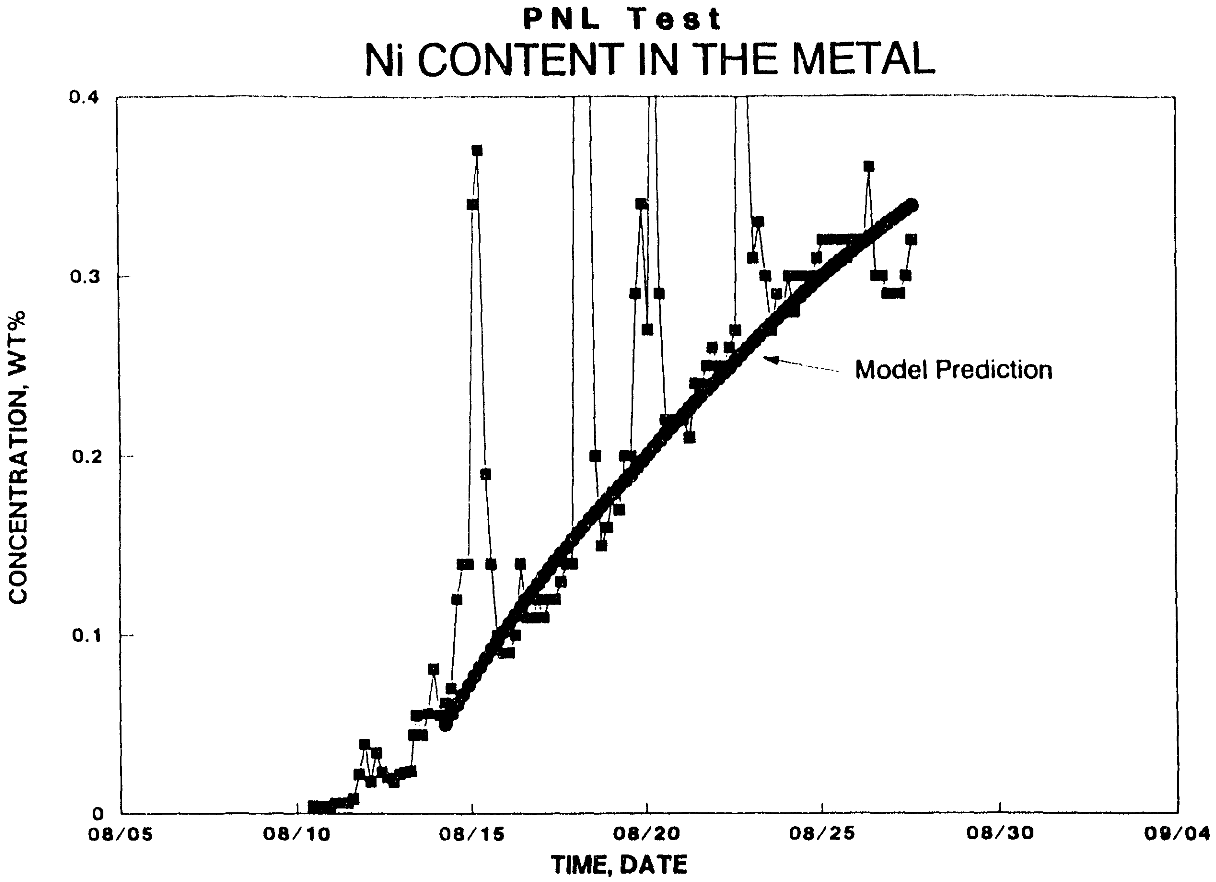

Figure 35.

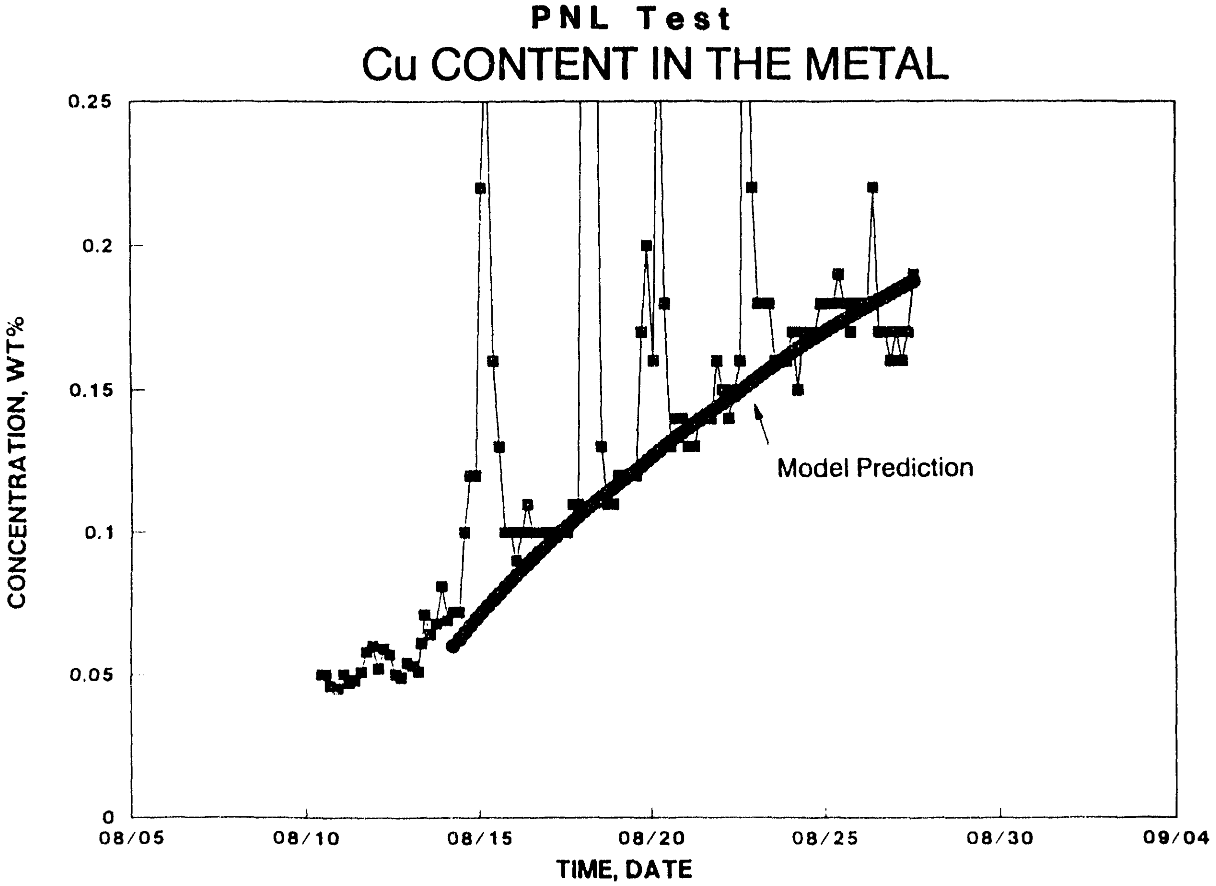

Figure 36.

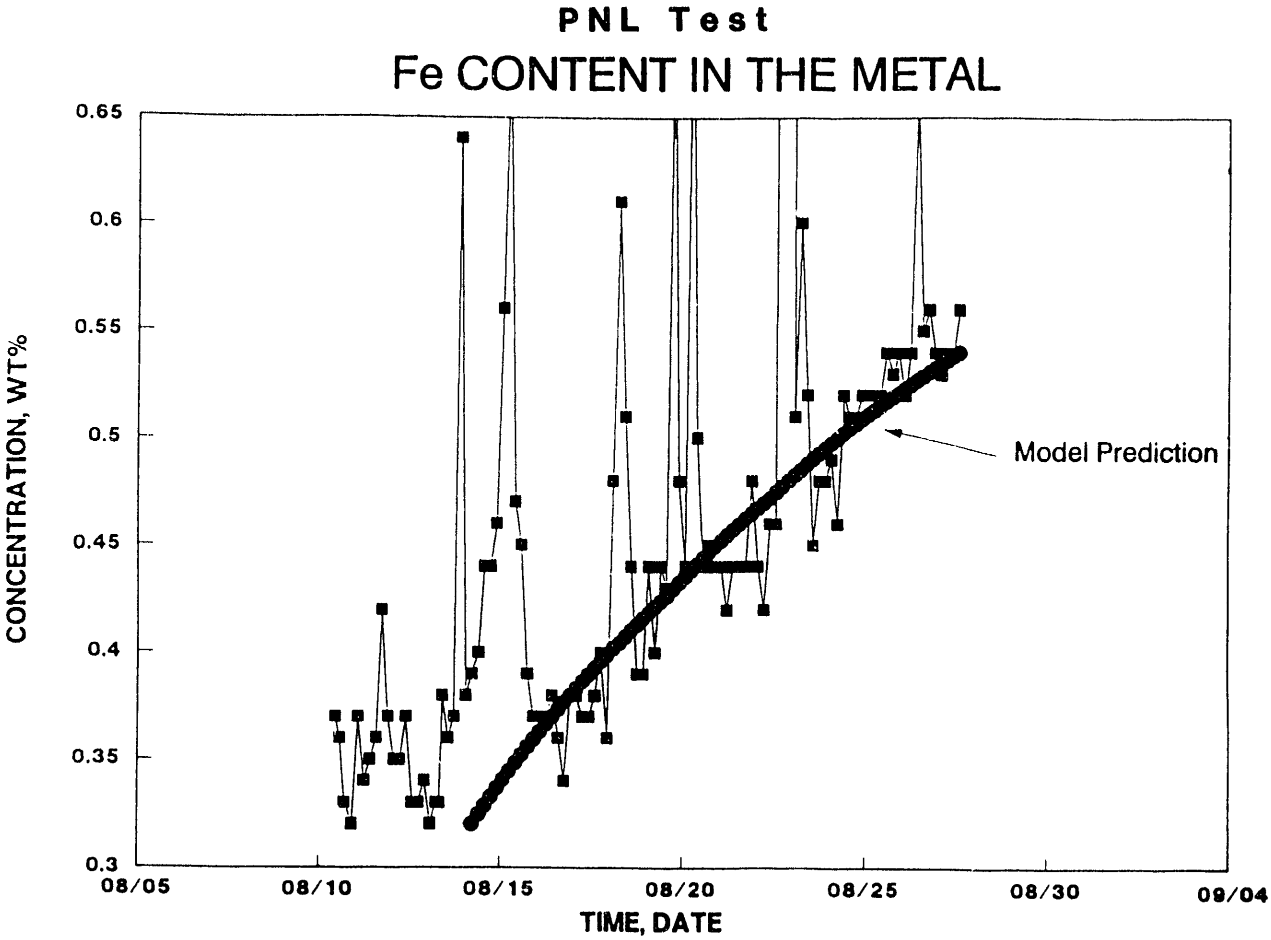
PNL Test
Fe CONTENT IN THE METAL
CONCENTRATION, WT%
0.65
0.6
0.55
0.5
0.45
0.4
0.35
0.3
08/05
08/10
08/15
08/20
08/25
08/30
09/04
TIME, DATE
Model Prediction

Figure 37.

twice that of the CEROX-coated anodes.

Because anodes during both tests had cracks, and pieces or chips of the anode fell into the bath (see subsection 4.2), the metal impurities may not be a good measure of the corrosion of the surface of the anodes. Because cracks were present to the center, some cryolite may also have contacted the Ni (PNL) or Inconel 601 (ELTECH) connector rods. In addition (because of the cracks) much more surface area was exposed to the electrolyte than would be for an intact anode.

The difference in the PNL and ELTECH test conditions also makes it difficult to make a comparison between the cermets operated with and without a CEROX coating. As shown in Figures 38 and 39, the Al_2O_3 concentration was maintained closer to saturation, and the temperature was generally kept below 1000°C during the PNL test. During the ELTECH test, the higher temperature and lower Al_2O_3 contents may have increased the corrosion. Alcoa has shown that both conditions led to increased dissolution of the oxides.[3] The effect of temperature on the CEROX coated anodes has not been studied, but laboratory studies on CEROX coated anodes at low Al_2O_3 concentrations has shown an increase in corrosion.[6]

The Fe, Ni, and Cu levels in the cryolite melt were also monitored throughout the testing period. Average levels during most of the PNL test ranged from 0.001 to 0.003% Cu, 0.005 to 0.009% Ni, and 0.02 to 0.05% Fe. Levels were similar during the ELTECH test; 0.001 to 0.006% Cu, 0.001 to 0.010% Ni, and 0.020 to 0.080% Fe. During the tests, some values were lower or higher than these averages; levels are similar to the solubility limits measured by Alcoa for Ni and Fe from NiO and $NiFe_2O_4$.[3] Alcoa measured solubilities of 0.01 to 0.02% Ni and 0.05 to 0.08% Fe from $NiFe_2O_4$, depending on temperature and bath composition. The solubility of Ni from NiO was around 0.02 to 0.08%. It appears that the Fe and Ni may be near the solubility limit in the bath during portions of these tests. During the PNL test at the high CD and low alumina concentration, somewhat higher levels were recorded.

4.2 Macroscopic Examination of Anodes

The untested and tested anodes were macroscopically and microscopically examined. Each of the tested anodes was cracked upon removal from the cell. The cracks generally radiated from the center of the anode and broke the anode into two or more pieces. In some places, of the top rims of the anodes were chipped off. Each anode will be described in some detail, and then the common features summarized. A sketch of each anode (from the top) is shown in Figure 40 delineating the cracking orientation. The anode positions in the cell refer to Figure 3. The anode locations in the cell and whether the anode was adjacent to another cermet anode or next to the carbon anode had a large effect on the CEROX coating and corrosion of the cermet.

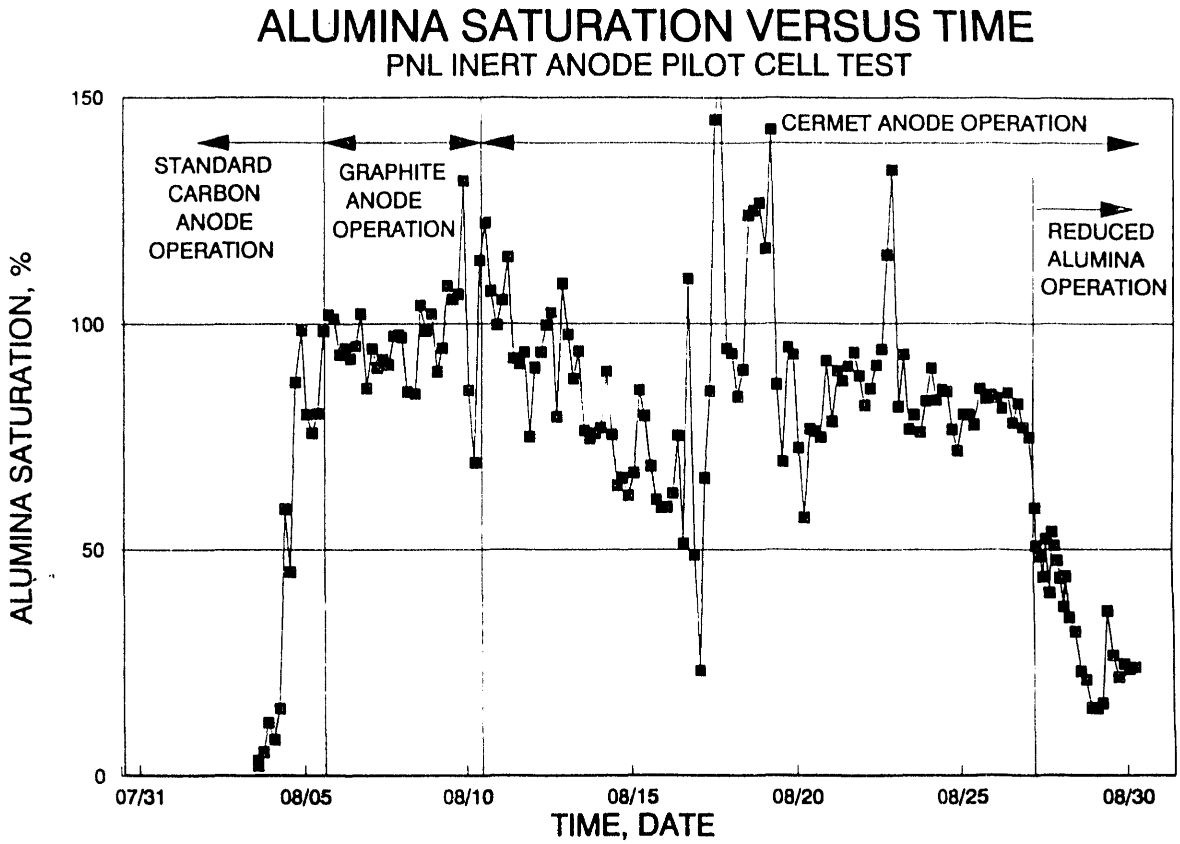

Figure 38.

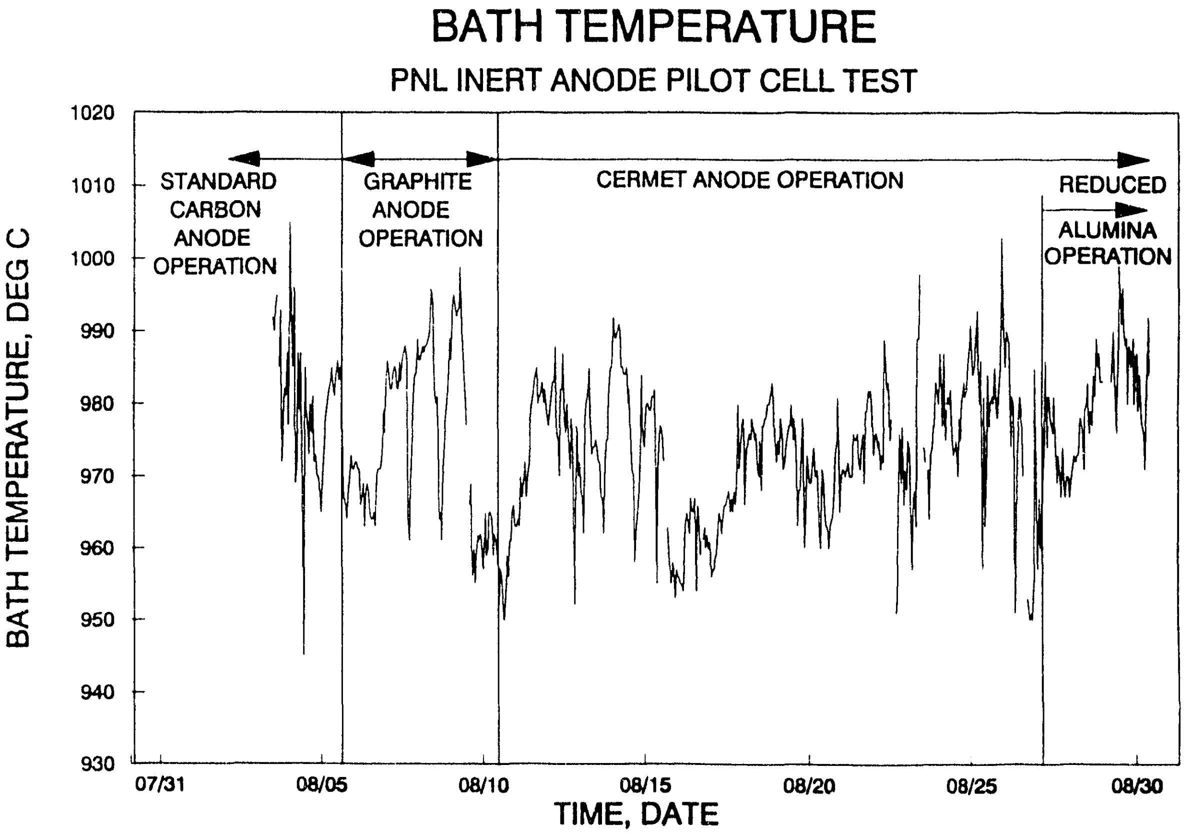

Figure 39.

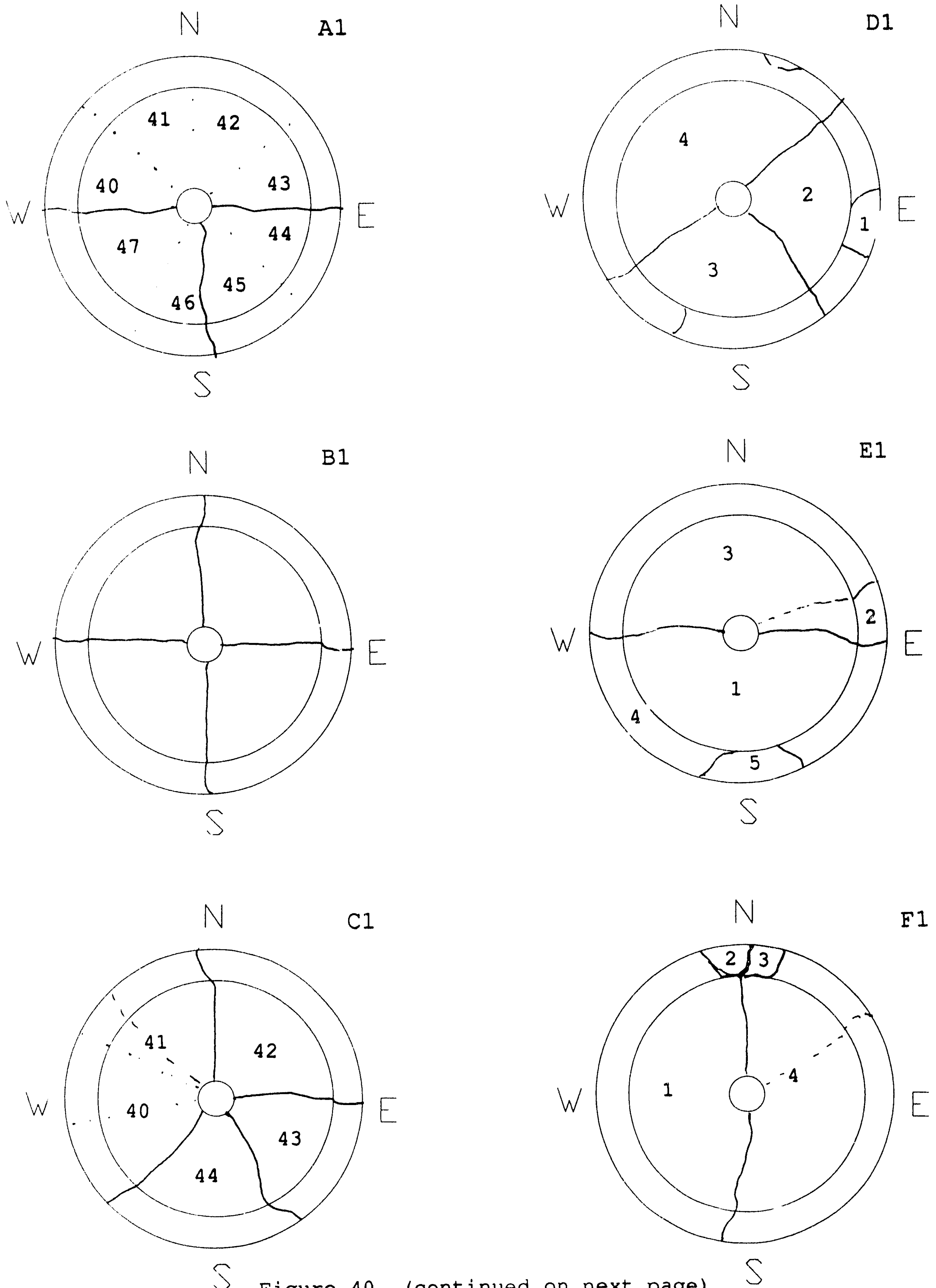

Figure 40. (continued on next page)

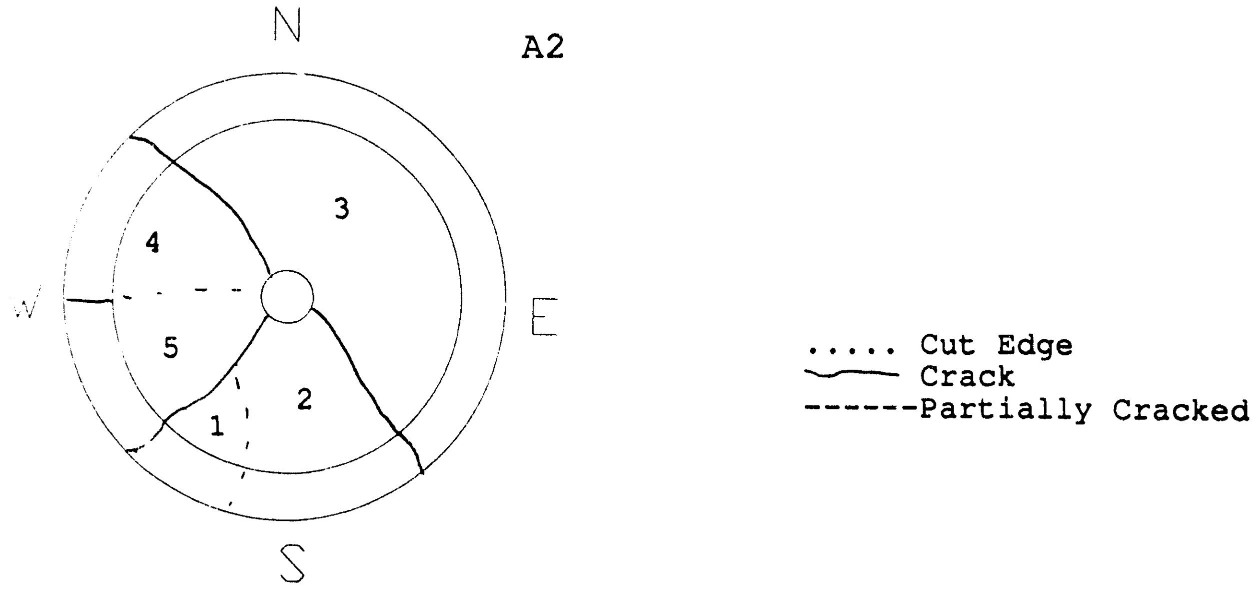

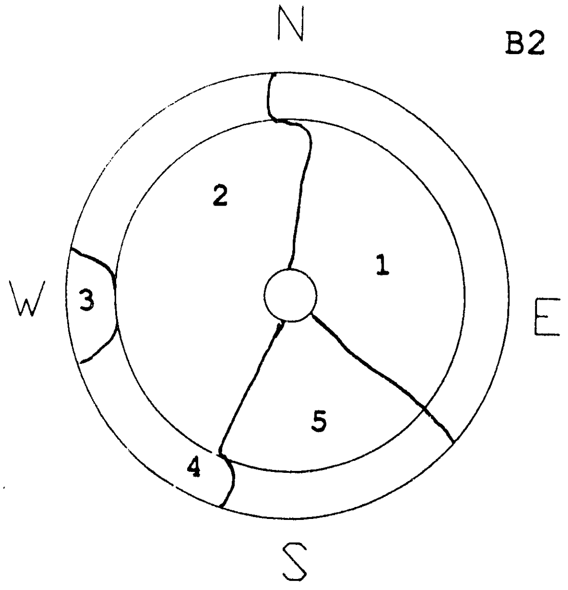

Figure 40. (continued)

Sketches of each tested anode showing the orientation of cracks. Cracked pieces were numbered for identification.

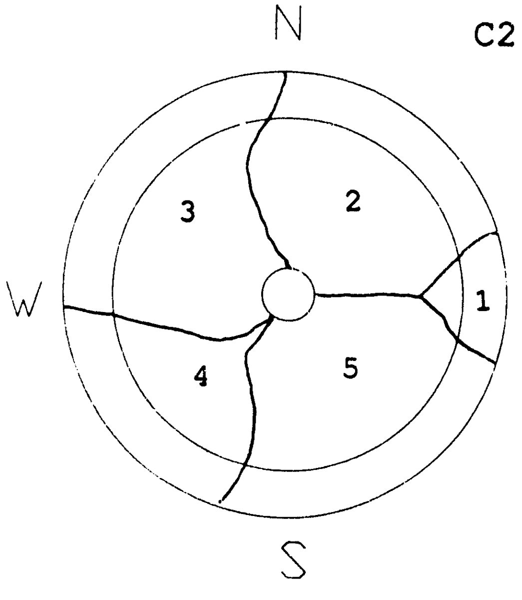

4.2.1 Description of the Anodes

Untested Anodes (Anode #13 cross sectioned for microscopy).

The untested anode shapes were described in Subsection 2.2. Two untested anodes are shown in Figure 41. The anodes were generally smooth with a straight side and a radiused bottom. On some of the anodes the surface was slightly rough with scratches, probably formed on the green body. Occasionally a small bead of Cu was squeezed out on the exterior surface. Cross sections of the anodes showed that there were some dark bands parallel to the bottom surface of the anodes. These will be described in detail in the microscopy section.

Anode B1--~1 h (Cross sectioned for microscopy).

Anode B1 was removed after ~1 h in the cell because it was noticeably cracked and not conducting current. The cracks radiated from the center (Figures 40 and 42) breaking the anode into four pieces. There was no macroscopic change in the dimensions of the anode or in its appearance. A cross section of the anode is shown in Figure 43.

Anode A1--~213 h, average current = 46 A (Cross sectioned for microscopy).

Anode A1 was cracked into three main pieces that radiated from the center (Figure 40). A 3 mm dimensional loss was measured from inside the lip to the bottom of the anode. This is probably not significant within our macroscopic measurement capabilities because some anodes showed a small loss while others showed a small increase in size. Only gross dimensional changes could be recorded because of difficulties in measuring the dimensions in the same spot and in measuring a CEROX coated and cryolite covered anode. No gross dimensional changes were noted on any of the anodes.

In general, the CEROX coating was ~0.5 to 1.5 mm thick on the sides and the bottom of the anode. On the west side of the anode (facing the carbon anode) the CEROX coating level dipped down and was mostly absent from that side, as shown in Figure 44. In addition, the bare cermet in that region was covered with roundish corroded areas and the cermet was indented on that side. The corroded areas were also found a short distance into an open crack on that side of the anode. No macroscopic difference was evident in the cermet on the indented side.

On the side of A1 facing the east and northeast (Figure 3) the CEROX coating was up to 8 cm high and was also thickest on that side (~up to 3 mm thick, Figure 45). A cross section of the southeast side (no indentation, CEROX coating present) is compared to the west side (indentation, no CEROX coating) in Figure 46 in order to compare the loss of cermet material from the indented

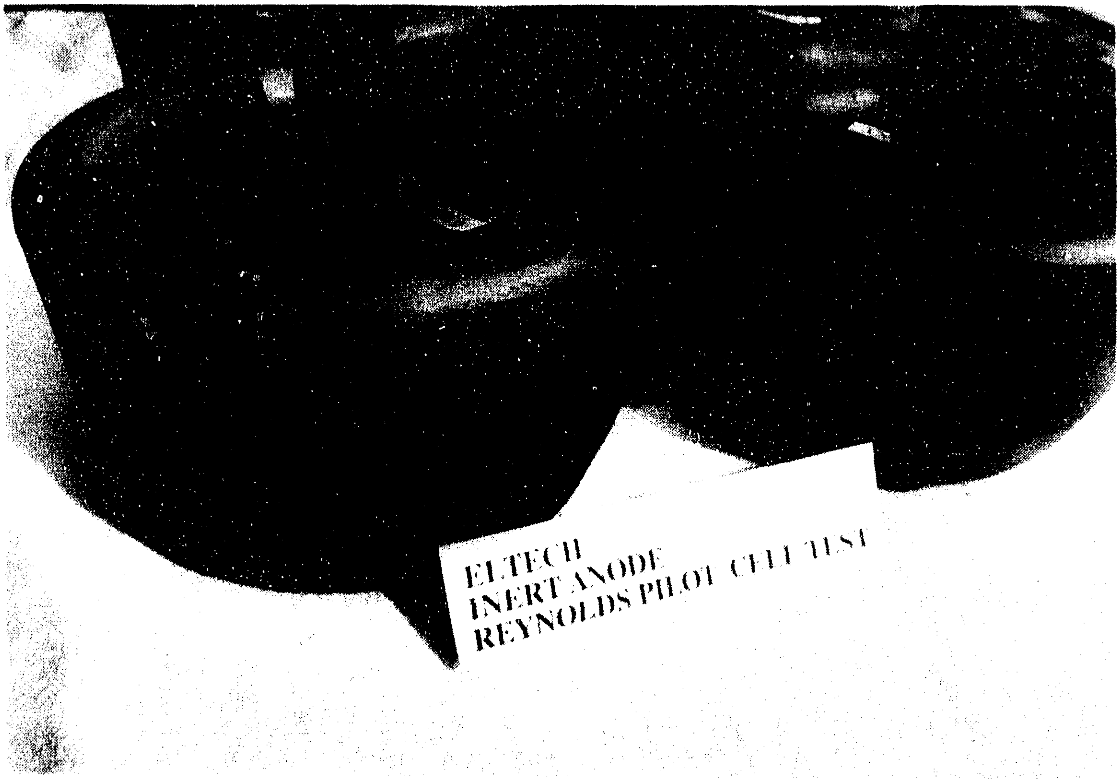

Figure 41. Untested Anodes.

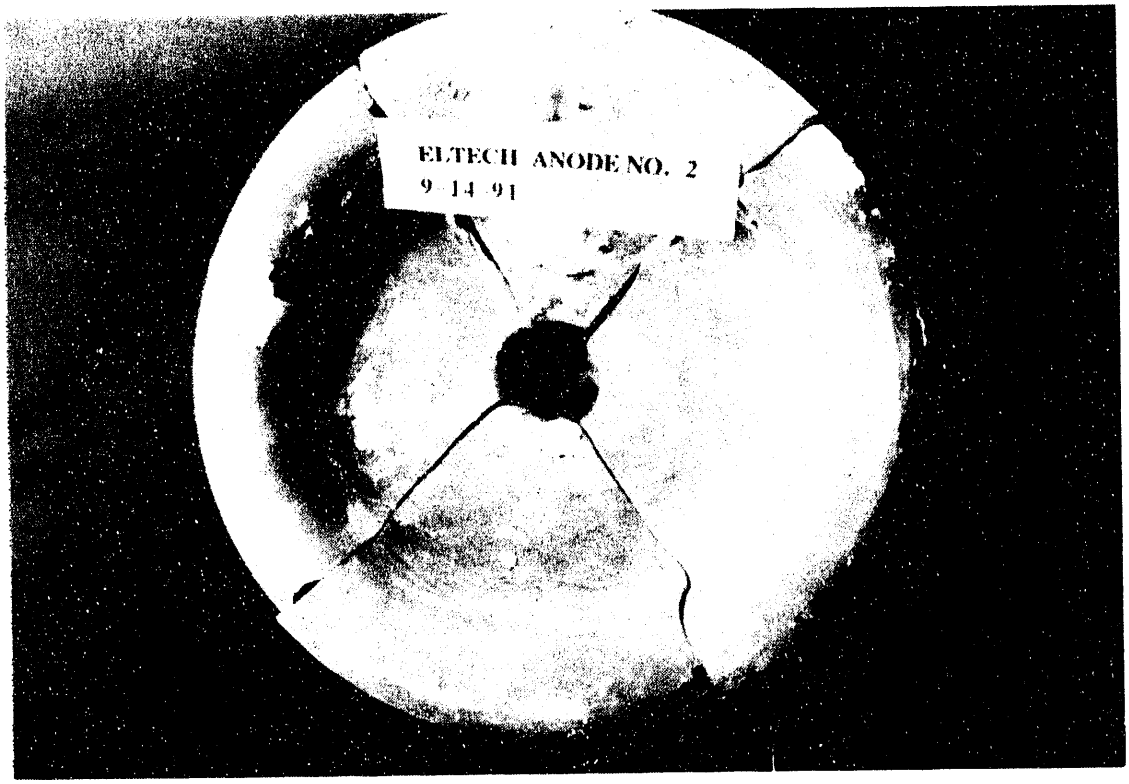

Figure 42. Anode B1 after removal from the test cell. Cracks radiate from the center.

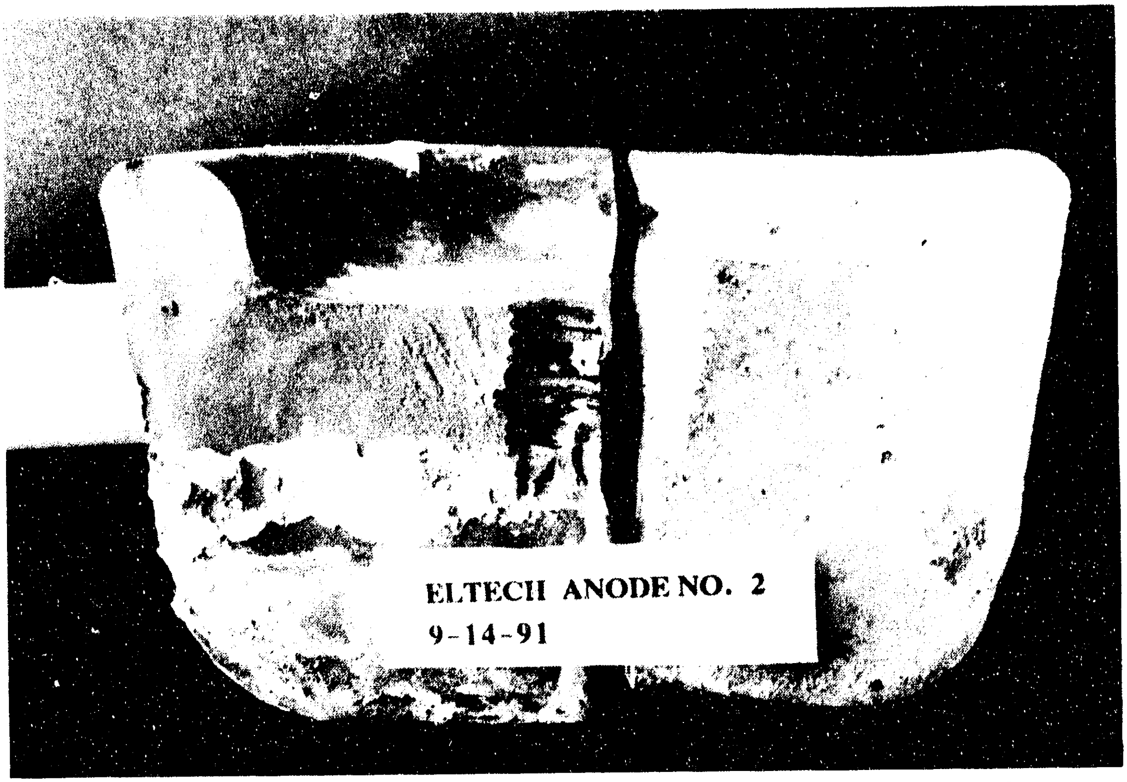

Figure 43. Cross-section of Anode B1 along a crack surface.

Figure 44. The west side of Anode A1 (which was next to the Carbon Anode) shows a dip in the Cerox coating height and also has a pitted corroded region on that side.

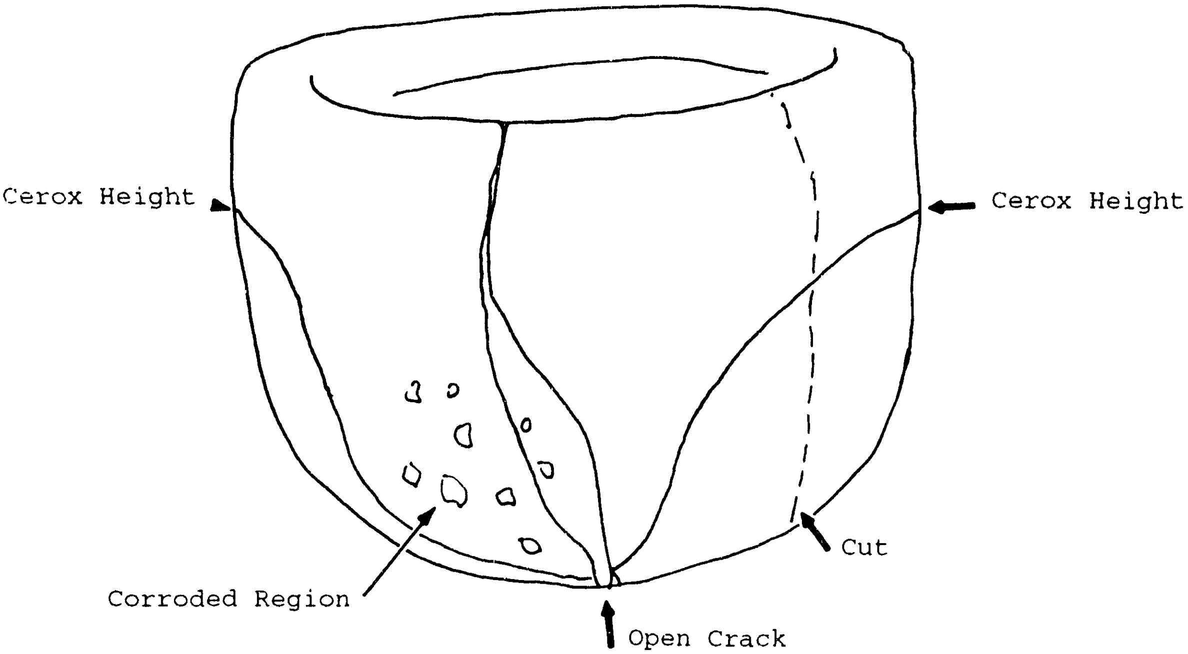

(Sketch of Figure 44)

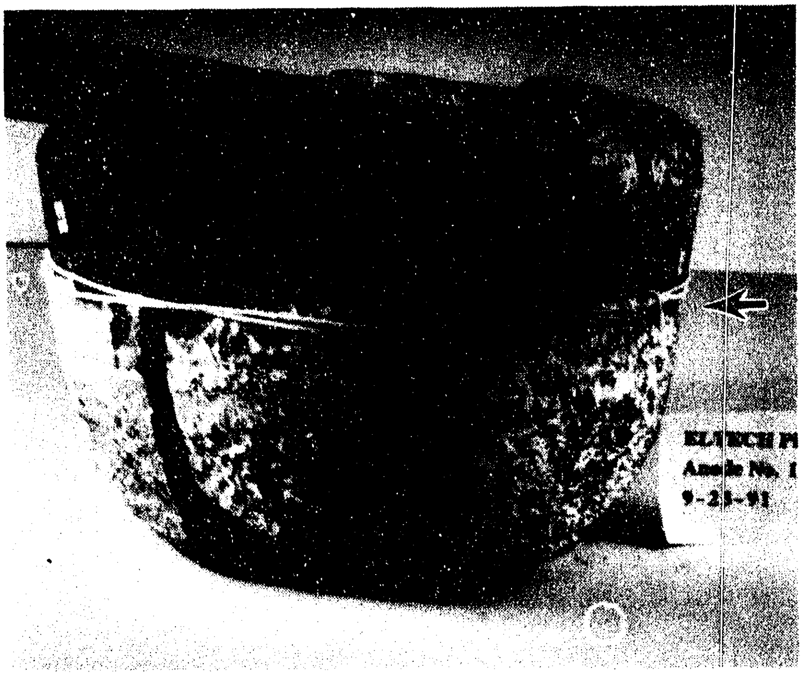

Cerox Height
Up to 8 cm High

Figure 45. A thick Cerox coating was present on the northeast side of Anode A1.

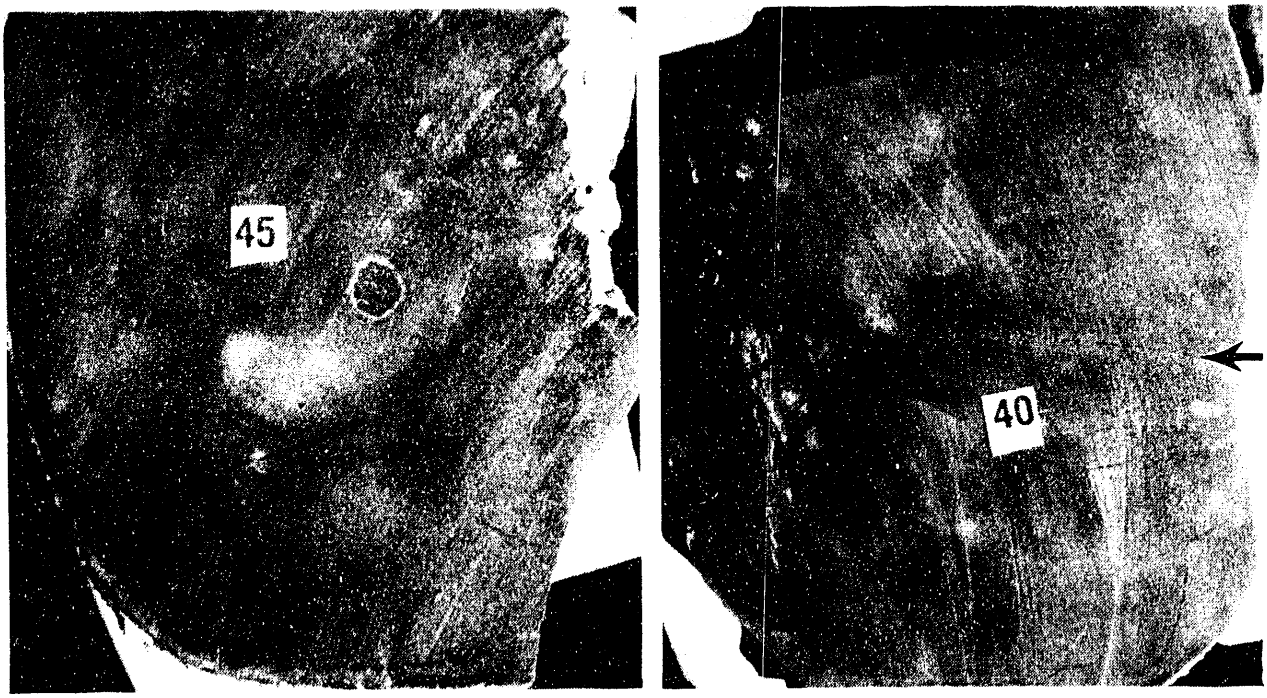

Figure 46. A cross-section of the southeast part of Anode A1 (left) is compared to the west side (right) to show the extent of the indentation (arrow) on the west side facing the carbon anode.

region.

When the anode was cross sectioned a darker gray area (less Cu colored) was found on the bottom surface of the anode and a short distance up the sides. This region appeared devoid of Cu metal and was up to 0.5 mm thick on the side of the anode but up to 7 mm on the bottom of the anode.

<u>Anode C1</u>--~275 h, average current = 67 A (Cross sectioned for microscopy).

Anode C1 was broken into five pieces when it was removed from the cell. There was no macroscopic dimensional change. The CEROX coating was ~11 cm high on all sides of the anode (Figure 47). The thickness of the CEROX coating was fairly even and averaged 2 to 4 mm on the side and 1 to 3 mm thick on the bottom. As seen in Figure 47, the cracks sometimes appear to be wide open and missing chips of the cermet. In one of the open cracks the CEROX coating grew 3 cm deep into the crack. A gray oxidized layer up to 2 mm thick on the sides and 6 mm thick on the bottom and corners was present in the outer surface of the anode. A similar indentation in A1 occurred in the side of the anode facing the carbon anode (west side). However, the CEROX coating did cover the indented region on C1.

<u>Anode A2</u>--~312 h, average current = 101 A (Cross sectioned for microscopy).

Anode A2 was cracked in three sections upon removal from the cell. Along the cracks there was some evidence of a Cu metal phase. The CEROX coating and the cryolite level along the side of the anode are at an angle, indicating the anode was probably hanging at an angle in the cell as shown in Figure 48. The CEROX coating angles from about a height of 3.7 cm to a height of 6.8 cm up the sides of the anode.

On the west side facing the carbon anode, there was an indentation in the cermet anode as shown in Figure 49 but a CEROX coating was still present. On the south side of the anode, adjacent to anode B2, the CEROX coating dipped down to a height of 1.8 cm as shown in Figure 49. The coating was thickest on the northeast side of the anode but averaged ~1 mm thick everywhere it was present. The gray oxidized layer on the bottom of the cermet was 0.6 to 3 mm thick and was 0.3 to 1.4 mm thick on the side of the anode.

<u>Anode B2</u>--~312 h, average current = 103 A

Anode B2 was the best example of the absence of a CEROX coating on regions very close to another cermet anode. On the south and east sides (adjacent to cermet anodes C2 and E1), the CEROX coating was very thin to nonexistent as shown in Figure 50. On the west side, facing the carbon anode, a thin CEROX coating was present and no

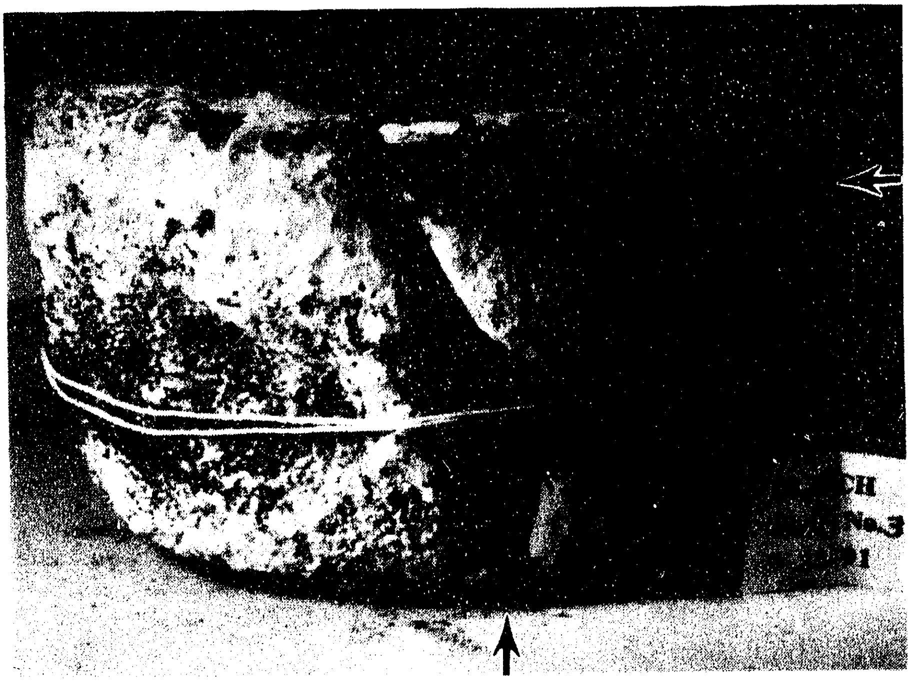

Cerox
up to 11 cm
High

Large open crack

Figure 47. Anode C1 has a thick Cerox coating and a large open crack.

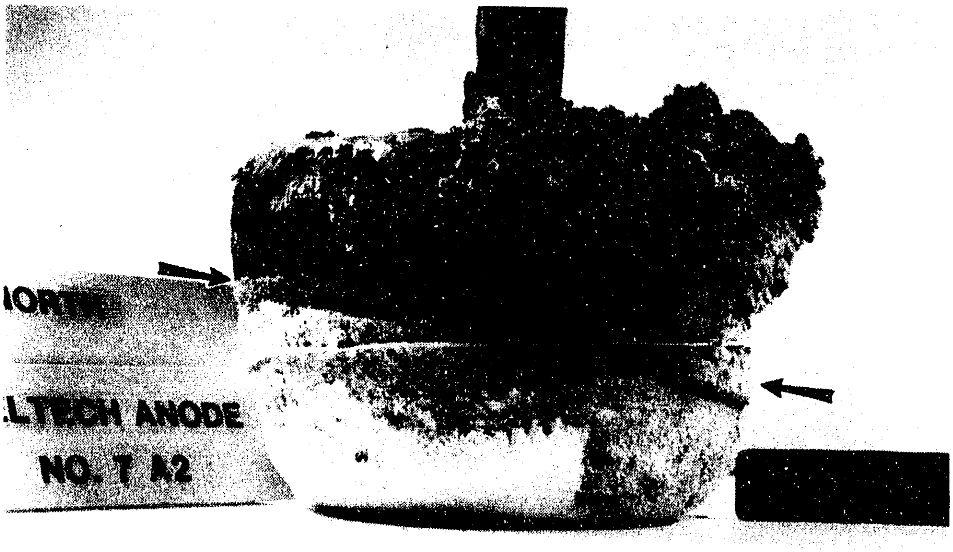

Figure 48. The Cerox coating and Cryolite crust are at an angle on Anode A2, indicating the Anode was hanging at an angle during testing.

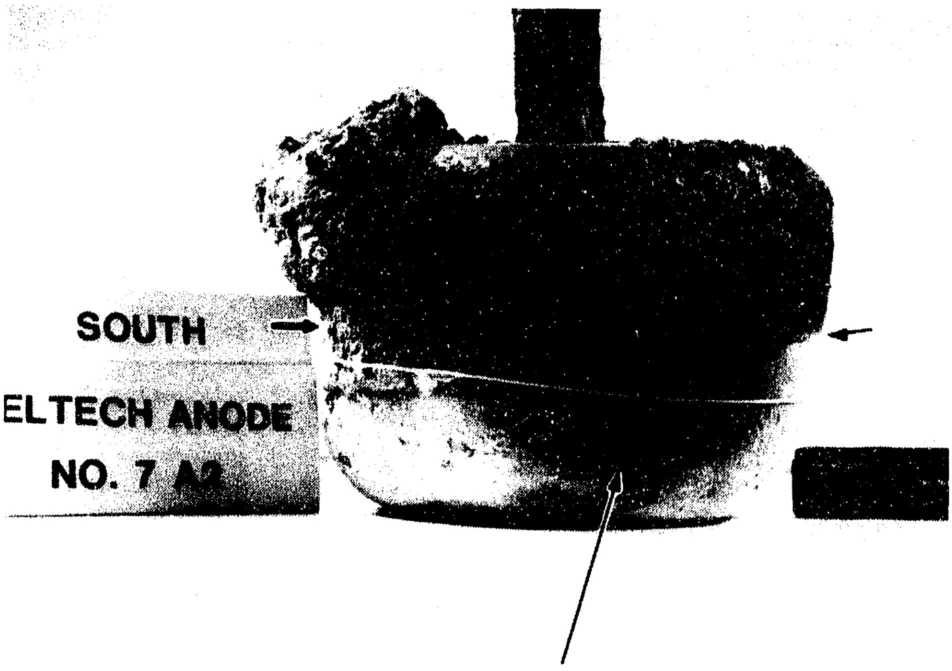

Shadow Region

Figure 49. There is an indentation on the west side of Anode A2 (left arrow) facing the Carbon Anode. a "shadow region" where the Cerox coating is thin to absent is present on the south side of A2 adjacent to Anode B2.

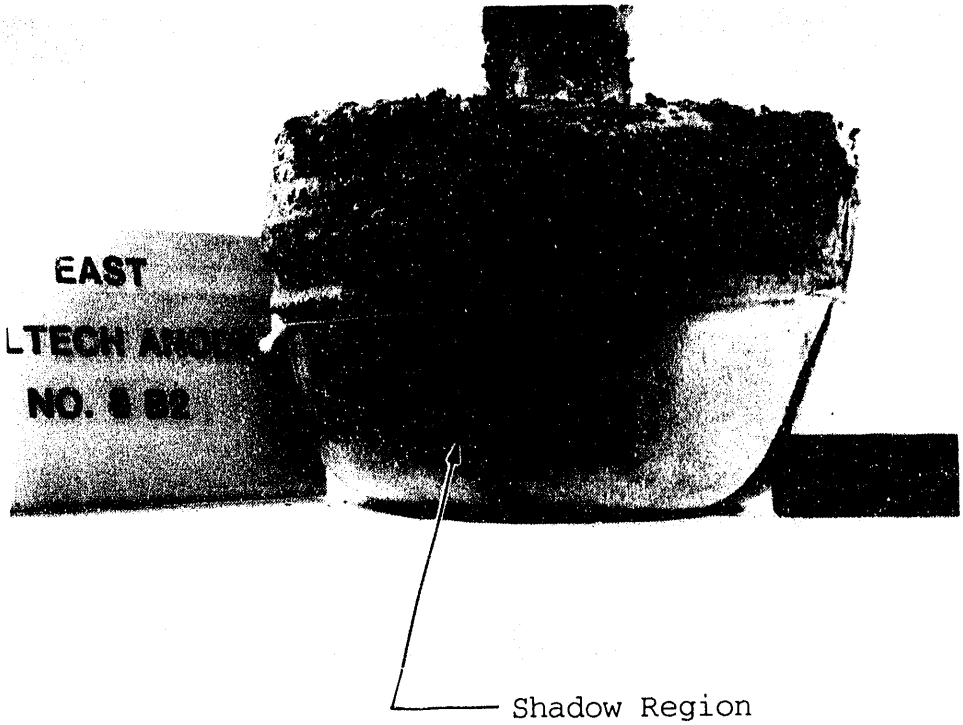

Figure 50. The east side of Anode B2 has a "shadow region" facing Anode E1, where the Cerox coating height dips down.

Figure 51. The west side of Anode B2 had a thin Cerox coating. A crack is evident on that side.

indentation was found as shown in Figure 51. The CEROX coating on the bottom of the anode was ~1 mm thick. Anode B2 had one main crack running north to south in the anode; the CEROX coating grew to a depth of 1.2 cm into this crack as shown in Figure 52. Along the crack surface, Cu metal could be found.

Anode C2--~312 h, average current = 75 A

Anode C2 was cracked into multiple pieces (Figure 40 and 53). The CEROX coating was 1 to 3 mm thick on all sides and the bottom. Cryolite and some CEROX could be found a short distance into the cracks. The CEROX coating extended up the sides to a height of 8.5 cm on the southwest side and up to 4 cm on the northeast side, indicating this anode was also probably tilted slightly during testing. Some cryolite crust was found on the southwest side of the anode (near the sidewall) on top of the CEROX coating, indicating that a frozen crust may have been forming around that side of the anode. A thin layer of Cu metal was present along the crack surface.

Anodes D1, E1, F1--~614 h,
average current = 40 A, 44 A, 53 A, respectively
(E1 cross sectioned for microscopy).

Anodes D1, E1, and F1 became frozen into the cryolite crust during the last half of the testing. The east side of the cell (opposite the carbon anode) became cool, leading to the crusting. When anodes D1 and F1 were removed from the cell, it appeared that each was missing part of the bottom of the anode as shown in Figure 54 and 55. The bottom may have been missing during testing or, more likely, may have broken off during removal from the cell. Parts of the CEROX coating were also missing. Each of the anodes was cracked into two to four main pieces.

Anode E1 was the most intact of the three anodes tested for 614 h. The anode was cracked into two main halves. Half of the anode is shown in Figure 56. Some Cu metal was found along the crack surface.

On the west side of the anode the CEROX coating was 4 to 5 mm thick while on the east side it was >5 mm thick. On the east side the CEROX coating was extremely thick, porous, and mixed with frozen cryolite. A chunk of the CEROX coating and frozen cryolite broke off from the east side and is shown in Figure 56. The gray oxidized region on the exterior surfaces of the anode is up to 2 to 10 mm thick on the side and 13 to 18 mm thick on the bottom of the anode.

Inconel 601 Connector Rods

A typical Inconel 601 connector rod is shown in Figure 57. The rods maintained their integrity during the testing, but often had

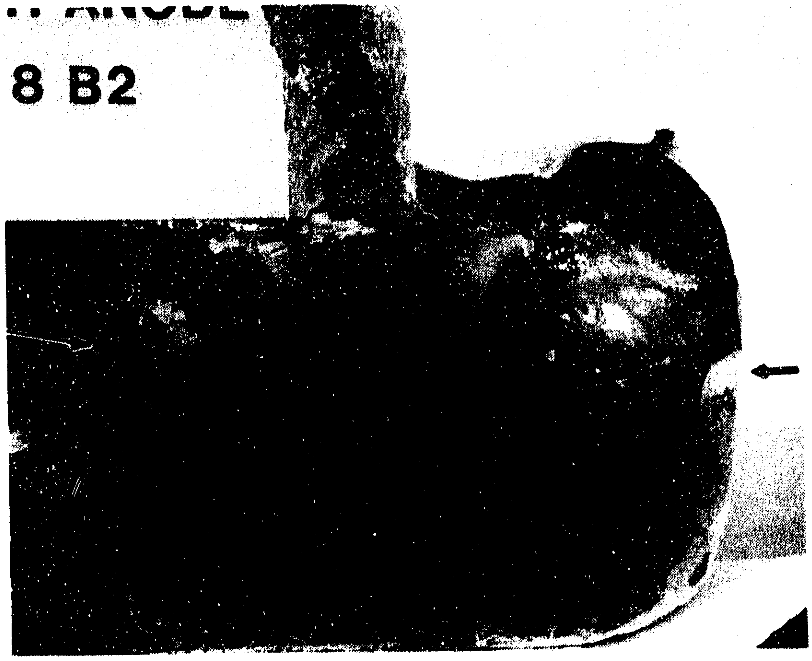

Figure 52. Cross-section of Anode B2 along a cracked surface. The Cerox coating grows into the crack and Cu metal occurs along the crack surface.

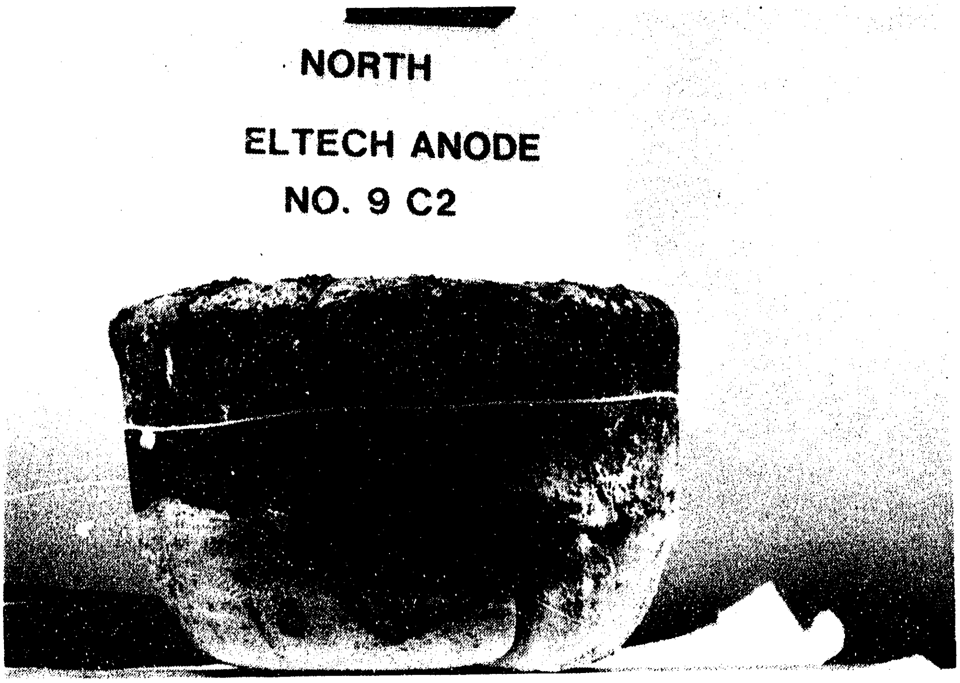

Figure 53. Anode C2 is cracked into multiple pieces. The Cerox coating is present on all sides.

Cerox
coating
Height

Figure 54. In Anode D1 the north and east sides and part of the bottom of the Anode is missing.

Figure 55. Anode F1. East side bottom of Anode is missing.

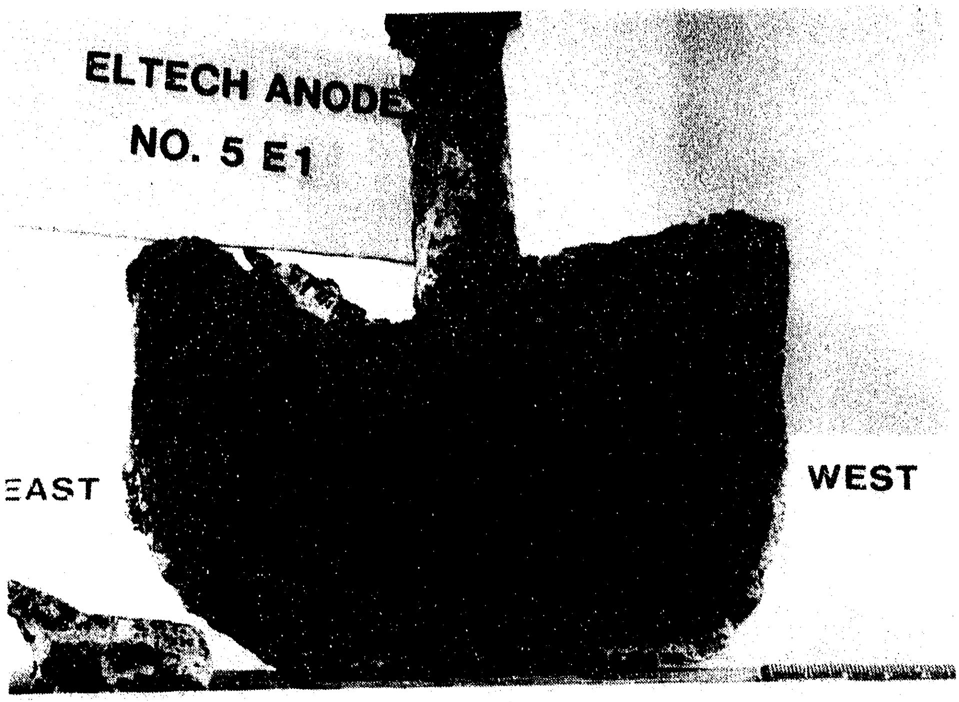

Figure 56. Cross-section of Anode E1 along a crack surface. On the east (left) side, a chunk of the thick Cerox and Cryolite has fallen off.

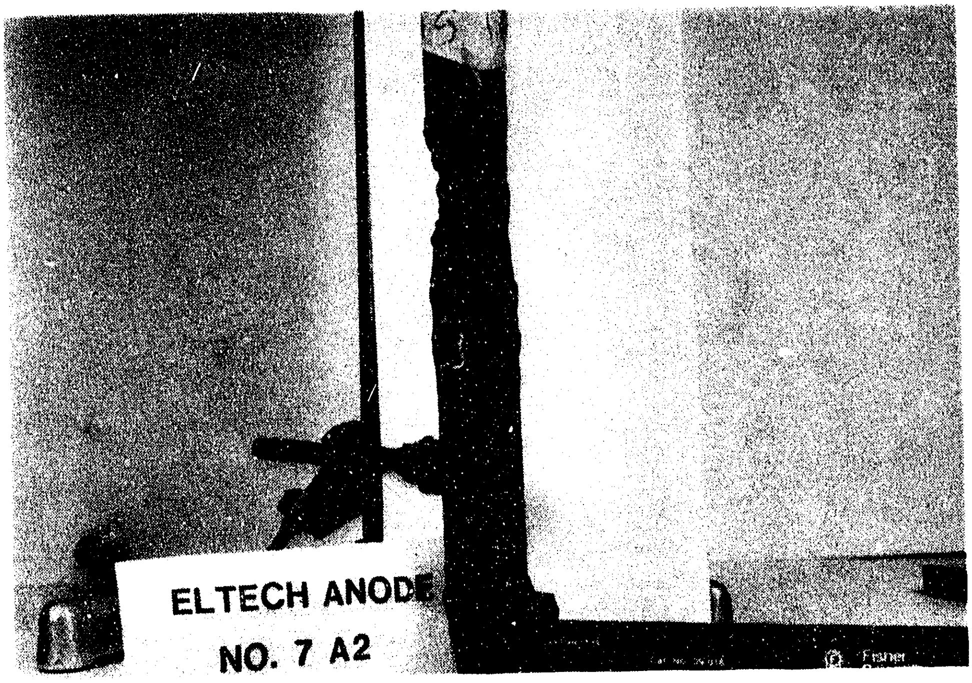

Figure 57. Typical Inconel 601 Anode connector rod after testing for 312 h.

an indentation in the rod at ~4 in. above the anode: where the alumina sleeve and alumina cement ended. In some cases there was ~25% reduction in the diameter of the rod at this point. The microstructure of the rods will be described in Subsection 4.3.

4.2.2 Summary of CEROX Coating and Oxidation Thickness

The CEROX coating normally ranged from 0.5 to 3 mm thick, which was close to the targeted thickness of ~1 mm. It varied in thickness between anodes and around the sides of the individual anodes. The sides of the anodes that were adjacent to the carbon anode or another cermet were expected to carry less current than the sides that were not adjacent to another anode. The distribution of the CEROX coating appears to mimic this current distribution; where CD was very low the CEROX coating was very thin or non-existent, where CD was higher, the CEROX coating was thicker.

Table 4 summarizes the Ce concentrations and Ce thicknesses when the tested anodes were removed from the cell. Anodes A1 and C1 were operated under similar test conditions. However, when A1 was removed from the cell the Ce concentration in the bath was around 0.31 wt% and the CEROX coating averaged ~1 mm thick. When C1 was removed the Ce concentration in the bath was ~0.52% and the CEROX coating averaged ~2 to 3 mm thick. Anodes A2, B2, and C2 were coated with a CEROX coating under the same conditions as A1 and C1, but after 72 h the CD was increased and then BR was decreased from ~1.5 to ~1.15. Laboratory tests by ELTECH have shown that the CEROX coating is thinner in more acidic baths, and the 0.6 to 1.4 mm thick CEROX coating on A2, B2, and C2 support those tests. During much of the time those anodes were operated the Ce concentration was high and erratic, when the anodes were removed the concentration in the bath was ~0.5 wt% (similar to C1) yet coatings were thinner. Anodes D1, E1, and F1 were also removed when the Ce concentration was ~0.5 wt%. Because of the cryolite crusting around the anodes, the CEROX coating was extremely thick (>4 mm), porous, and mixed with cryolite.

Table 5 summarizes the thickness of the gray oxidation layer on the exterior of the anodes. The oxidized zone will be discussed in more detail in Subsection 4.3. To summarize, the anode operated for the longest time period (E1) had the thickest oxidation layer, up to 18 mm thick. The amp-hours of that anode was similar to anode A2, which only had a 3 mm thick oxidation layer. Anodes A1 and C1 (operated under similar test conditions) had about the same amount of oxidation, even though anode C1 was operated for a longer period of time and passed more amp-hours. Therefore, oxidation thickness in this test does not seem to be directly relatable to hours of operation, average current, or amp-hours. The oxidation may have more to do with local conditions (in the vicinity of that particular anode) that may cause the oxygen to accumulate or disperse beneath an anode. For example, anode E1, which was

Table 4. Ce concentration and CEROX coating thickness.

Anode	Approximate Ce concentrations when the anodes were removed		Average CEROX coating Thickness (mm)
	Ce_{bath} (wt%)	Ce_{metal} (wt%)	
A1	0.31	2.27	0.5 to 1.5
C1	0.52	3.88	2 to 3 mm
E1	0.50	2.92	4 to 5 on W side 10 on E, frozen side
A2, B2, C2	0.50	2.92	0.5 to 1.4 mm

Table 5. Oxidation thickness.

Anode	Avg. Current (A)	Hours of Operation	A-h	Maximum Oxidation Thickness (mm)
A1	46 A	213	9798	7
B1	0	1	0	0.3
C1	67	275	18,425	6
D1	40	614	24,560	MB
E1	44	614	27,016	18
F1	53	614	32,542	MB
A2	101	312	31,512	3
B2	103	312	32,136	~4
C2	75	312	23,400	N/A

N/A indicates the anode was not cross sectioned.
MB indicates that parts of the bottom of the anode was missing.

partially frozen with the cryolite had the highest oxidation. Anode A2 operating under a higher CD and lower BR than A1 or C1 had a thin oxidation layer.

PNL also observed oxidation thicknesses of ~1 to 13 mm thick in their anodes tested under their standard conditions.[7] Their conclusions differ in that they can detect a relationship between the oxidation thickness and the current times time (A-h). They estimated that thickness (mm) = 5 E-4 x (Current times Time). They also concluded that low alumina content and high CD led to higher oxidation (reaction) layer thicknesses.

4.3 Microscopic Examination of Tested Anodes

An untested anode and anodes A1, B1, C1, E1, and A2 were chosen for cross sectioning and microscopic examination. The anodes were examined with an optical microscope (Nikon Optiphot) and with a Hitachi S-2300 (both secondary and backscatter imaging) Scanning Electron Microscope (SEM). Phases were analyzed by Energy Dispersive x-ray Spectroscopy (EDS) analysis with a Noran Series II x-ray Analyzer. Phase composition was calculated with the Noran SQ standardless quantitative analysis program. The presence of light elements (i.e., O, F, C) could be detected with an ultra thin window detector, but only cations could be recalculated for phase composition; the anion % in the phase was assumed.

4.3.1 Microscopic Evaluation of the CEROX Coating

The density and thickness of the CEROX coating varied from anode to anode and around the sides of the anodes. In Figures 58 through 67 the CEROX coating is labeled with a C, and the cermet substrate is labeled with an S.

On the side of anode A1 facing the carbon anode, the CEROX coating was thin to non-existent. Figure 58 shows the beginning of the CEROX coating on the side facing the carbon anode. The coating is ~4.5 cm up the side of the anode and is ~70 μm thick. The coating appears fairly continuous and even in thickness at that point. On the northeast side of anode A1 (~7 cm up the side), where the CEROX coating was thickest, the coating is up to 3 cm thick (Figure 59) and is dense. On both sides, the interface between the CEROX and the substrate appears mostly porefree. On the northeast section of the anode near the curved edge on the bottom, the CEROX coating (Figure 60) appears more irregular in thickness, less dense, and is generally thinner (up to ~1.3 mm thick). The interface between the substrate and the CEROX coating is still mostly pore-free, but is much rougher than in the other cases.

Anode C1 had a more even and thicker CEROX coating than A1. The CEROX coating on the bottom of the anode near the west side, is shown in Figure 61. The coating is continuous up to ~2.25 mm in thickness, with a fairly even thickness. Some elongated pores are

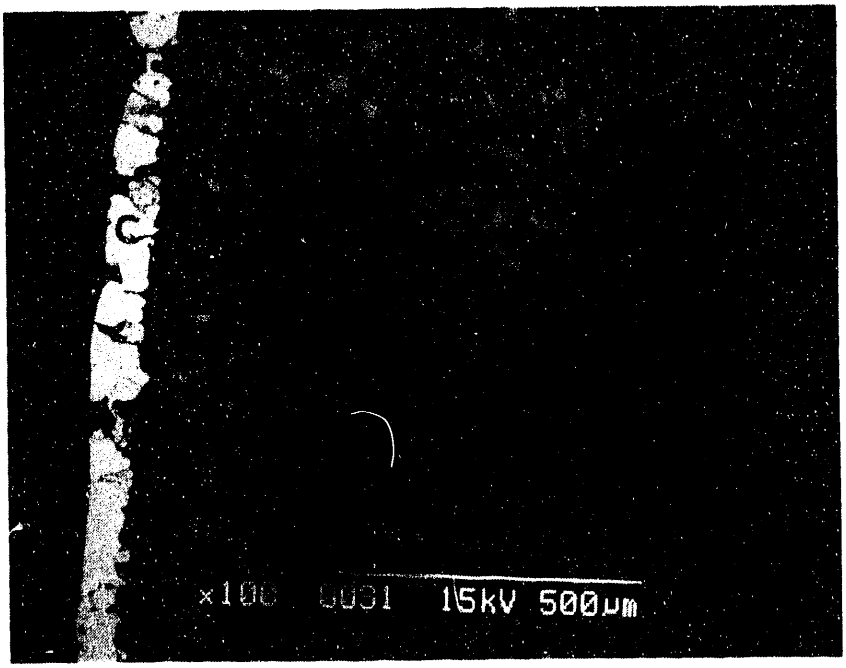

Figure 58. A thin Cerox Coating occurs on the side A1 facing the Carbon Anode.

Figure 59. Cerox coating on the northeast side of anode A1.

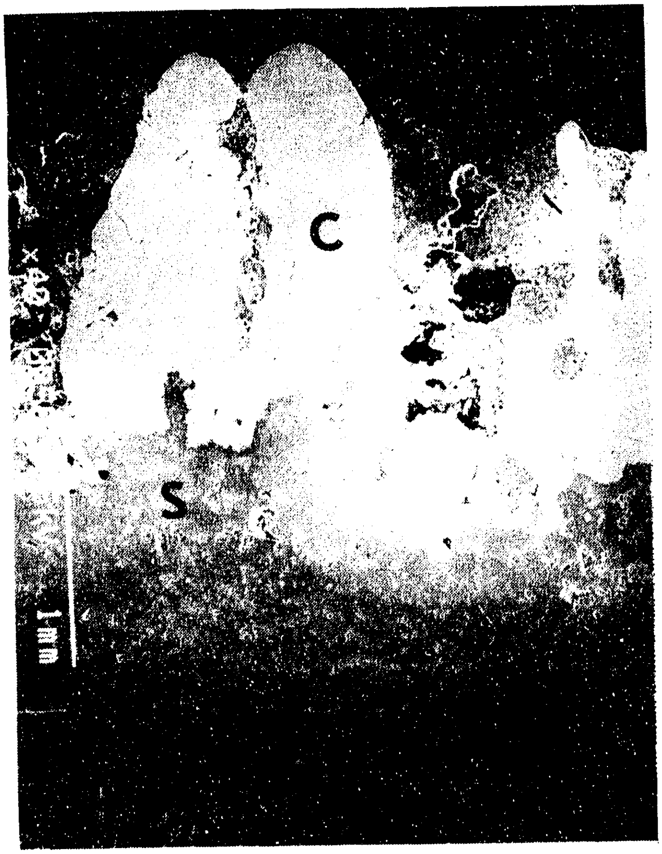

Figure 60. The bottom corner of Anode A1 has a thinner coating than the sides. The coating is also of a more irregular thickness.

Figure 61. The Cerox coating on the bottom of Anode C1 is thick and continuous.

present, but do not appear to penetrate to the substrate. The pores often contain cryolite. The CEROX coating on the northeast side of the anode ~7 cm up the side is shown in Figure 62. The CEROX coating is ~3 mm thick, dense, with a smoother, pore-free interface with the substrate. A clump of Al metal (A in Figure 62) is present at the edge of the CEROX coating. The elongated grains within the Al metal appear to be intermetallics containing Cu, Fe, and Ni in addition to Al.

Another region of the CEROX coating on anode C1 (from the northeast bottom corner) is shown in Figure 63. In that region the CEROX coating is also ~3 mm thick, but contains some larger pores in the exterior half of the coating. These pores do not appear to penetrate to the substrate. Again, some of the pores contain cryolite.

As described in Subsection 4.2.1, anode E1 experienced different conditions on the east and west sides of the anode. On the west side (~3 cm up from the bottom), where it appeared that current was still flowing at the end of the test period, the CEROX coating (Figure 64) appears similar to that in Figure 63 (anode C1). The coating is 3 to 3.75 mm in thickness, with some elongated cryolite-filled pores, particularly in the exterior half of the coating.

On the east side of the anode (where the anode was frozen into the cryolite) the character of the CEROX coating is completely different. The CEROX coating is so thick (~8.5 mm), that it is shown in Figures 65 (a) and (b). The inner half of the coating [Figure 65 (a)] shows a good, fairly pore-free interface between the CEROX coating and the substrate. The CEROX coating itself has large, roundish pores within it. In the exterior part of the coating [Figure 65 (b)], the coating appears less dense, and many "sawtooth" patterns appear to be present. In addition, numerous small pores occur, which appear to outline $Ce(O,F)_2$ grains within the coating. It is not known if this pattern is from the growth of the coating or from the dissolution of the CEROX coating at some time after it had been deposited.

Anode A2 operated during the last half of testing. The CEROX coating was deposited under the same conditions as those for A1 and C1. However, after ~74 h of testing the CD was increased, and after another ~160 h of testing the BR was decreased to ~1.15 for the remaining testing. During the testing of A2 the temperature and Ce concentrations fluctuated and averaged higher than during the first half of the test. The CEROX coating as shown in Figure 66 is much different in character on A2 then that on A1 and C1. The outer surface of the coating is much rougher, and it appears that the coating is less continuous. The coating is thinner, ~1.5 mm in thickness, and contains some of the "sawtooth" or the porous pattern noted in the exterior portion of the CEROX coating on anode E1. A close-up of this pattern is shown in Figure 67. Because this pattern was observed in both anodes examined that were in the

Figure 62. The Cerox coating on the northeast side of Anode C1 is up to 3 mm thick.

Figure 63. Bottom corner of the northeast side of Anode C1. The Cerox coating is thick but contains some pores.

Figure 64. The Cerox coating on the west side of Anode E1 is 3 to 4 mm in thickness and porous.

Figure 65a. The inner Cerox coating, next to the substrate, on the east side of Anode E1.

Figure 65b. The outer portion of the Cerox coating, on the east side of Anode E1.

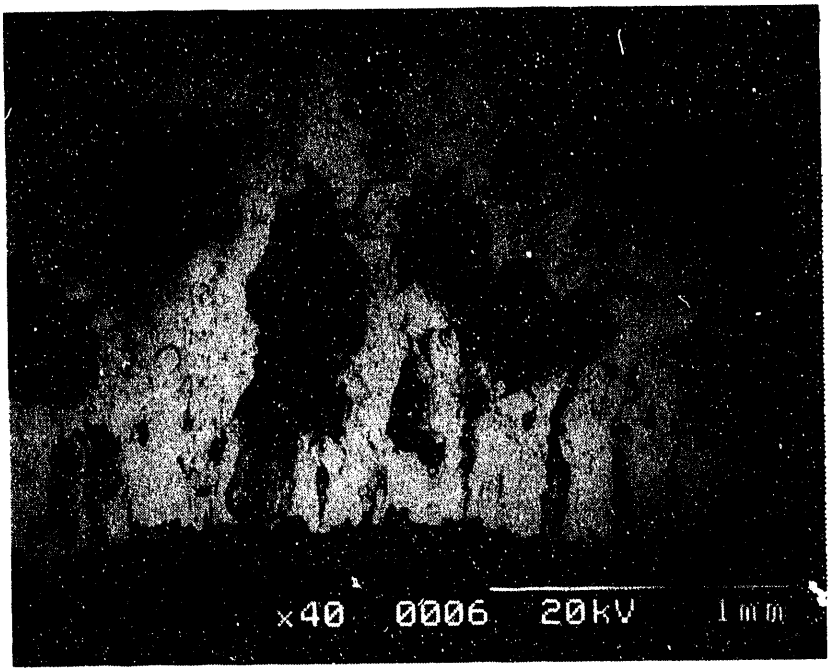

Figure 66. The Cerox coating on the bottom of Anode A2 is irregular and less continuous than on the other Anodes.

Figure 67. A close-up of the "sawtooth" pattern within the coating on Anode A2.

cell during the last part of testing,this pattern must result from something in the test conditions during that time.

The density and thickness of the CEROX coatings on anodes A1 and C1 are similar to the best coatings obtained in laboratory testing at "optimum" conditions (BR of ~1.5 to 1.6). Laboratory tests at lower BR have shown that the thickness of the CEROX coating decreases, and this is supported by anode A2. However, the extremely thick CEROX coating on the east side of E1, and the "sawtooth" pattern within the CEROX coatings of anodes A2 and E1 has not been noted in laboratory cells. Therefore, these characteristics are probably the result of the unique conditions that these anodes underwent during the latter phase of testing, with the thick E1 coating resulting from the cryolite crusting, and the porous pattern was most likely the result of fluctuating temperature and Ce levels.

4.3.2 Microstructures of the Cermet Anodes

The microstructure of the cermets were examined before and after testing. The untested cermet is a three-phase mixture that consists of Ni ferrite (spinel structure), Ni oxide (rock salt structure), and a Cu alloy phase. These phases undergo a variety of phase transformations during electrolysis. The original cermet material and the changes it undergoes are described below.

Microstructure of the Untested Substrates

Figure 68 is a low magnification photograph of the untested material while Figure 69 is a backscatter scanning electron image (BEI) of the sample. The backscatter mode (as compared to the secondary electron image) enhances differences in the atomic number, where phases having heavier elements (higher average atomic number) appear brighter than phases with lighter elements (which appear darker). In Figure 69, the bright features (A) are a Cu-Ni alloy phase, the lighter gray features are the (Fe,Ni)O phase (B), and the darker gray areas are the $Ni_{1-x}Fe_{2+x}O_4$ phase (C). The black spots are pores.

Figure 70 is a higher magnification secondary electron image (SEI) of Figure 69. The brighter features (A) in both figures are the copper rich phase. The light gray, dense grains are the NiO (B) phase and the darker grains are the Ni ferrite phase (C). Note that no obvious interphases exist at the grain boundaries of the different phases. The Cu grains are irregular in shape and range from ~10 to 125 μm in size. The NiO grains are also irregular in shape but are ~10 to 25 μm long. The $NiFe_2O_4$ occurs as rounded or equant grains, sometimes with a sharp crystal shape, and are ~10 to 30 μm in size.

Average compositions of the three phases are listed in Table 6.

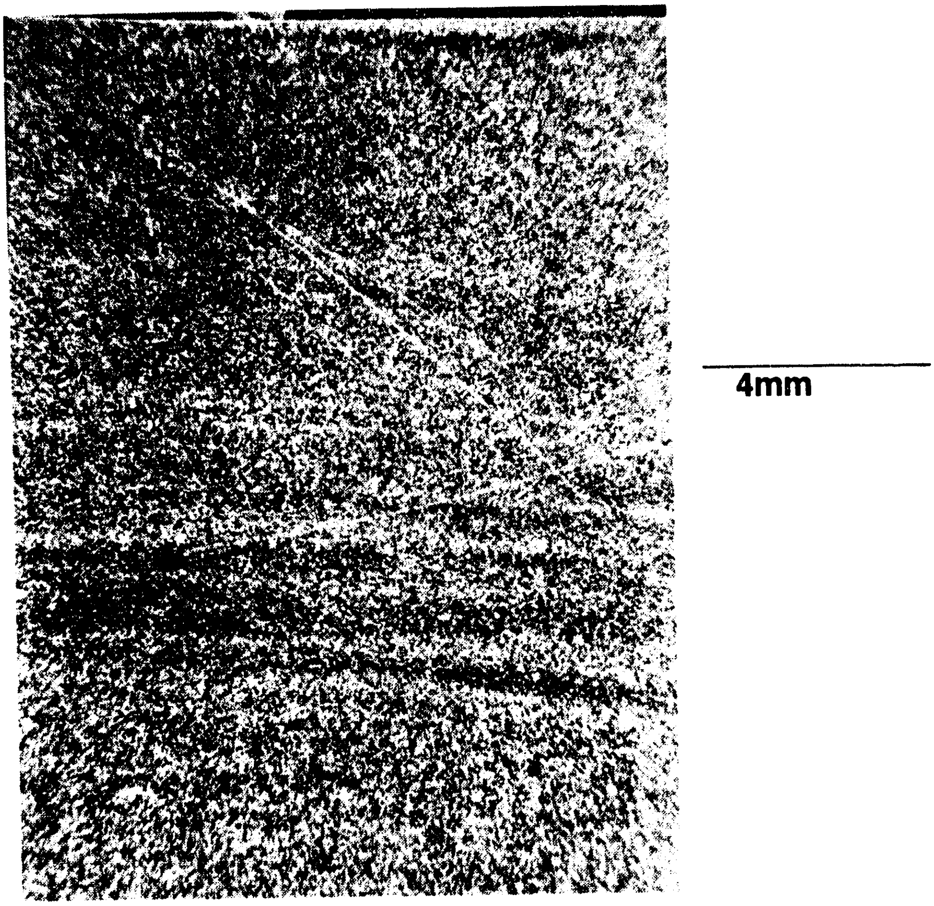

Figure 68. Low magnification cross section of the untested cermet.

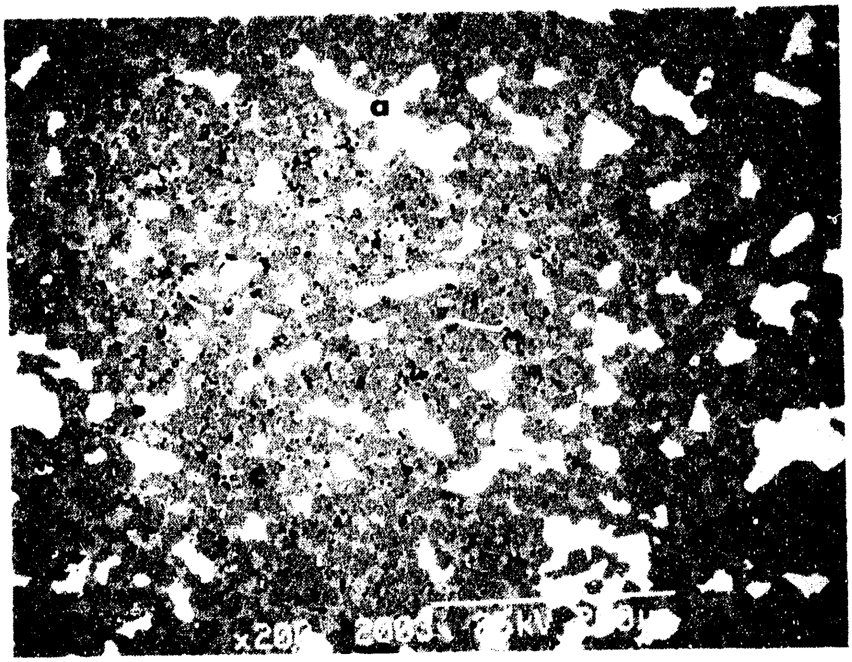

Figure 69. BEI of the untested cermet (200 X).

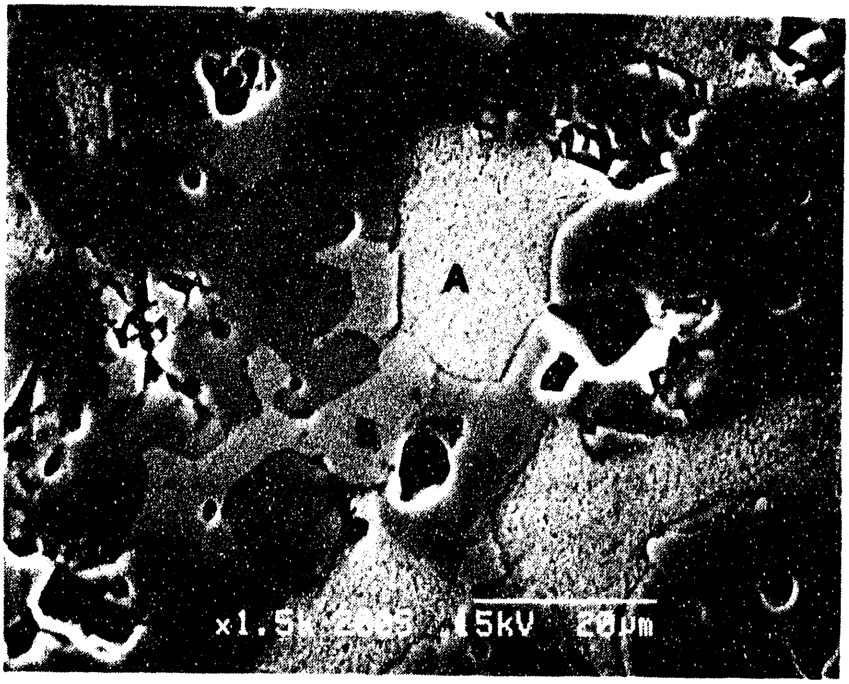

Figure 70. SEI of the untested cermet. A=Cu alloy, B=NiO, C=$NiFe_2O_4$.

Table 6. Phase compositions in the untested material.

Phase	% Fe	% Ni	% Cu	Cation Ratios
Ferrite	72.0	28.0	0	Fe/Ni = 2.57
NiO	10.5	89.5	0	Ni/Fe = 8.52
Cu Alloy	1.7	15.0	83.3	Cu/Ni = 5.61
Overall[a]	37.4	42.7	19.9	

Note: Compositions are given in mol% on a cation basis.
a. Based on the nominal batched composition.

The compositions are presented as a mol% basis for the metal content of the phase and this convention will be used throughout the report. There are some interesting observations that can be made from Table 6, one of which is the ferrite phase is not stoichiometric $NiFe_2O_4$. If it were stoichiometric, the Ni content would be 33.3%. Table 6 shows that the actual Ni content is 28%, so the ferrite is Ni deficient and Fe rich. Other observations are that the NiO phase contains 10.5% Fe while the copper alloy phase contains ~15% Ni and 1.7% Fe.

At the preparation conditions of 1200°C and 1.5×10^{-4} atm of oxygen, the resultant compositions of the $NiFe_2O_4$ and NiO phases agree extremely well with the equilibrium compositions that are predicted using the published thermodynamic data for the Fe-Ni-O system.[3,9,10,11] Figure 71 shows the NiO-Fe_2O_3-temperature phase diagram in air. At 1200°C, the ferrite is slightly Fe rich compared to $NiFe_2O_4$ and the NiO contains ~10% Fe_2O_3. Decreasing the PO_2 moves both the $NiFe_2O_4$ and the NiO phase composition toward the Fe side of the diagram; both compositions become enriched in Fe.

Published phase diagrams for the Cu-O system[12,13] show that pure, unalloyed Cu metal is not the thermodynamically stable phase under the cermet fabrication conditions. Instead, the stable composition consists of a two phase mixture of solid Cu_2O and a solution of oxygen dissolved in liquid copper (Figure 72). The phase equilibria of the Cu-O system dramatically changes when the temperature is raised by 25°C and the oxygen pressure is doubled.

Examination of Figures 69 and 70 show that the Cu phase appears as isolated grains and no evidence of Cu_2O is present, unless it is on such a small scale that the SEM cannot detect it. Figure 69 also shows that porosity is present in the anode. There appears to be a bimodal distribution of pore sizes where the pores range from 2 to 5 and 10 to 20 µm in size. As discussed in Subsection 2.2, the measured density on this sample was ~5.74 g/cm^3, which may be from 92 to 94% of the theoretical density (TD). Based on mass balance considerations and using the compositions in Table 6, a TD of 6.53 g/cm^3 was calculated. This would mean that the sample is only ~88.5% of TD and would suggest that porosity is much higher than previously assumed. Which ever TD is correct, it suggests that some open porosity is present in the untested cermet. Image analysis of Figure 69 showed that the area percent of porosity was 4 to 5% and the area percent of the Cu alloy was 14%. As discussed in Subsection 2.2, the porous nature of the samples is a result of the low densification pressure. Because some open porosity may exist in the untested anodes, it would be easy for the cryolite electrolyte to penetrate into the sample and attack the grain boundaries.

Cu depletion seams are found in the cermets (Figure 73) and tend to run parallel to the bottom surface of the anode. These seams can be observed in Figure 68 and are often easily visible

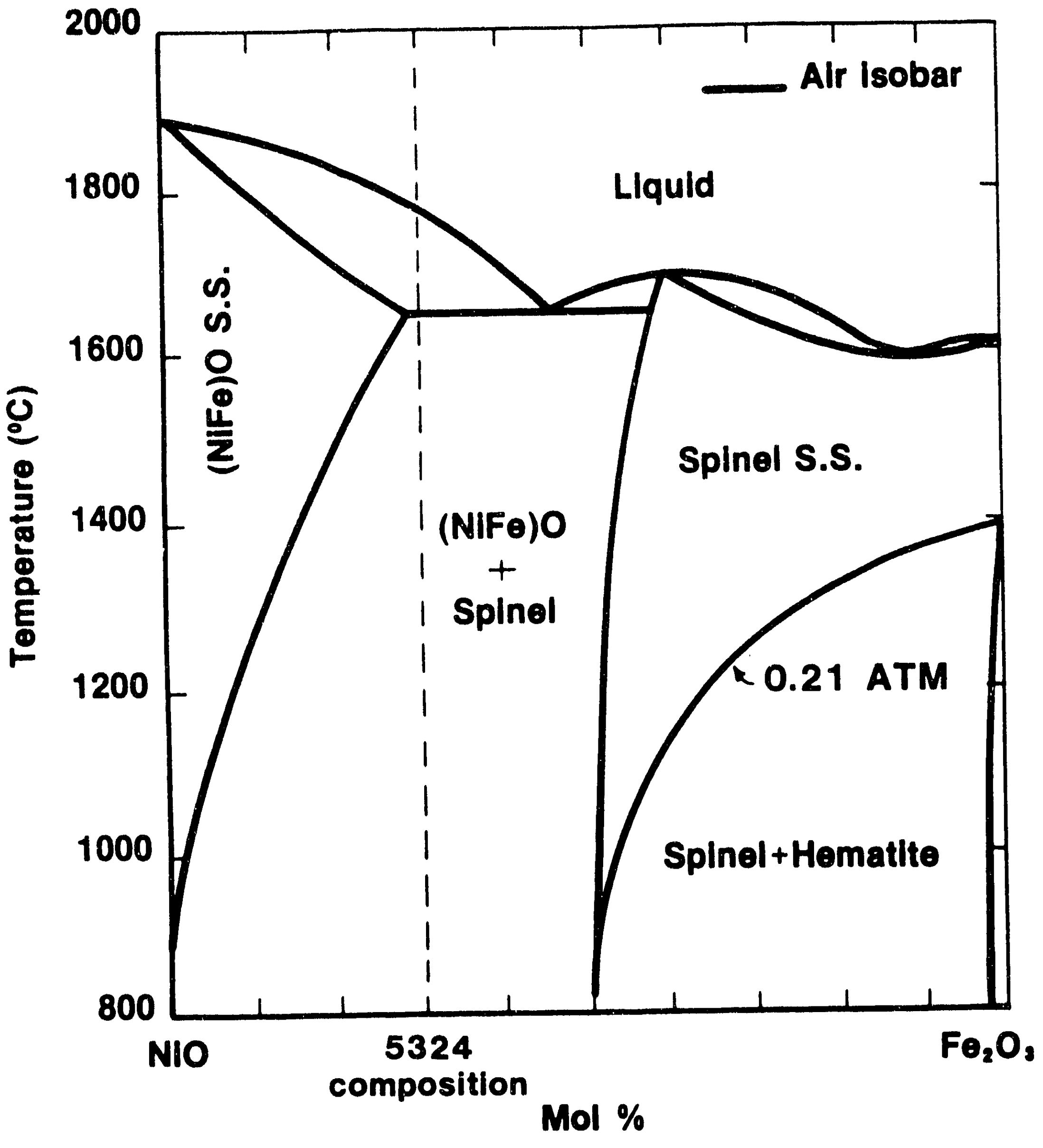

NiO-Fe$_2$O$_3$ Phase Diagram

Figure 71.

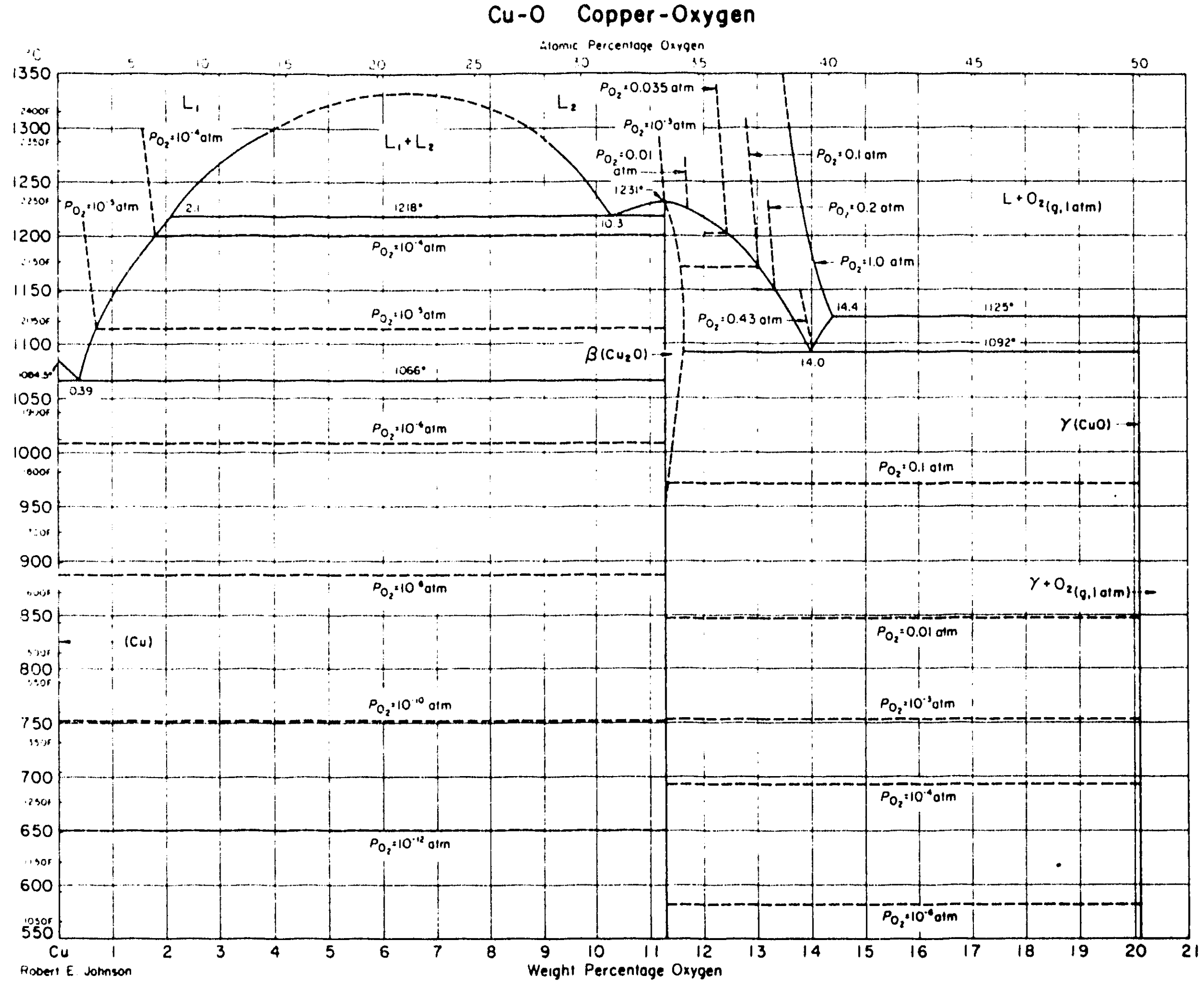

Figure 72. Cu-O phase diagram as a function of PO_2 and temperature.

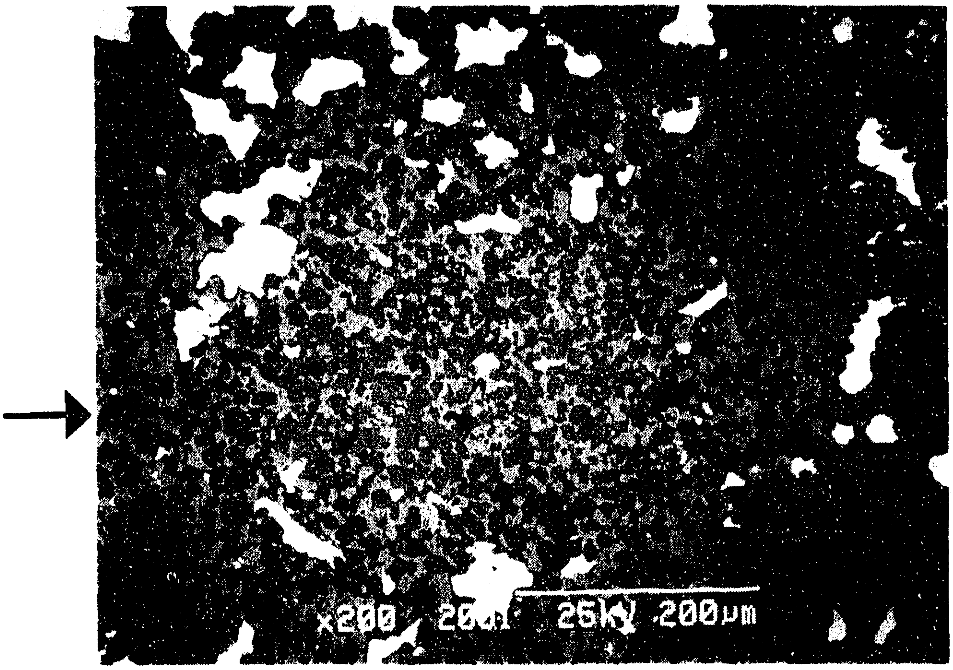

Figure 73. A copper depletion seam is shown within the untested cermet (arrow).

macroscopically. Figure 73 shows a seam that is ~200μm wide; they have been observed to be up to several cm long.

Although the electrical conductivity of these particular anodes were not measured, many measurements have been performed in the past on the $NiO-NiFe_2O_4-Cu$ cermet composition.[3,6,14] This composition does not behave like a classical cermet material. The electrical conductivity of this material occurs by a p-type semiconducting mechanism while the Alcoa reaction sintered Fe-Ni cermet with a continuous nickel metal bonding phase conducts metallically. The conductivity of the PNL laboratory cermet is 50 $(ohm-cm)^{-1}$ at ~900°C, while ELTECH has shown that the conductivity of their Cu cermet at ~1000°C ranges from 60 to 160 $(ohm-cm)^{-1}$, depending on the preparation and sintering procedures. ELTECH has also shown that (depending on the preparation procedure) not only will the room temperature and 1000°C conductivity change, but the character of the conductivity (more metallic or more semiconductive) changes.[6] The conductivity of pure Cu metal decreases as the temperature and amount of impurities (especially iron and oxygen) increases, while the conductivity of Cu_2O (a p-type conducting material) is ~3 $(ohm-cm)^{-1}$ at 900°C and $PO_2=10^{-3}$ atm.[15]

PNL has performed an extensive study on the mechanical behavior of this cermet material, both before and after testing.[7] They have shown that the mechanical properties are also not typical of a cermet (low fracture toughness, ~2.7 $MPa/m^{1/2}$, at room temperature) and that the untested cermet has a low strength (110 MPa, at room temperature). These results suggest this material should be approached, not as a classical metal-phase bonded cermet material (metal matrix composite) but instead as a ceramic matrix composite.

Microstructures of the Tested Anodes

Anode B1 - 1 h

Anode B1 was online for one hour before removal because of cracking. A section from the bottom corner of the west side of the anode (the side that faced the carbon anode) was mounted and polished, and a macroscopic photograph of the section is shown in Figure 74. This section of the anode has four distinct microstructural layers, with three of these layers occurring within the substrate. A BEI of the outer surface (Figure 75) shows three of the four regions. The dark region (D) is frozen cryolite from the bath. No CEROX coating (typically bright in BEI) was present because the CEROX coating did not form during the first 12 h of the test (Subsection 3.2). The bright features within the cryolite was found to be a Cu oxide phase.

The central region (C) of Figure 75 shows that a 500 μm thick reaction layer has formed on the outer surface of the substrate. Figure 76 (a) and (b) shows higher magnification micrographs of

Figure 74. Exterior bottom corner of Anode B1.

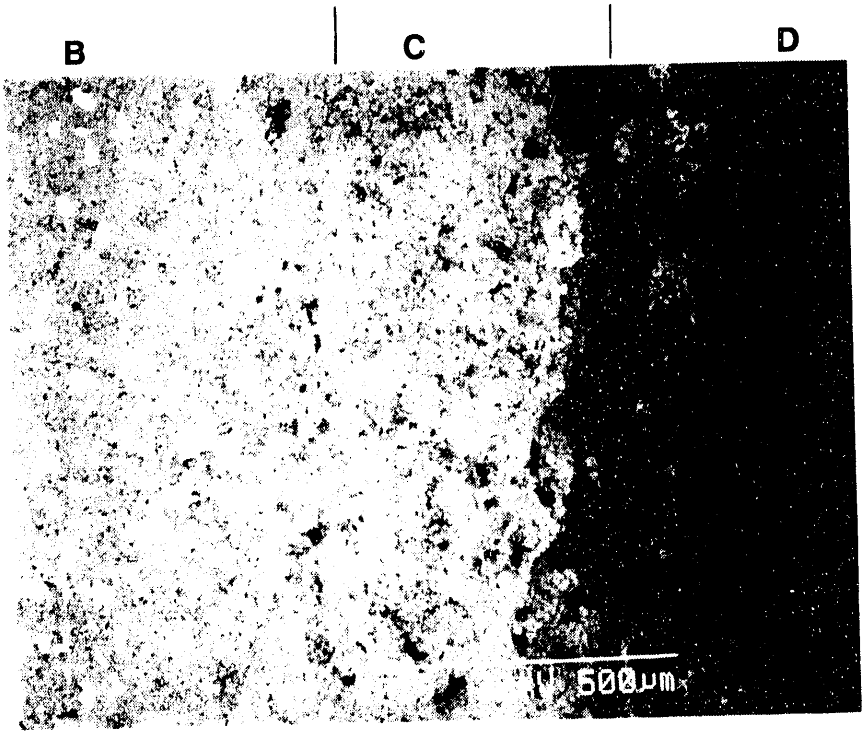

Figure 75. Outer edge of B1, tested for 1 h. D=cryolite, C=Cu depleted layer, B=porous region with Cu metal.

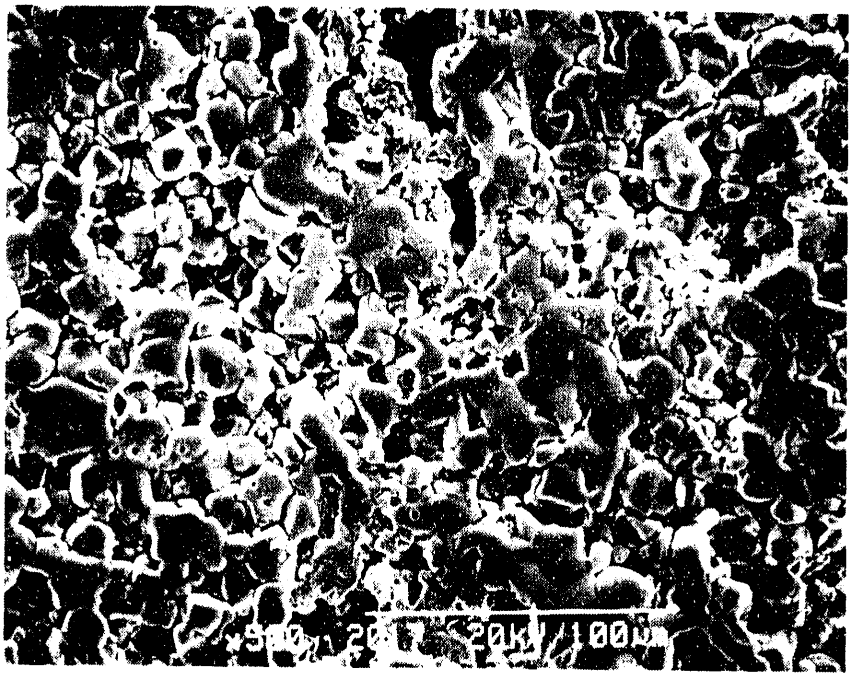

Figure 76a. SEI of the porous Cu depleted layer in Anode B1 (Layer C in Figure 75).

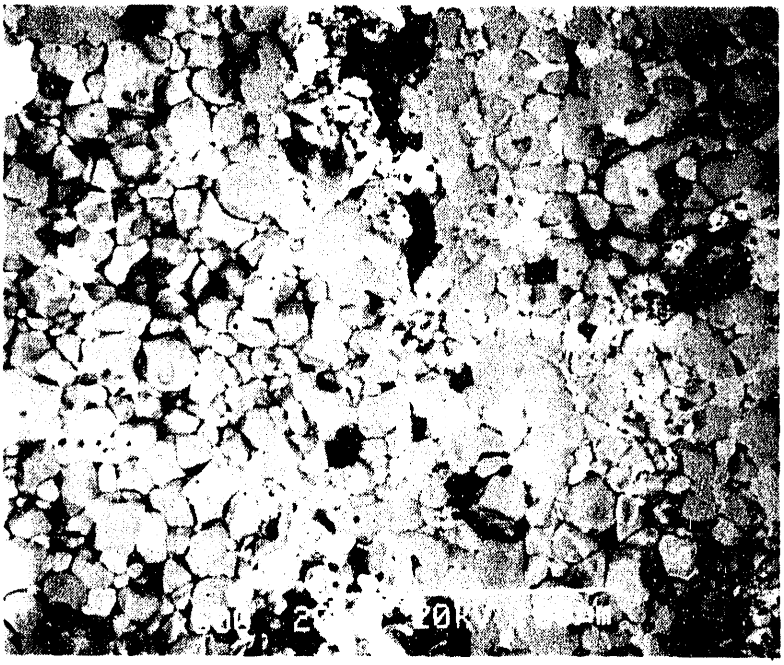

Figure 76b. BEI of the same area as 76a. The rate light grains are Cu-rich phases.

the inner boundary of this reaction layer. The bright features in Layer B are a Cu alloy phase and these are obviously missing in the reaction layer (Layer C). Electron probe microanalysis (EPMA) was performed at 500X in Layer C to estimate a bulk composition of the cermet, and it was found that this region was Cu depleted, containing 8.3 mol% Cu as compared to the starting bulk cermet with 19.9% Cu, 42.8% Ni and 37.4% Fe (all compositions are given in mol%). The Ni/Fe ratio was 1.133, which is very close to the batched ratio of 1.142. Thus, Cu is preferentially removed in this region. Most of the grain boundaries and triple grain junctions are rounded from corrosion with the cryolite and porosity is increased compared to the untested material. EPMA spot analysis on the ferrite grains showed that their composition is changed and they are now nearly stoichiometric $NiFe_2O_4$. Thus, Fe was removed from the ferrite grains.

The boundary between Layers A and B (Figure 74) are shown in Figure 77. This boundary occurred 4.2 mm in from the outer surface of the substrate. Higher magnification micrographs of the Layer A (inner) and Layer B (outer) regions are presented in Figures 78 and 79. Layer A (Figure 78) shows that the microstructure is very similar to the untested anode (see Figure 69). In contrast, Layer B (Figure 79) is very porous, probably because of grain boundary attack of the substrate. EPMA analysis showed that there is no significant difference in the overall composition of the two regions. It cannot be determined if the grains in the outer porous region were removed during operation of the anode (by dissolution) or if a grain boundary phase (cryolite) weakened the grain boundaries, causing pullout during the metallographic preparation procedure. The important conclusion is that the grain boundaries in this region were weakened during the initial stages of operation of the anode. Because all anodes underwent the same preheat procedure, it is expected that all of the anodes had a similar weakening during the preheat and early stages of testing.

Because the porous zone was ~4.2 mm in from the outer edge of the sample, and because the anode operated for only 1 h, the average penetration velocity of this front was 1.2×10^{-4} cm/s. The diffusion coefficient, D, of the penetrating species was estimated using the equation $x^2 = Dt$ and to give a value of $D = 5 \times 10^{-5}$ cm^2/s. This value is over 2 orders of magnitude greater than the diffusion coefficient of Cu in Cu_2O and six orders magnitude greater than the diffusion coefficient of Ni in NiO[15] so it is very doubtful that solid state diffusion is responsible for this microstructure. A more likely explanation would be the penetration of liquid cryolite along any existing open pores and along grain boundaries. The presence of this porous zone emphasizes the need to fabricate completely dense anodes to prevent or slow the rapid penetration and weakening of the cermet by cryolite. If the anode was immersed in molten cryolite for longer than an hour (during the heat-up period), more time might have been available for diffusion into

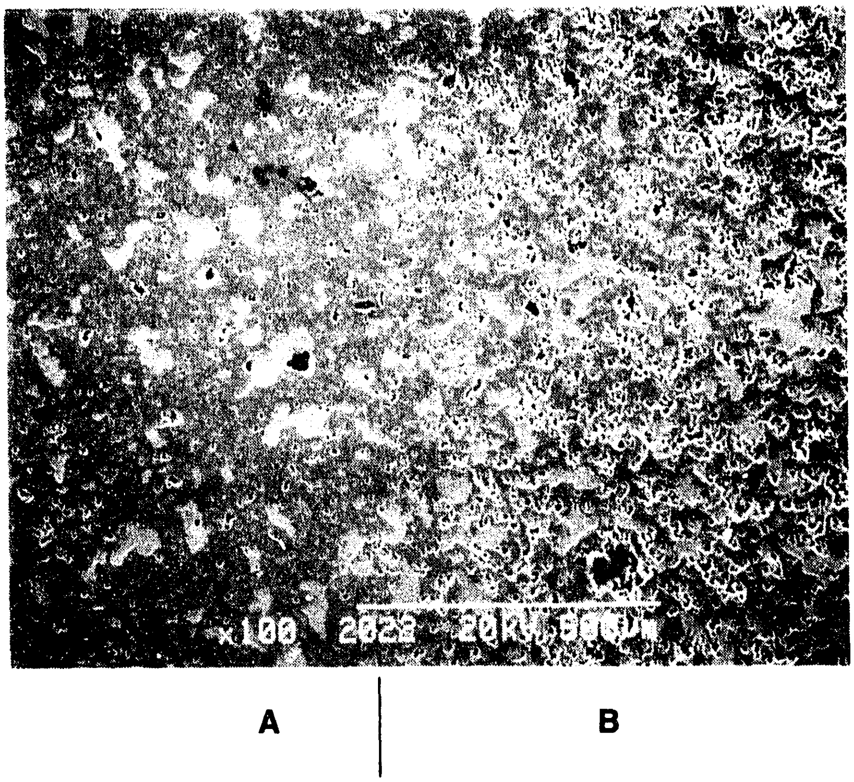

Figure 77. Anode B1, showing the boundary between the porous zone (B) and the dense zone (A) is ~4.2 mm into the sample.

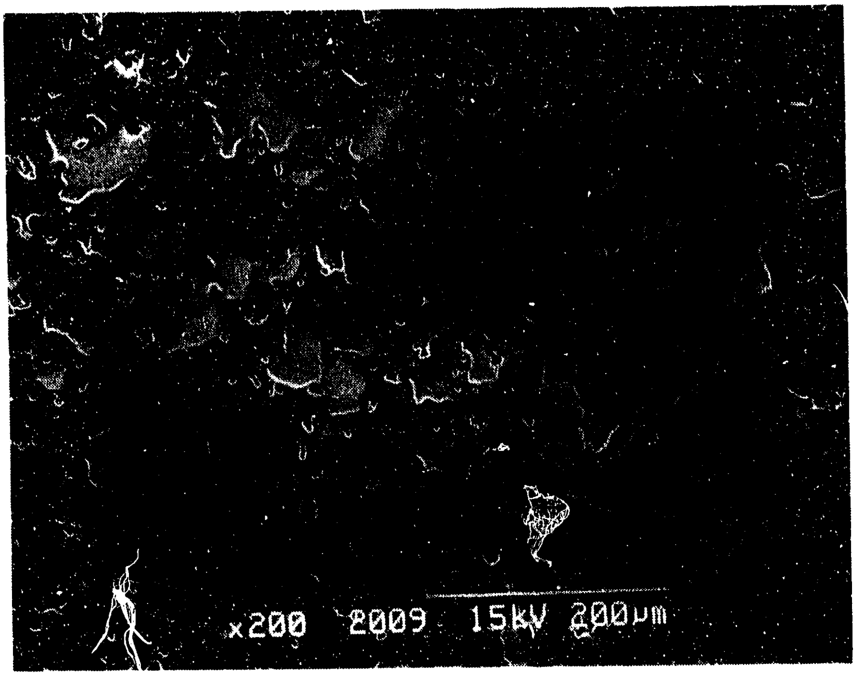

Figure 78. Inner dense zone (A) of Anode B1.

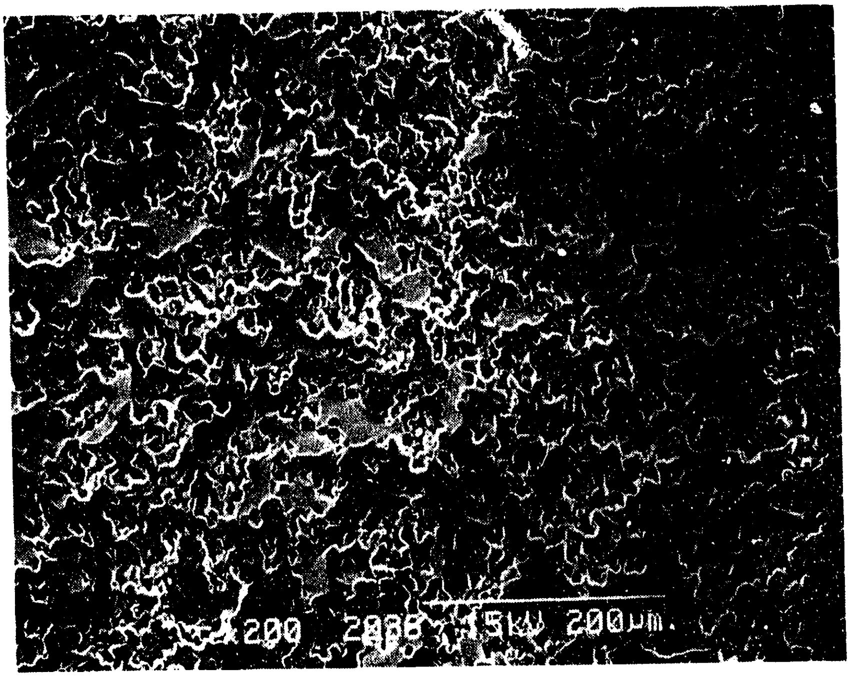

Figure 79. Outer porous zone (B) of Anode B1.

the sample.

Several observations were made on the changes in chemical composition of the individual phases. As mentioned above, some of the ferrite grains in the outer reaction layer had the stoichiometric $NiFe_2O_4$ composition (Fe/Ni = 2) but, although the Fe/Ni ratio in the ferrite phase increased with distance into the anode, it did not reach the ratio of the untested sample, Fe/Ni = 2.57. This is presented graphically in Figure 80 which shows that the stoichiometric Fe/Ni ratio of 2 is present up to 1 mm in from the outer surface and increases to a value of 2.45 at 4.65 mm into the sample. The boundary between layer A and B occurred at 4.2 mm. Thus, although the microstructure of the anode within layer A is very similar to the untested microstructure, changes in the chemical composition have occurred in this area.

Also shown in Figure 80 is a plot of the Cu/Ni ratio in the Cu-Ni alloy phase with distance into the anode. The Cu/Ni ratio decreases with distance into the anode, approaching the ratio in the untested anode (5.61). The Cu phases present in the outer Cu depleted reaction zone (layer C) had Cu/Ni ratios ranging from 10.5 to 27.5. Outside of this reaction zone, the Cu/Ni ratio decreased from a value of 7.18 at 1.6 mm into the anode to 6.28 at 4.65 mm. The iron content in the Cu alloy remained unchanged in this region.

These results are consistent with reported corrosion data on this system. Alcoa originally used nickel metal as the bonding phase but they found that nickel is electrochemically corroded when it is in the metallic state and it is preferentially removed from Cu-Ni alloys.[3] This appears to be evident in the Cu-Ni-Fe alloys in B1.

The NiO composition was essentially unchanged throughout the outer region. The only change in the composition occurred at 4.65 mm where one grain was slightly lower in Ni, containing 87 mol% Ni (Ni/Fe = 6.7) compared to 89 to 90 mol% (Ni/Fe = 8.1 to 10) in the other areas of the anode and in the untested anode.

Anode A1 and C1, 213 and 275 h, respectively.

Anodes A1 and C1 were operated in an electrolyte that had an average BR of 1.44 and averaged ~70% Al_2O_3 saturation (6.9 wt%). A sample from Section 40 of anode A1 was taken from the northwest side of the anode (thin CEROX side) while a sample from Section 43 of this anode was taken from the northeast side (thick CEROX side). The sample of anode C1 was taken from section 40 on the west side of the anode. These samples were mounted and polished and they represent the bottom corners of the anodes.

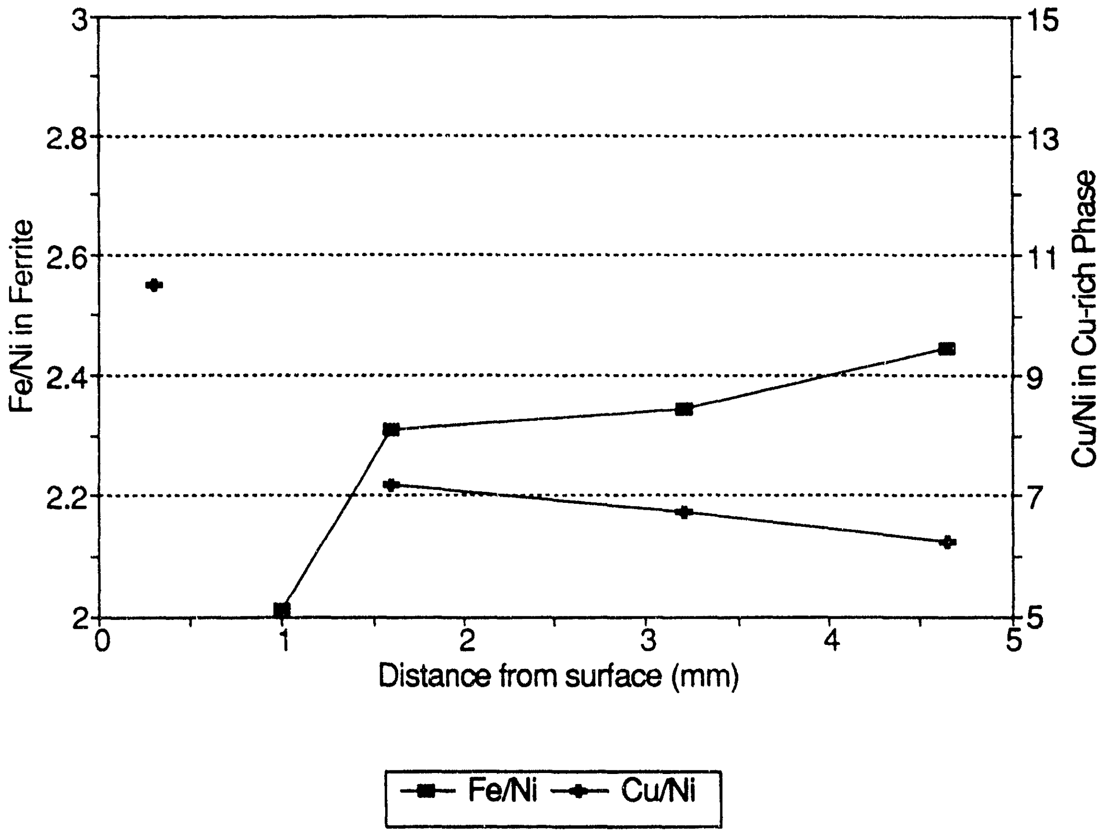

Figure 80. Composition of ferrite and Cu alloy phase in anode B1.

Macroscopic photographs of the polished cross sections of the samples taken from Sections 40 and 43 of Anode A1 are presented in Figures 81 and 82, respectively, while a photograph of Anode C1 is shown in Figure 83. These figures show that the resultant oxidation zones for the sections of anode A1 were 5 to 6 mm thick compared to 2 to 2.5 mm for the C1 sample. However, the thickness of the oxidation zone cannot be used as a quantifiable parameter for this experiment because the thickness also varied within each particular section. The thickness of the zone varied from 1 to 5 mm for Section 40 (northwest) of Anode A1 while the thickness of Section 43 (northeast) ranged from 5 to 10 mm. The thickness of Section 40 of Anode C1 (west) varied from 1 to 5.5 mm. It was decided to examine the microstructures of these particular samples because they showed features and reaction layers that were characteristic of other regions in the anodes.

There are many similarities but also some differences between these three sections. All anodes have a unique microstructure near the substrate/CEROX interface and these differences will be discussed beginning at the bottom of page 93. However, the composition and structure of the anodes away from this interface are very similar between the anodes. These samples all exhibit a porous Cu depletion zone that is ~500 µm to 1 mm thick, starting at the edge of the unique surface structure and extending into the substrate. At this point, the copper reappears in the form of a Cu-rich oxide phase. This phase forms an oxidation zone that is black to the naked eye and these zones are marked by the O in Figures 81 through 83. Further into the center of the anode, this black zone converts to a Cu colored structure that is present throughout the remainder of the anode. The change in color from black to copper signifies a phase transition from a Cu oxide (probably Cu_2O) to a Cu metal alloy.

Figure 84 (Anode A1) shows an example of the Cu depleted region (N). The CEROX coating is to the left (C) and the region containing Cu-oxide is to the right (O). Within the Cu depleted region NiO, $NiFe_2O_4$, and porosity occur. In the oxidized zone, NiO, $NiFe_2O_4$, and porosity occur, along with Cu oxide (the bright phase within the oxidized zone, Figure 84). A typical interface between the Cu metal and Cu oxide region is shown in Figure 85 (Anode C1). The boundary is usually sharp and can be seen in Figure 85 by the transition from the medium gray Cu-oxide to the slightly brighter Cu metal (in BEI). The shape of the Cu oxide and Cu grains are similar but the Cu oxide is more likely to be present in places as a grain boundary phase.

The chemical composition of the NiO and $NiFe_2O_4$ phases remain fairly constant throughout the Cu depletion zone, oxidation zone and the unoxidized region. The compositions are also the same for both anodes. The ferrite phase transforms from being slightly Ni deficient (in the untested) to a nearly stoichiometric composition. As reported in the B1 section, it was shown that the stoichiometric

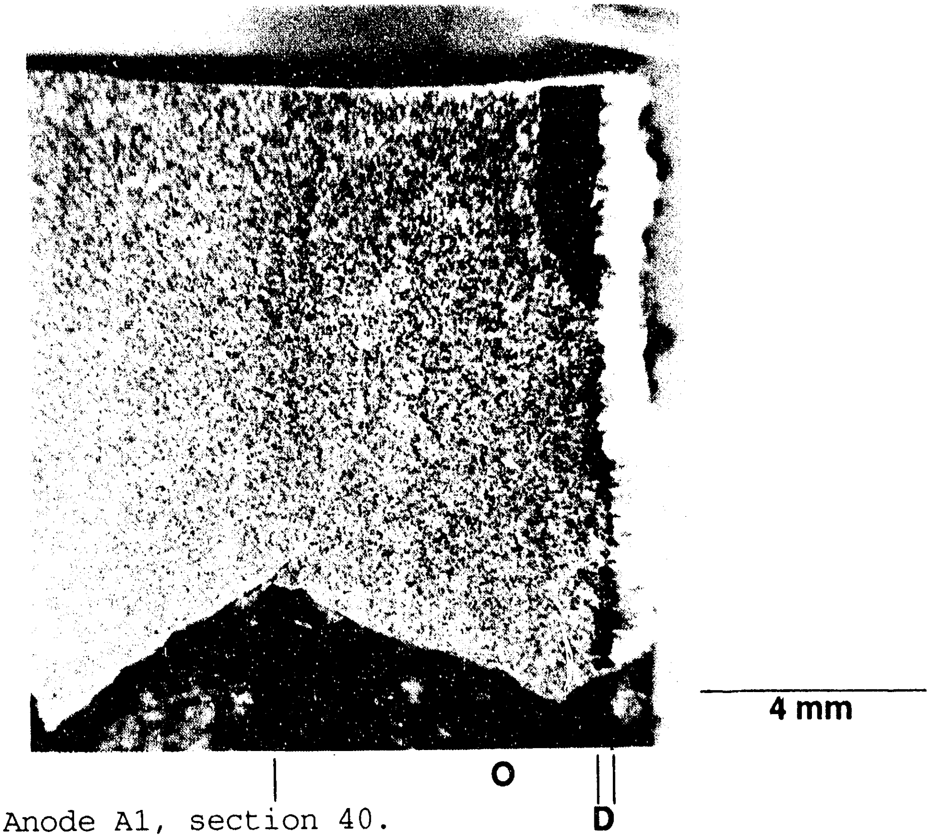

Figure 81. Anode A1, section 40.

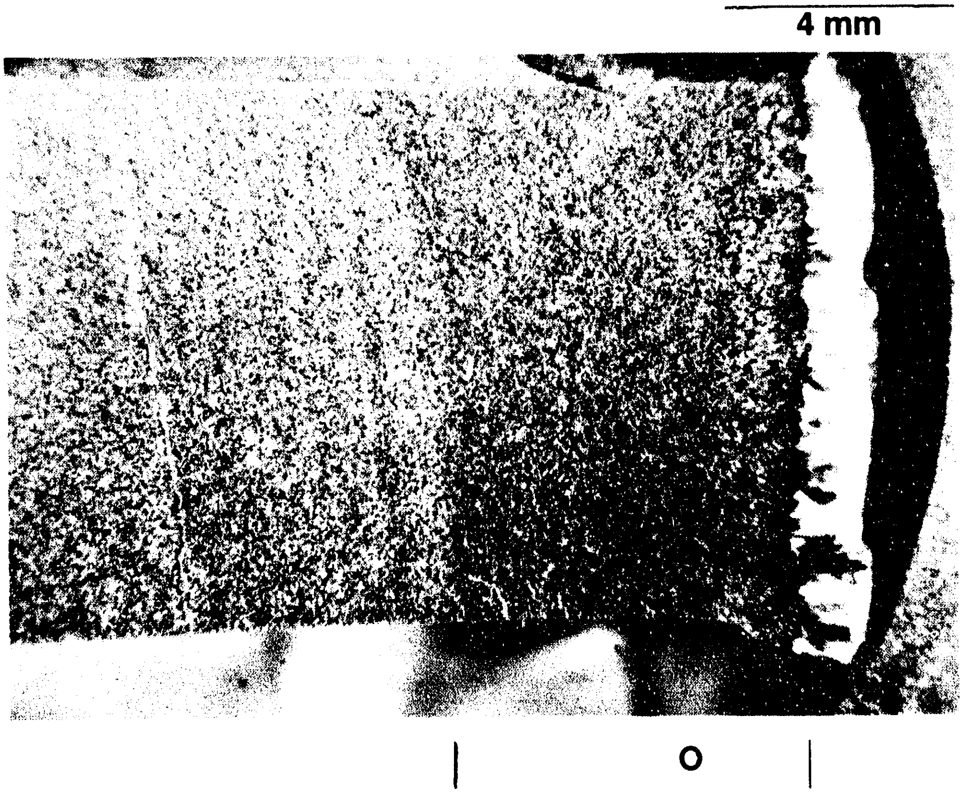

Figure 82. Anode A1, section 43.

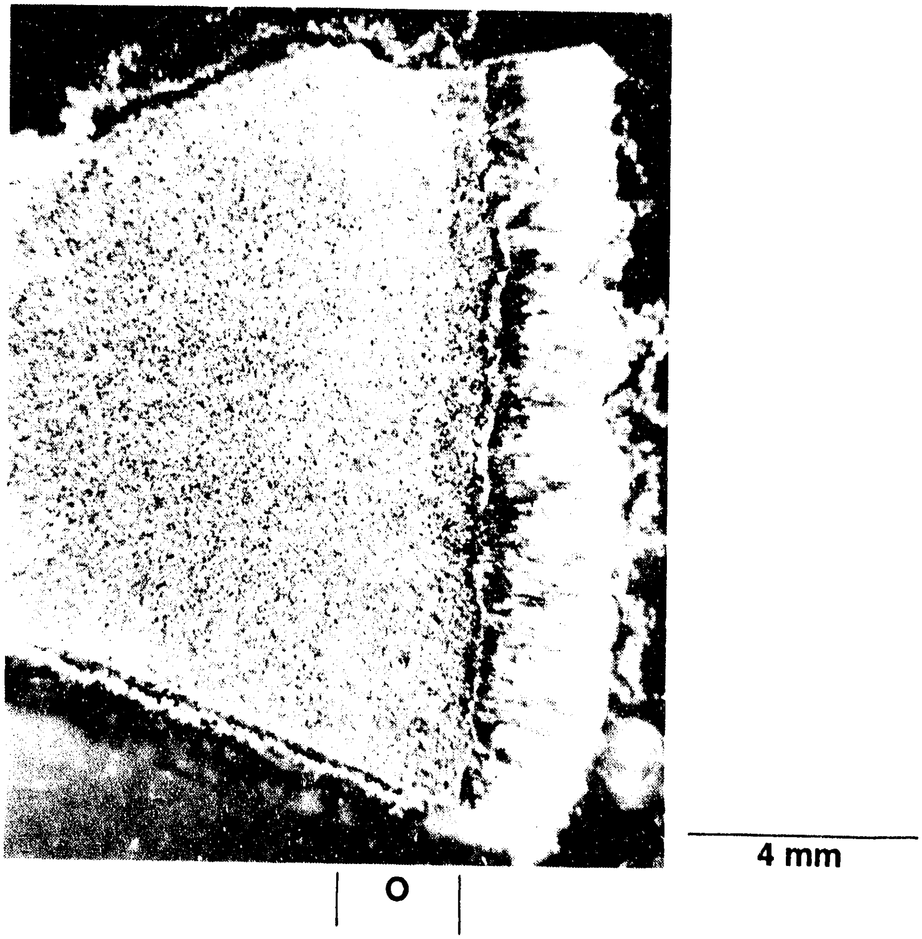

Figure 83. Anode C1, section 40.

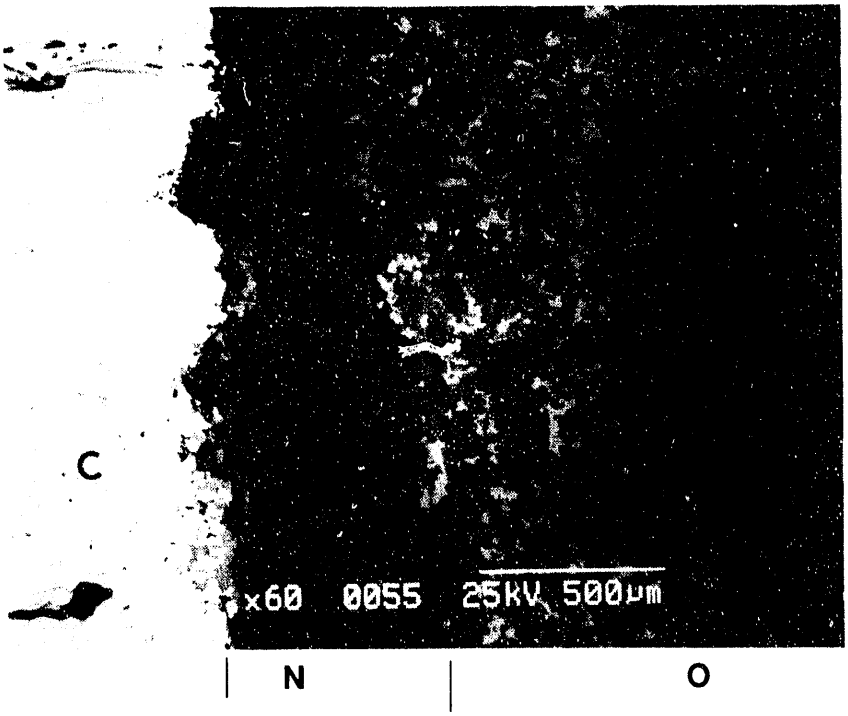

Figure 84. Anode A1, section 43. O=oxidized region, N=Cu depleted region, C=Cerox.

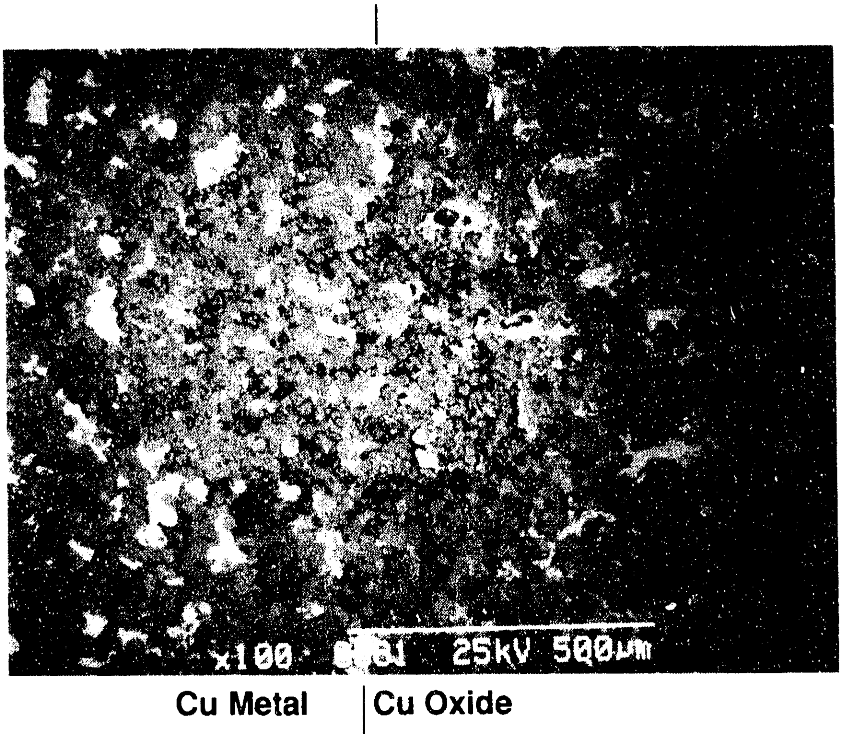

Figure 85. Anode C1, section 40. Boundary between Cu metal and Cu-O zones.

ferrite composition, $NiFe_2O_4$, was detected in the surface reaction zone after only 1 h of operation. Therefore, it is not surprising to observe this composition in these anodes. The composition of the NiO does not significantly change from its original composition of 89.5 mol% Ni and 10.5 mol% Fe. The only change observed is that quite often, minor amounts of Al and Cu are detected (<2 mol% each) in the ferrite and NiO phases. Al and Cu tend to substitute for Fe and Ni (respectively) in the ferrite phase while they substitute for Fe in the NiO phase.

These anodes probably underwent an oxygen chemical potential gradient across them such that the activity of oxygen decreased with distance into the sample. The inner areas would be expected to have a lower oxygen activity while the outer areas should have a higher activity. The composition of the ferrite phase can be explained using the phase equilibria for the Ni-Fe-O system. The phase diagram for this system at 1004°C as a function of PO_2 is presented in Figure 86. This diagram shows that as the oxygen pressure of the system increases, the equilibrium concentration of the ferrite becomes more stoichiometric (less Fe) and the Fe content in the NiO should also decrease. The trend from Fe rich ferrite to a stoichiometric Ni ferrite was observed in all the anodes after testing. However, there was little change in the composition of the NiO within the Cu depleted, Cu oxidized, central Cu metal region (tested), and the untested anodes, although the phase diagram predicts that the Fe content should decrease at higher PO_2.

One very interesting observation is that the cation composition of the Cu-rich phase is the same in the Cu_2O oxidation and Cu metallic zones. The composition is ~95 to 96% Cu, 1 to 1.5% Ni, 1 to 3% Fe, and 0 to 2% Al (all mol%).

The compositions of the ferrite, NiO, and Cu rich phases in regions outside of the surface copper depletion zones for Anodes A1 and C1 are summarized in Table 7. These compositions are representative of both the copper oxidation and copper metal zones. Table 6 lists the compositions of the untested material and a comparison of Tables 6 and 7 readily shows that the Ni is depleted from the Cu rich phases. Also, the ferrite phase becomes more stoichiometric $NiFe_2O_4$ during operation because the Fe content decreases from 72 to ~64 mol%. Table 7 suggests that the ferrite phase may be slightly Fe deficient. This is possible because Al, and a small amount of Ni, can substitute for ferric iron (+3) in the lattice of the spinel. Finally, these tables show that the composition of the NiO phases do not significantly change.

The microstructure at the substrate/CEROX interfacial region differs between the three samples. In Section 40 of Anode A1, Figure 81 shows that a dark dense patchy region (D) is present at the substrate/CEROX interface, within the substrate. In Figure 87, the CEROX coating (C) is at the right of the micrograph and the

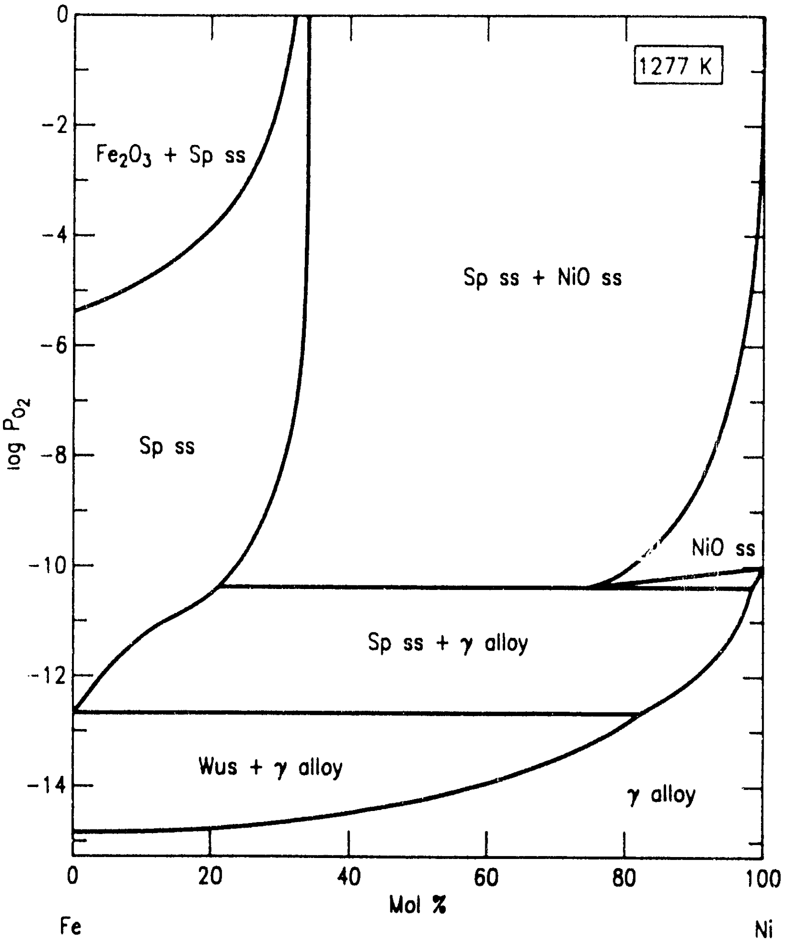

Figure 86. Fe-Ni-O phase diagram at 1277 K.

Table 7. Average phase compositions in Cu metal and Cu oxide regions in Anodes A1 and C1 (in mol%).

Phase	%Fe	%Ni	%Cu	%Al
Ferrite	64 to 67	30 to 33	0 to 2	0 to 2
NiO	8 to 10	88 to 91	0 to 2	0 to 2
Cu rich phase (Cu oxide or Cu metal)	1 to 3	1 to 2	94 to 97	0 to 2

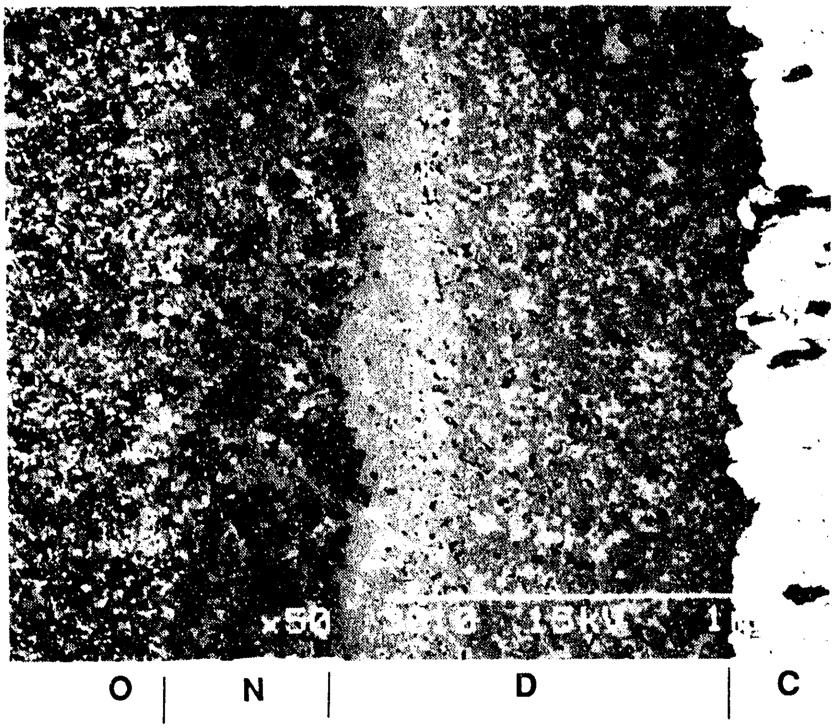

Figure 87. Exterior section of Anode A1, section 40. D=dense region, N=Cu depleted zone, O=Cu oxide region, C=Cerox.

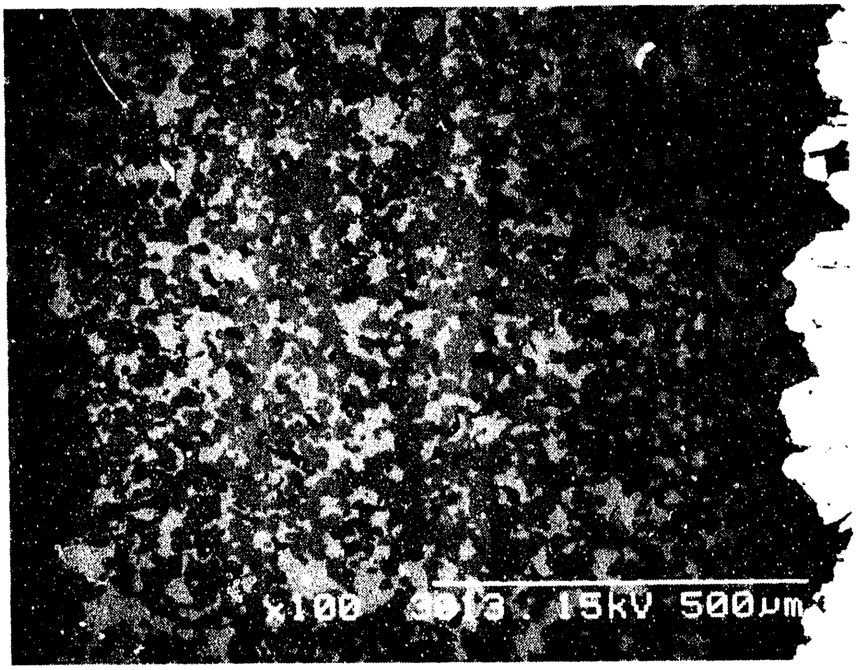

Figure 88. Higher magnification BEI of the dense area in Figure 87 (Anode A1, section 40).

dense surface region (D) lies next to it. The Cu depleted zone (N) is the dark porous band adjacent to the dense region and on the far left is the oxidation zone (O) where the individual bright features are Cu_2O grains.

Figure 88 is a higher magnification BEI of the dense surface region. Although the region is denser than the surrounding substrate, pores (the black spots) are still present. The dense region consists of NiO (light gray) and the Ni ferrite (dark gray). The chemical composition of the NiO phase near the outer surface is 71% Ni, 7% Fe, 2.5% Al, and 19.5% Cu but gradually changes to 64% Ni, 10.5% Fe, 1.5% Al, and 24% Cu near the Cu depletion zone (all values in mol%). Similarly, the composition of the ferrite changed from 51% Fe, 29% Ni, 17% Al, and 3% Cu near the surface to 63% Fe, 30% Ni, 3% Al, and 4% Cu near the Cu depletion zone. Thus, significant amounts of Cu is dissolved in the NiO phase while Al is dissolved in the ferrite phase.

No Cu metal or Cu-rich oxide phase is present in this region. Rather, the majority of the Cu that is present in this layer exists as the Cu^{2+} ion in the NiO phase. This can be considered to be a solid solution of NiO-CuO because the solubility limit of CuO in pure NiO is 28 to 35 mol% CuO.[16,17] However, it is possible that this solubility limit could be lower in the presence of 7 to 10 mol% FeO. Knowledge of the phase behavior of the Cu allows us to estimate the oxygen activity gradient within the anode. This can be accomplished by following the transformation of the copper from (Ni,Cu)O (ss) $\rightarrow$ Cu_2O $\rightarrow$ Cu metal. The activity of CuO in (Ni,Cu)O solid solutions at 1000°C has been measured in[16] and the thermodynamic data for the Cu-O system has been published[12]. Using these two sources, it was calculated that the reaction $Ni_{0.76}Cu_{0.24}O$ $\rightarrow$ Cu_2O occurs at an oxygen activity of $\sim 5 \times 10^{-2}$ atm while $Cu_2O \rightarrow Cu$ (metal) occurs at an oxygen activity of 4×10^{-7} atm.

Significant amounts of aluminum were found in the ferrite phase near the substrate/CEROX interface, but the Al content decreased further into the substrate within the dense region. Alcoa also observed diffusion of Al into the ferrite phase of their Cu-cermet anodes.[3] The phase diagram of the Fe-Al-O system (constructed from 1280 to 1500°C)[18] shows that Fe_3O_4 and $FeAl_2O_4$ can form a complete solid solution. In addition, up to 20 mol% Al can be easily dissolved in Fe_3O_4 over 6 orders of magnitude of oxygen pressure. The Ni-Al-O phase diagram[19] shows that $NiAl_2O_4$ and NiO coexist as the stable phases at 980°C and $PO_2 > 5 \times 10^{-6}$ atm. Thus, it is not surprising to observe Al in the ferrite phase, especially because a large driving force exists for aluminum diffusion into the material because of the aluminum concentration gradient that exists at the surface.

A 10 μm thick reaction layer exists between the dense region and the CEROX coating. A BEI of this layer is presented in Figure 89,

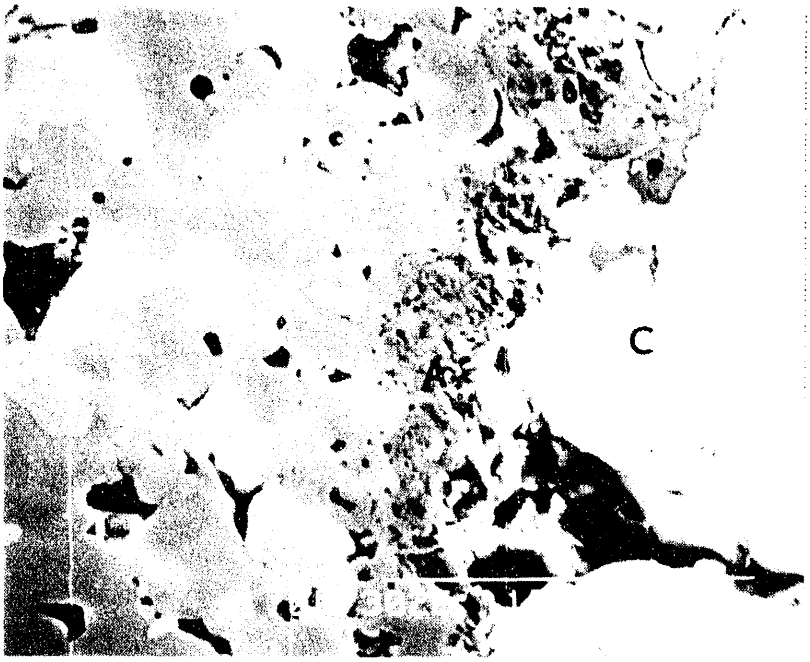

Figure 89. A porous 10 µm thick aluminate layer (A) is between the Cerox (C) and the substrate.

which shows that this layer appears to be porous. EPMA was performed in two spots of this layer and both spots had a composition that is ~67% Al, 11.5% Fe, 18% Ni, and 2.5% Cu (mol%). The light element window was used in the analysis and a large oxygen peak was detected. This EPMA coupled with the above discussion suggests that the layer is a mixed aluminate with the composition, $(Fe,Ni)Al_2O_4$. However, x-ray diffraction was not performed to confirm this hypothesis.

The microstructure at the outer surface of Section 43 of Anode A1 is shown in Figures 90 and 91. Figure 90 is a low magnification SEI that shows that a dense surface layer (D) lies between the CEROX coating and the porous copper depletion layer. The layer in this section is thinner and less continuous than that observed in Anode A1 Section 40. Figure 91 shows the substrate/CEROX interface in more detail. In a few isolated areas at the interface, 1.5 μm thick interlayers exist that are an oxide containing 96.7 mol% Cu and 3.3 mol% Al. However, it was mentioned above that the composition of Cu in the Cu rich phases in the bulk of the material is typically 96 mol% so it cannot be determined if the microstructure of this feature is strictly because of surface effects.

The top of Figure 91 shows a 10 μm thick layer at the interface that is very similar in structure and composition to the Al rich layer that was shown in Figure 89. The NiO within the dense region, however, unlike Section 40, contained no significant amounts (>2 mol%) of Cu. The remaining behavior of this sample outside of the surface region is very similar to that of Section 40.

Figures 92 and 93 shows two BEI of the interfacial region for Section 40 of Anode C1. These micrographs show that the interface of this sample is distinctly different than the samples from anode A1. This interface has a columnar duplex structure that is comprised of a Ce fluoride (F) and a Cu oxide (O). The CEROX coating (C) is the bright layer that appears similar in contrast to the Ce fluoride grains (the bright lines in the SEM photo are an artifact of the carbon coating applied to the sample to make it conductive for SEM analysis). In the CEROX coating, only cerium is detected but in the Ce fluoride, calcium is found in addition to Ce and F. The Cu phase in the duplex region is similar to Cu oxide in the bulk of the sample because it contains 98 mol% Cu and minor amounts of Al, Ni, and Fe, in addition to oxygen.

On the left of the duplex layer in Figure 93 is a denser area consisting of the ferrite phase. The composition of the ferrite phase in this layer is 22% Al, 46.5% Fe, 27.5% Ni, and 4% Cu (mol%). At lower magnification (Figure 92) the dark region to the left of the ferrite layer is the beginning of the copper depletion zone. The ferrite phases within this region (at 500 μm into the anode) becomes nearly stoichiometric. Similarly, the NiO phase

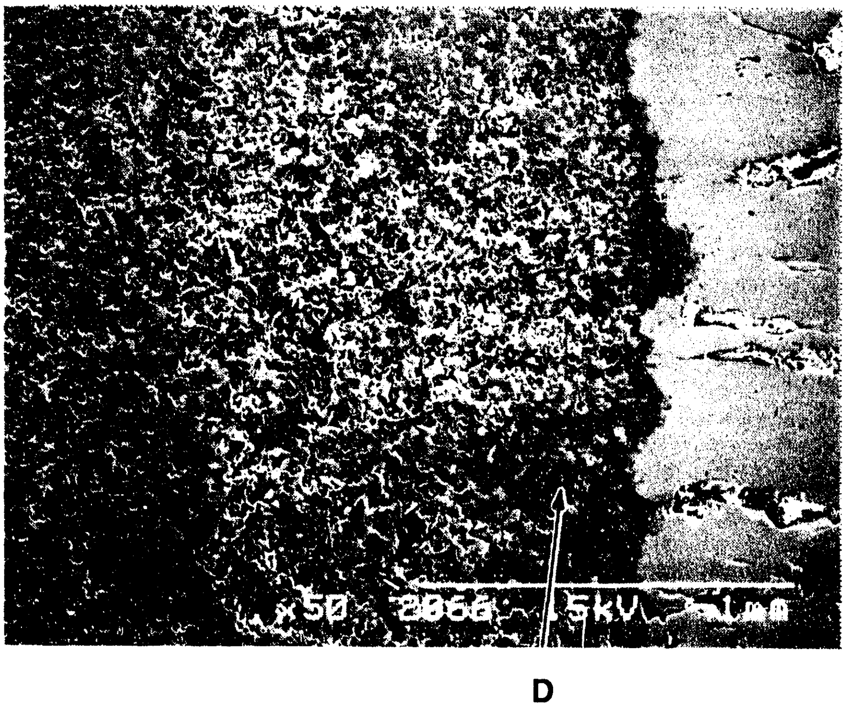

Figure 90. Anode A1, section 43 (SEI) showing the dense region (D) next to the Cerox coating.

Figure 91. Anode A1, section 43, at the Cerox-substrate interface.

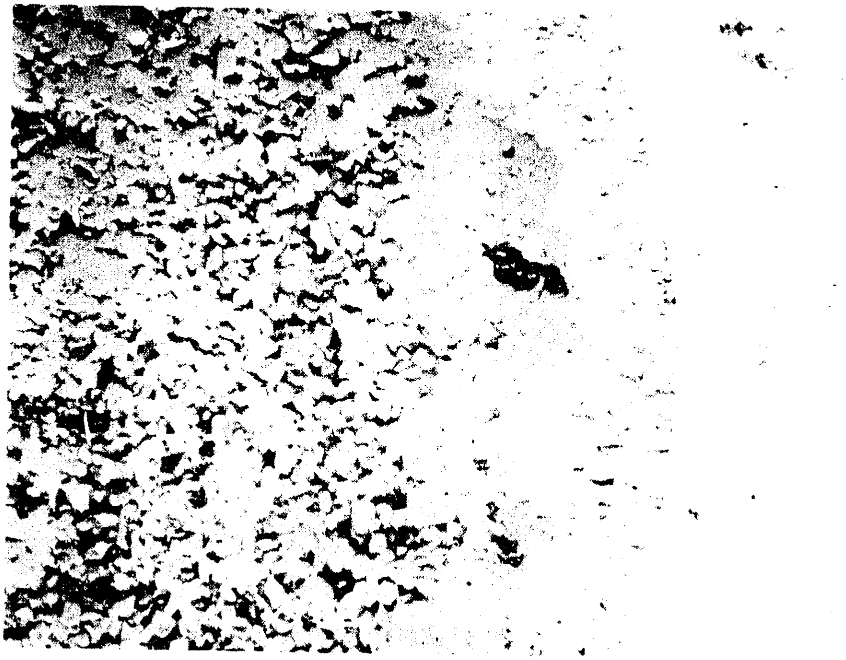

Figure 92. Anode C1, section 40, interface between the Cerox coating (far right) and the substrate (left).

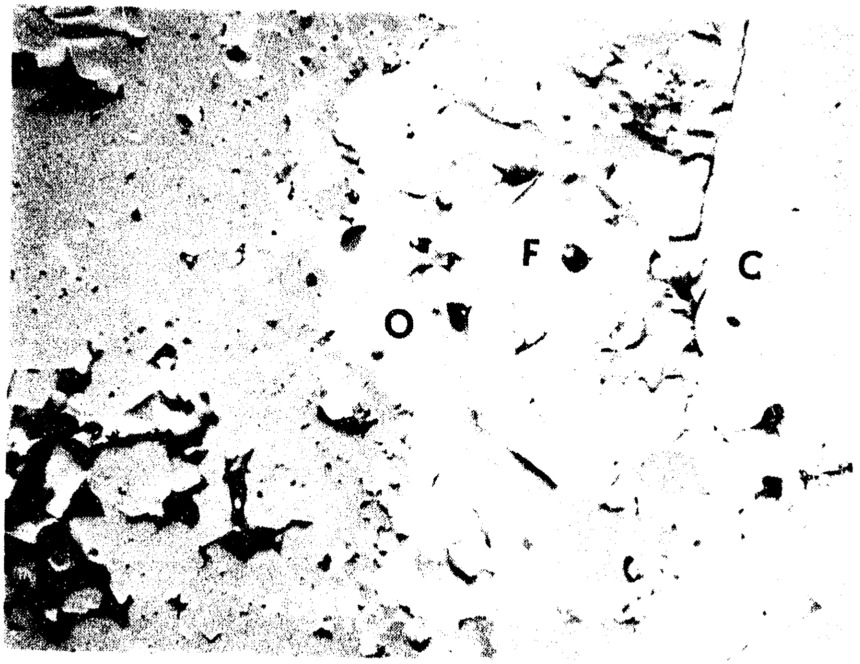

Figure 93. Anode C1, section 40, duplex structure next to the Cerox (C), consisting of Ce Fluoride (F) and Cu oxide (O).

near the surface is 1.2% Al, 6.9% Fe, 78.3% Ni, and 13.6% Cu (mol%), but the Cu content rapidly decreases and the NiO composition approaches its original composition of 90 mol% Ni, 8 mol% Fe (with the remainder being Al and Cu).

Anode E1-614 h

Anode E1 was run in the cell for the entire test and operated under a range of CD, bath composition, and temperature. The section examined was taken from the corner of the northeast side of the anode. The oxidation zone in this section was 17 mm thick and two metallographic mounts were needed to prepare a complete cross section from the exterior into the region where Cu metal was present.

A macroscopic photograph of the polished cross section near the CEROX/substrate surface of anode E1 is shown in Figure 94. The macroscopic color differences were helpful in distinguishing the different zones in the anode. The CEROX coating located at the top of the photo is 8 mm thick. A large pore in the right side of the CEROX is filled with the polymer mounting medium (M). The vertical line in Figure 94 shows the path along which the microstructure was evaluated with the SEM/EDX. A crack exists in the anode ~2 to 2.5 mm from the surface. The top part of this crack is red (macroscopically) and red specks are observed in a zone below it.

Secondary electron micrographs of the outer 2 mm of the substrate are shown in Figures 95 and 96. The right side of Figure 96 overlaps with the left side of Figure 95. Figure 95 shows that a dense zone exists at the substrate/CEROX interface and this zone extends ~1 mm into the substrate. This feature corresponds to the dark band that is present below the CEROX coating in Figure 94. It was found that this region is very similar to the dense region that exists near the surface of Section 40 in Anode A1 (see Figure 87). Like A1, the composition of the NiO phase (in mol%) in E1 contains 18 to 21% Cu, however, the Fe content of this region is only 1 to 6% compared to 7 to 9% in Anode A1. The Ni content in the NiO is 71 to 78% while the Al content is 1 to 2%. In Section 40 of Anode A1, the Ni content of the NiO phase was 66 to 71%.

Significant amounts of Al were detected in the ferrite phase but the composition of this ferrite is slightly different from other ferrite phases in the other samples. This phase contains 4 to 8 mol% Cu and 19 to 61 mol% Al. Thus, the ferrite in this region of the sample contains more Cu then the ferrite phases in Section 40 Anode A1. It appears that the Al in the ferrite preferentially substitutes for Fe (as Al content goes up, Fe content goes down), as was also observed in the other samples.

Like the other anodes examined, this anode also has a copper depletion zone ~1 mm into the substrate (Figure 96, layer D). The composition of the NiO phase in the copper depletion zone is the

Figure 94. Macroscopic section of Anode E1 from the northeast side.

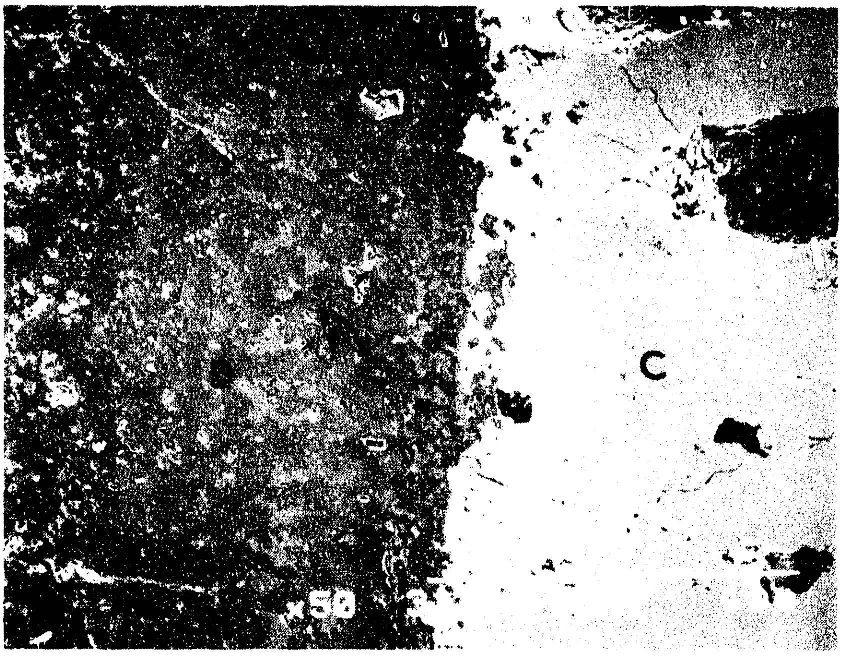

Figure 95. Interface between the Cerox and substrate in Anode E1. C=Cerox, D=dense, Cu depleted zone.

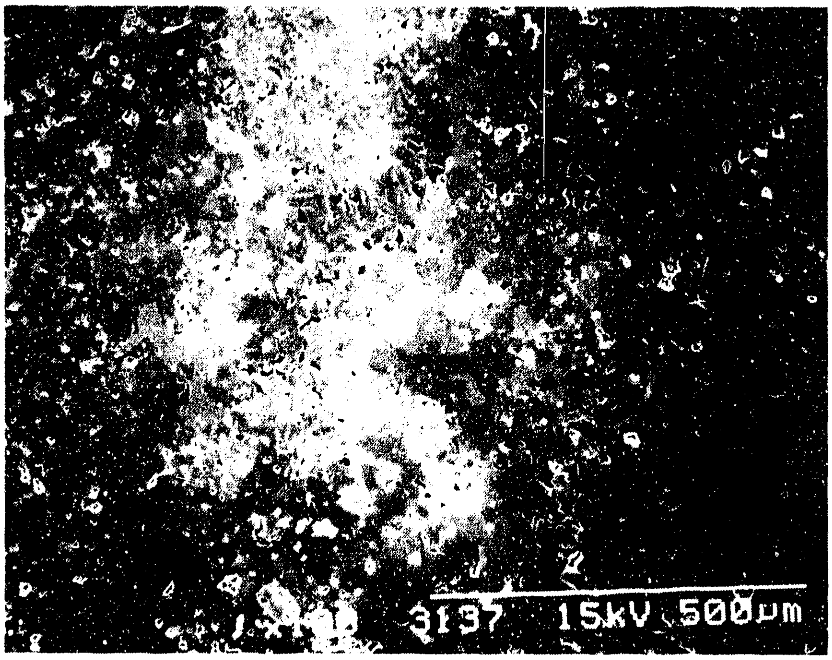

Figure 96. Porous zone between Cu depletion zone (D) and the Cu-O region further into the interior of E1.

same as the composition of the NiO in the dense region. The ferrite in the Cu depletion zone is nearly stoichiometric $NiFe_2O_4$, as was noted in the other anodes. The composition of the ferrite phase remains fairly constant (1 mol% Al, 64.5 mol% Fe, 33.5 mol% Ni, and 1 mol% Cu) throughout the rest of the anode.

Figure 94 shows that a crack exists 2 to 2.5 mm into the substrate. Figures 97 and 98 are BEI micrographs of both sides of the crack. Figure 97 shows the region to the right (exterior) of the crack, including the Cu depletion zone (N). The isolated bright spots present in the Cu depletion zone are a Ce fluoride. Minor amounts (<3 mol%) of the Ce fluoride (with some Ca) are present throughout the anode.

The large light colored band next to the crack in Figure 97 corresponds to the red zone that was macroscopically observed in Figure 94. EDS analysis shows that this feature is a Cu oxide (97 mol% Cu with 3 mol% of Fe + Ni). Because Cu_2O often has a red color, which is caused by internal reflections within its structure[20], the red phase on both sides of the crack is probably Cu_2O instead of CuO.

As shown in Figure 97, there are alternating layers of Cu depletion (N) and "normal" oxidized (O) microstructure (~250 μm wide). All layers contain NiO and $NiFe_2O_4$, but only the oxidized zone also contains Cu oxide (light in BEI micrographs). The NiO contains little Cu within the oxidized and the second (left) Cu depletion zone. The composition of the NiO phase in those layers becomes 1 mol% Al, 3 mol% Fe, 93 mol% Ni and 3 mol% Cu as compared to 18 to 21 mol% Cu in the NiO in the outer dense and Cu depleted region. On the other side of the crack (Figure 98) there is a Cu depletion zone 300 μm thick and then a "normal" oxidized region containing $NiFe_2O_4$, NiO, and Cu_2O. Therefore, Cu_2O is concentrated along the crack while a Cu depleted zone is present on either side of the Cu_2O layer.

Figures 99 and 100 show the microstructure progressing from Figure 98 into the interior of the metallographic mount. Throughout the region NiO, $NiFe_2O_4$, and Cu_2O are present. The only differences in the composition of the three phases compared to the compositions described above is in the NiO phase. The Al and Fe content does not change but the Ni content decreases from 93 mol% near the crack to 85 mol% at the interior edge of the mount while the copper content increases from 3 to 11 mol%.

The dark gray regions between the individual grains in Figures 98,99, and 100 is a two-phase mixture of frozen cryolite and a solid solution of nickel and aluminum fluoride. EPMA was performed on two spots of the frozen fluoride feature where the spots were separated by a distance of only 15 μm. The cation composition of the cryolite phase was 43.4 mol% Al, 52.8 mol% Na, 1.5 mol% Ca and <1 mol% each of Fe, Ni, and Cu. Converting these to weight

Figure 97. Anode E1 next to a crack. Alternating layers of Cu depleted zones (N) and oxidized zones (O) are present. Cu oxide occurs along the crack.

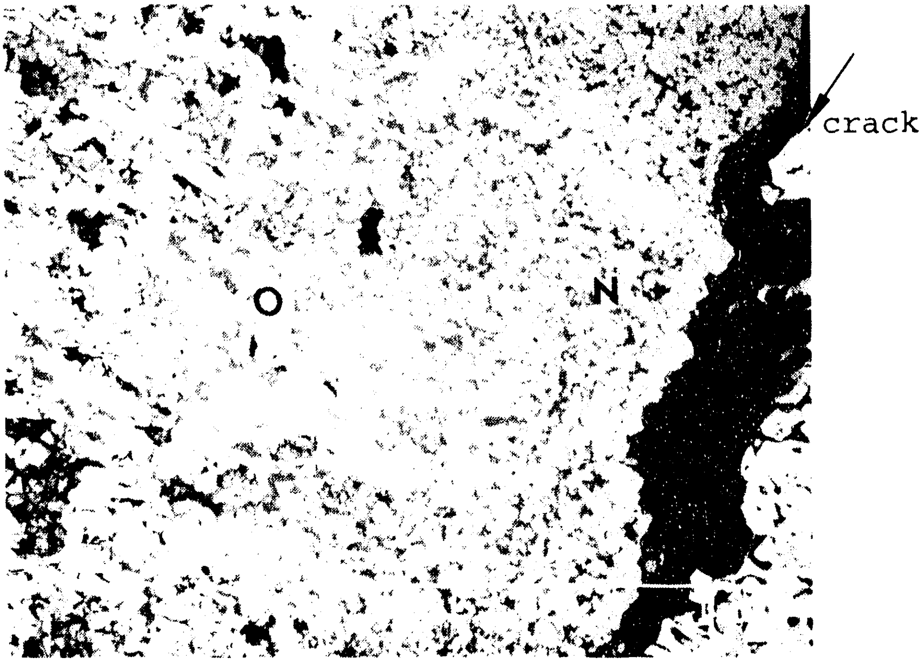

Figure 98. Anode E1, on the left (interior) side of the crack in Figure 97. A Cu depleted zone (N) occurs next to the crack while further into the interior Cu oxide (O) is present with NiO and $NiFe_2O_4$.

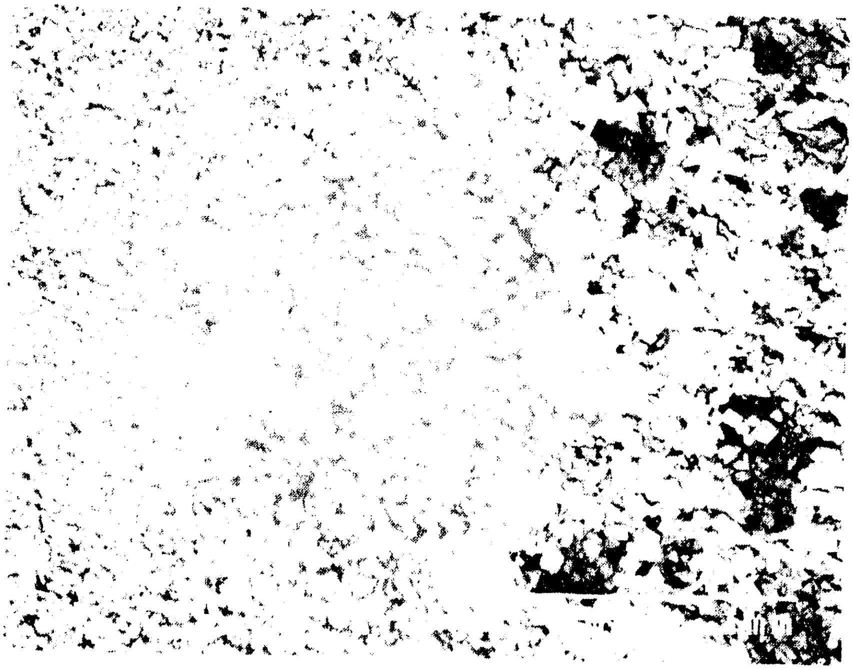

Figure 99. Interior of the oxidized zone in Anode E1.

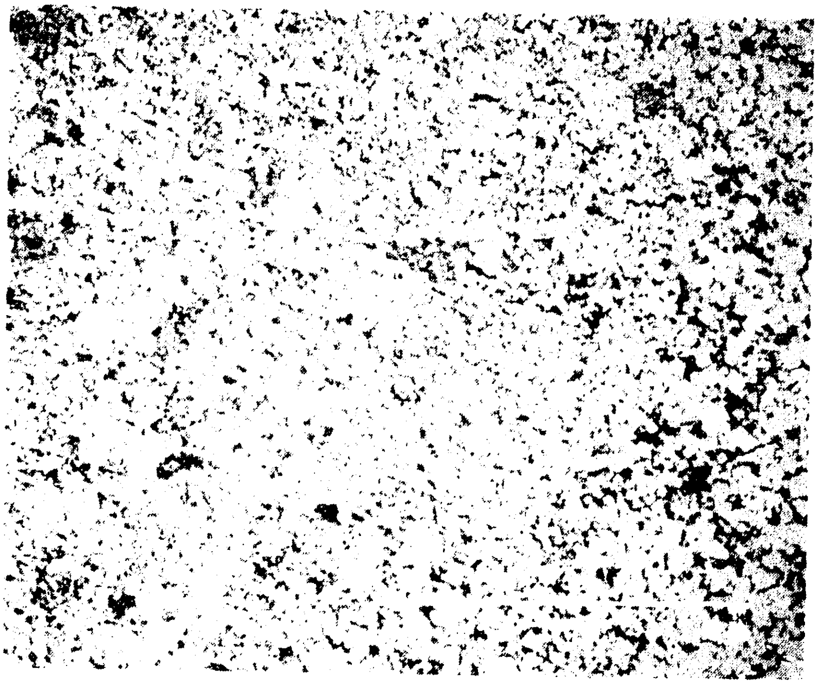

Figure 100. Further into the interior of the oxidized zone in E1.

percents gives 45.4 wt% Al, 47.1 wt% Na, and 2.3 wt% Ca. This corresponds to a BR of 0.61. This BR is much lower than the measured ratio of the electrolyte in the pilot study, which ranged from 1.1 to 1.8. A second fluoride phase was found <15 µm from this cryolite phase and EPMA found that it contained 24.8 mol% Ni, 43.1 mol% Al, 27.8 mol% Na, and <2 mol% each of Fe, Cu, and Ca. This corresponds to a BR of 0.32. Thus, this second fluoride phase contains a large amount of Ni and Al with a lower level (compared to typical bath compositions) of Na.

BEI micrographs of the second metallographic mount of this section of Anode E1 are presented in Figures 101 through 107. Figures 101 and 102 are low magnification images of the outer surface of this mount. The outer surface of this mount was next to the inner surface of the previous mount. Therefore, the structure in the center and right side of Figure 101 is the same structural zone as the left side of Figure 100. Figure 102 (which is further into the interior than Figure 101) shows a different structural zone where the bright features (Cu oxide) of Figure 101 are absent in Figure 102. Higher magnification micrographs of the area in Figure 102 are presented in Figure 103. EDS analysis of the area in Figure 103 (in which the Cu oxide was absent) gave an overall composition of 42.7 mol% Fe, 45.1 mol% Ni, 5.8 mol% Cu, and 6.4 mol% Al showing the region is Cu depleted. The thickness of this depletion zone is ~2 mm thick. This is much larger than the thickness of the Cu depletion zones that were observed in the untested material (see Figure 73) so it is probably the result of chemical reactions that are occurring within the anode.

A higher magnification BEI of Figure 103 is presented in Figure 104. EPMA was performed at the spots designated by the letters in Figure 104 and the results are summarized in Table 8. According to Table 8, NiO (A), Ni ferrite (B), and Ni fluoride (C,D) coexist in the structure. It should be stressed that these three phases are the dominant phases in this region of the anode and they are not present in trace amounts. The concentration of Ni in the NiO phase is 79 mol% but the Cu concentration is increased to 15.6 mol%. Thus, the Cu concentration in the NiO phase is increasing with penetration distance into the sample. The NiO contained 3 mol% Cu near the crack (see Figure 97), 11 mol% at the edge of the first mount (Figure 100), and to 15.6 mol% in this region as shown in Figure 102. The Ni rich fluoride phase is primarily Ni with some Mg as the cation constituents.

The black patches in this region (Figure 104, spot E) is a solution of frozen Ni, Al, and Na fluoride. The Ni content is 37.5 mol% while Cu and Fe combine to account for an additional 6 mol%. The Na and Al contents in this phase are equivalent to a BR of 0.26, which also is much lower than the ratio of the electrolyte (1.1 to

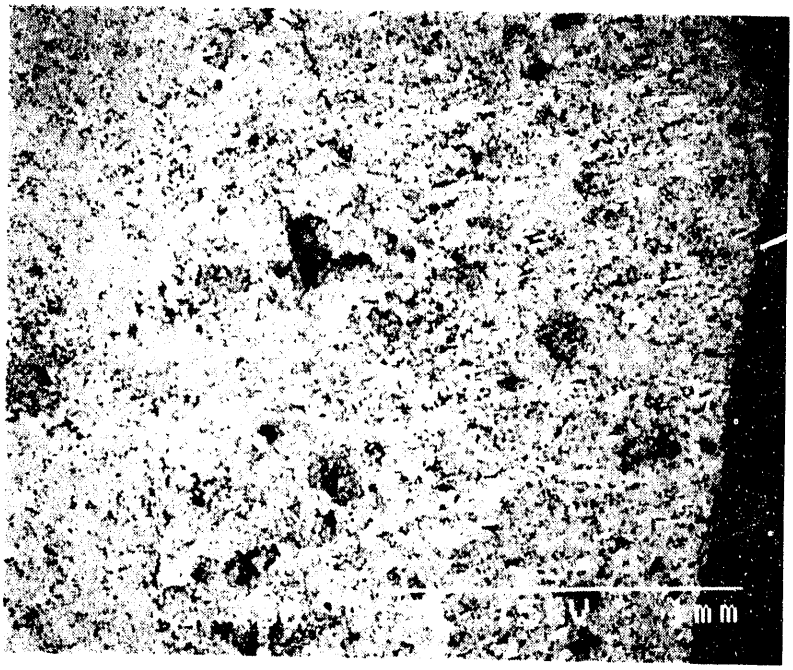

Figure 101. Anode E1, further into the interior of the Anode than Figure 100.

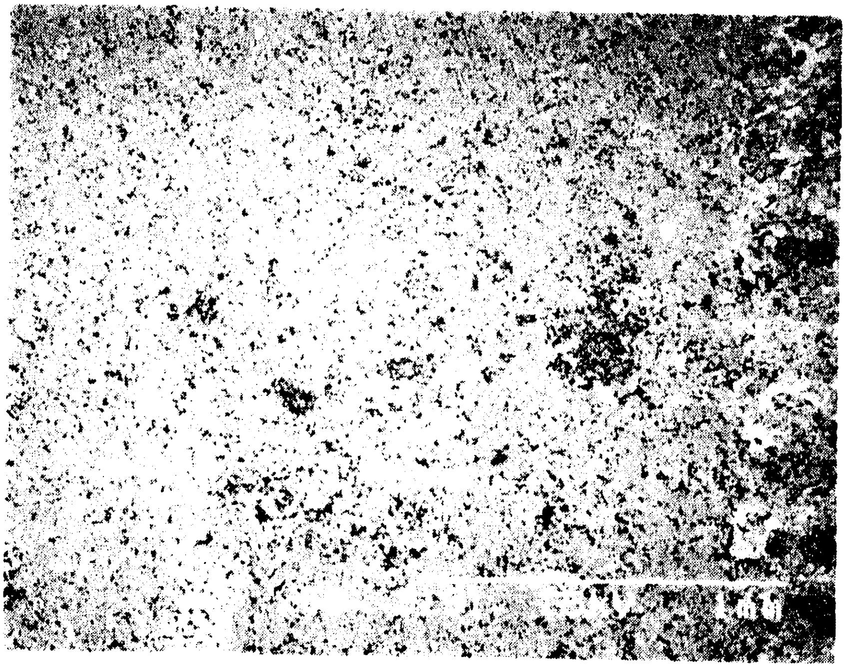

Figure 102. Anode E1, further into the interior than in Figure 101.

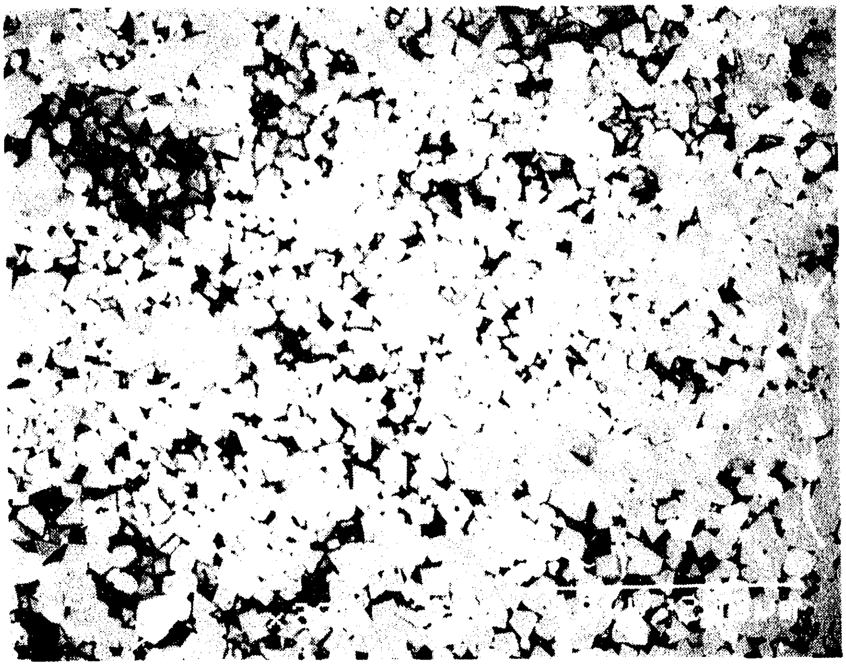

Figure 103. Higher magnification on the Cu depleted zone in Figure 102, Anode E1.

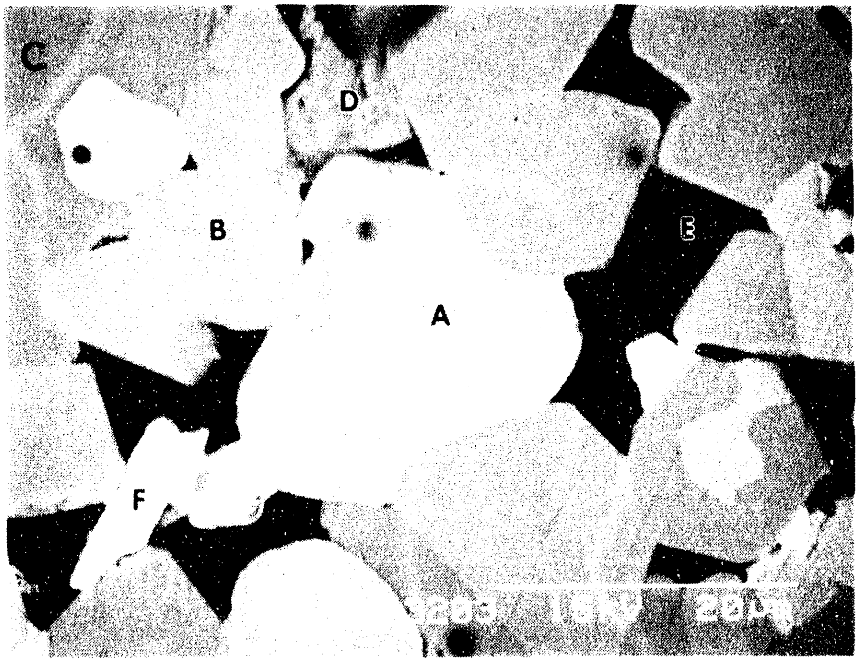

Figure 104. BEI of Figure 103, Anode E1, showing the individual phases from Table 8.

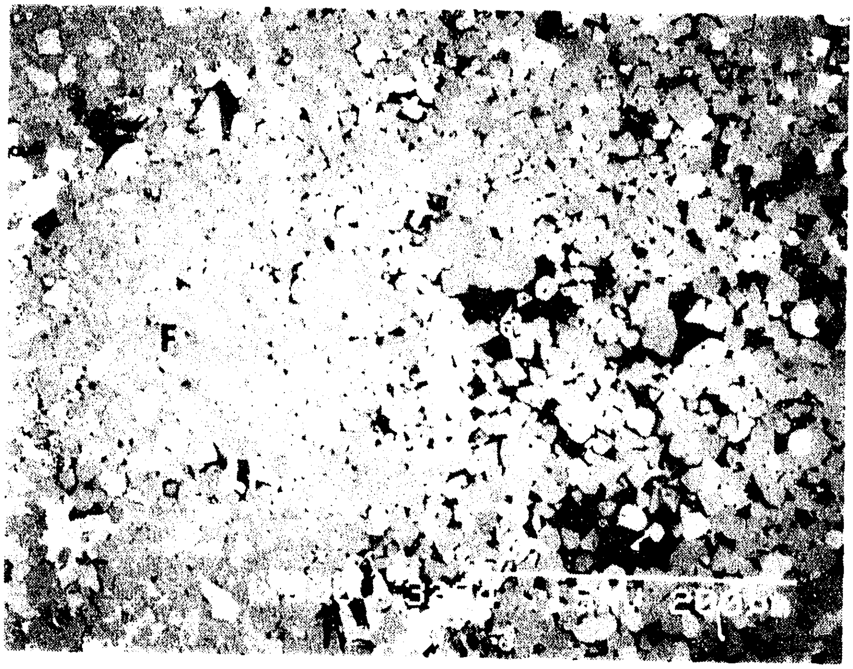

Figure 105. Further into the interior of E1, showing the boundary between the fluoride-containing region (F) and the Cu depletion region.

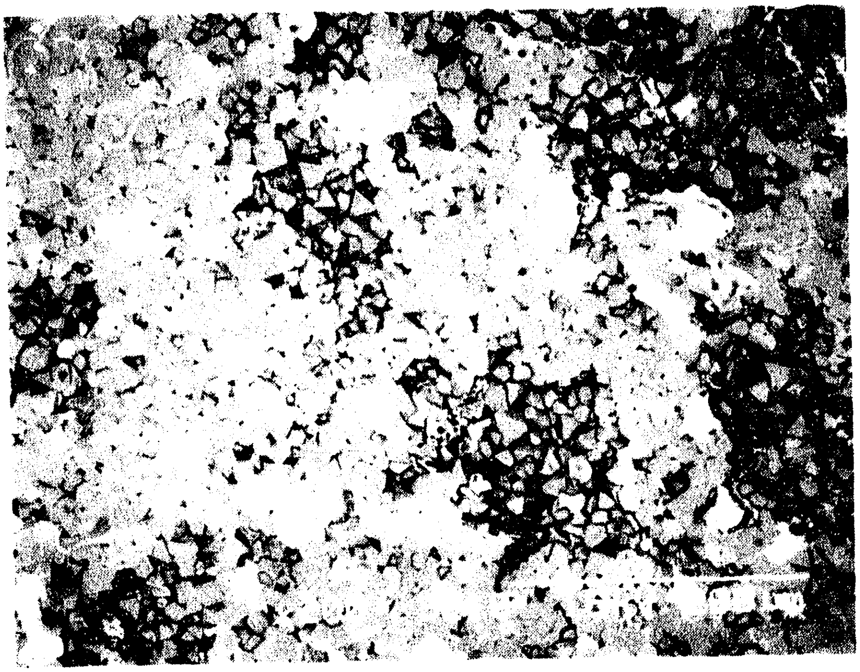

Figure 106.~19 mm into the center of Anode E1, where Cu metal occurs (bright phases).

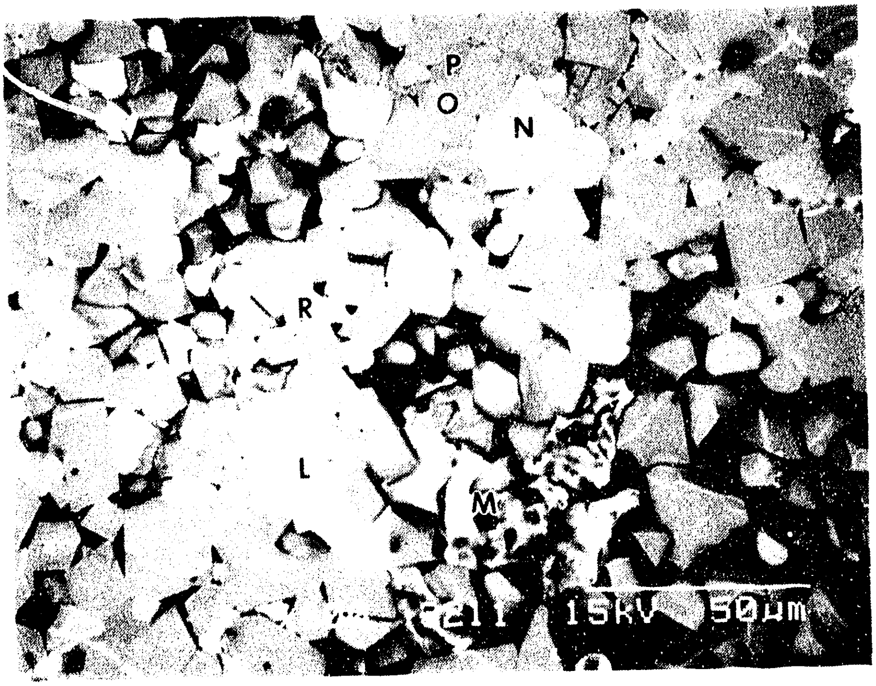

Figure 107.Higher magnification of Figure 106.

Table 8. Compositions of the phases (mol%) in the various regions in Figure 104.

Spot	Phase	% Fe	% Ni	% Cu	% Al	Others(%)
Overall[a]	---	42.7	45.1	5.8	6.4	
A	NiO	4.6	79.2	15.6	0.6	
B	Ferrite	64.2	33.3	1.2	1.3	
C	Fluoride	3.8	76.8	4.1	3.0	12.3% Mg
D	Fluoride	4.7	76.4	3.1	1.9	13.9% Mg
E	Fluoride	3.9	37.5	2.0	35.8	18.7% Na 2.0% Ca
F	Ce Fluoride	4.3	4.4	0.8	3.0	84.9% Ce 2.6% Ca

---

a. Overall composition taken from Figure 103

1.8), so this phase is also Al rich versus Na. The composition of this fluoride phase is very similar to the Ni-Al-Na fluoride that was described earlier (Figures 98 through 100). Ce fluoride grains (Figure 104, spot F) are also dispersed within the pores.

Further into the sample, next to the Cu depletion layer in Figure 102, there is a dense layer, ~300 µm thick. A BEI of the boundary between these two regions is shown in Figure 105. The dense zone lies to the left in Figure 105 and marks the last zone within the macroscopically black oxidation zone. EDS analysis at 500X on this area shows that the overall composition is very similar to the nominal batched composition in Table 6. However, the phase composition is different. The dense layer contains Cu oxide, Ni fluoride, Ni ferrite, and no NiO. The composition of the Cu oxide phase is very similar to the composition given in Table 7. The EPMA composition of the Ni fluoride phase is very similar to the compositions that are listed in Table 8. However, the intensity of Mg K_α is qualitatively less dominant in this fluoride phase as compared to the Ni fluorides of Table 8. No compositional changes are observed in the ferrite phase and its composition is similar to the compositions that are reported in Tables 7 and 8.

The final microstructural region of this anode is presented in Figures 106 and 107 (again, the bright lines in the SEM photograph are an artifact of the carbon coating). This region lies further into the interior of the anode than in Figure 105. In this region, Cu is present in the metallic state. EPMA was performed at the various spots indicated in Figure 107. The composition of the Cu (spot L), and ferrite (spot O) phases are the same as the ones reported in Table 7. The composition of the NiO phase (spot N) is 94.3 mol% Ni, 4.5 mol% Fe, and 1.2 mol% Al. Comparison of this NiO composition with the compositions of the NiO phases in the unoxidized regions of Anodes A1 and C1 (see Table 7) shows that less Fe and more Ni is present in this anode.

The region in Figures 107 has two additional microstructural features. The first one is spot M of Figure 107, which shows a particle that appears to have been reacted. However, the EPMA composition of this feature falls within the compositional range for a Cu rich particle in Table 7. No fluorine or other impurities were detected. This feature appears reacted but the exact nature of the reaction cannot be determined.

The second feature is a grain boundary Ni fluoride phase that is designated by spot P in Figure 107. A pronounced Mg peak was detected in the EPMA spectrum and the Fe content was higher than the values reported in Table 8. However, the higher Fe content is probably an artifact of the EPMA process because of excitation of the surrounding ferrite phase. This Ni fluoride phase is found along the grain boundaries of both the NiO and ferrite phases.

The microstructure of Anode E1 can be summarized as follows. Many distinct microstructural zones were found in this anode and each zone is comprised of a unique combination of phases. A dense outer zone, ~1 mm thick, exists below the CEROX coating. This zone consists of ferrite and NiO phases. The ferrite phase has high Al (19 to 61 mol%) and Cu (4 to 8 mol%) contents and Al tends to substitute for Fe in the ferrite. The NiO phase contains 18 to 21 mol% Cu (presumably present as the oxidized Cu^{2+} ion) but only 1 to 6 mol% Fe. A porous Cu depletion zone lies next to the dense region. The composition of the NiO phase is the same as in the dense layer but the ferrite phase becomes nearly stoichiometric and the composition of the ferrite is the same for the remainder of the anode interior.

A macroscopic crack exists 2 to 2.5 mm into the body of the anode. A dense copper oxide layer, probably Cu_2O, lies on the outer edge of the crack and a Cu depletion zone lies on both sides of the Cu_2O layer.

The next inward zone is ~1 mm thick and the ferrite, NiO, and Cu_2O phases coexist in this region. The only change in composition occurs in the NiO phase, where the Cu content increases from 3 to 11 mol%. Also, a two-phase fluoride mixture is present at the grain boundaries of the oxides. This fluoride mixture consists of a cryolite phase that has a BR of 0.61, and a (Ni,Na, and Al)F_x phase that contains 24.8 mol% Ni and the Na to Al ratio is equivalent to a BR of 0.32.

Further penetration into the anode reveals a Cu depletion zone. This region is ~2 mm thick so it is probably not an artifact of the untested material but rather is formed during operation of the anode. Four phases are observed in the microstructure: ferrite, NiO, nickel fluoride, and (Ni,Na,Al)F_x. Thus, two oxides and two fluorides coexist in this region and all compounds contain at least 33 m% Ni (see Table 8).

Finally, a dense layer of ~300 µm thick lies next to the Cu depletion zone and this layer represents the last oxidation zone in the anode. NiO is not found in this zone but Ni fluoride is present in addition to the ferrite and Cu oxide. In all regions interior to this zone, Cu is present in the metallic state. Cu metal, $NiFe_2O_4$, and NiO coexist in the interior and Ni fluoride is also present. Porosity is higher than in the untested anode.

The thickness of the entire oxidation zone (including dense, oxidized, and Cu depleted regions) is ~17 mm and fluoride phases were detected throughout the section. Ce fluoride was found up to 15 mm into the interior.

5.3.3 Microstructure of the Inconel Rod

Inconel 601 rods were used to supply the electrical current to the anodes. The nominal composition of Inconel 601 is presented in Table 9.[21] The quantitative analyses that will be presented in this section will be on a weight percent (wt%) basis and will only include Ni, Cr, Fe and Al in the compositions. Ni 200 [99.5 wt% Ni, 0.06% (max) C] rods were used by PNL in their pilot test (before our test) as current collectors. The Ni rods failed during their test leading to the use of the Inconel 601 instead of the Ni in the ELTECH test.

The electrical connection between the rod and anode was made by simply screwing the rod into the anode. The rods were 18 in. long, 1 in. in diameter, and they were tapped with male 1-8 threads. The microstructure of the threaded region is presented in Figures 108 and 109, where Figure 108 represents the region near the tip of the thread and Figure 109 represents the base of the thread. The rod is the brighter feature that lies to the left side of the images. The figures clearly show that the rod was severely attacked and corroded by the local environment. Specifically, the rod underwent pronounced corrosion at the grain boundaries suggesting an enhanced stress corrosion cracking mechanism. A detailed discussion of the corrosion behavior of the rod will be presented, starting at the center of the rod and moving toward the outer surface.

Figure 110 shows BEI micrographs of a section from ~10 mm into the center of the rod. Figure 111 shows that the grain boundaries near the center of the rod contain a Cr-rich second phase (C). At ~6 mm in from the edge of the rod there is a reaction zone (Figures 112 and 113). Figure 112 shows how the rod is preferentially attacked along the grain boundaries. The outer surface of the rod lies to the right of Figures 112 and 113. The dark grain boundary phase in the right side of Figure 113 is AlF_3 (A), which is penetrating into the center of the rod along the grain boundaries. It appears to react with or dissolve the Cr rich boundary phase (C) in the left of Figure 113. No Na or Ca was detected in the penetrating AlF_3. The compositions near the centers of the grains in both regions fall within the compositional range of Table 9.

Higher magnification BEI micrographs of the rod, near the base of the thread of Figure 109, are presented in Figures 114 and 115. In each, the brighter phases are the metallic phases. Location A of Figure 114 is AlF_3, but below this phase is a lighter feature that is designated C. EPMA of C shows that it is a fluoride that contains Al, Cr, and Ti. Ti is not listed in Table 9 as a constituent of Inconel 601 and it is not known how it entered the system. EPMA determined the atomic Cr:Al ratio in the fluoride to be ~4:5; however, it is possible that Al was detected from the surrounding AlF_3 phase. Location B is a reaction phase that

Table 9. Limiting chemical composition (in wt%) of Inconel 601.

Element	Content
Nickel	58.0 to 63.0
Chromium	21.0 to 25.0
Iron	Remainder
Aluminum	1.0 to 1.7
Carbon	0.10 max.
Manganese	1.00 max
Sulfur	0.015 max.
Silicon	0.50 max.
Copper	1.00 max.

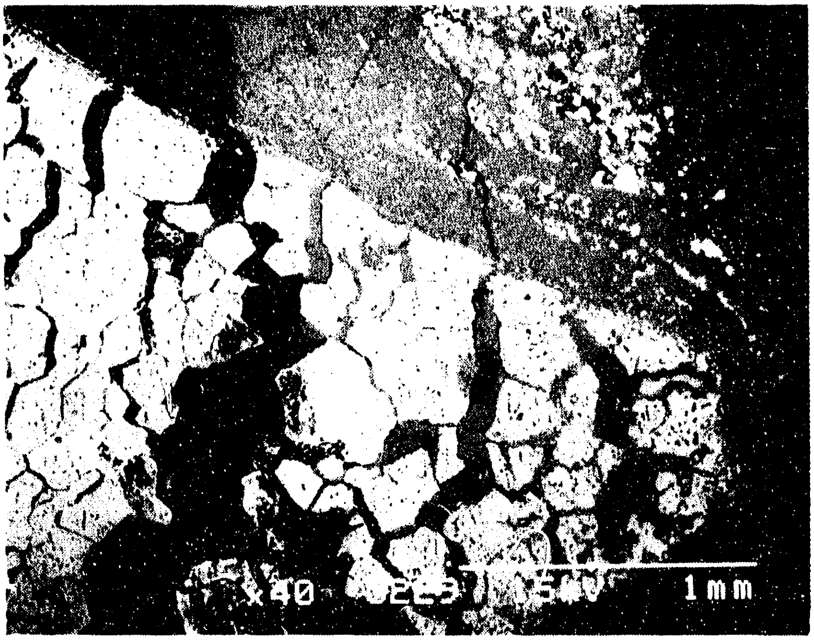

Figure 108. Tip of one of the threads on the Inconel 601 connector rod within the Cu cermet.

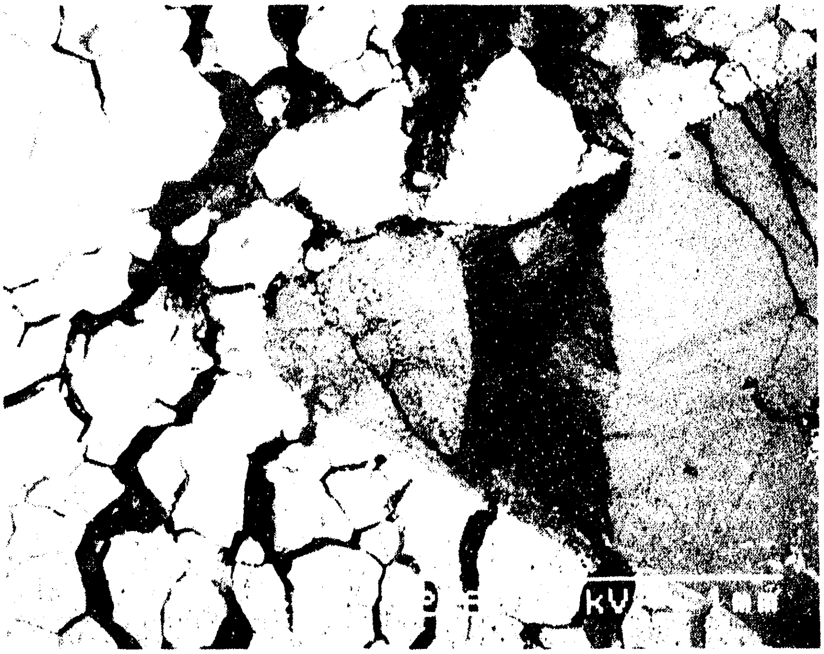

Figure 109. Base of one of the Inconel 601 threads within the Cu cermet.

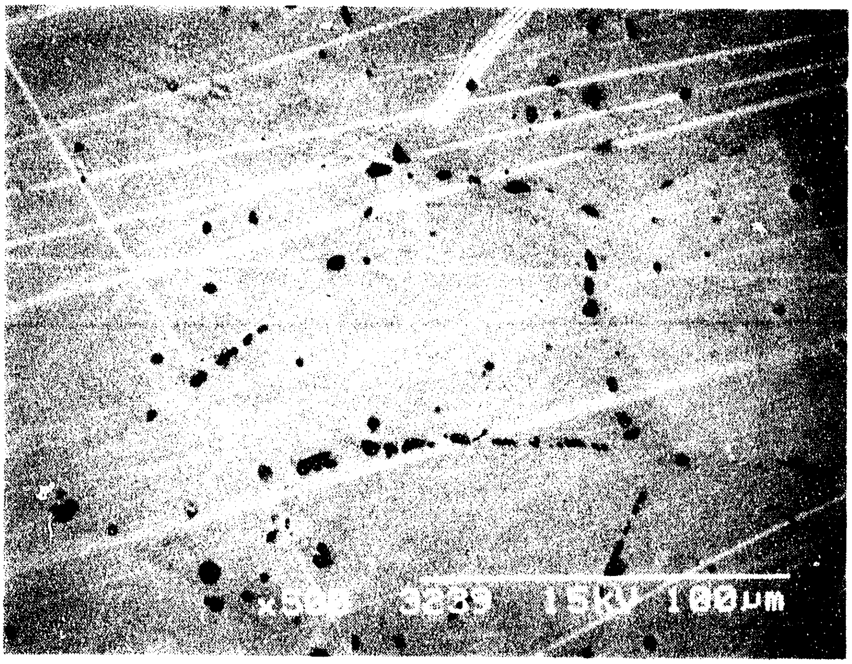

Figure 110. BEI micrograph of the Inconel 601 collector rod near the center.

Figure 111. Close-up of the Cr-rich grain boundary inclusions in Figure 110.

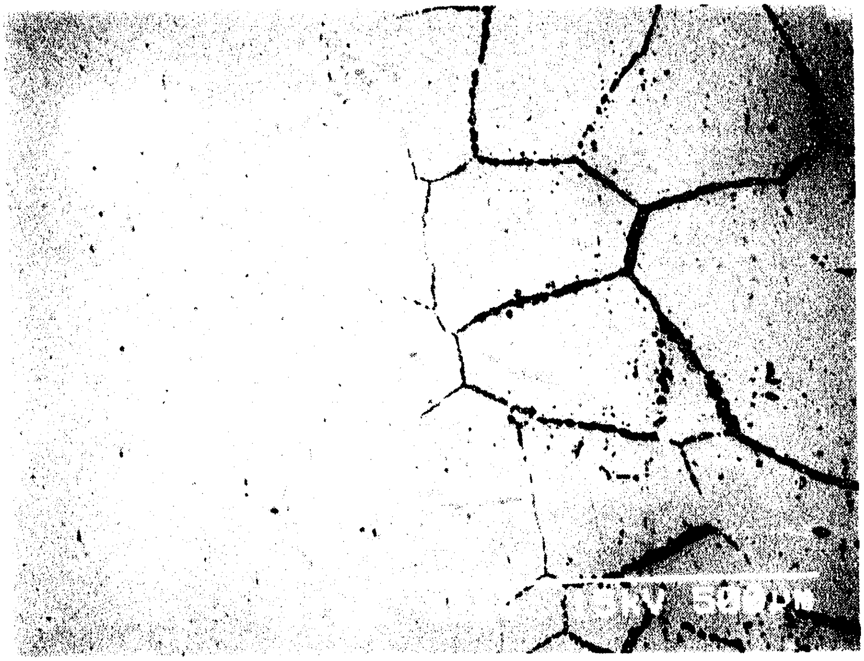

Figure 112. Edge of the reaction zone within the Inconel rod, 6 mm into the rod.

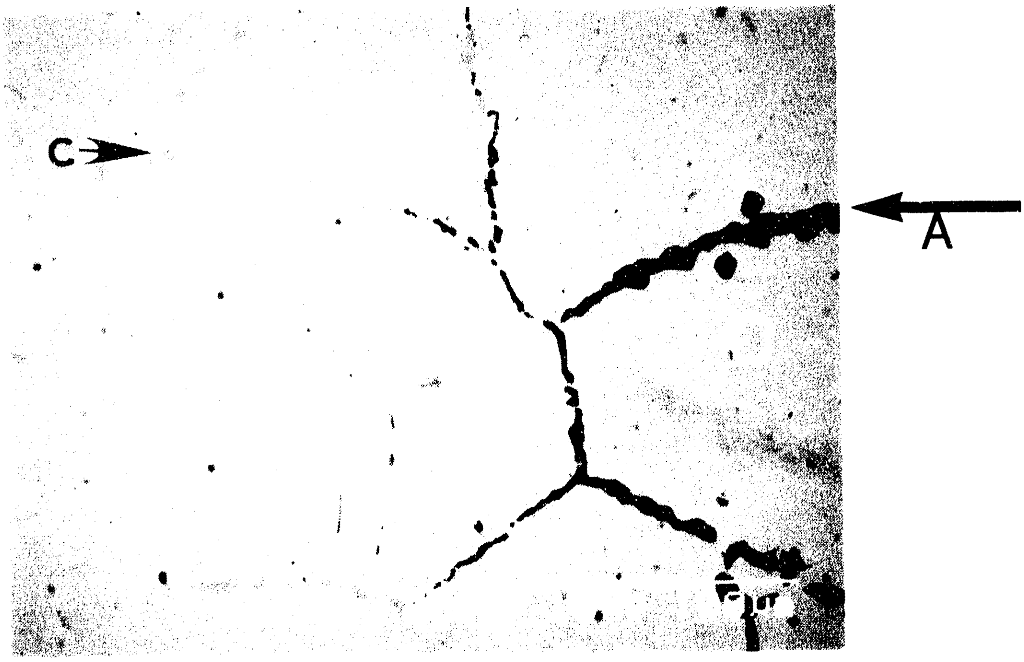

Figure 113. Higher magnification of Figure 112. A=AlF_3, C=Cr-rich phase.

Figure 114. Region of corroded Inconel showing the AlF_3 grain boundary phase (A).

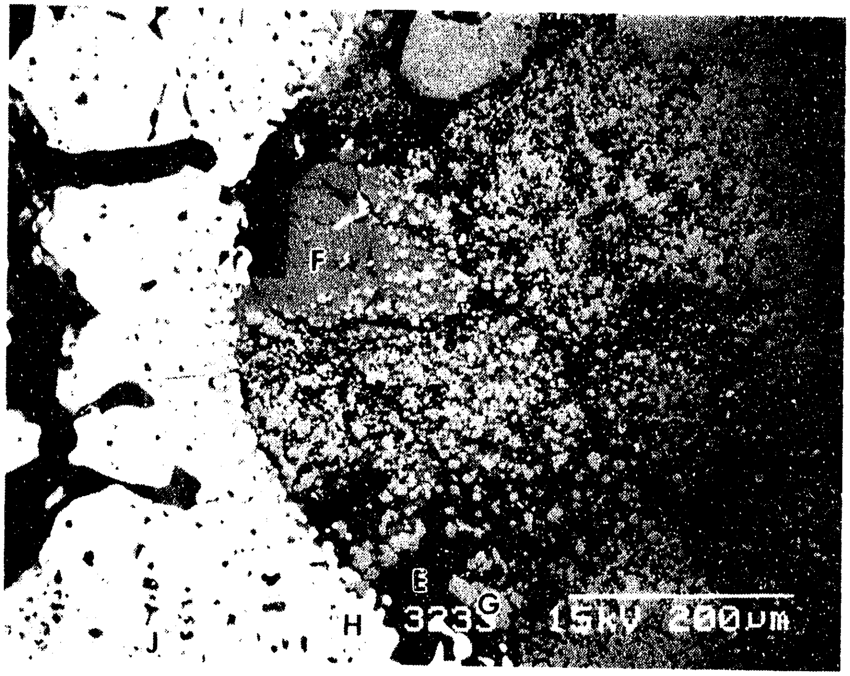

Figure 115. Edge of the Inconel rod at the base of the thread.

contains 70 wt% Ni, 20 wt% Fe, 7.7 wt% Al, and 2.3 wt% Cr. It is difficult to determine if it is an oxide, or a metallic phase that is severely depleted in Cr. Location D in the center of a large metal grain has the composition 67.5 wt% Ni, 19.7 wt% Cr, 12 wt% Fe, and 0.8 wt% Al. According to Table 9, this region of the alloy has become depleted in Cr and Al and has a higher Ni content.

Figure 115 shows the microstructure of a different area of Figure 109. EPMA was performed at five different spots in Figure 115 and the locations are designated by the various letters in the image. A higher magnification BEI micrograph of the central lower region of Figure 115 is presented in Figure 116. Location J is located in the center of a large alloy grain and it is at least 200 μm from a grain boundary. However, the Cr and Al contents of the alloy at location J are only 14.5 and 0.4 wt%, respectively while the corresponding Ni is 72.4 wt%. According to Table 9, Cr and Al are depleted from this region causing the Ni concentration to increase. Location H is ~30 μm from the surface and the Cr concentration at this spot is only 2.9 wt%. Thus, the alloy is severely depleted in Cr at the edge.

Locations E, F, and G lie in an area that should contain the threads of the anode substrate material. However, EPMA analysis of these spots shows that they are not the ferrite, NiO, or Cu rich phases that are typically observed in the substrate material. Instead, they are rich in Cr or Al or both. Table 10 lists the compositions of these three spots.

Table 10 shows that locations E and F are fluorides while G is an oxide phase. Also, minor amounts of Ca and Ti were detected in the material. Figures 109 and 116 show that location E is at the exterior of the Inconel and along the grain boundaries of two Inconel grains. As had been found in the interior, E was an Al rich (86.9 wt%) fluoride phase. Because AlF_3 was previously found along the grain boundaries, it was expected that this phase would be rich in Al and this was observed (86.9 wt% Al). However, the Cr content of the fluoride phase significantly increases from 10.3 wt% at location E to 54.9 wt% at F. Location G is a Cr rich (96.9 wt%) oxide phase surrounded by the AlF_3 phase.

A mechanism for the formation of these Al and Cr rich phases can be formulated from the above discussions. It is clearly demonstrated that AlF_3 preferentially attacks the Cr in the alloy by corroding Cr rich inclusions at the grain boundaries and dissolving Cr from the bulk of the lattice. The dissolved Cr is than transported to the surface of the rod through the liquid AlF_3 grain boundary phase. Locations E, F, and G of Figure 115 are evidence that the amount of Cr that was removed from the alloy and the transport rate of Cr through the molten AlF_3 grain boundary phase is large enough to form Cr rich phases elsewhere in the microstructure.

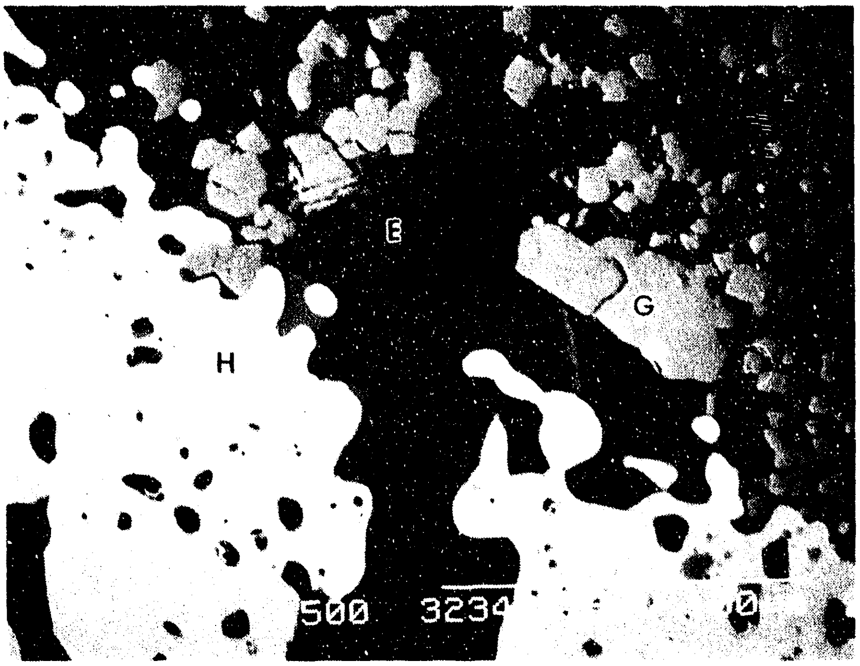

Figure 116.Higher magnification of Figure 115.

Table 10. Compositions (in wt%) of Cr and Al reaction phases from Figure 115.

Location	Phase	%Cr	%Al	%Ti	%Ca
E	Fluoride	10.3	86.9	2.1	0.7
F	Fluoride	54.9	43.3	0.7	1.1
G	Oxide	96.9	1.5	1.2	0.4

The discussion of this section describes how Inconel 601 undergoes severe stress corrosion cracking when it is exposed to the molten cryolite environment. However, it must by emphasized that no anodes failed because of corrosion of the rod in this pilot test while 25% of the anodes that were run in the PNL pilot test failed because of the severe corrosion of the Ni 200 rods.[7] Thus, Inconel 601 is a superior connector rod material compared to Ni 200.

6. Conclusions

Conclusions from the testing are divided into four areas involving the CEROX coating, the corrosion rates, the pilot cell operation, and the Cu cermet substrate and connector. The test was successful in demonstrating that inert anodes could be coated and operated with a CEROX coating in a pilot cell for up to 614 h. However, the test was unsuccessful in showing exactly what the performance advantage is of a CEROX-coated cermet over an uncoated cermet.

CEROX Coating

- The CEROX coating could be deposited and maintained in a pilot cell. At "optimum" conditions (BR 1.6, CD of 0.5 A/cm^2) the coating was dense and 1 to 3 mm thick.
- On the sides of adjacent cermet anodes, where CD was low, the CEROX coating was not deposited or was very thinly deposited. There was no macroscopic evidence of increased corrosion on the uncoated sides.
- The anodes that were CEROX coated at "optimum" conditions and then tested at higher CD (0.65 A/cm^2) and then lower BR (1.15) had a more irregular and thinner CEROX coating. It could not be determined from the impurities in the metal if the change in the character of the coating led to a change in the corrosion rates.
- The CEROX coating can grow a short distance into cracks in the cermets.
- The Ce in the bath and the metal can be controlled if the pilot cell is operating smoothly. If the cell is experiencing mucking or crusting/melting periods, the Ce level is more difficult to control and the coating may undergo deposition/dissolution periods that correspond to the changing Ce concentration in the bath. This may not be detrimental as long as the Ce concentration remains high enough to maintain a CEROX coating.
- The CEROX coating did not grow on the sides of cermets that were very close to the carbon anode. This may be caused by the low current density on that side or the presence (absence) of CO_2(O_2) or both.
- A CEROX coating was present in the areas where cryolite froze around the anodes, however, the coating became very thick and porous. This condition must be avoided in order to maintain a good CEROX coating and good current distribution to the anodes.

- Testing could not determine the influence of the introduction and the CEROX coating of new anodes while old CEROX-coated anodes were operating.

Corrosion Rates

- The corrosion rates calculated from the impurity levels in the aluminum were 0.075 lb/d Cu, 0.13 lb/d Ni, and 0.30 lb/d Fe. Some of the Fe is probably because of contamination from Fe tools. An adjusted Fe corrosion of 0.12 lb/d was calculated. These rates are half of those calculated for uncoated anodes from the PNL testing.

- Due to the cracking problems with the anodes and the difficulties with cell operation, neither these nor the PNL corrosion rates are indicative of the real corrosion levels that could be achieved in an industrial cell.

- The calculated surface area loss was 0.1 mm/d (3.65 cm/y), half that of the uncoated anodes. This is too high a corrosion for an inert anode material. Again, because of the cracking, this may not be a realistic estimate of the surface cermet anode wear.

- The operation at slightly higher CD and lower BR did not significantly change the corrosion rate as determined by the impurities in the aluminum metal.

Pilot Cell Operation

- Operation near alumina saturation resulted in muck accumulating in the cell. This led to a decrease in the cell volume and a large temperature gradient (30 to 50°C) from top to bottom as the muck accumulated on the bottom. In addition, the muck led to uneven anodes current.

- The lack of individual current control to each cermet anode led to varying CD on the anodes with time and with location in the cell. This made it very difficult to draw any conclusions based on CD to an anode.

- The low CD on the cermet anodes (and consequently low heat) led to crusting around the anodes furthest from the carbon anode, which was supplying most of the heat to the cell. This may be a continued difficulty in a self-heated cell with inert anodes at low CD unless an auxiliary heat source is available or a different cell design is used.

- Operation of inert anodes and carbon anodes together in a cell is possible. However, the current efficiency of each cannot be calculated individually. In addition, the aluminum formed from the carbon anode dilutes the impurities in the aluminum formed from the cermet anodes. Thus, the impurity levels in the aluminum will not be indicative of those that could be achieved with cermet anodes. Calculations of the loss of the material from the inert anodes from the impurity levels should still give an idea of the wear rate of the inert anodes.

Cu Cermet Substrates and Inconel Rod

- The cracking of the Cu cermet substrates and the loss of chips or pieces in the bath resulted in corrosion rates that are not useful for predicting impurity levels or wear of the anodes.

- The cracking was the result of thermal shock on introduction of the cermets into the test cell. The design of the metal current connector within the machined cermet probably contributed to the formation of the cracks.

- There is probably some open porosity in the starting material that may have allowed initial penetration of the cryolite into the anode. The cryolite formed a porous corroded zone over 4 mm thick in an anode that had been operated for only 1 h.

- Cu in the metallic form was not present in the outer layers of any of the anodes. The depth of oxidation in the anodes ranged from 3 to 18 mm thick. Within the oxidized zone there existed Cu depletion zones, Cu oxidized zones, and unique outer surface zones.

- A Cu depletion zone exists near the surface in all anodes. This zone typically begins within 1 mm from the outer surface of the substrate and is up to 1 mm wide. Although Cu depleted seams were observed in the untested material, the presence of these zones consistently near the exterior surface of the anode, and the observation of Cu oxide stringers in the cryolite in B1, suggest that this particular feature is a result of operation in the cell.

- The composition of the ferrite and Cu-rich phases remain fairly constant from the copper depletion zone to areas inward in all anodes and are the same for all anodes. The NiO composition is fairly constant from the Cu depletion zone inward for anodes A1 and C1. In anode E1, the Cu in solid solution within the NiO phase <u>increases</u> with depth into the anode.

- Within the Cu depleted, oxidized, and Cu metal containing regions in tested anodes there was an increase in porosity. Bath components could be found in some anodes throughout the sections examined. Bath mixtures in the pores had a lower

Na:Al ratio than was present in the bath.

- At the surface of the anode, next to the CEROX coating, unique surface structures were observed. These layers varied within an anode and from anode to anode. In some areas, the surface structure was a dense zone that contained NiO and Ni ferrite of different composition from the rest of the sample. In the ferrite, Al substituted for the Fe and small amounts of Cu were present as well. In that region, a Cu oxide phase was generally absent but Cu was present in the +2 state as part of a (Fe,Ni,Cu)O solid solution. The PO_2 within the anode can be estimated based on the Cu oxidation reactions.

- In some areas, a dense Ce fluoride and Cu oxide layer lies between the CEROX coating and the ferrite substrate. In addition (in some anodes), Ce fluoride was noted as small isolated grains within the interior oxidized region, up to 15 mm into the sample (E1). The Ce fluoride within the sample may simply be the result of dissolved Ce in the cryolite penetrating the grain boundaries and freezing there upon removal from the cell. However, the dense and thick layers of mixed Ce fluoride and Cu oxide cannot yet be explained.

- Two different Ni fluoride phases were observed within the sample. One phase was a Ni rich NiF_2 while the other contained Ni, Al, and Na as a $(Ni,Na,Al)F_x$. Cryolite and $(Ni,Na,Al)F_x$ coexist as separate phases. It is unknown if these compounds phase separate at cell operating conditions or if they separate upon cooling. It is not known why NiF_2 is present in certain layers, while NiO coexists with AlF_3 in other layers.

- The above conclusions indicate that this Cu cermet material as currently produced is not a stable material as a long term inert anode. The increase in porosity and the changes in phase composition show that the material composition was not stable under the conditions of penetrating AlF_3 and cryolite. The Cu depletion in some areas, and the reaction of Cu metal to Cu_2O and to Cu^{2+} in the NiO solid solution may lead to a loss of electrical conductivity in the anode. The oxidation thickness appears to increase with the length of time tested, which may yield a finite lifetime on an anode.

- The Inconel 601 microstructure exhibits signs of stress corrosion cracking. Cr rich precipitates at the grain boundaries in the center of the alloy were preferentially attacked by AlF_3 and Cr was depleted within the grains. Cr fluorides and oxides were observed as reaction products. However, no rods failed and this material is superior to Ni 200 for this application.

7. Recommendations

Based on the pilot cell testing recommendations can be made on ways to improve future pilot cell testing of inert anodes. In addition, recommendations are made on the substrate material and CEROX coating.

- In future pilot cell testing with inert anodes, the pilot cell should ideally contain all cermet anodes so that real estimates of current efficiency and corrosion can be made. In addition, the current to each inert anode should be individually controlled and monitored.

- Modeling and testing should be performed on the inert anode and current connector design in order to prevent any thermal stress cracking of the anodes.

- Low inert anode CD will make it difficult to control the heat balance in a self-heated pilot cell. The cell should be carefully designed to take this problem into account.

- Mucking of the cell by excess undissolved alumina led to operation problems. Careful design of the anode or cell may help to operate at high alumina concentrations. If this is not possible, inert anode materials that are less affected by low alumina concentrations should be employed.

- A longer alumina sheath on the current connector is needed such that it extends above the crust. This should prevent corrosion of Inconel 601 stems above the meltline. Rods within the anode may still be in contact with AlF_3. Additional experiments to determine a better (more corrosion resistant, more conductive, and cheaper) connector material may be necessary. The reaction of AlF_3 with Cr suggests a lower Cr contents may be desirable.

- This Cu cermet material, as currently fabricated is not an acceptable material for a long term inert anode. Research on either improving this cermet (increase density, change composition or processing) or on a new material, with and without a CEROX coating, should be performed.

- Because the development of the CEROX coating as a protective coating for an anode substrate is at the pilot cell level, for future commercialization of the technology removal of Ce from the aluminum (to acceptable levels) should be demonstrated.

Based on the observations in this test, another pilot cell test is not recommended at this time with the present Cu cermet substrate material. Rather, materials research and small-scale testing of alternative ceramic or cermet materials is recommended before longer term testing. The present Cu cermet would be useful in short-term pilot cell tests in order to further develop a pilot cell that is adequate for longer term controlled testing of inert anode materials. In addition, the cermet is also adequate for other engineering studies, such as testing different shapes of anodes, if the cracking thermal shock problem is remedied.

8. REFERENCES

1. Grjotheim, K; Krohn, C.; Molinovsky, M.; Matiasovsky, K. and Thonstad, J.; Aluminum Electrolysis Fundamentals of the Hall-Heroult Process, 2nd Edition, Aluminum-Verlag, Dusseldorf, 1982.

2. Billehaug, K. and Oye, H.A.; "Inert Anodes for Aluminum Electrolysis in Hall-Heroult Cells," Aluminum 57 (2), 1980, pp. 146-150.

3. Weyand, J.D.; Ray, S.P.; Baker, F.W.; DeYoung, D.H.; and Tarcy, G.P.; "Inert Anodes for Aluminum Smelting," Final Report, February 1986; DOE/CS/40158-20.

4. Strachan, D.M.; Marschman, S.C.; Davis, N.C.; Friley, F.R.; and Schilling, C.H.; "Inert Electrodes Program Fiscal Year 1988 Annual Report," October 1989; PNL-7106/UC-313.

5. Strachan, D.M.; Windisch, C.F., Jr.; Koski, O.H.; Morgan, L.G.; Peterson, R.D.; Richards, N.E.; and Tabereaux, A.T.; "Results from Electrolysis Test of a Prototype Inert Anode," May 1990; PNL-7345/UC-313.

6. Gregg, J.S. and Frederick, M.S.; "Evaluation of Cerium Oxide Coated Cu Cermets as Inert Anodes For Aluminum Electrowinning," March 1992; DOE/ID/12949.

7. Windisch, C.P., Jr.; Strachan, D.M.; Henager, C.H., Jr.; Greenwell, E.N.; and Alcorn, T.R.; "Results from a Pilot Cell Test of Cermet Anodes," May 1992.

8. Skybakmoen, E.; Solheim, A.; and Sterten, A.; "Phase Diagram Data in the System Na_3AlF_6-Li_3AlF_6-AlF_3-Al_2O_3 Part II: Alumina Solubility," Light Metals 1990, C.M. Bickert (ed.), The Minerals, Metals, & Materials Society, Warrendale, PA, 1990.

9. Pelton, A.D.; Schmalzried, H.; and Sticher, J.; "Computer-Assisted Analysis and Calculation of Phase Diagrams of the Fe-Cr-O, Fe-Ni-O, and Cr-Ni-O Systems," J. Phys. Chem. Solids, 40 (12), 1979, pp. 1103-1122.

10. Dalvi, A.D. and Sridhar, R.; "Thermodynamics of the Fe-Ni-O and Fe-Ni Systems at 1065K to 1380K," Can. Metall. Q., 15 (4), 1976, pp. 349-357.

11. Thompson, W.T.; Bale, C.W.; and Pelton, A.D.; "F*A*C*T (Facility for the Analysis of chemical Thermodynamics)-Guide to Operations," McGill University Computing Centre, Montreal, 1985.

12. Schmid, R., "A Thermodynamic Analysis of the Cu-O System with an Associated Solution Model," Metall. Trans. B, 14B (5), 1983, pp. 473-481.

13. Metals Handbook, Volume 8, T. Lyman, Ed., The American Society For Metals, Metals Park, Ohio, 8th Edition, 1973.

14. Windisch, C.F., Jr.; Strachan, D.M.; Davis, N.C.; Morgan, L.G.; Shade, J.W.; Stice, N.D.; and Westerman, R.E., "Inert Electrodes Program Fiscal Year 1990 Annual Report," August 1991; PNL-7777/UC-313.

15. Kingery, W.D.; Bowen, H.K.; and Uhlmann, D.R., Introduction to Ceramics, 2nd Edition, John Wiley & Sons, New York, New York, 1976.

16. Bularzik, J.; Davies, P.K.; and Navrotsky, A., "Thermodynamics of Solid-Solution Formation in NiO-CuO," J. Amer. Ceram. Soc., 69 (6), 1986; pp. 453-457.

17. Eric, H. and Timucin, M., "Equilibrium Relations in the System Nickel Oxide-Copper Oxide," Metall. Trans. B, 10B (6), 1979; pp. 561-563.

18. Meyers, C.E.; Mason, T.O.; Petuskey, W.T.; Halloran, J.W.; and Bowen, H.K.; "Phase Equilibria in the System Fe-Al-O", J. of the Amer. Cer. Soc., 63 (11-12), 1980; pp. 659-663.

19. Elrefaie, F.A. and Smeltzer, W.W., "Thermodynamics of Nickel-Aluminum-Oxygen System Between 900 and 1400 K," J. Electrochem. Soc., 128 (10), 1981; pp. 2237-2242.

20. Craig, J.R. and Vaughan, D.J., Ore Microscopy and Ore Petrography, John Wiley & Sons, New York, New York, 1981.

21. "Inconel 601," Inco Alloys International, Huntington, West Virginia.

Appendix 1

Reynolds Manufacturing Technology Laboratory (MTL) Report

MTL Report 1073

TIC 43-2411

Manufacturing Technology Laboratory

ELTECH CERMET ANODE PILOT CELL TEST

Project J-006-001
Subcontract to DOE Contract
DE-FC07-9 OID12940

Tom R. Alcorn **January 28, 1992**

Submitted By:

Tom Alcorn
Tom R. Alcorn

Approved By:

Alton T. Tabereaux
A. T. Tabereaux

N. E. Richards

ELTECH CERMET ANODE
PILOT CELL TEST

TABLE OF CONTENTS

MTL Report 1073
TIC 43-2411
Project J-006-001

I. SUMMARY

The effectiveness of cerium oxide coating technology developed by ELTECH for cermet anodes was evaluated in a pilot aluminum reduction cell operated at Reynolds Metals' Manufacturing Technology Laboratory. This was the second test of a module of six cermet anodes in the pilot reduction cell, with the first being with uncoated cermet anodes with Battelle's Pacific Northwest Laboratory (PNL). Individual cermet anodes were in continuous operation for as long as 614 hours (26 days) during the test with ELTECH and were intact upon removal.

The cermet anodes were operated for the majority of the test period at an anode current density of 0.5 amp/cm^2 and with the alumina content of the electrolyte near saturation. These conditions resulted in muck buildup in the cell bottom reducing available cell liquid volumes. Minor changes in the test parameters were made near the end of the test period with a slightly higher anode current density (0.65 amp/cm^2) and lower bath ratio (1.25 versus 1.50). No measurable effect on cermet anode performance or cell condition (muck buildup) was observed as a result of these changes.

Material problems, which occurred during the previous PNL cermet anode test, were greatly reduced during the ELTECH test. Inconel 600 was used as the material for the anode stem conductor, which proved to be an improvement over Nickel 200 used initially in the PNL test. The thermal stress cracking of the cermet anodes still remained a significant problem with this particular design of the cermet anode. However, through minimizing disturbances and movement of the cermet anodes, only two anodes were removed prematurely due to cracking or breakage.

Corrosion rates of the cermet anodes with a "Cerox" coating, as determined by the rate of metal impurity (iron, nickel, copper) increase in the aluminum metal, was approximately half that experienced in the previous PNL test with uncoated cermet anodes as shown below.

	PNL	ELTECH
Iron increase, lb/day	0.31 (0.21)	0.30 (0.12)
Nickel increase, lb/day	0.26	0.13
Copper increase, lb/day	0.13	0.075
Surface area loss, mm/day	0.2	0.1

The rate of iron increase in the aluminum metal pad was affected by other sources than the cermet anodes, such as tapping and sampling. The values for iron in parenthesis are the quantity which can be attributed to the cermet anodes.

It was observed that for some anodes the variability in the current gradients around the surface of individual cermet anodes greatly affected the "Cerox" coating thickness. Individual anodes were observed to have "Cerox" coating thickness varying from approximately 1/8 inch thick to none, where no, or very limited, current flow occurred from the anode surface. It is uncertain as to what effect these uncoated areas of the cermet anodes had on the corrosion rates of the anode material.

Maintaining the desired thickness of cerium oxide coating on the cermet anodes required maintaining cerium in the electrolyte through the routine additions of CeF_3. The resulting equilibrium concentrations of cerium in the bath and metal are as follows:

Cerium in the bath	0.44%
Cerium in the metal	3.23%

This high concentration of cerium in the metal will require that an economical technology be proven feasible for reducing the cerium concentration in the primary metal to an acceptable level (<1 ppm) before the "Cerox" technology would be accepted by industry. Advances in the cermet anode technology must also occur. Additional material characterization needs to occur as well as innovations in cell/anode design which will minimize the problems associated with the thermal stress cracking, low anode current density operation, and reduction cell operation with high alumina concentration in the electrolyte.

II. INTRODUCTION

ELTECH Research Corporation has developed the technology to form and maintain a cerium oxide coating on cermet anodes during the operation of an aluminum reduction cell. As part of a Department of Energy contract (cost shared), Reynolds Metals Company operated a pilot reduction cell at its Manufacturing Technology Laboratory to allow larger scale testing of this "Cerox" coating technology. This was the second test of a module of six cermet anodes conducted in the pilot cell, with the first being with Battelle's Pacific Northwest Laboratories (PNL). Both tests used cermet anodes manufactured by Ceramic Magnetics, Fairfield, New Jersey.

The objective of the pilot cell test was to evaluate the performance and determine the corrosion rate of the cermet anodes with the "Cerox" coating in an industrial size application and compare that data with the similar operation of the cermet anodes without the "Cerox" coating during the previous PNL test. Corrosion rates were primarily determined through the rate of increase of metal impurities (iron, nickel, and copper) in the aluminum metal pad. Material evaluations of the removed cermet anodes will be reported separately by ELTECH.

Primary evaluation of the cermet anodes was conducted under pilot cell test conditions of 0.5 amp/cm^2, alumina saturation, and a bath ratio of 1.5. Additional evaluations were conducted at a slightly higher anode current density (0.65 amp/cm^2) and at a lower bath ratio (1.25).

III. CONCLUSIONS

Major conclusions from the operation of the reduction pilot cell with cermet anodes using ELTECH's "Cerox" coating are:

1. Major design problems exist with the cermet anodes as manufactured for the pilot cell test as demonstrated by the thermal stress causing cracking and breaking of the anodes. The actual breakage of the anodes, which was experienced in the previous PNL test, was minimized by adopting a policy of not disturbing the cermet anodes once installed. Only two cermet anodes were removed prematurely due to cracking/breaking.

2. Use of Inconel 600 for the anode stem conductor rod, along with a ceramic barrier just above the anode top, proved to be satisfactory for the duration of the pilot cell test.

3. Corrosion rates of the cermet anodes as determined by metal impurity increases in the aluminum metal pad were:

Copper	0.075 lb/day
Nickel	0.13 lb/day
Iron	0.30 lb/day

The iron corrosion rate is inflated due to contamination from other sources and should be 0.12 lb/day based upon the ratio of materials in the anode and the rate of corrosion of copper and nickel.

4. These corrosion rates result in a surface area loss of 0.1 mm/day, based on uniform loss from all six anodes. This corrosion rate is approximately one half of that determined during the previous testing of similarly manufactured cermet anodes without "Cerox" coating for PNL.

5. Operation of the cermet anodes with slightly higher anodic current density and/or lower bath ratio did not significantly change the corrosion rates as determined by metal impurity increases in the aluminum metal pad.

6. Continuous operation of the cell near alumina saturation resulted in extreme mucking conditions which reduced the cell liquid volumes of bath and metal. This condition also resulted in a 30-50°C temperature gradient vertically in the bath.

7. Uneven current flow from the surfaces of individual cermet anodes resulted in uneven "Cerox" coating formation with some areas without any coating. This current flow imbalance was caused by the effects of the adjacent carbon anode which operated at a considerably higher amperage and voltage, and the location of other cermet anodes.

8. Average equilibrium levels of cerium in the pilot reduction cell were:

Cerium in the bath	0.44%
Cerium in the metal	3.23%

Higher temporary concentrations of cerium (approximately 0.8% in the bath) were needed during the actual coating process to be effective.

IV. EXPERIMENTAL DESIGN AND PROCEDURES

A. Pilot Aluminum Reduction Cell Design

MTL's pilot reduction cell, as shown in Figure 1, is a small, self-heated cell with the capacity for running two industrial-size carbon anodes. Figures 2 - 3 show schematics of the pilot cell design. Key features of this design include the following.

1. Two 15.5" x 21.5" anodes located 4 inches apart, centered over two standard amorphous cathode blocks.
2. Sidewall construction consisting of rammed carbon, prebake carbon blocks, and TR-19 vermiculite insulation to minimize heat losses.
3. Alumina feed through a point feed system located between the two anodes.
4. A cell cavity 44" x 33" x 17" deep. A 5 inch gap exists between the edge of the anode on two sides and a 6 inch gap on the other two sides. Metal tapping is normally done using a vacuum crucible between the two anodes.

Special modifications were done to the system to accommodate the testing of the cermet anodes. One of the carbon anodes (east) was replaced by an inert anode cluster consisting of six cermet anodes in a 2 by 3 arrangement as shown in Figures 4 and 5. The identification (A-F) of the anode positions is shown in Figure 4 and will be used throughout this report. The holder system allowed for removal of each individual anode. Current was supplied to the anode cluster by means of cables connected to the top of each stem. Current was monitored to each cermet anode by means of a calibrated current shunt located near the top of the superstructure. The shunts were calibrated at 100 mv being equal to 500 amps. Each of the anodes was electrically isolated from the holder by means of an alumina insulator. Current to the cermet anode cluster was isolated from the adjacent carbon anode, allowing individual control of current or voltage of the carbon anode and cermet anode cluster. This allowed operation of the carbon anode under such conditions to provide sufficient heat for maintaining a proper thermal balance in the cell.

B. Cermet Anode Design

The cermet anodes of the type $NiO-NiFe_2O_4-Cu$ were manufactured by Ceramic Magnetics Inc., Fairfield, N.J. These anodes contained approximately 42.9% NiO, 40.1% Fe_2O_3, and 17% Cu. The cermet anode is shown in Figure 6. The anodes were cylindrical with a radius of 3 inches and a height of 3 inches with an additional 1 inch lip extending above the top face of the cylinder. The bottom edges of the anodes were rounded with a radius of curvature of 1.5 inch. An 18 inch long, 1 inch diameter Inconel 600 connector rod was screwed into the center of each cermet anode. A 1.25 inch diameter alumina sleeve was placed over the rod, extending 3 inches up from the top of the cermet anode, to serve as a chemical protection to the rod. This sleeve was then packed with an alumina castable.

C. Testing Procedures

Test data was routinely collected from the cell in order to monitor the performance of the anodes and control the cell operation. These items were recorded on a log sheet during each of the three daily shifts as shown in Figure 7. In addition to this, current of each

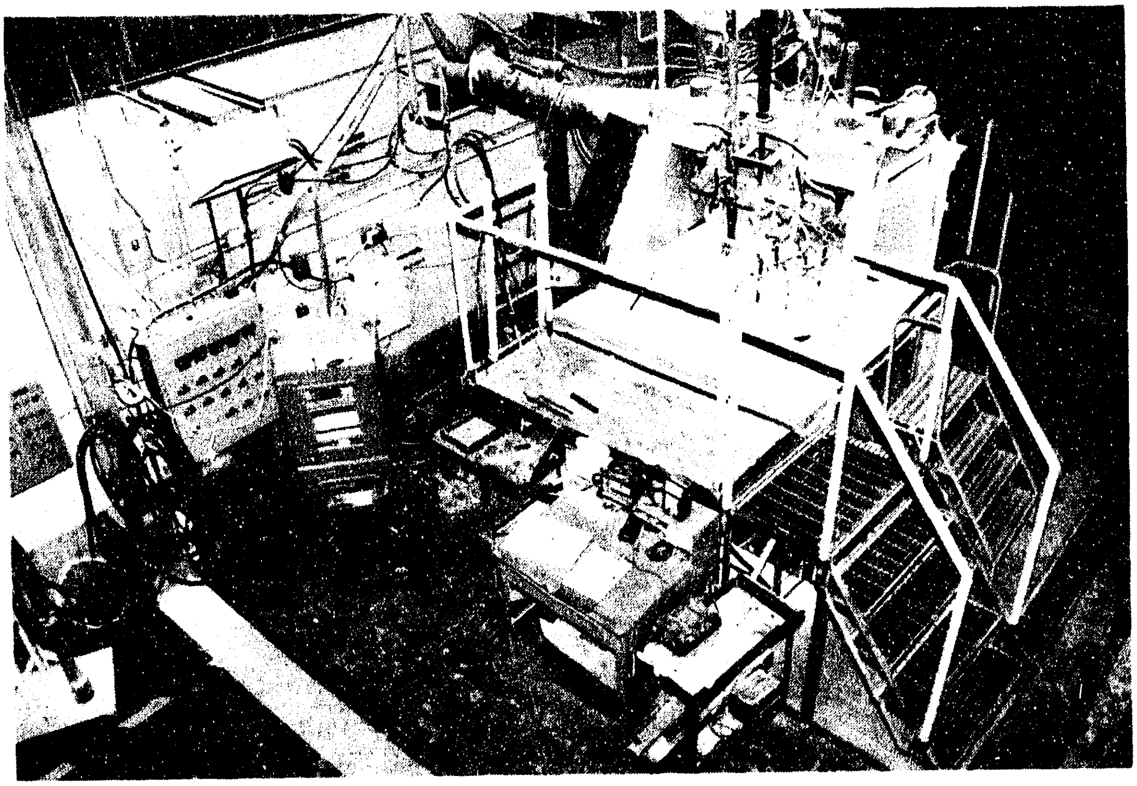

Figure 1. MTL's Pilot Reduction Cell

Pilot Cell Design
Plan View

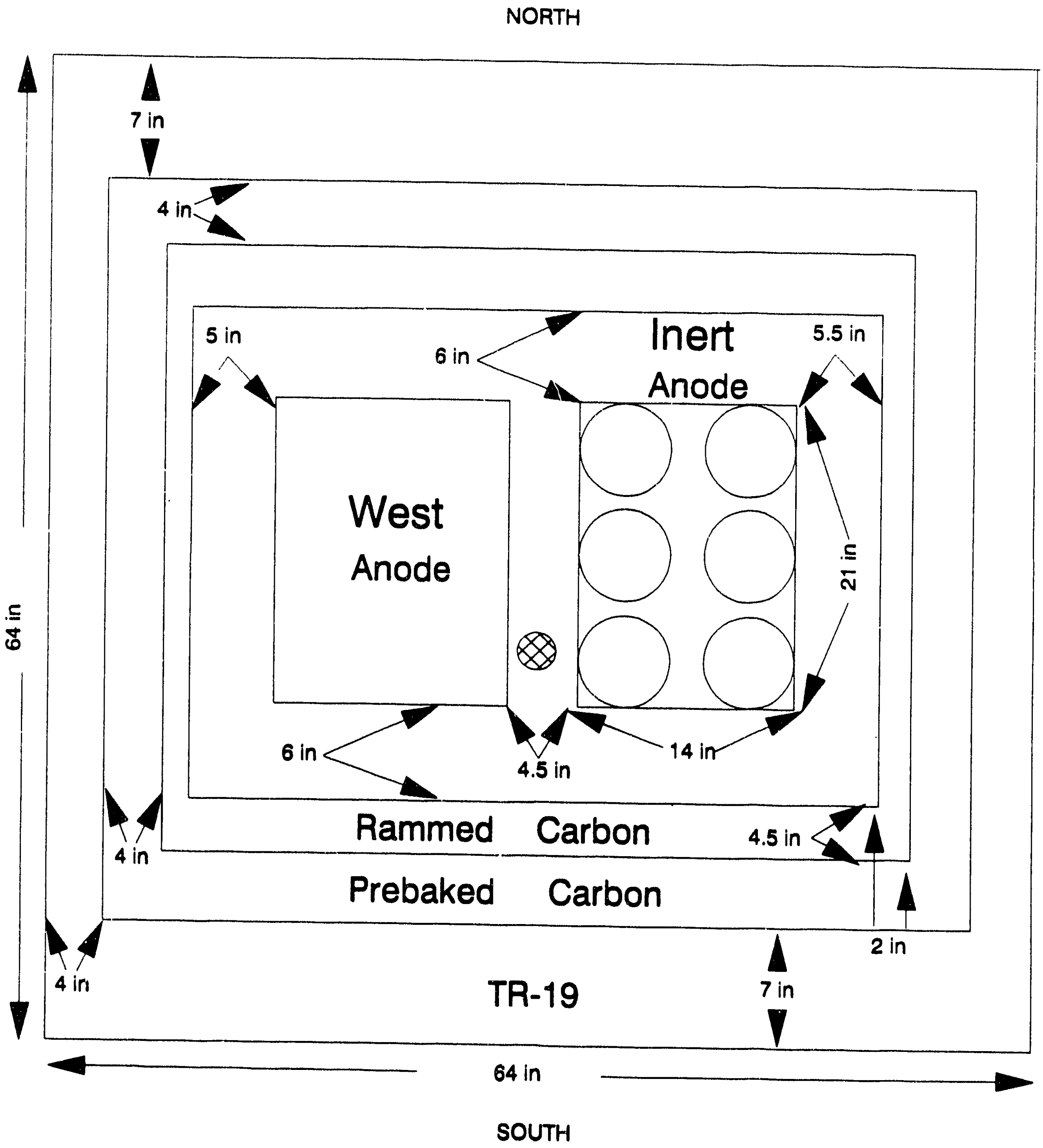

Figure 2

PILOT REDUCTION CELL DESIGN

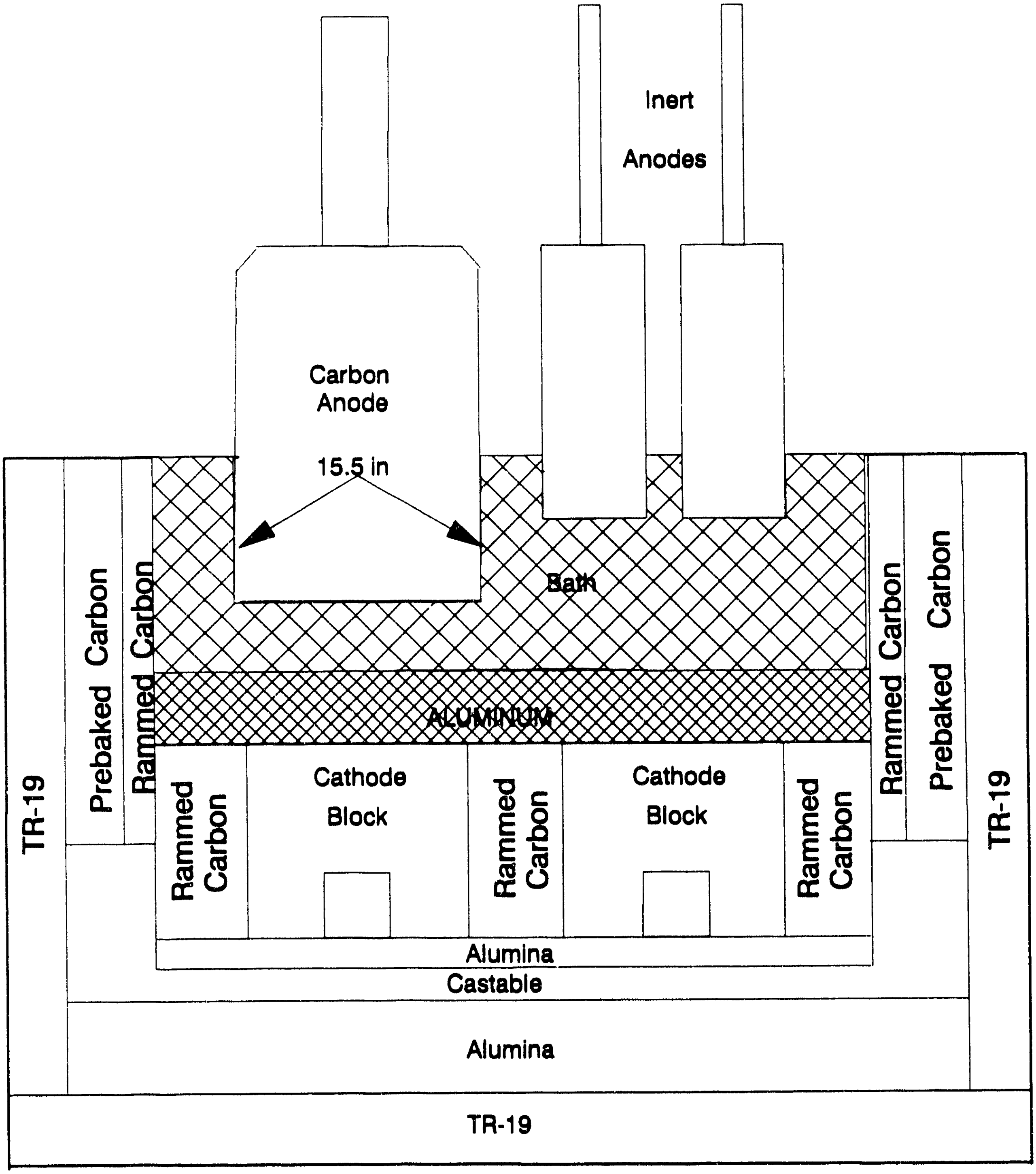

Figure 3

Inert Anode Layout

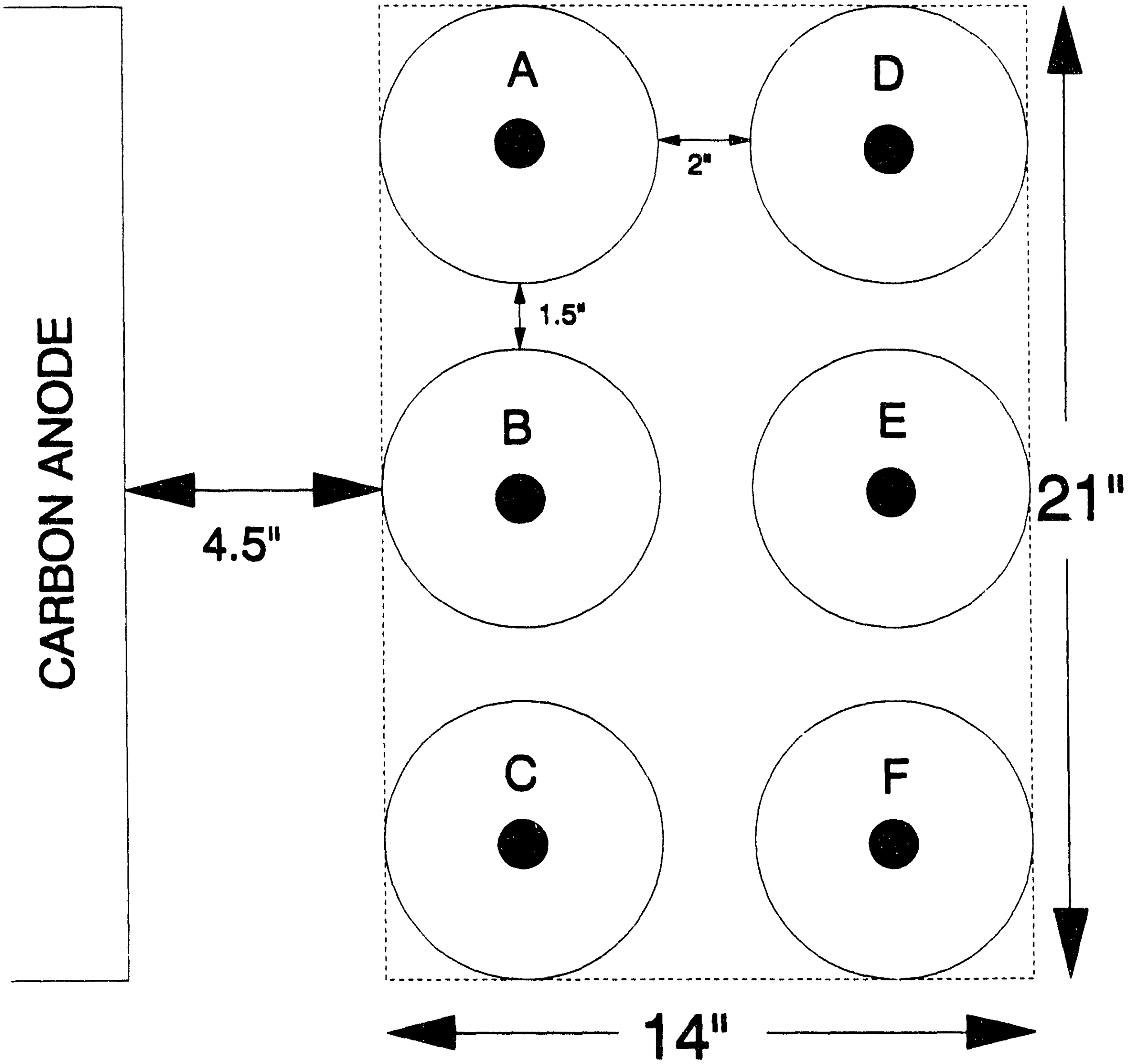

Figure 4

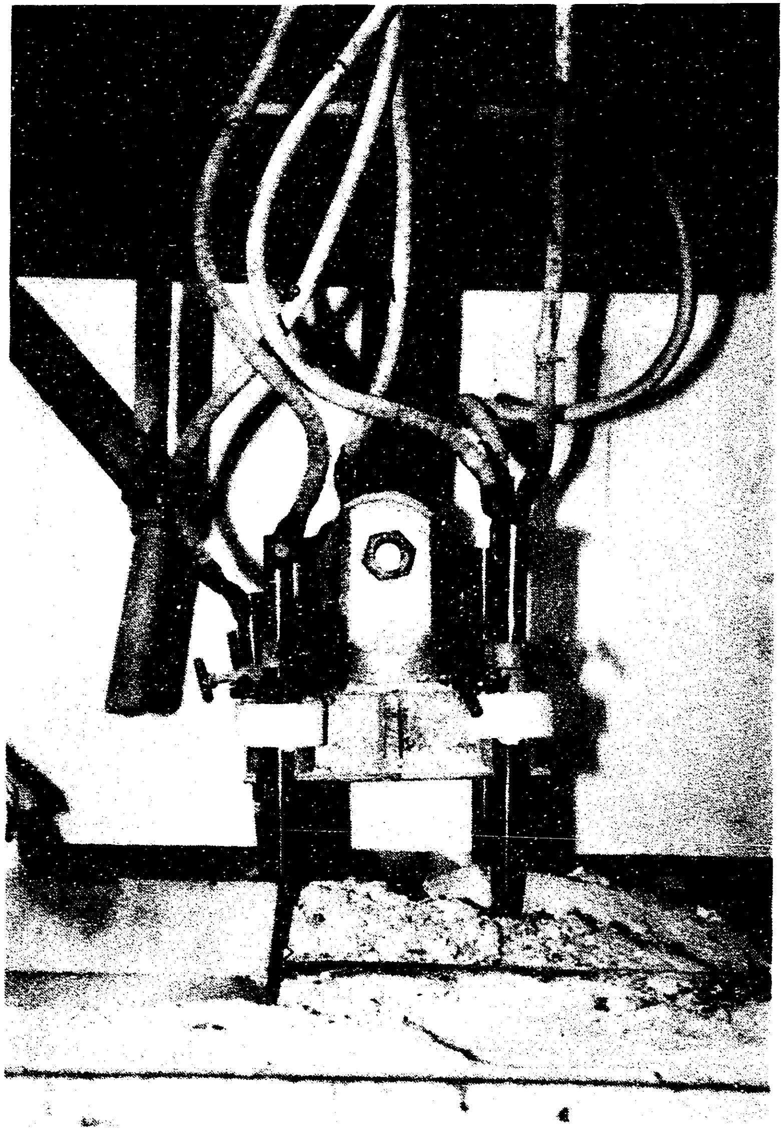

Figure 5. Cermet Anode Cluster

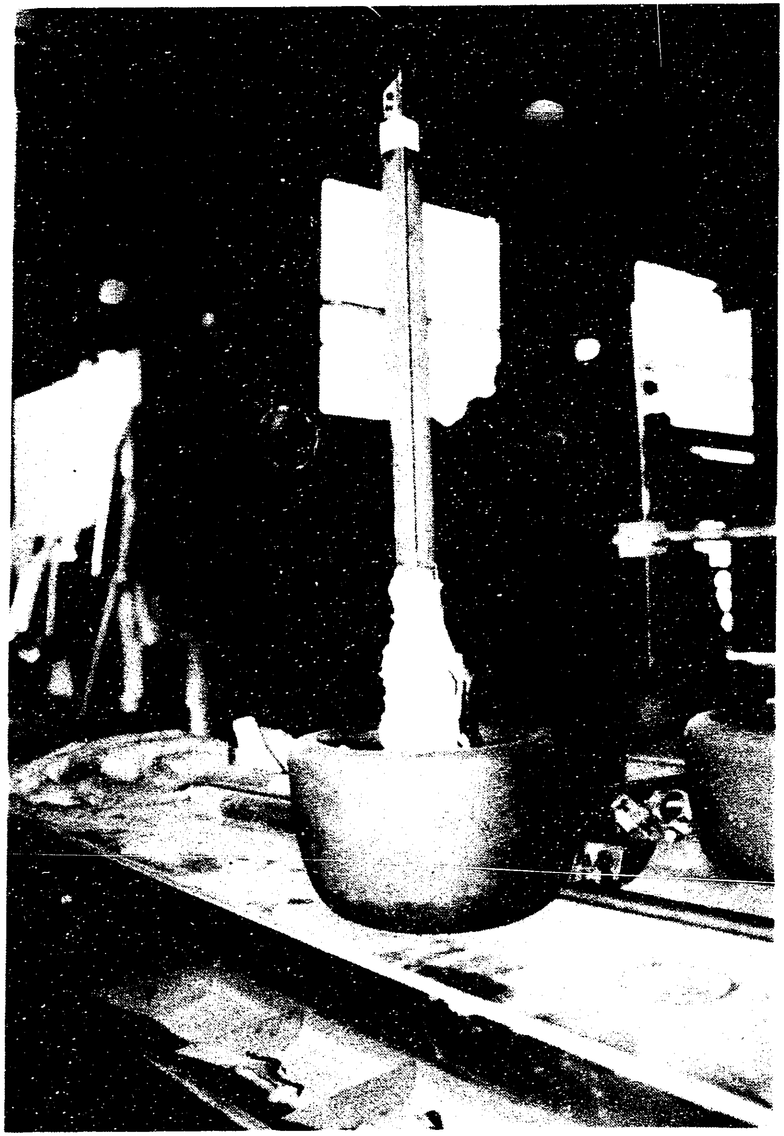

Figure 6. Cermet Anode with Alumina Sleeve

Pilot Reduction Cell
Inert Anode Test

Date ____________

Operators
____
____
____

		Time							
		7	8	9	10	11	12	13	14
Bath Temperature									
Cell Voltage –	East Anode								
	West Anode								
Cathode Drop		▨	▨	▨		▨	▨	▨	▨
Anode Drop –	East Anode	▨	▨	▨		▨	▨	▨	▨
	West Anode	▨	▨	▨		▨	▨	▨	▨
Current –	East Anode								
	West Anode								
	Inert A								
	Inert B								
	Inert C								
	Inert D								
	Inert E								
	Inert F								
Bath Depth		▨		▨	▨	▨		▨	▨
Metal Depth		▨		▨	▨	▨		▨	▨
Anode Immersion –	East Anode	▨		▨	▨	▨		▨	▨
	West Anode	▨		▨	▨	▨		▨	▨
Metal Sample		▨	▨	▨		▨	▨	▨	
Bath Sample		▨	▨	▨		▨	▨	▨	
Point Feed Check									
Ore Bin Level		▨	▨		▨	▨	▨		▨
Alumina Meter Reading		▨		▨		▨		▨	

Comments: ____

Figure 7

cermet anode, voltage of the east and west anodes, and total current to each anode (or cluster) was logged every 30 seconds by means of a Dianachart data acquisition system and a personal computer. Non-routine data and activities were recorded in log books.

V. RESULTS

A. Cell Preparation

Following the completion of the PNL pilot cell test in August, the cermet anodes were replaced with a standard carbon anode and the cell was operated for a time to return the cell to a normal operating condition. Primary emphasis was in achieving a clean cathode, free of muck, and to reduce the major metal (iron, copper, and nickel) impurities' concentrations to normal, baseline levels. Target baseline concentration levels were:

Iron	0.380%
Copper	0.050%
Nickel	0.003%

The metal pad was tapped low (2-3 inch) and numerous anode effects were forced to enhance the return to normal operating conditions. The cell bottom was essentially muck-free by September 3; however, additional time was required to obtain the stable, lower concentration levels of the major impurities in the metal. Figures 8 - 10 show the impurity levels during this time period. On September 11, 100 lb of pure aluminum was added to the cell to dilute and thus lower the levels of metal impurities. By September 14, the impurity levels had stabilized at sufficiently low levels to begin the test of the cermet anodes with the "Cerox" coating. Only nickel had not returned to the initial low level, as shown below.

Iron	0.440%
Copper	0.020%
Nickel	0.030%

B. Preheating and Installation of Cermet Anodes

The cermet anodes were heated on the cell, similar to procedures developed during the previous PNL test. The cermet anodes were placed on the deck plate and covered with a kaowool blanket on September 8 (4:00 p.m.), where they remained until September 13 (11:30 a.m.), at which time they were placed in the "six-pack" holder over the crust, as shown in Figure 11. A kaowool blanket was then placed over the cermet anodes, and they were gradually lowered onto the crust and into the bath. The anodes were moved into the bath at 1:30 p.m. on September 14 and began to conduct current. Figure 12 shows the heatup of the cermet anodes during this period as measured by thermocouples located on top of the anodes. As this plot indicates, the anodes were heated to 130-230°C when placed over the cell crust, then gradually heated to 600-650°C, prior to contacting the molten bath.

This procedure appeared to work reasonably well; however, the anode in position B developed a noticeable crack through the center of the anode shortly after installation and was removed at 5:00 p.m. on September 14.

An identical heatup procedure was used for installation of the 3 replacement anodes used during the testing on September 26 and 27.

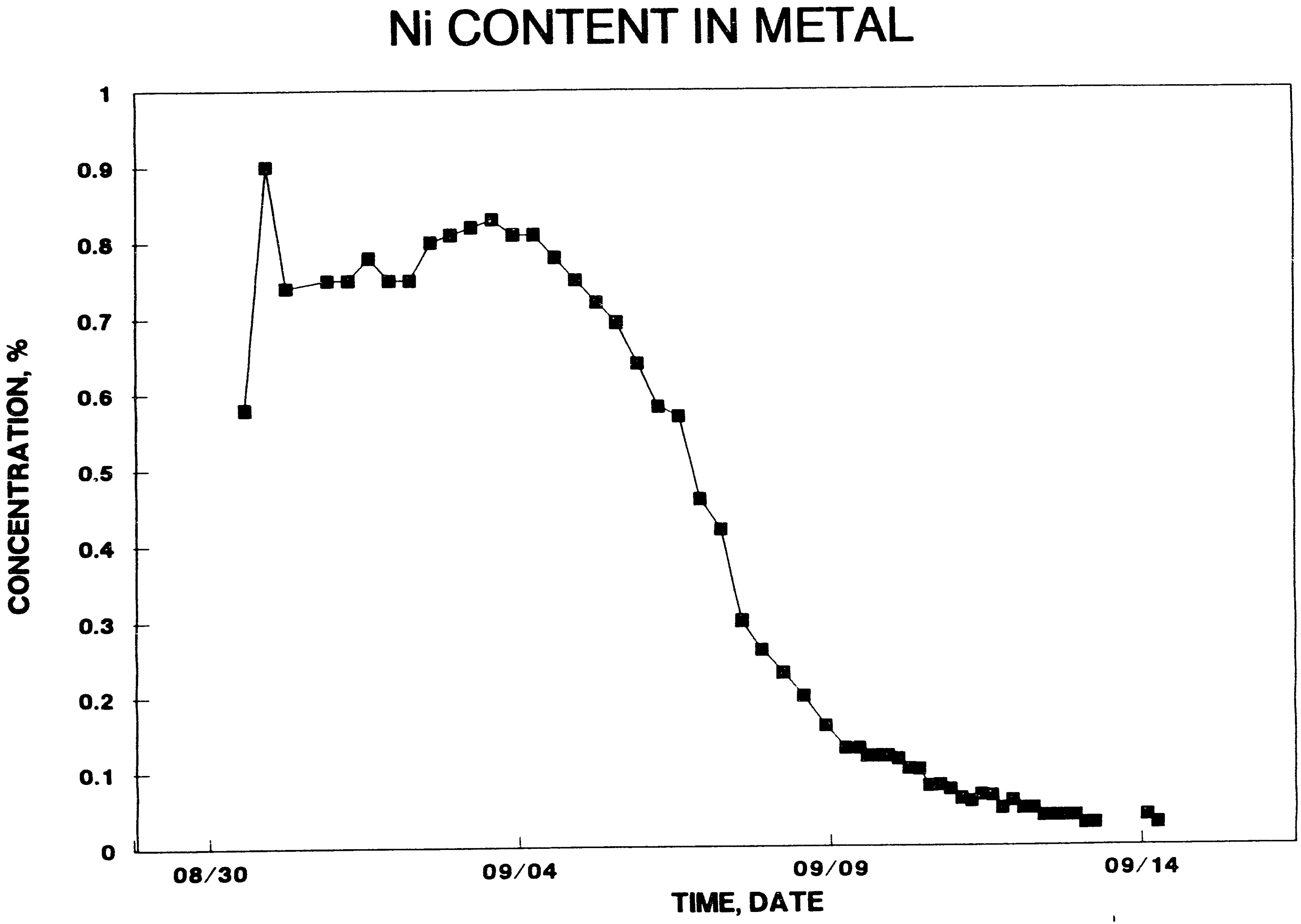
Ni CONTENT IN METAL
CONCENTRATION, %
1
0.9
0.8
0.7
0.6
0,5
0.4
0.3
0.2
0.1
0
08/30
09/04
09/09
09/14
TIME, DATE

Figure 8

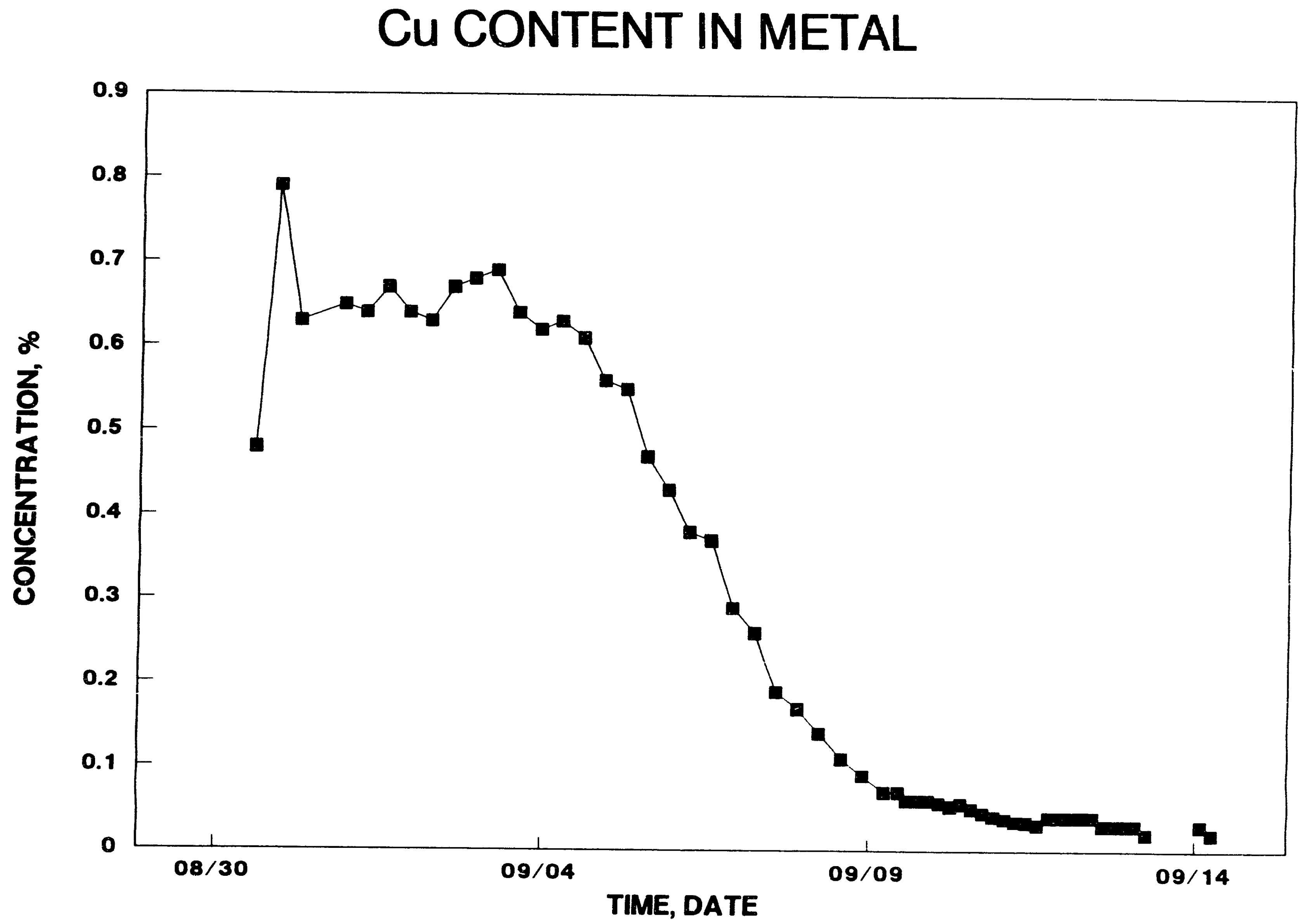
Cu CONTENT IN METAL
CONCENTRATION, %
0.9
0.8
0.7
0.6
0.5
0.4
0.3
0.2
0.1
0
08/30
09/04
09/09
09/14
TIME, DATE

Figure 9

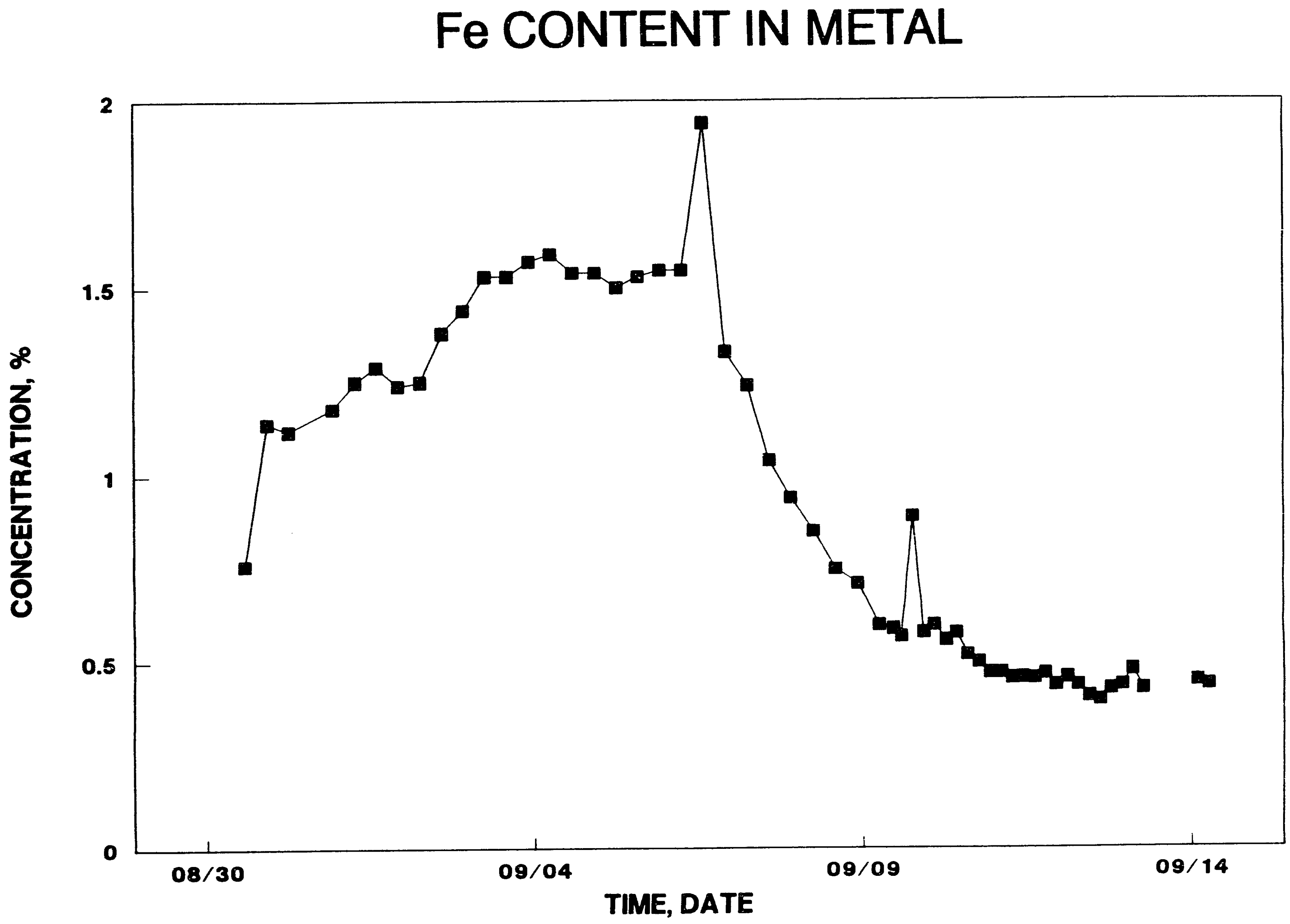
Fe CONTENT IN METAL
CONCENTRATION, %
2
1.5
1
0.5
0
08/30
09/04
09/09
09/14
TIME, DATE

Figure 10

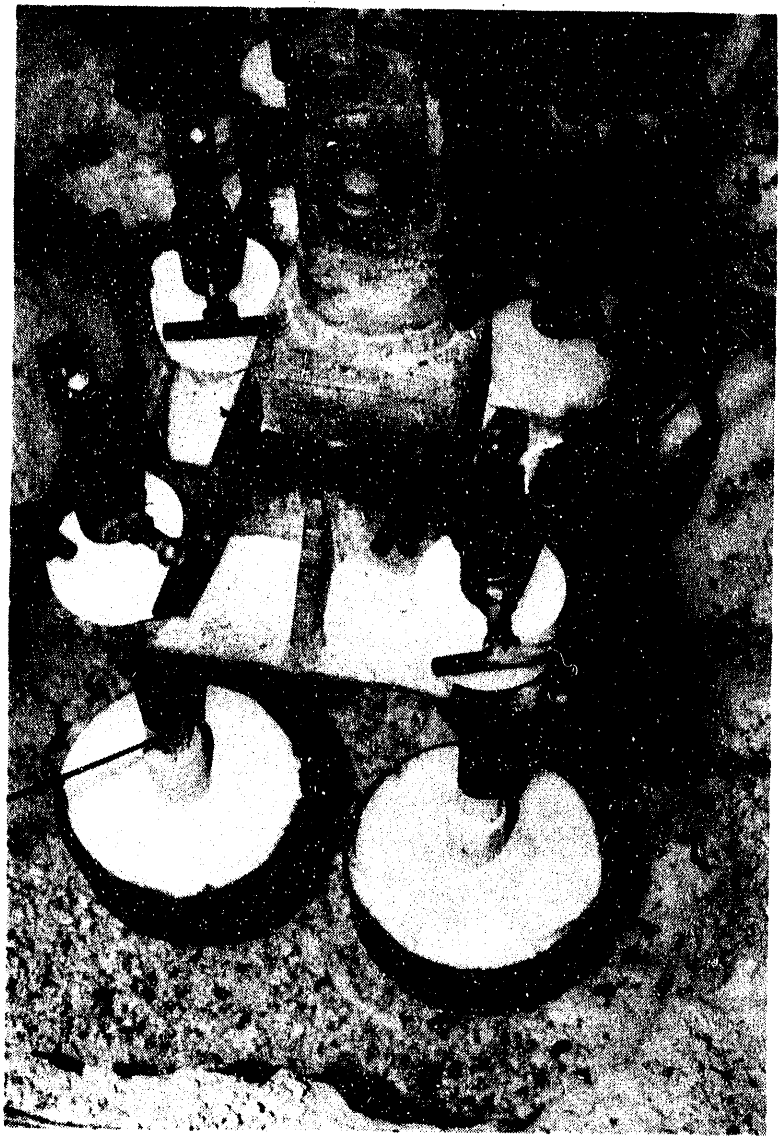

Figure 11. Cermet Anode Cluster preheating over Cryolite Crust

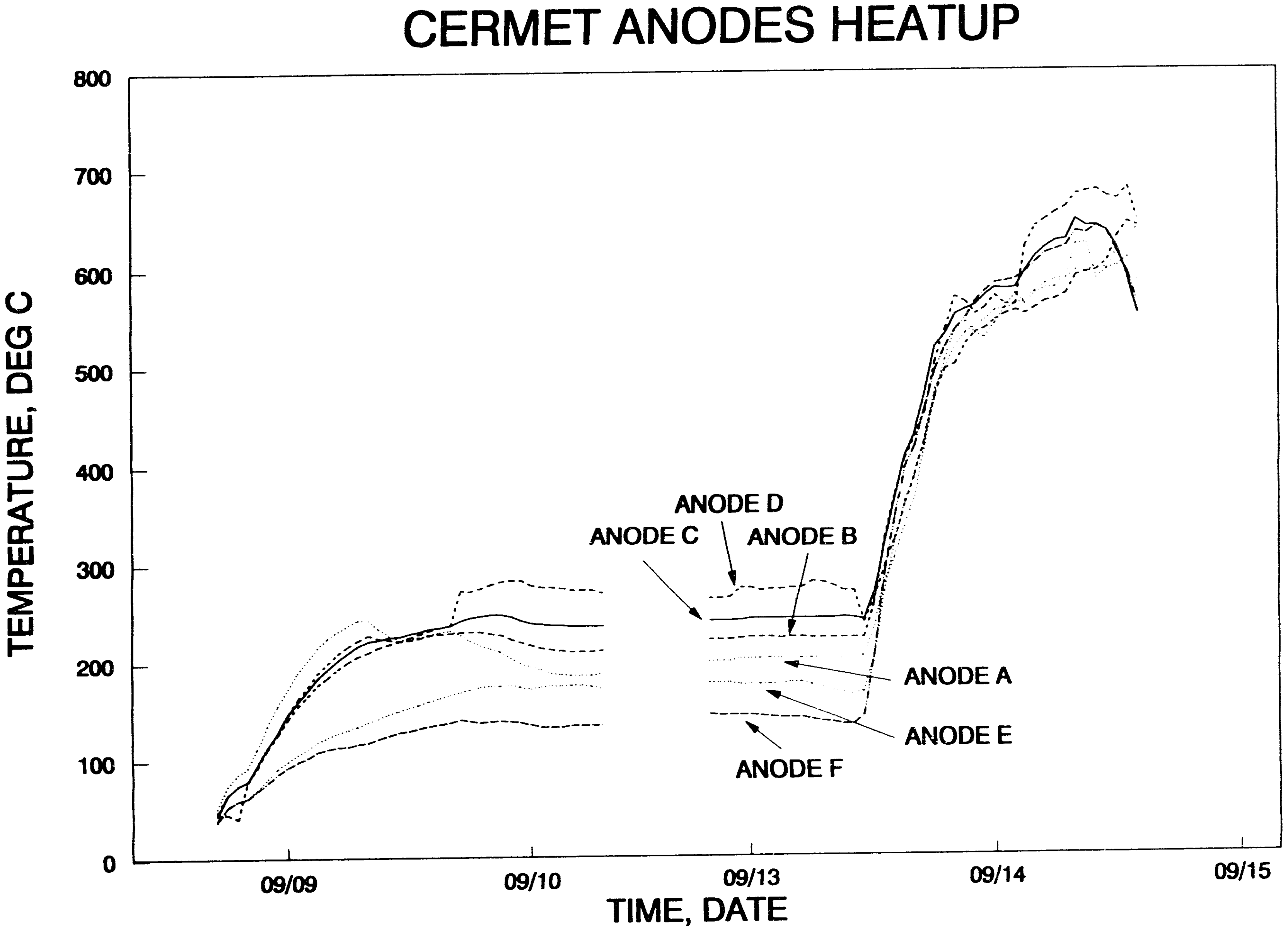
CERMET ANODES HEATUP
TEMPERATURE, DEG C
800
700
600
500
400
300
200
100
0
ANODE D
ANODE C
ANODE B
ANODE A
ANODE E
ANODE F
09/09
09/10
09/13
09/14
09/15
TIME, DATE

Figure 12

Ce CONTENT IN THE METAL

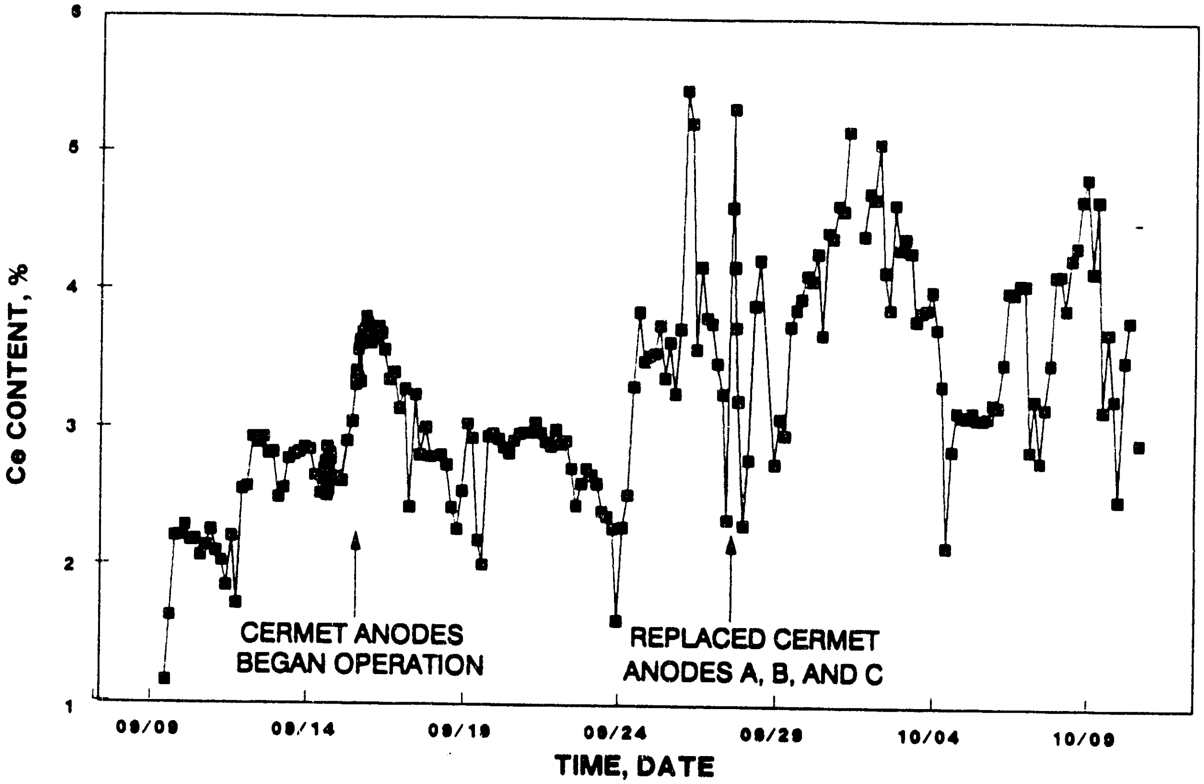

Ce CONTENT IN THE BATH

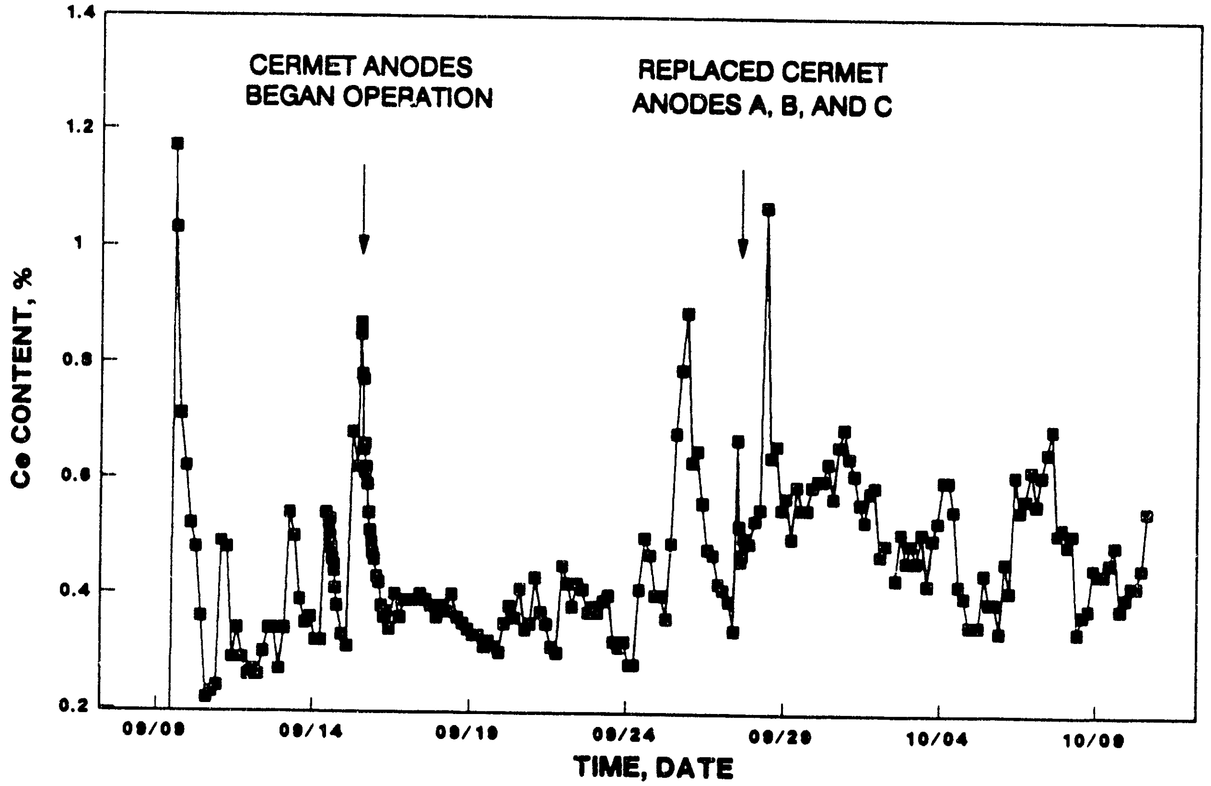

Figure 13

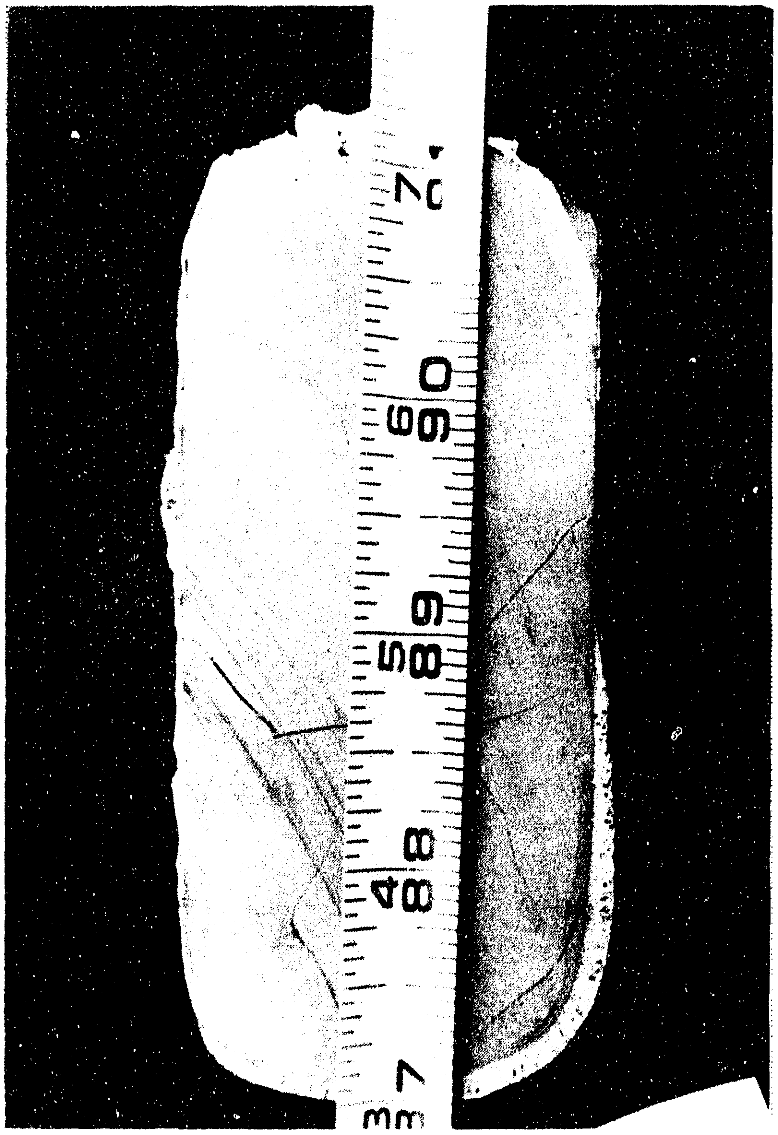

Figure 14. Reference Cermet Anode cross-section showing "Cerox" coating

CERIUM CONTENT IN BATH VERSUS IN METAL

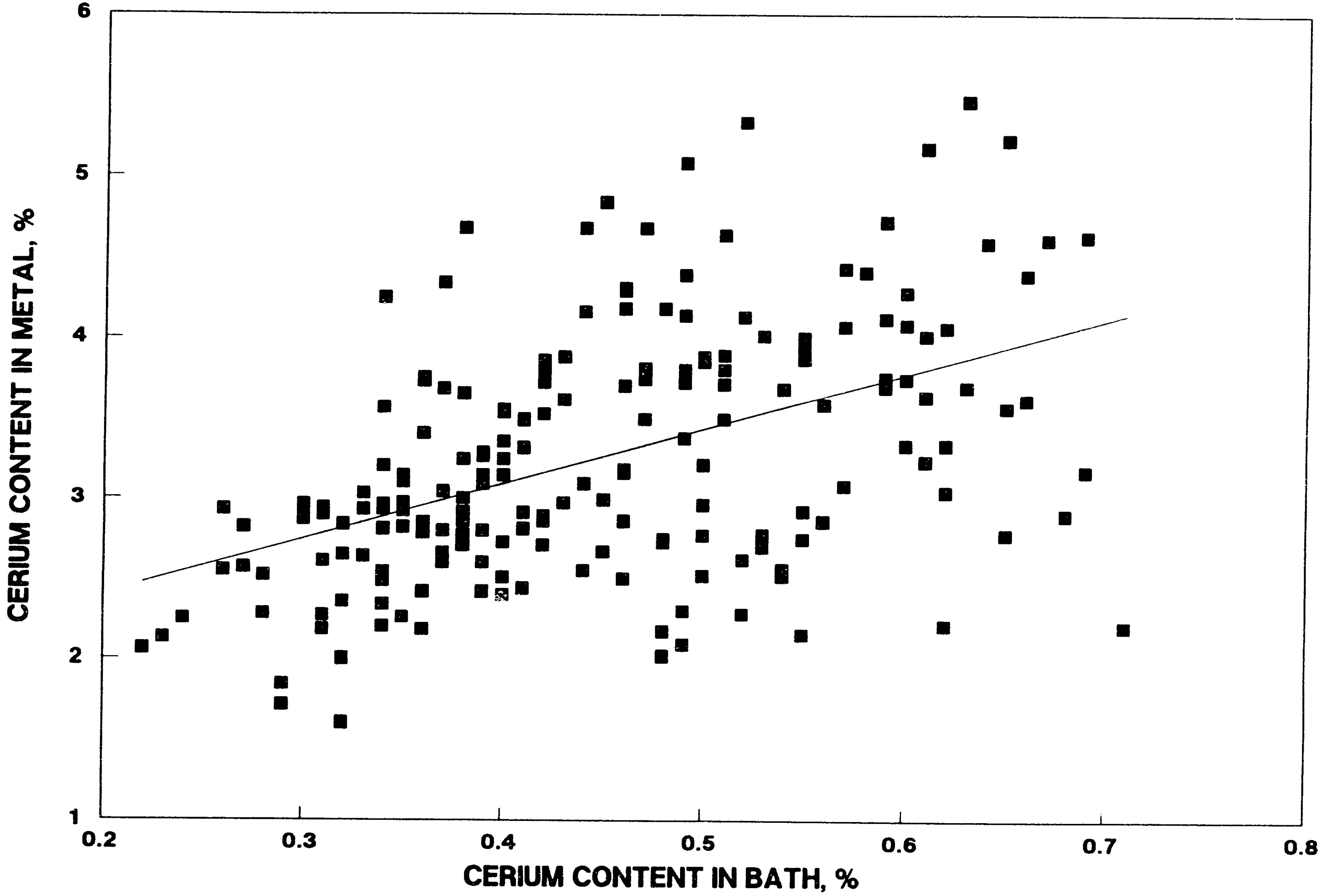

Figure 15

C. Cerox Cermet Anode Coating Procedure

The cermet anodes were coated with cerium oxide in the pilot reduction cell by controlling the additions of cerium fluoride (CeF_3) to the electrolyte. For the coating to occur properly, it is critical to have sufficient concentrations of cerium fluoride in the cell bath. The majority of the cerium added to the bath reported to the aluminum metal pad. These values for cerium are shown in Figure 13. Typical equilibrium concentration values for the distribution of cerium between the bath and aluminum are as follows:

Cerium in bath	0.44%
Cerium in metal	3.23%

At the time (September 15 and September 26) of the initial coating of the anodes, increased amounts of CeF_3 were added to the cell, temporarily achieving higher levels of cerium in the bath. A separate, small (reference) cermet anode (1.5" diameter) was placed into the electrolyte, operating on a separate power supply, to evaluate the cerium coating process. The anode operated for a few hours and then was removed to evaluate the coating. The first evaluation was on September 13 at 3:30 p.m. in which no coating was observed on the cermet anode upon removal 5 hours later. A second evaluation was made on September 14 and again little or no cerium coating of the cermet anode occurred. On September 15, after increased amounts of CeF_3 were added to the cell, a coating was observed to have formed on the anode. This anode and its coating is shown in Figure 14. As these photographs show, a significant coating did occur, approximately 1/8" thick, on a portion of the cermet anode. The side of the cermet anode next to the carbon anode did not form a coating, as minimal current flow occurred from this area of the cermet anode.

After obtaining the initial coating, a maintenance (25-60 g/hr) amount of CeF_3 was added to the cell to compensate for the cerium removed in the aluminum metal being produced. Figure 15 shows the distribution between cerium in the bath and that in the metal. As this plot indicates, the cerium in the bath will normally remain in the 0.3-0.6% range with the excess amounts reporting to the metal.

A question did arise concerning the cerium coating procedures and process for the replacement anodes installed on September 26. It was uncertain what effect the high levels of cerium, required to coat the new anodes, would have on the three remaining cermet anodes with a coating already applied. Analysis and evaluation of the three removed anodes by ELTECH may provide information regarding this aspect of the coating process.

D. Cermet Anodes Operation

Operation of the cermet anodes in the pilot cell began on September 15 and continued through October 10. The cermet anodes actually operated for a time (12 hours) on September 14, but current was interrupted after determination that insufficient cerium existed in the electrolyte for coating to occur. After adding more cerium to the electrolyte, the anodes were restarted on September 15 at 1:00 p.m. The majority of the test period was directed toward evaluation of the cermet anodes under "normal" test conditions; that is, a nominal anodic current density of 0.5 amp/cm^2 and alumina saturation. Target test conditions for this phase of cell operation were as follows:

Date	Sept 15 - 30
Maximum individual anode current	90 amp
Bath Ratio	1.4 - 1.6
CaF_2	4 - 6 wt%
Al_2O_3 (100% saturation)	8 - 10 wt%

On September 30, the test target operating condition was changed such that maximum current to an individual cermet anode was increased to 115 amp. An additional change was made on October 6 with the target ratio being lowered to 1.2.

1. Electrolyte Chemistry

Bath Additives

Figures 16 and 17 show the primary components of the bath. Actual results are contained in Appendix A. Large variations in bath ratio were found to occur whenever rapid changes in bath volume occurred in the cell due to freezing and melting of the ledges caused by large bath temperature variations. The CaF_2 was generally controlled within target limits of 4-5%. Trace amounts of LiF (<0.3%) and MgF_2 (<0.15%) were also present in the electrolyte, along with the CeF_3.

Bath Temperature

The electrolyte temperature measured on an hourly basis is shown in Figure 18. A very large variability in the bath temperature occurred as the dynamics of the pilot cell is such that quick response in temperature occurs with disturbances to the cell alumina crust cover or changes in the cell energy input. Thick muck developed in the cell bottom as the pilot cell operation progressed due to requirements to overfeed the cell with alumina in order to maintain alumina in the bath near saturation. As a result, extreme temperature gradients developed vertically in the bath. Temperatures near the top of the bath would be as much as 40-50°C higher than near the cathode bottom. The reported bath temperatures were measured approximately 2 inches into the bath and represent the higher bath temperature of the cell. Operating temperatures were controlled at high temperatures (above 1000°C) during the later periods of the test to minimize freezing of bath on the bottom of the cell.

Alumina Concentration

One of the key operating parameters was to maintain alumina content in the bath as close to saturation as possible. Bath samples were taken every 4 hours for alumina analysis and the alumina content in the bath was monitored every two hours with the Reynolds' Mark V alumina meter. Generally, the bath samples were taken between the east anode cluster and the west carbon anode. The results of the measured alumina content in the bath and the calculated alumina saturation throughout the test are shown in Figures 19 and 20. The calculated values for percent alumina saturation were obtained using the formula developed by Skybakmoen, et al., presented in Light Metals 1990. The calculated percent alumina saturation is greatly influenced by the operating bath temperature as shown in Figure 21. This plot also indicates the problem operating near saturation in a reduction cell which can experience great swings in bath temperature such as the pilot cell. Significant amounts of alumina are deposited on the cell bottom when a cell is operating near

RATIO VERSUS TIME

ELTECH CERMET ANODE PILOT CELL TEST

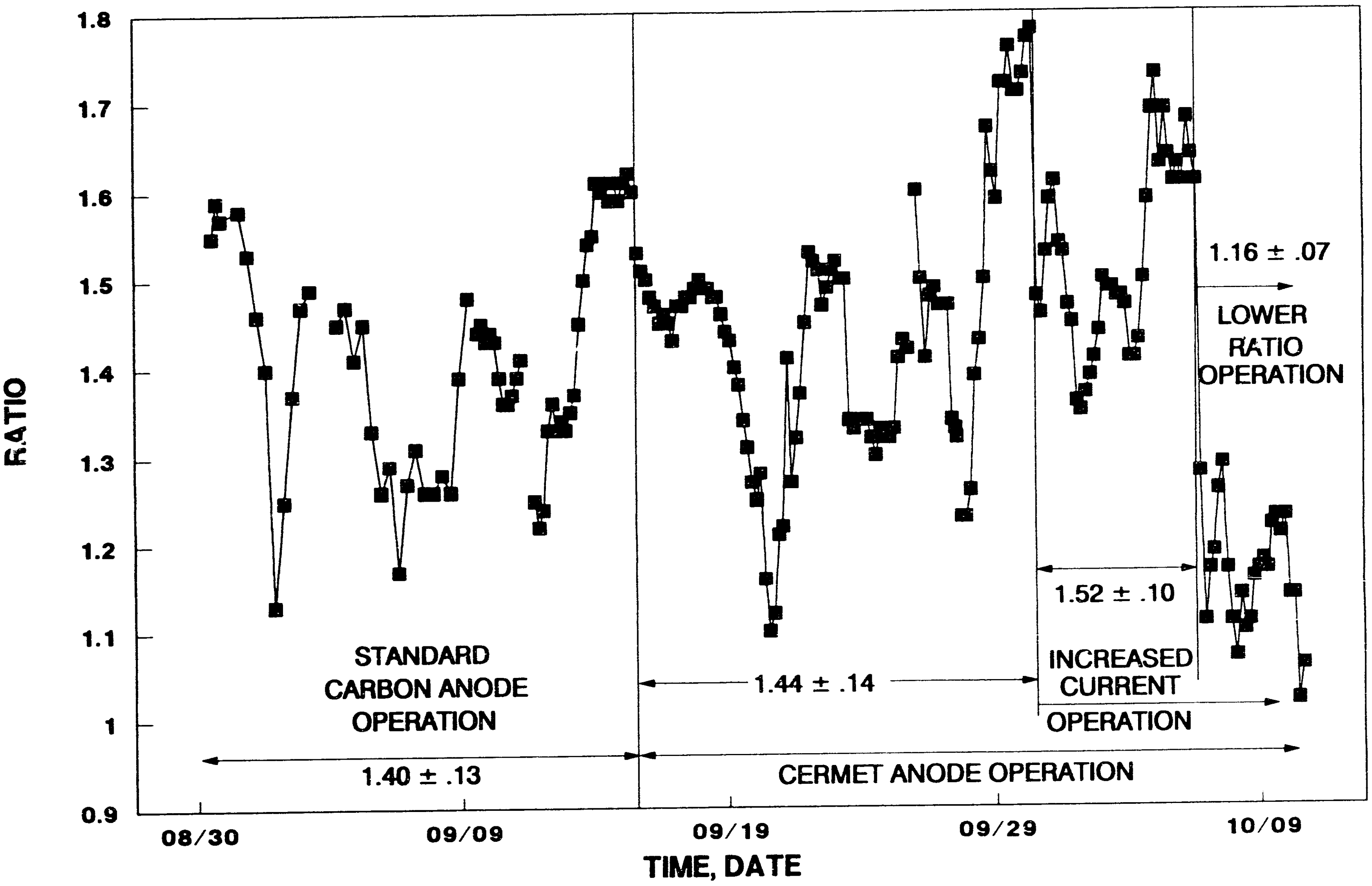

Figure 16

CaF_2 CONTENT IN BATH VERSUS TIME

ELTECH CERMET ANODE PILOT CELL TEST

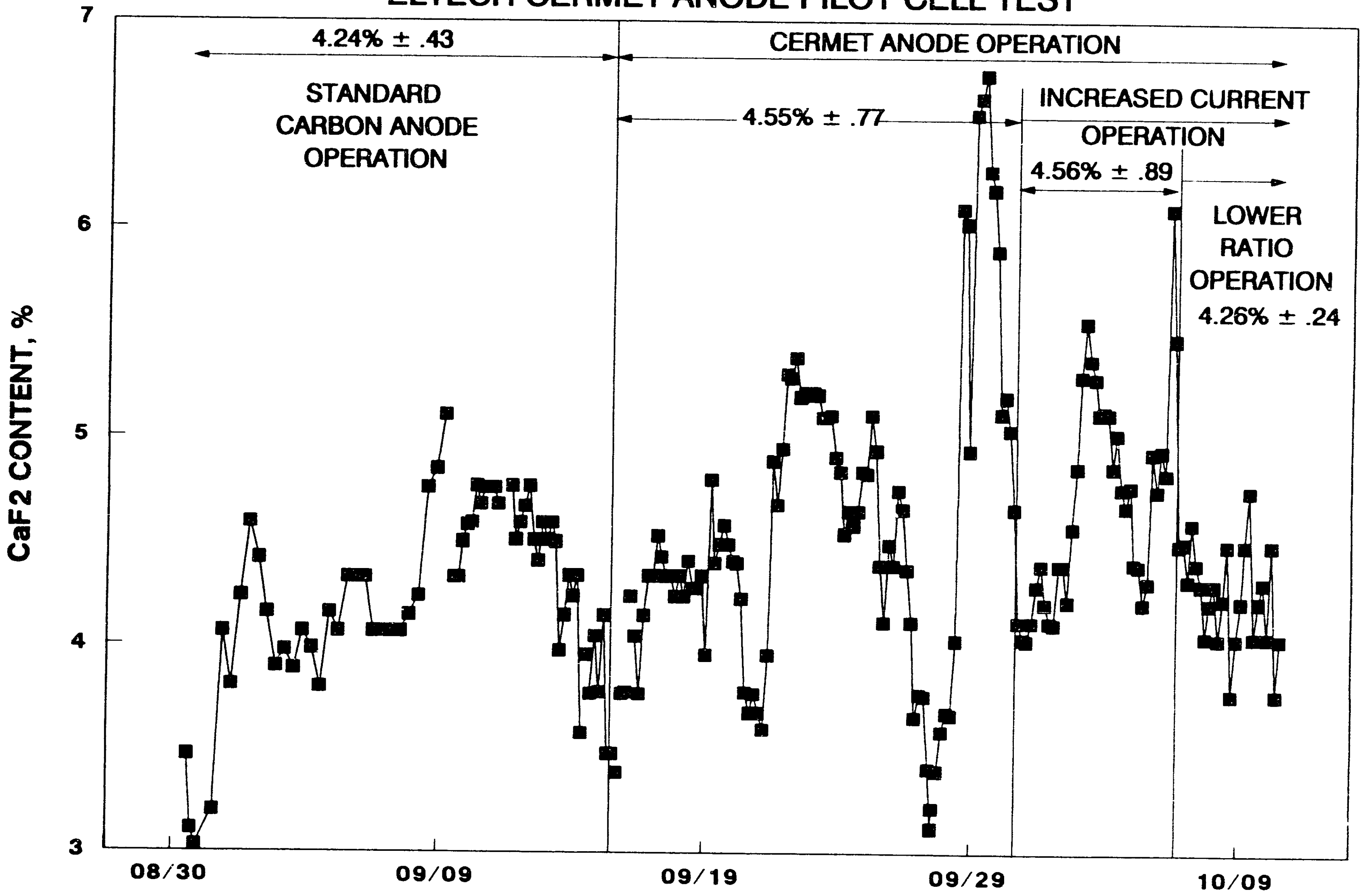

Figure 17

BATH TEMPERATURE VERSUS TIME

ELTECH CERMET ANODE PILOT CELL TEST

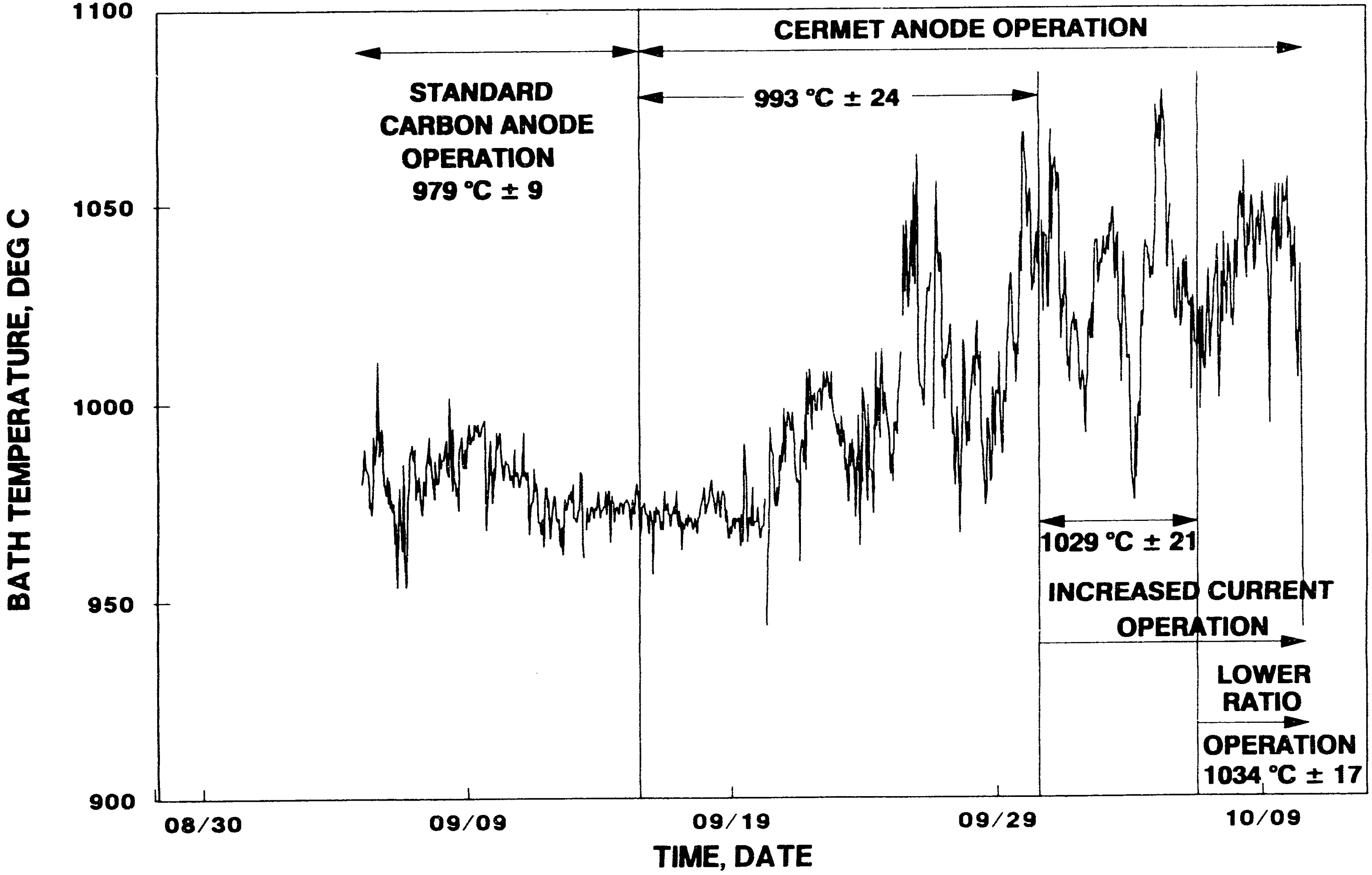

Figure 18

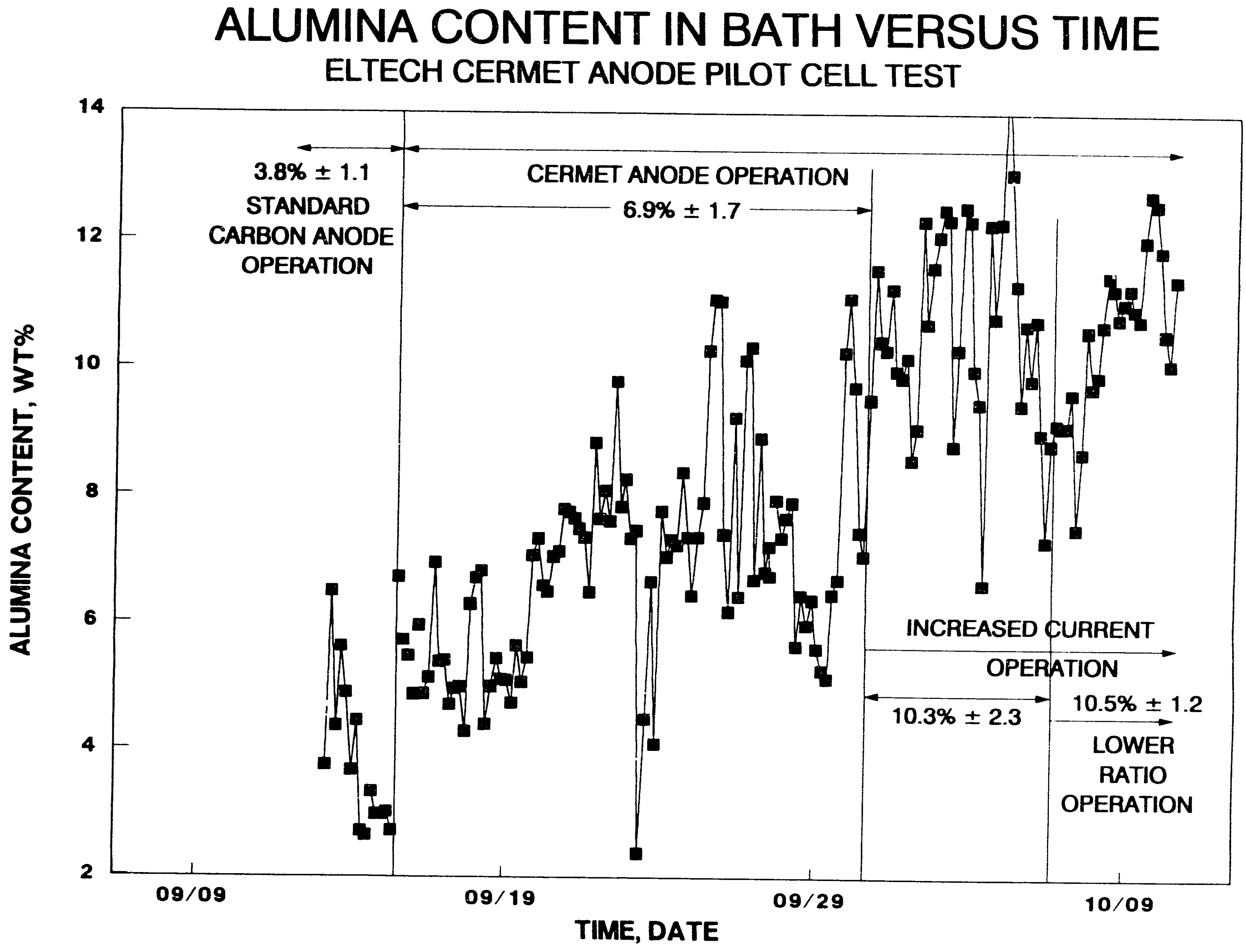
ALUMINA CONTENT IN BATH VERSUS TIME
ELTECH CERMET ANODE PILOT CELL TEST

Figure 19

ALUMINA SATURATION VERSUS TIME
ELTECH CERMET ANODE PILOT CELL TEST

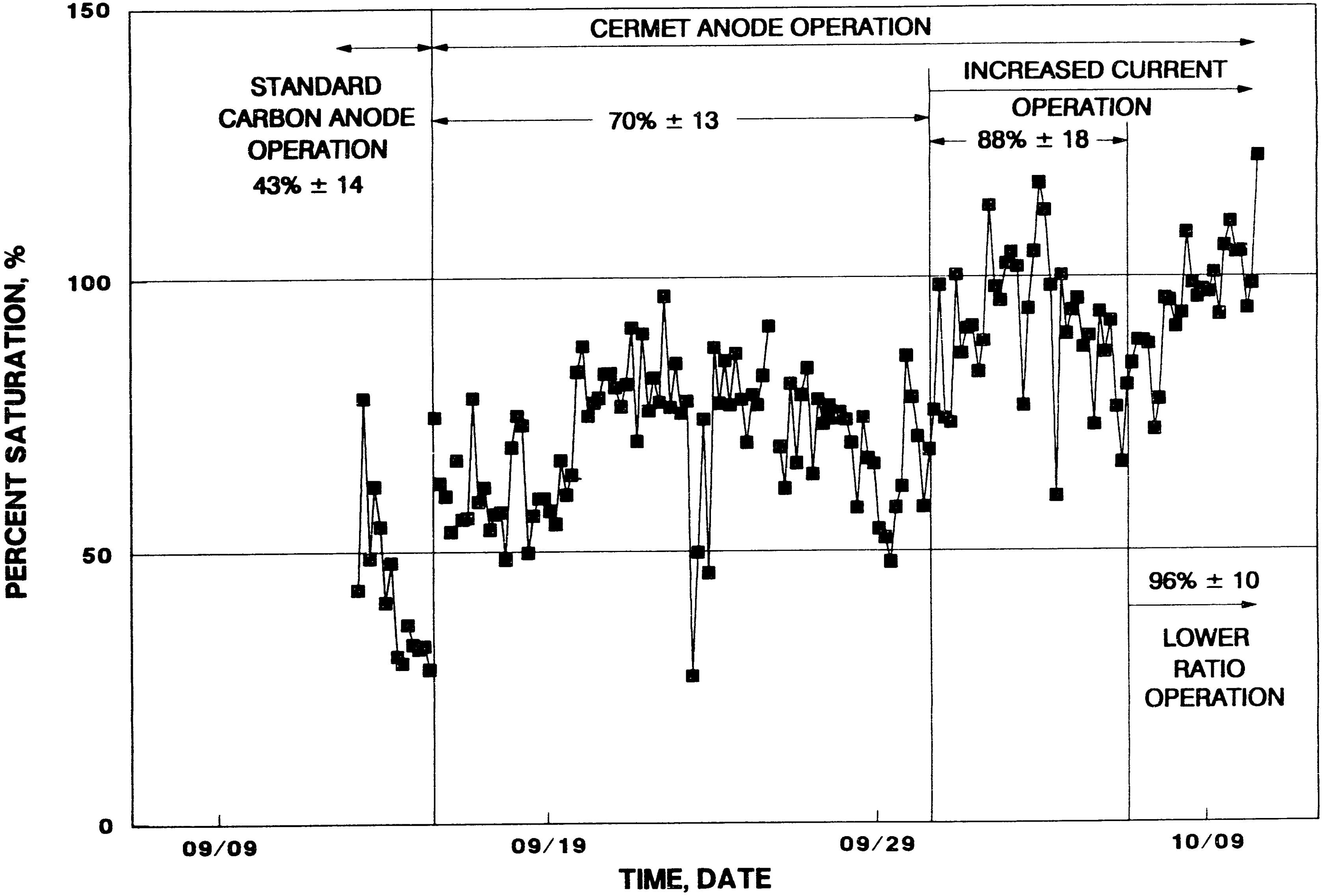

Figure 20

EFFECTS OF TEMPERATURE ON ALUMINA SATURATION
1.3 RATIO, 5% CAF2, 7.6% ALUMINA

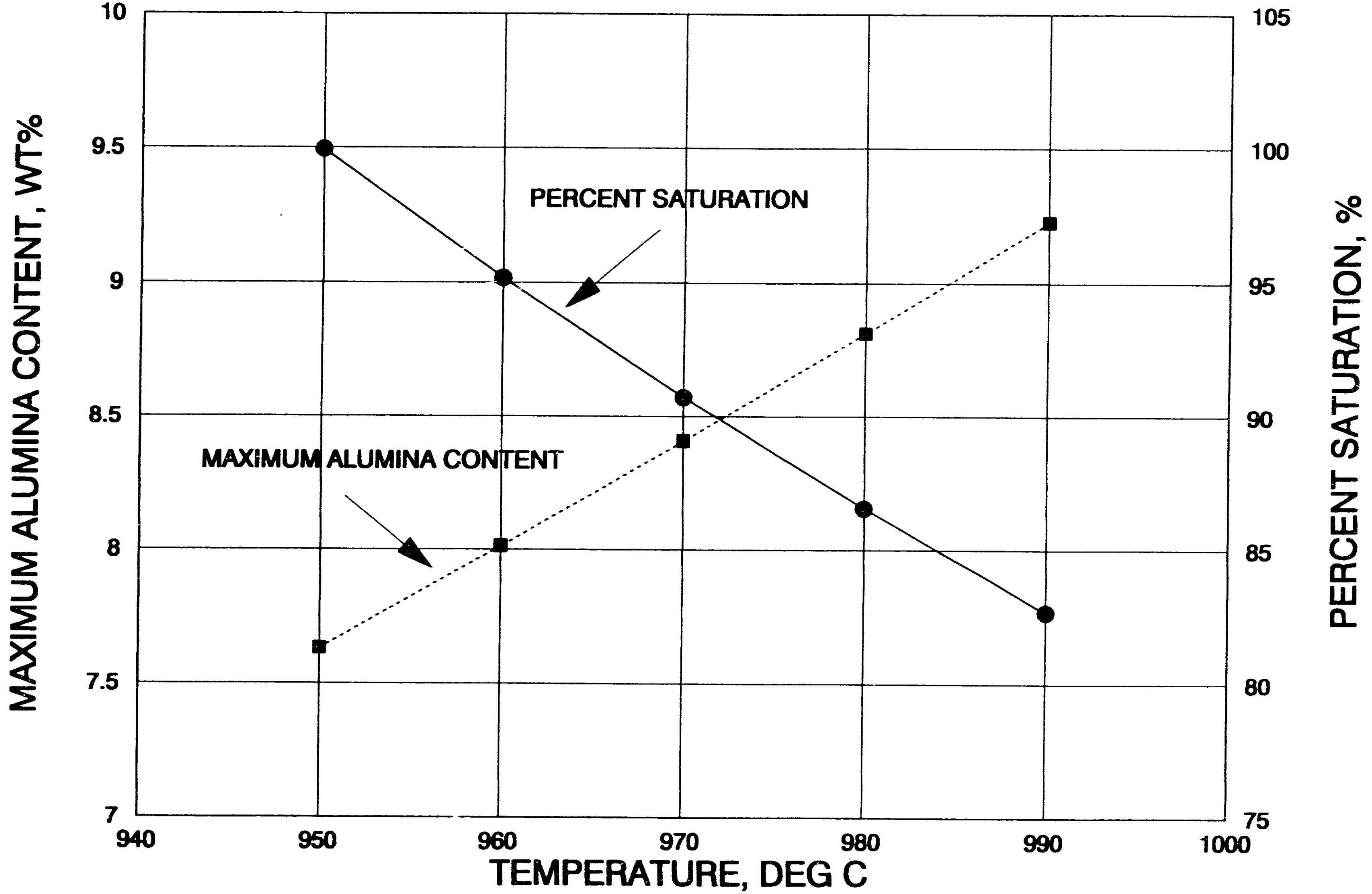

Figure 21

saturation and experiences an upset condition resulting in a 20-30°C drop in bath temperature.

Average operating parameters determined for the various phases of the test are presented below.

Date	Sept 1-15	Sept 15-30	Sept 30-Oct 6	Oct 6-10
Current	Carbon anode	Max 90 amp	Max 115 amp	Max 115 amp
Ratio	1.40	1.44	1.52	1.16
CaF_2	4.24%	4.55%	4.56%	4.26%
CeF_3	-----	0.47%	0.50%	0.49%
Temp.	979°C	993°C	1029°C	1034°C
Al_2O_3	3.8 wt%	6.9 wt%	10.3 wt%	10.5 wt%
% Sat.	43%	70%	88%	96%

2. Liquid Level Control

An initial operational target was to maintain the anodes' immersion in the bath at 2-3 inches, and to minimize any movement of the anodes. Frequent dipping of metal in small increments (5-20 lb) from the cell and occasional dipping of the bath was required to maintain the anodes at the immersion target. Figure 22 shows the anode immersion levels throughout the run. The initial coating of the anodes on September 15 was done with a high cermet anode immersion level (3.5 inch), with the levels during the remaining operation generally remaining below this level. On September 26, when anodes in positions A, B, and C were replaced, they were set at 1 inch less immersion than D, E, and F. All values plotted represent the levels of D through F.

Throughout the operation, the bath level dropped from an initial level of 7-9 inch to 3-5 inch as shown in Figure 23. This change was a result of reduced available cathode cavity volume due to muck build-up on the bottom of the cell. The resulting anode-cathode distances are shown in Figure 2 The anode-cathode distance was reduced from the initial level of 5-6 inch to that of 1 inch as a result of the reduction in bath level.

Aluminum metal inventory was measured on two separate occasions to determine metal production rates. The results of metal dilution analysis using manganese were as follows:

September 23, 8:00 a.m.	208 lb aluminum
October 10, 8:00 a.m.	199 lb aluminum

Based on these aluminum inventory values and the weighed aluminum metal tapped during this period, an average aluminum metal production rate of 38.2 lb/day was calculated. Figure 25 shows the predicted aluminum metal inventory based on this rate with the metal tapped being included. This plot indicates the aluminum inventory was maintained between 150 and 250 lb.

ANODE IMMERSION VERSUS TIME

ELTECH CERMET ANODE PILOT CELL TEST

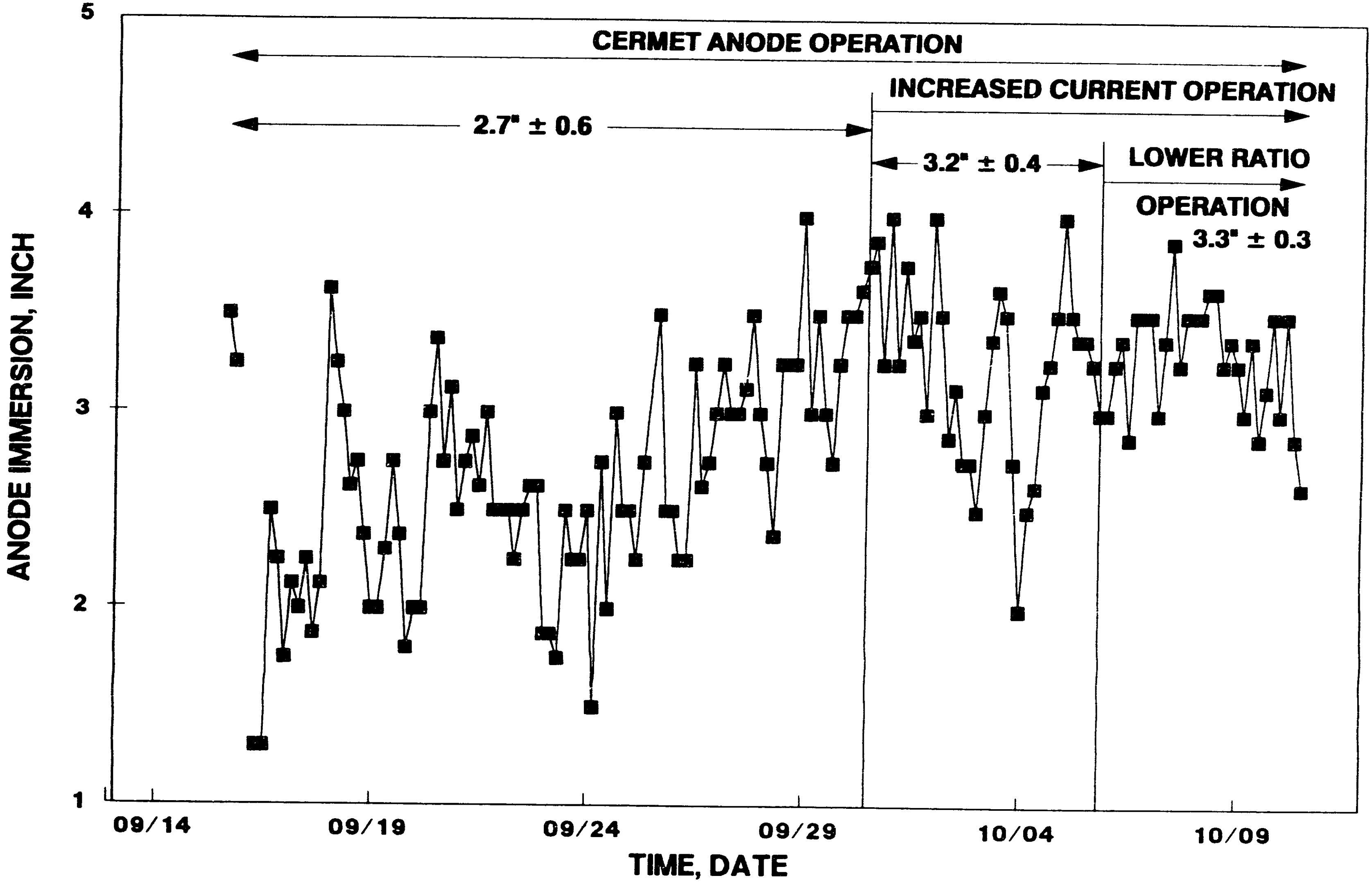

Figure 22

BATH LEVEL VERSUS TIME
ELTECH CERMET ANODE PILOT CELL TEST

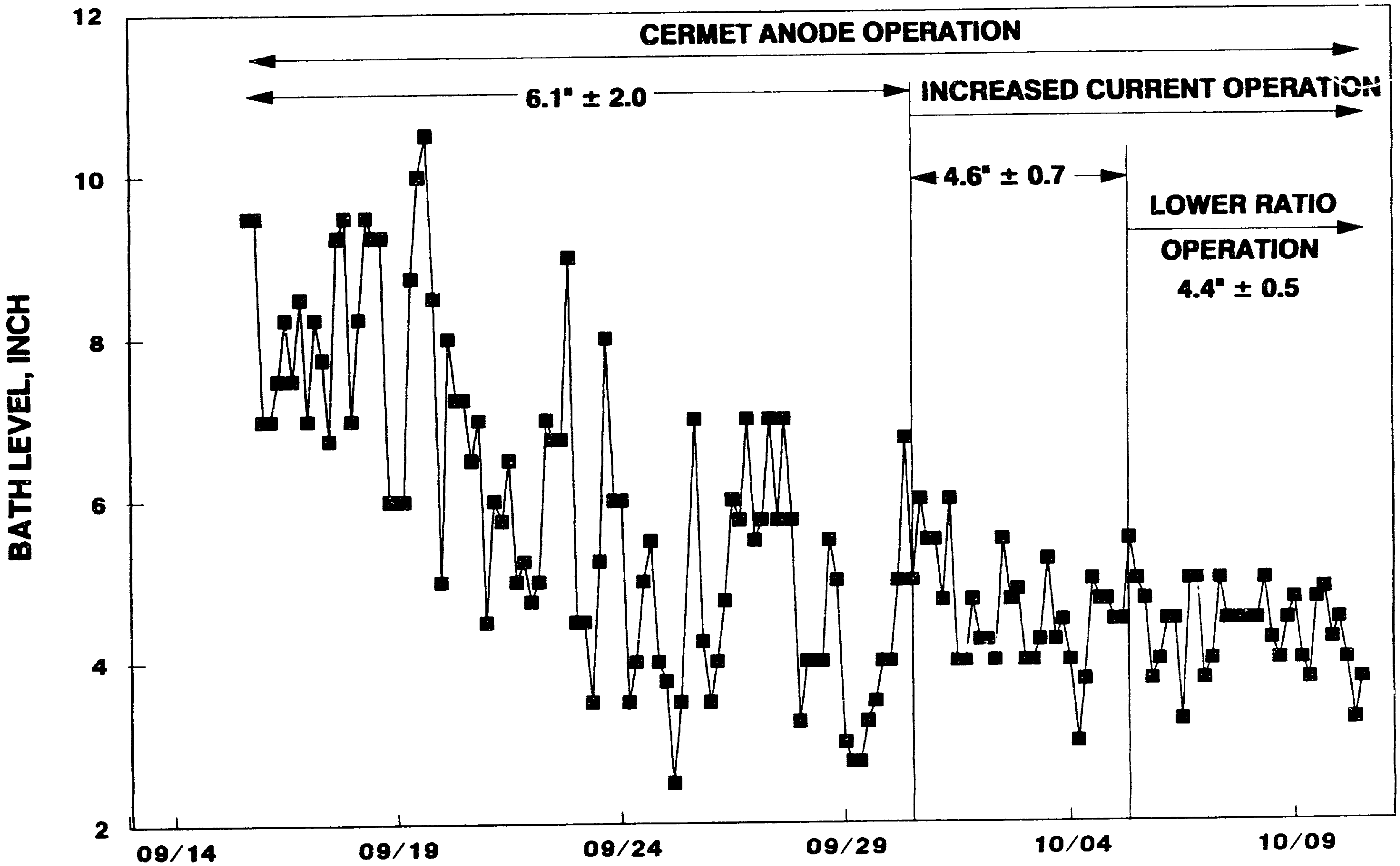

TIME, DATE
Figure 23

ANODE-CATHODE DISTANCE VERSUS TIME

ELTECH CERMET ANODE PILOT CELL TEST

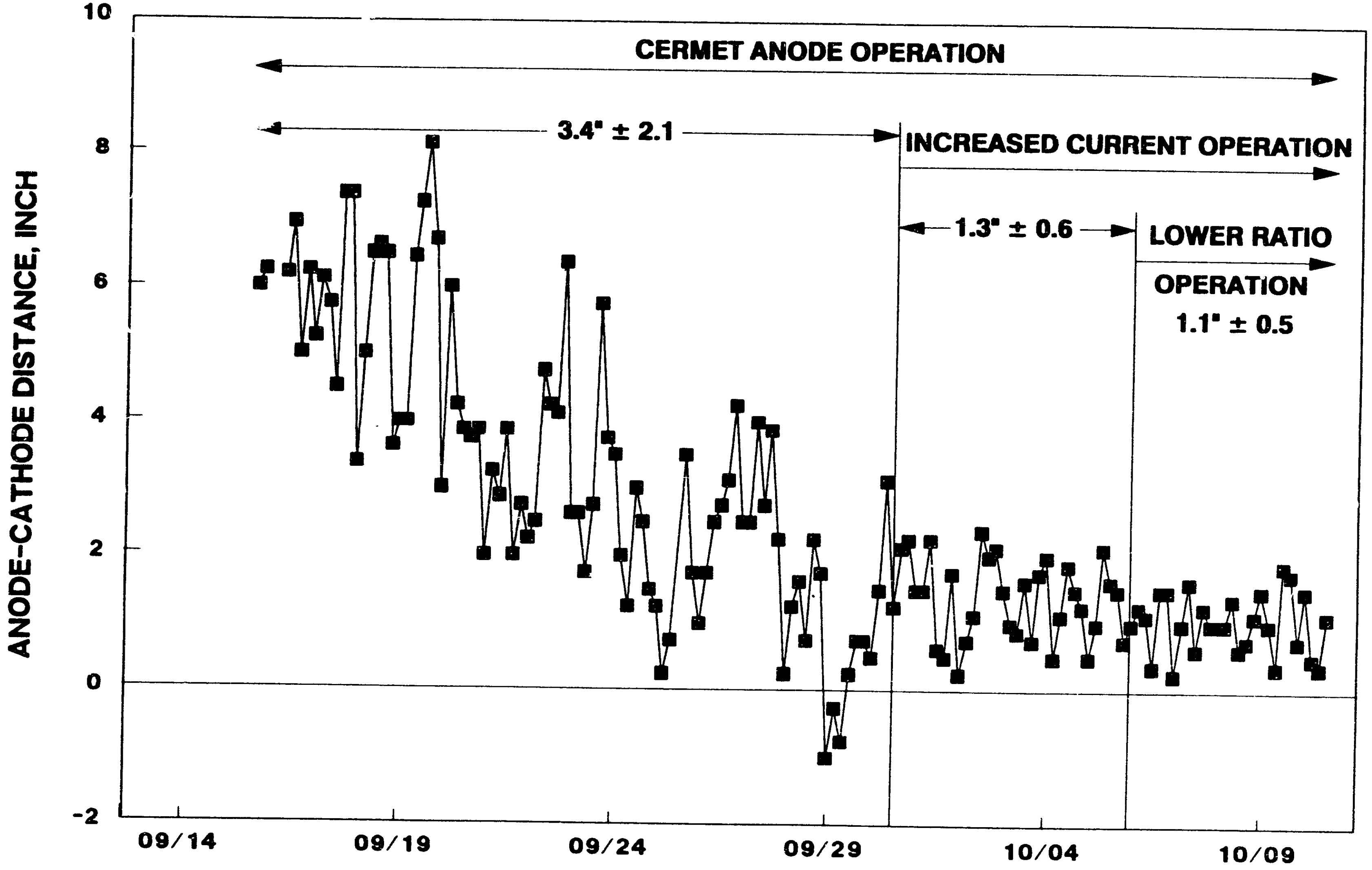

Figure 24

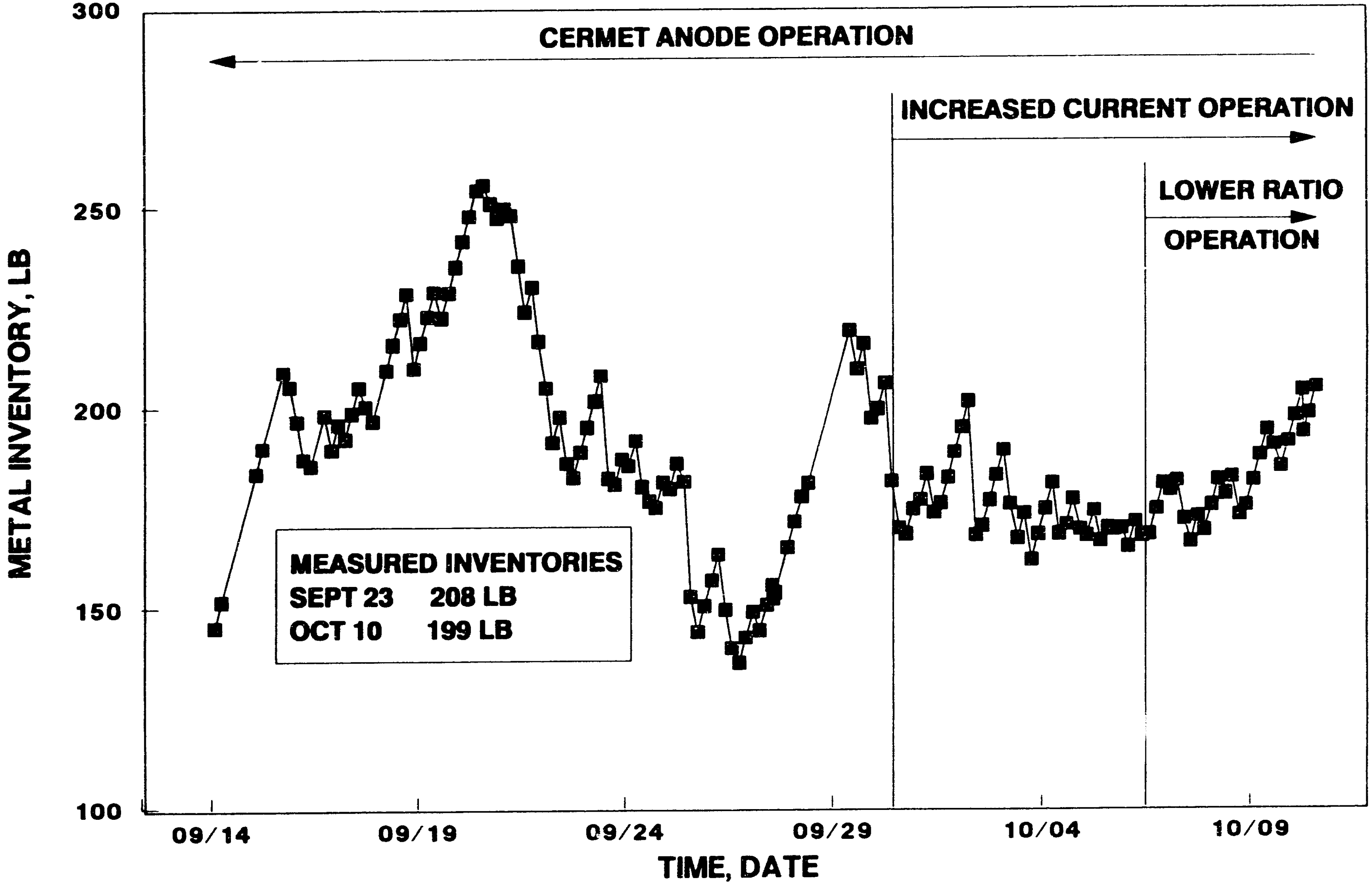

METAL INVENTORY VERSUS TIME

ELTECH CERMET ANODE PILOT CELL TEST

Figure 25

3. Anode Current Distribution

Nine cermet anodes were used during the pilot cell operation. The anodes were identified as 1 through 9. Table I summarizes the life of each of the anodes and Figures 26 - 31 show graphically the current carried by the anodes according to cell position. Anodes 4-6, located in positions D, E, and F, remained in operation for the entire test, 614 hours. Only anodes 1 (position A) and 2 (position B) were removed early due to breakage. Every effort was made to minimize the movement and disturbances to the anodes during the reduction cell operation. This probably contributed to the reduced breakage of the anodes as compared with that experienced during the previous PNL testing as well as the use of improved stem material and ceramic protectors.

The electrical current distribution among the six cermet anodes varied throughout the cell operation as shown in Figure 32. Generally, the current distribution was better than that experienced in the previous PNL testing. This can be attributed to operating with a narrower anode-cathode distance which lessened the effects of the adjacent carbon anode and sidewall conduction. As the cell operation continued, it can be seen that the current conducted by the anodes in positions D, E, and F was reduced while the current conducted by A, B, and C increased correspondingly. It is believed this was due to muck building under the cermet anodes, minimizing any metal inventory under them, such that the current path was through the bath to metal pooled under the carbon anode. This resulted in an extremely resistive path for those cermet anodes furthest away from the carbon anode.

4. Voltage Distribution

The voltage of the module of six cermet anodes varied considerably throughout the run as shown in Figure 33. This variation was due to a number of variables including cell condition (muck formation and metal level) and carbon anode condition (voltage and current). The average voltage of the cermet anodes was 6.49 volt with a total current to the anode cluster of 0.32 kA.

The cathode drop (voltage from the metal pad to negative metering point) of the cell increased from an initial value of 0.6 volt to about 1.5 volt, and then decreased to 0.8 volt after increasing of cermet anode current density shown in Figure 34. The high cathode drops were an indication of the extreme mucking conditions in the cell. Extremely high cathode drops and cermet anode voltages also existed during the period in which only the cermet anodes in positions D, E, and F were operating.

Anode drops were not routinely measured on the cermet anodes in an effort to minimize any possibility of breaking the anodes. Drops were measured on October 10, prior to shutdown, using a tantalum wire encased in a quartz tube. These results indicated the following drops:

Anode	A	B	C	D	E	F
Current, amp	113	104	80	17	20	49
Drop to top of stem, v	0.78	0.53	0.23	0.10	0.06	0.31
Drop to top of anode, v	1.77	1.85				
Drop to bottom of anode, v	2.70	2.52				

Due to the nature of the current paths, it is impossible to determine a more exact breakdown of the cermet anodes voltages. The changing of the current distributions within this run, as

Table I

ANODE SUMMARY

Anode	Cell Position	Operation	Comments
1	A	9/15-23 213 hr	Section of anode broke, removed.
2	B	9/14 1 hr	Cracked down center of anode at start-up.
3	C	9/15-26 275 hr	Removed on schedule.
4	D	9/15-10/10 614 hr	End of test.
5	E	9/15-10/10 614 hr	End of test.
6	F	9/15-10/10 614 hr	End of test.
7	A	9/27-10/10 312 hr	End of test.
8	B	9/27-10/10 312 hr	End of test.
9	C	9/27-10/10 312 hr	End of test.

CURRENT VERSUS TIME

POSITION A

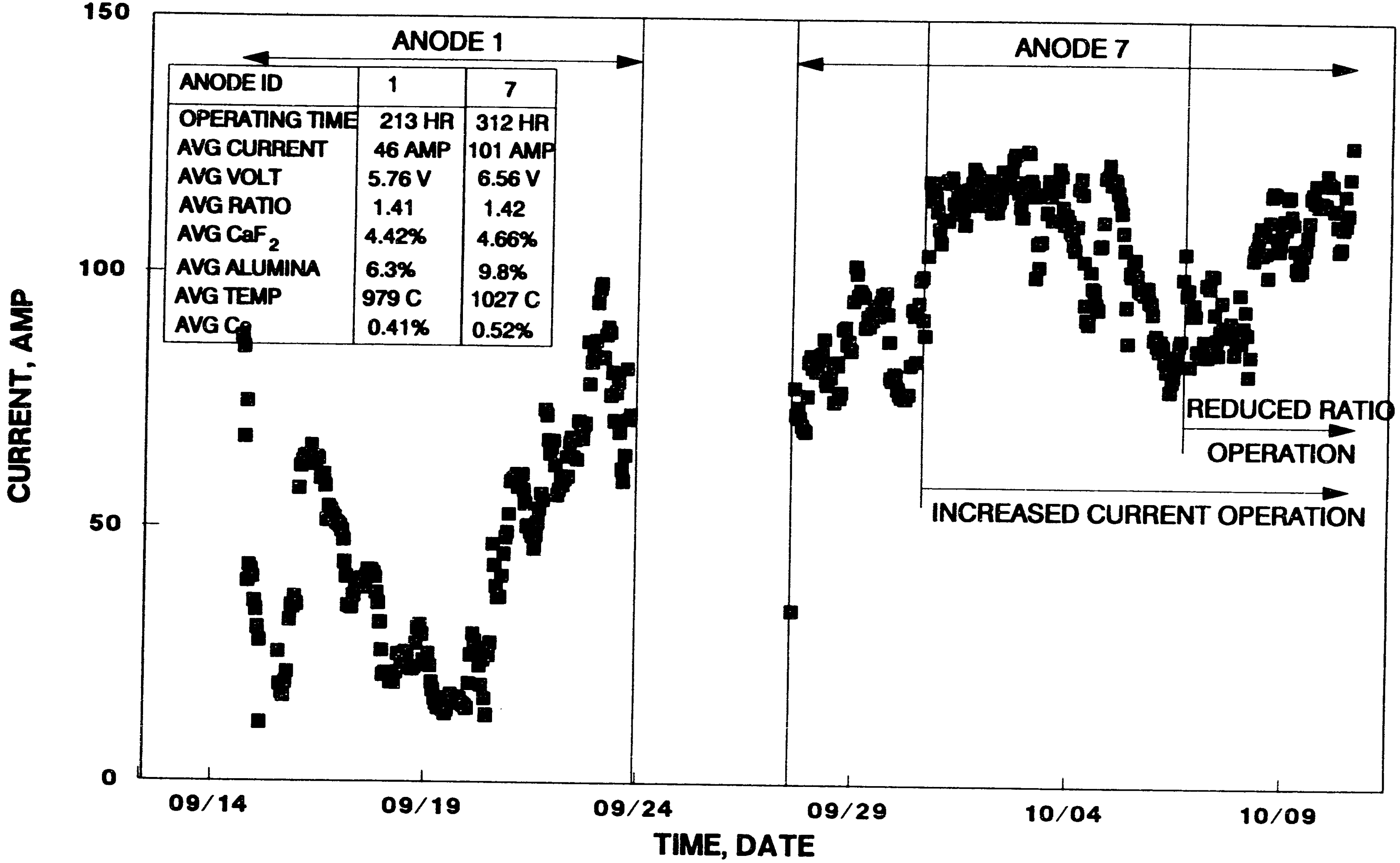

ANODE ID	1	7
OPERATING TIME	213 HR	312 HR
AVG CURRENT	46 AMP	101 AMP
AVG VOLT	5.76 V	6.56 V
AVG RATIO	1.41	1.42
AVG CaF_2	4.42%	4.66%
AVG ALUMINA	6.3%	9.8%
AVG TEMP	979 C	1027 C
AVG Ce	0.41%	0.52%

Figure 26

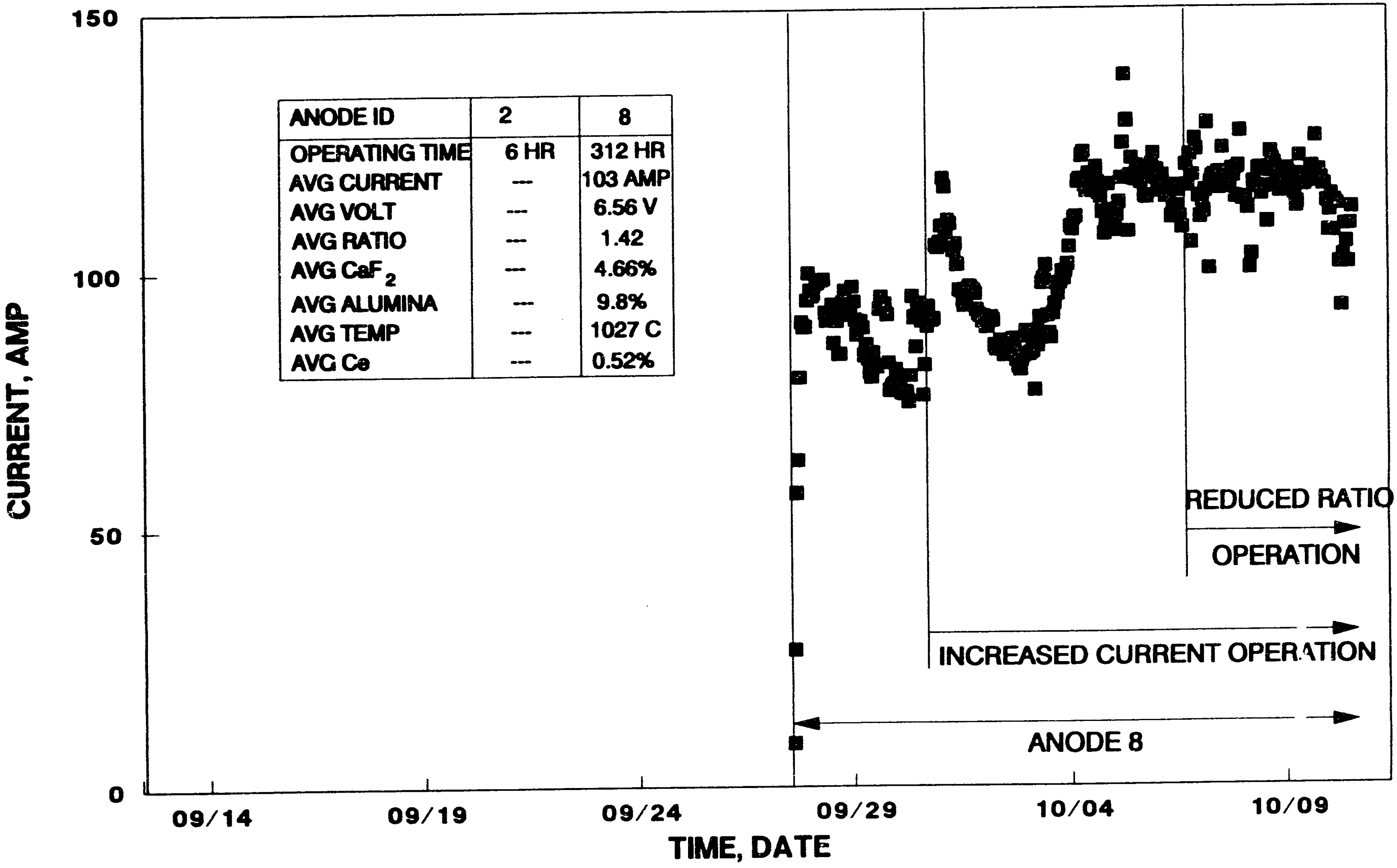

CURRENT VERSUS TIME

POSITION B

ANODE ID	2	8
OPERATING TIME	6 HR	312 HR
AVG CURRENT	---	103 AMP
AVG VOLT	---	6.56 V
AVG RATIO	---	1.42
AVG CaF_2	---	4.66%
AVG ALUMINA	---	9.8%
AVG TEMP	---	1027 C
AVG Ca	---	0.52%

Figure 27

CURRENT VERSUS TIME

POSITION C

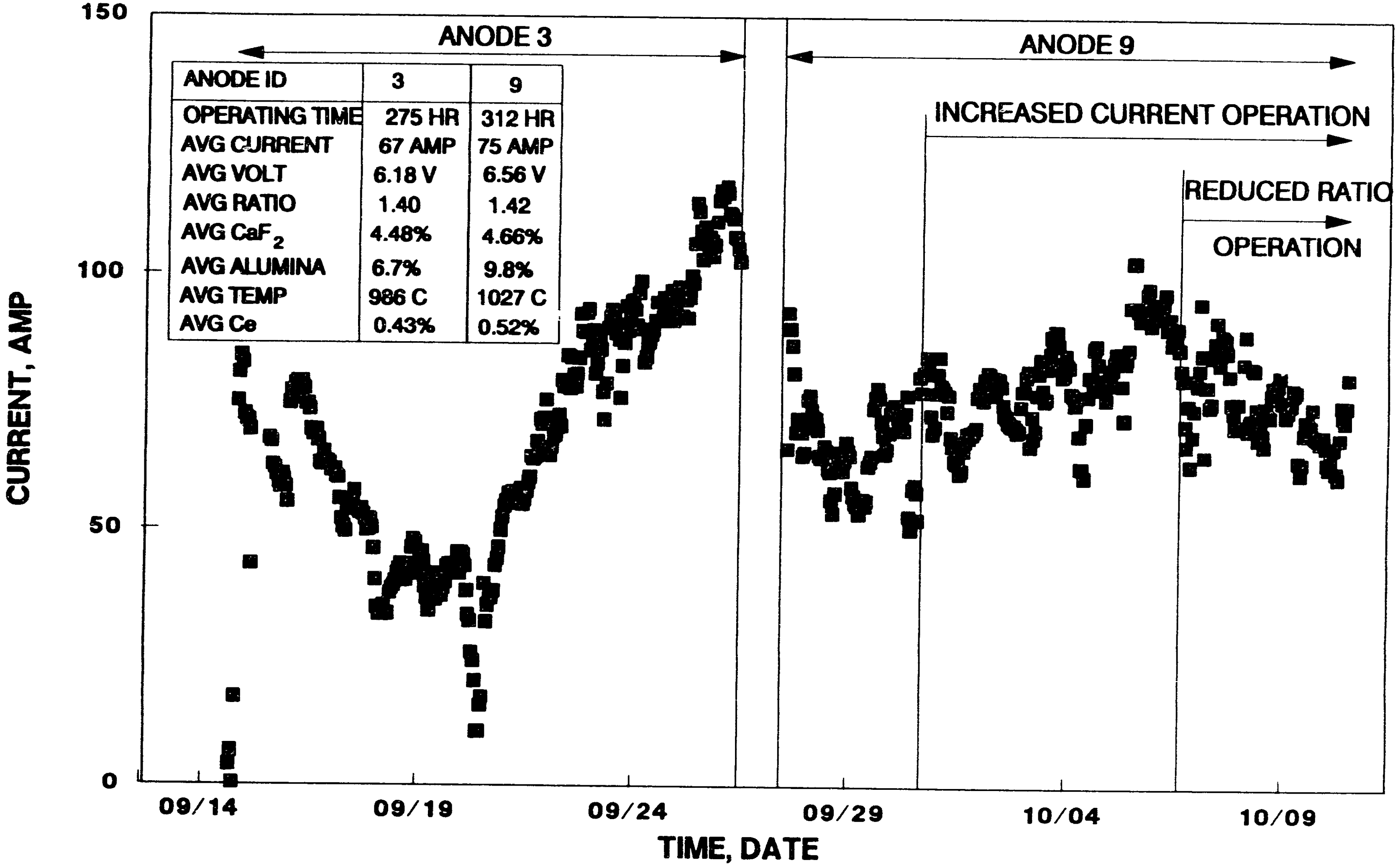

ANODE ID	3	9
OPERATING TIME	275 HR	312 HR
AVG CURRENT	67 AMP	75 AMP
AVG VOLT	6.18 V	6.56 V
AVG RATIO	1.40	1.42
AVG CaF_2	4.48%	4.66%
AVG ALUMINA	6.7%	9.8%
AVG TEMP	986 C	1027 C
AVG Ce	0.43%	0.52%

Figure 28

CURRENT VERSUS TIME

POSITION D

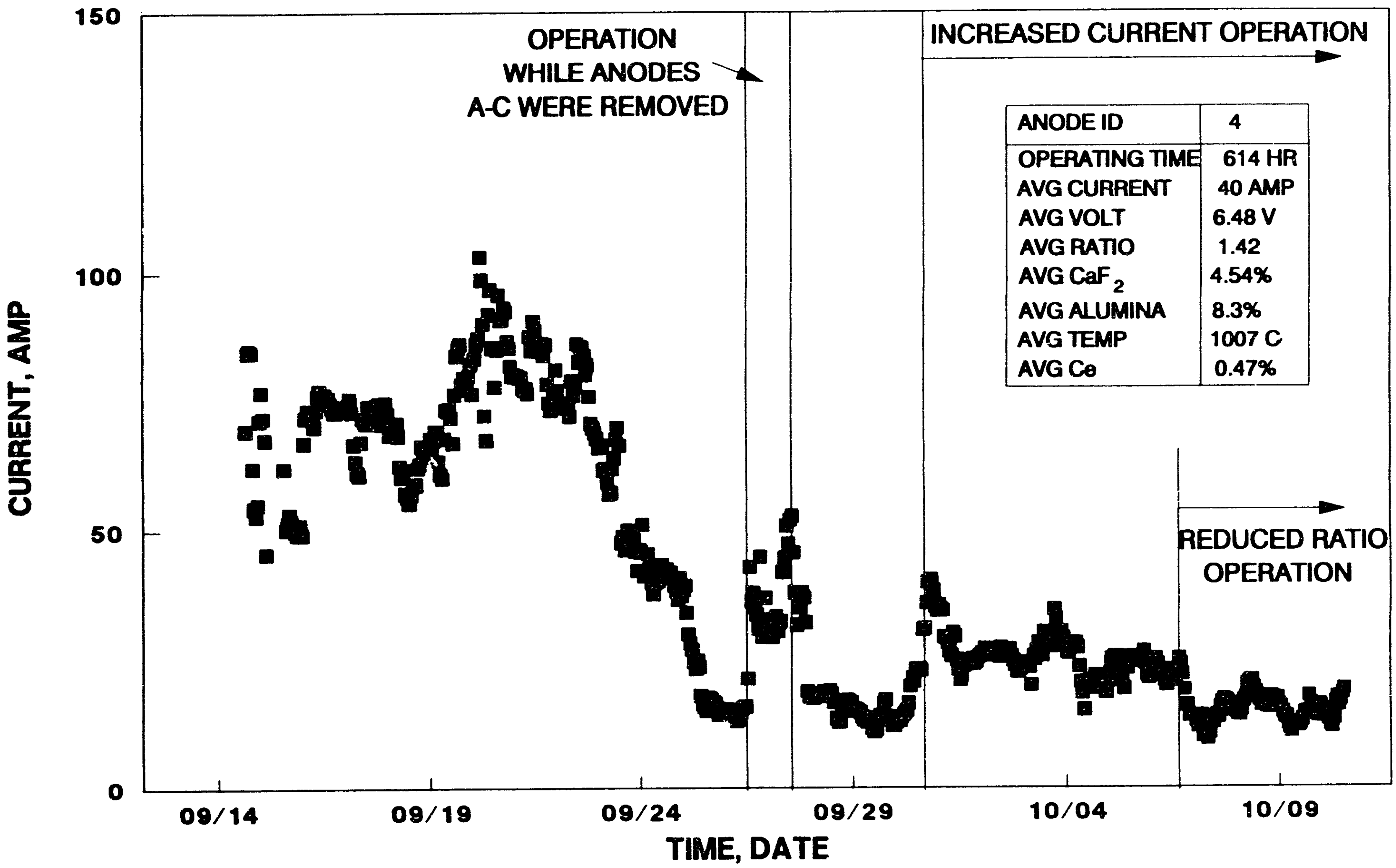

Figure 29

CURRENT VERSUS TIME

POSITION E

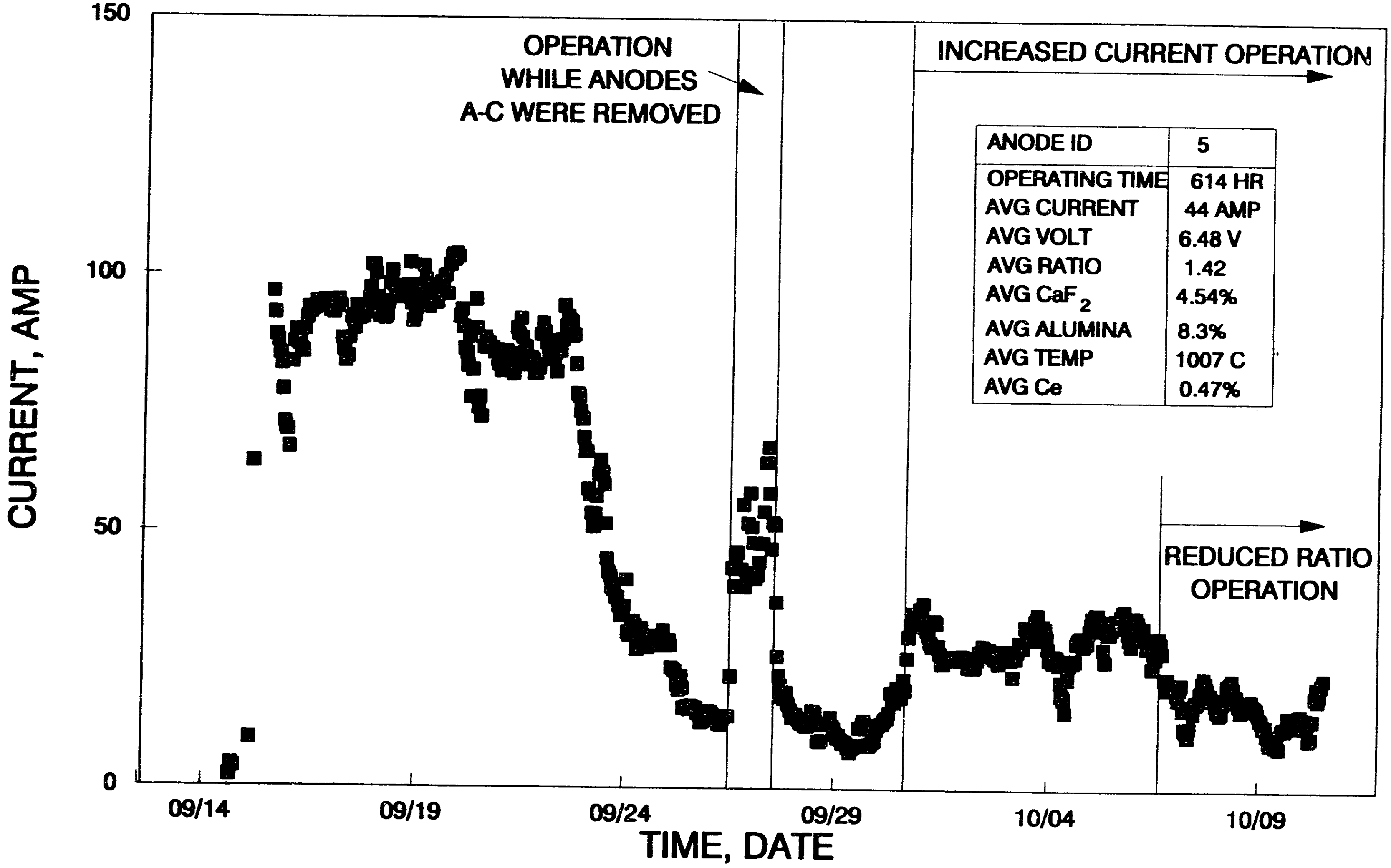

Figure 30

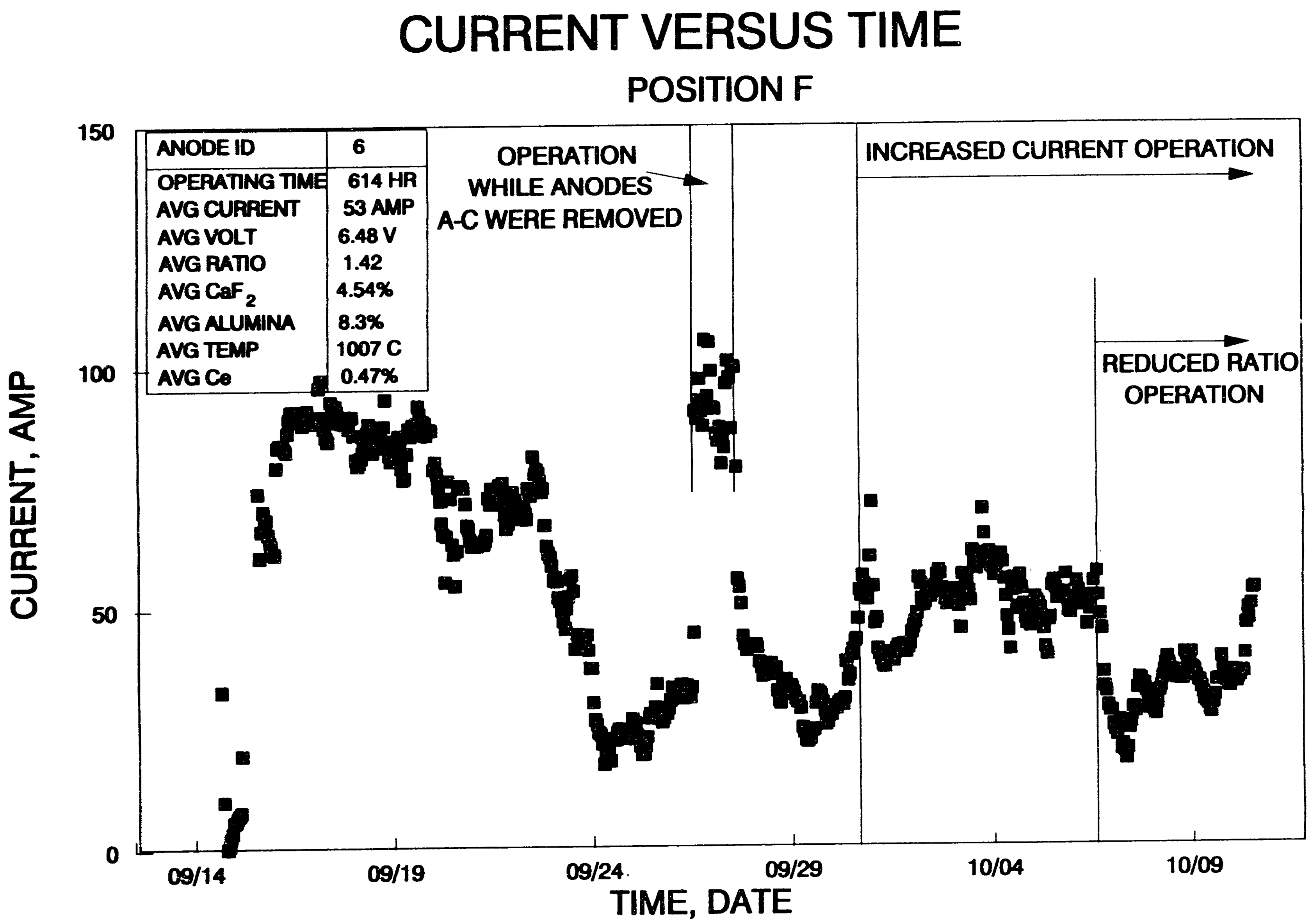
CURRENT VERSUS TIME
POSITION F
ANODE ID 6
OPERATING TIME 614 HR
AVG CURRENT 53 AMP
AVG VOLT 6.48 V
AVG RATIO 1.42
AVG CaF2 4.54%
AVG ALUMINA 8.3%
AVG TEMP 1007 C
AVG Ce 0.47%
OPERATION WHILE ANODES A-C WERE REMOVED
INCREASED CURRENT OPERATION
REDUCED RATIO OPERATION
150
100
50
0
CURRENT, AMP
09/14
09/19
09/24
09/29
10/04
10/09
TIME, DATE

Figure 31

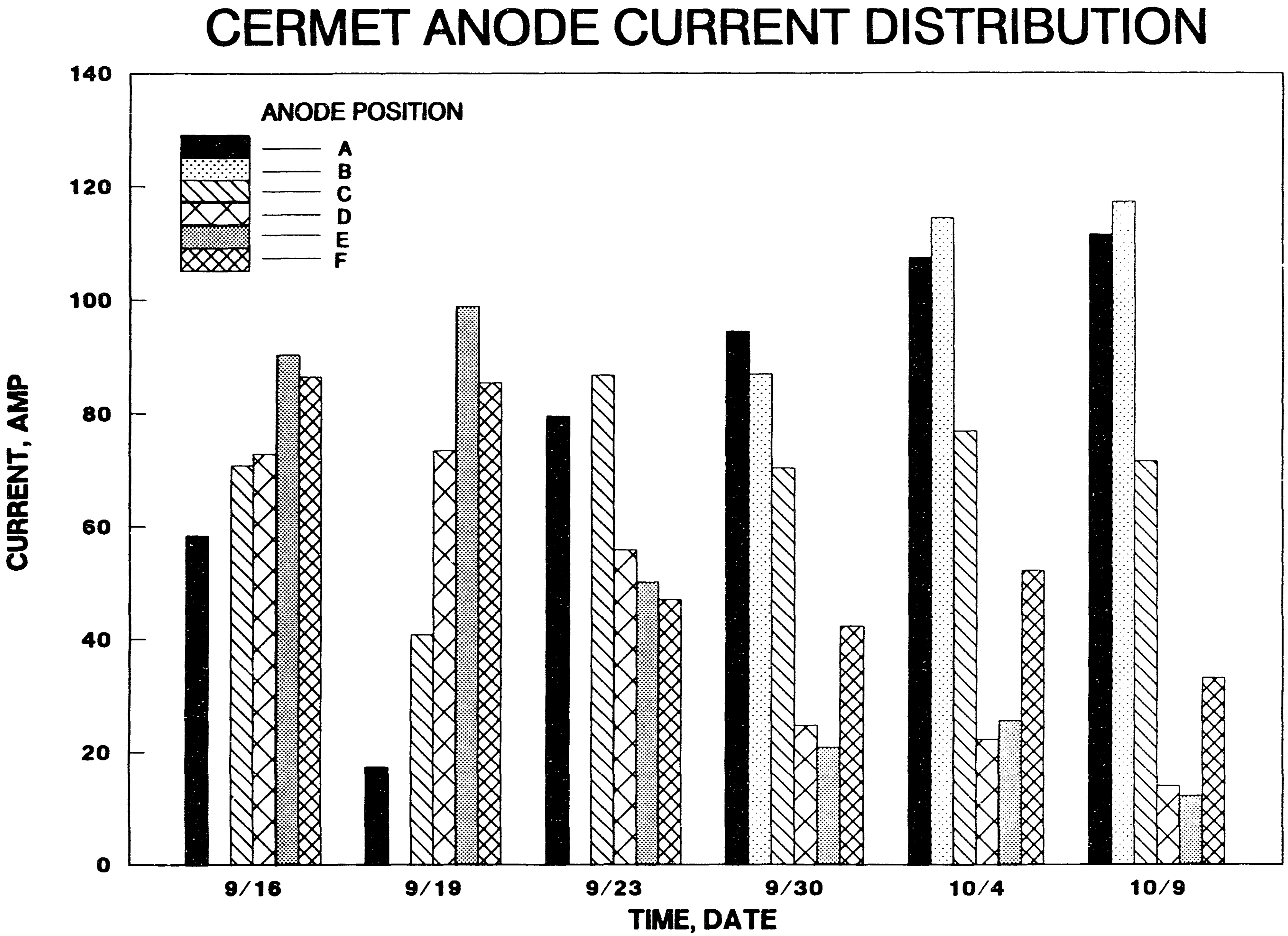
CERMET ANODE CURRENT DISTRIBUTION
ANODE POSITION
A
B
C
D
E
F
CURRENT, AMP
140
120
100
80
60
40
20
0
9/16
9/19
9/23
9/30
10/4
10/9
TIME, DATE

Figure 32

CERMET ANODES - CELL VOLTAGE VERSUS TIME

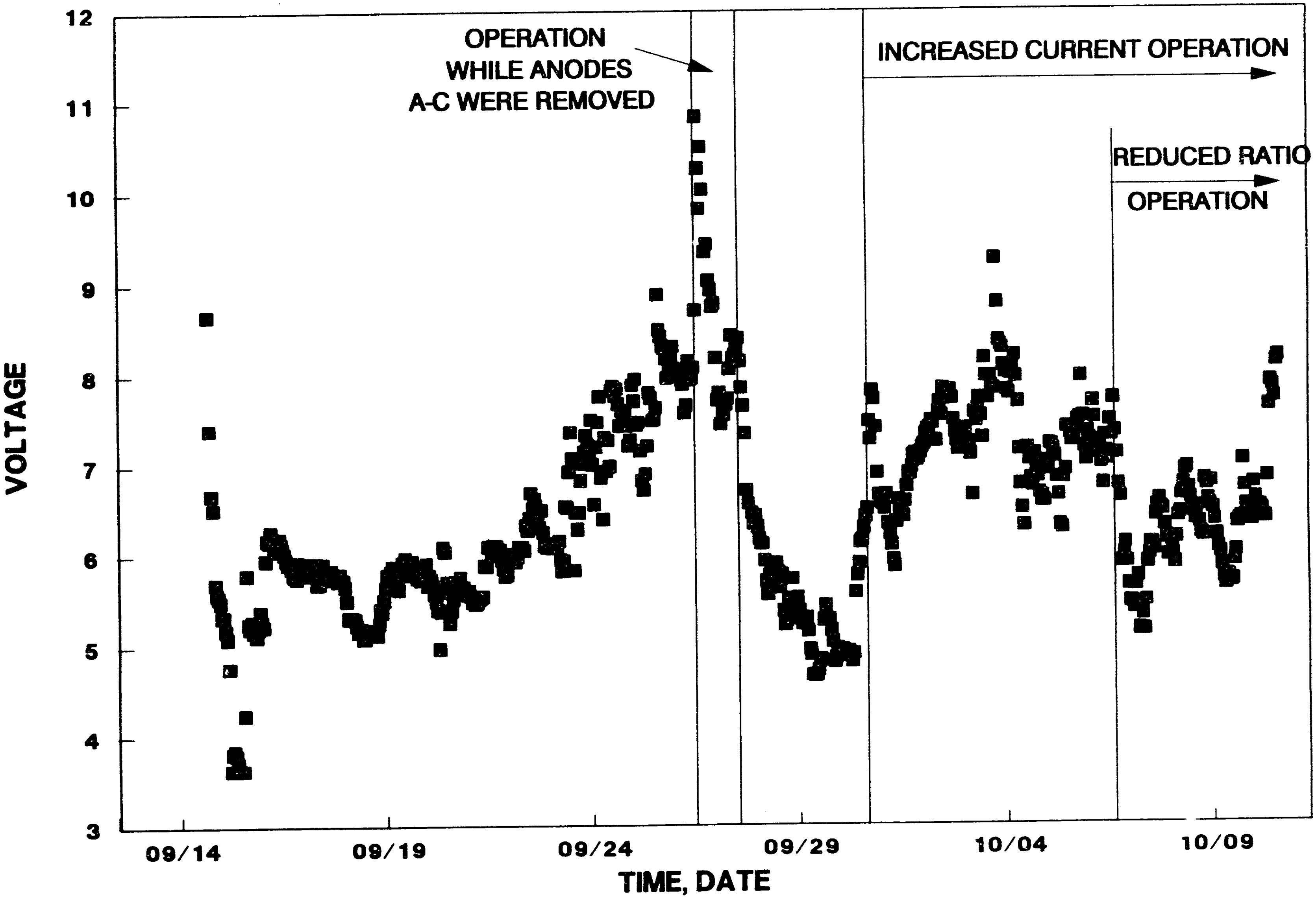

Figure 33

CATHODE DROP VERSUS TIME

ELTECH CERMET ANODE PILOT CELL TEST

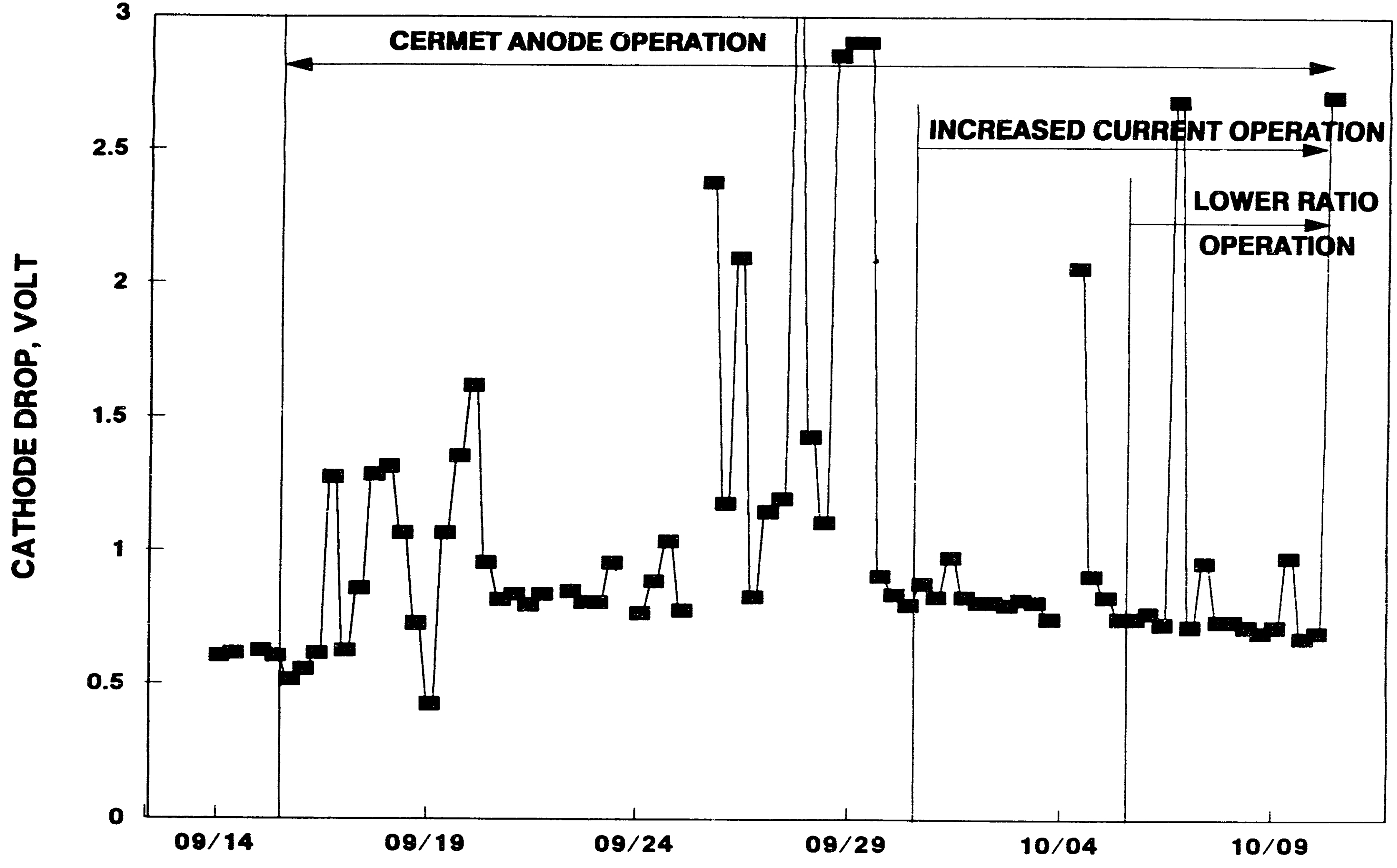

Figure 34

well as in comparison to the previous run with the PNL cermet anodes, makes it impossible to reliably predict the voltage penalty incurred by the "Cerox" coating.

5. Material Problems

The major problems experienced with the cermet anodes during the previous PNL test included (a) anode stems breaking and (b) the cermet anodes cracking and breaking. These problems were greatly reduced during the ELTECH test period.

(a) Anode Stem Material

As described earlier Inconel 600 was used for the anode stem conductor rod material in the ELTECH test rather than the Nickel 200 used for the PNL test. In addition to the change of material, the 3 inches extending out of the anode were protected by use of an alumina sleeve, filled with an alumina castable refractory. This combination of materials provided a satisfactory stem for the test period. None of the Inconel stems broke during the test. Additional evaluations of the stems will be conducted and reported by ELTECH.

(b) Anode Breakage

Only two cermet anodes were removed prematurely due to cracking or breakage during the total test period. The first was anode No. 2, position B, which was removed shortly after the initial installation on September 14. A crack down the center of the anode was first observed and it was then decided to remove the anode prior to its complete breakage which might cause contamination of the metal pad. Anode No. 2 is shown in Figure 35. The second anode was anode No. 1, position A, which was removed on September 23, after 213 hours of operation. Approximately 1/4 of the anode had broken and fallen to the bottom of the cell. The broken piece, along with the rest of the anode, was then removed from the cell. Anode No. 1 is shown in Figure 36.

All other cermet anodes were removed as scheduled. The six cermet anodes, upon removal at the end of the test period, are shown in Figures 37 and 38. These anodes were all removed together as a unit. As can be seen, numerous cracks did exist in the anodes, but the anodes were removed in one piece. Additional evaluation of each of these anodes will be conducted and reported by ELTECH.

6. "Cerox" Coating Evaluation

Analysis of the coatings formed on the cermet anodes will be performed by ELTECH. Observation of the removed anodes (both small test anode and larger anodes) indicated that they were not uniformly coated. There appeared to be sections with no coating. These sections were facing either the carbon anode or adjacent cermet anodes, thus emphasizing the uneven current distribution on individual anodes. It appears that anodes may be better suited to a "pre-coating" operation in which the anodes are actually coated outside the operating cell, in which uniform current distribution can occur on the anode.

7. Bath and Metal Impurities

The primary indicator of the corrosion rate of the cermet anodes was the rate of increase of nickel, copper, and iron impurity content in the aluminum metal during cell

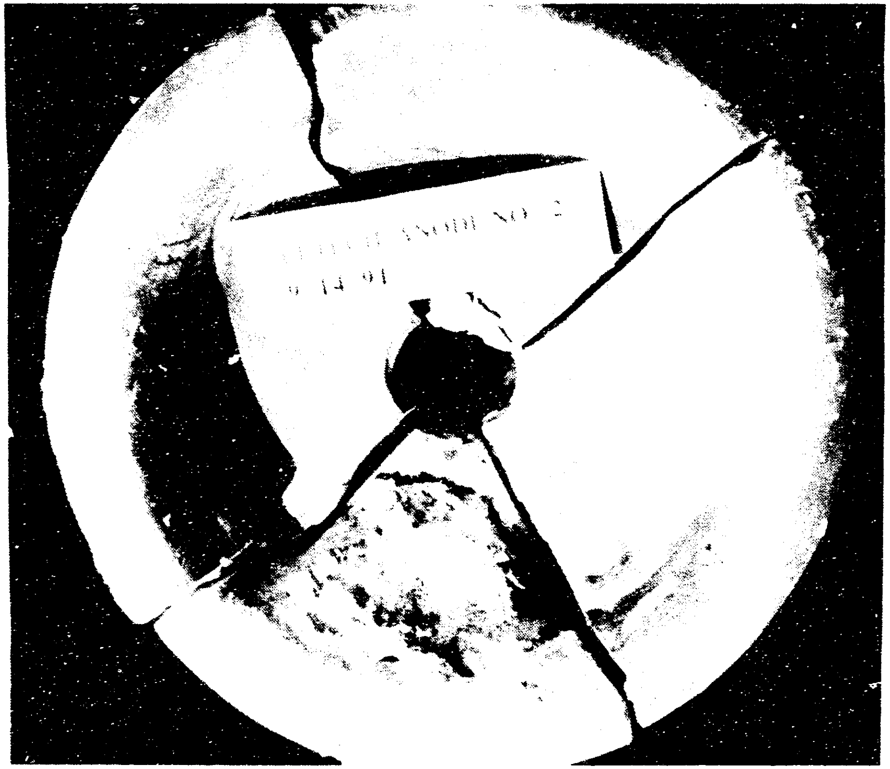

Figure 35. Cermet Anode No.2.
Position B - Sept. 14.

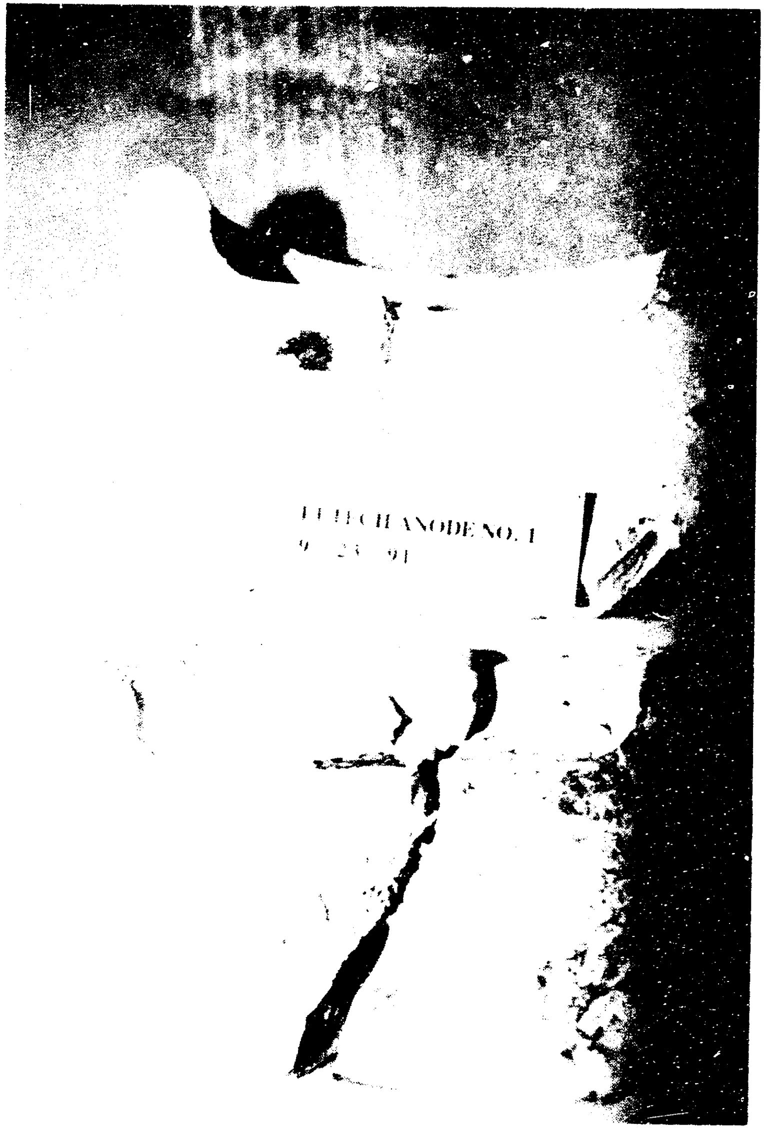

Figure 36. Cermet Anode No.1. Position
A - Sept. 23.

Figure 37. Cermet Anodes upon removal - Oct. 10

Figure 38. Cermet Anodes upon removal - Oct. 10

operation. Metal samples were collected every four hours to track the concentration of these elements. The results from these analyses are presented in Appendix B and Figures 39 - 41. Impurities from other sources were minimized during the operation of the cell (in particular that of copper and nickel). As previously discussed, the impurity levels were allowed to reach equilibrium prior to introducing the cermet anodes into the cell.

The data shows an initial increase in impurity levels with the introduction of the cermet anodes, but then a stabilization of the concentrations. It should be noted that the concentrations were much more sensitive to change than in the previous PNL testing as the cell was operating at a greatly reduced metal inventory (200 lb versus 750 lb). The data shows several spikes in the impurity concentrations which can possibly be attributed to segregation of the metal pad within the cell preventing obtaining representative analysis of the metal. The data does not clearly indicate any significant changes in corrosion rates with the changes in cell operation (increased current and lower ratio).

In an effort to quantify the corrosion rates, a model was constructed estimating the metal impurity concentrations based upon a fixed amount of each component (iron, nickel, and copper) reporting to the metal on a daily basis. This model accounts for the changing metal inventory in the cell, both through production and tapping. Using the following fixed amounts, concentrations were calculated and compared with the actual values as shown in Figures 42 - 44.

Cu	0.075 lb/day
Ni	0.13 lb/day
Fe	0.30 lb/day

As these plots show, the model fits the actual data reasonably well, with the exception of the period from September 24-30. It was during this period that fewer anodes were in the cell (4 anodes through September 27) and then initial operation and recoating of the replacement anodes.

The relative ratio of these impurities in the anodes are (Cu:Ni:Fe) 1:1.98:1.65. The calculated metal losses result in a ratio of 1:1.74:4. It is not surprising that the iron losses appears to be significantly higher than what would be expected from the anode, as frequent dipping of the metal from the cell was done with iron ladles. Based upon the composition of the anode and the rate of copper and nickel losses to the metal pad, the iron losses from the anode should be at the rate of 0.12 lb/day. Based upon these rates, a total loss of material from the cermet anodes (assuming the losses are actually Cu, NiO, and Fe_2O_3) was 0.41 lb/day. This corresponds to a volumetric loss of 31.0 cm^3, based on an anode density of 6 g/cm^3. Applying this loss uniformly from all the anodes, it would indicate a surface loss of 0.1 mm/day. These losses are approximately 1/2 that found during the PNL test, using a similar analysis procedure.

While only a limited number of cermet anodes were observed at MTL, it was noticed that the coating was not uniform on the anodes, with some sections not having any observable coating. The effect of the uncoated sections of the anodes on the corrosion rate is not defined, but it is expected to result in a higher corrosion rate.

The Fe, Ni, and Cu levels were also monitored in the bath throughout the operation. These values are presented in Appendix C and shown graphically in Figures 45 - 47. As shown in these plots, little change in the levels of these impurities existed throughout the run.

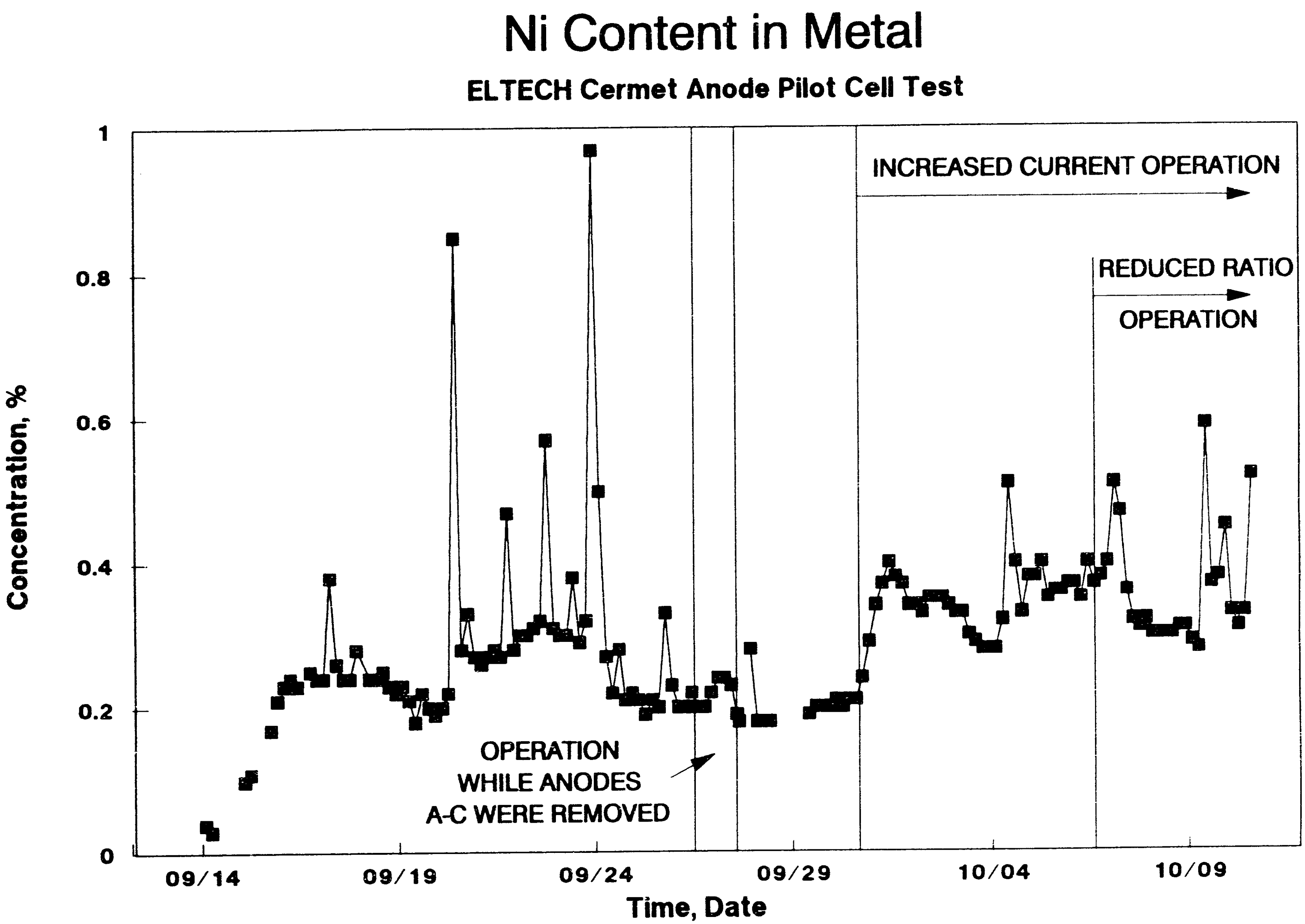
Ni Content in Metal
ELTECH Cermet Anode Pilot Cell Test
Concentration, %
1
0.8
0.6
0.4
0.2
0
09/14
09/19
09/24
09/29
10/04
10/09
Time, Date
INCREASED CURRENT OPERATION
REDUCED RATIO
OPERATION
OPERATION
WHILE ANODES
A-C WERE REMOVED

Figure 39

Cu Content in Metal

ELTECH Cermet Anode Pilot Cell Test

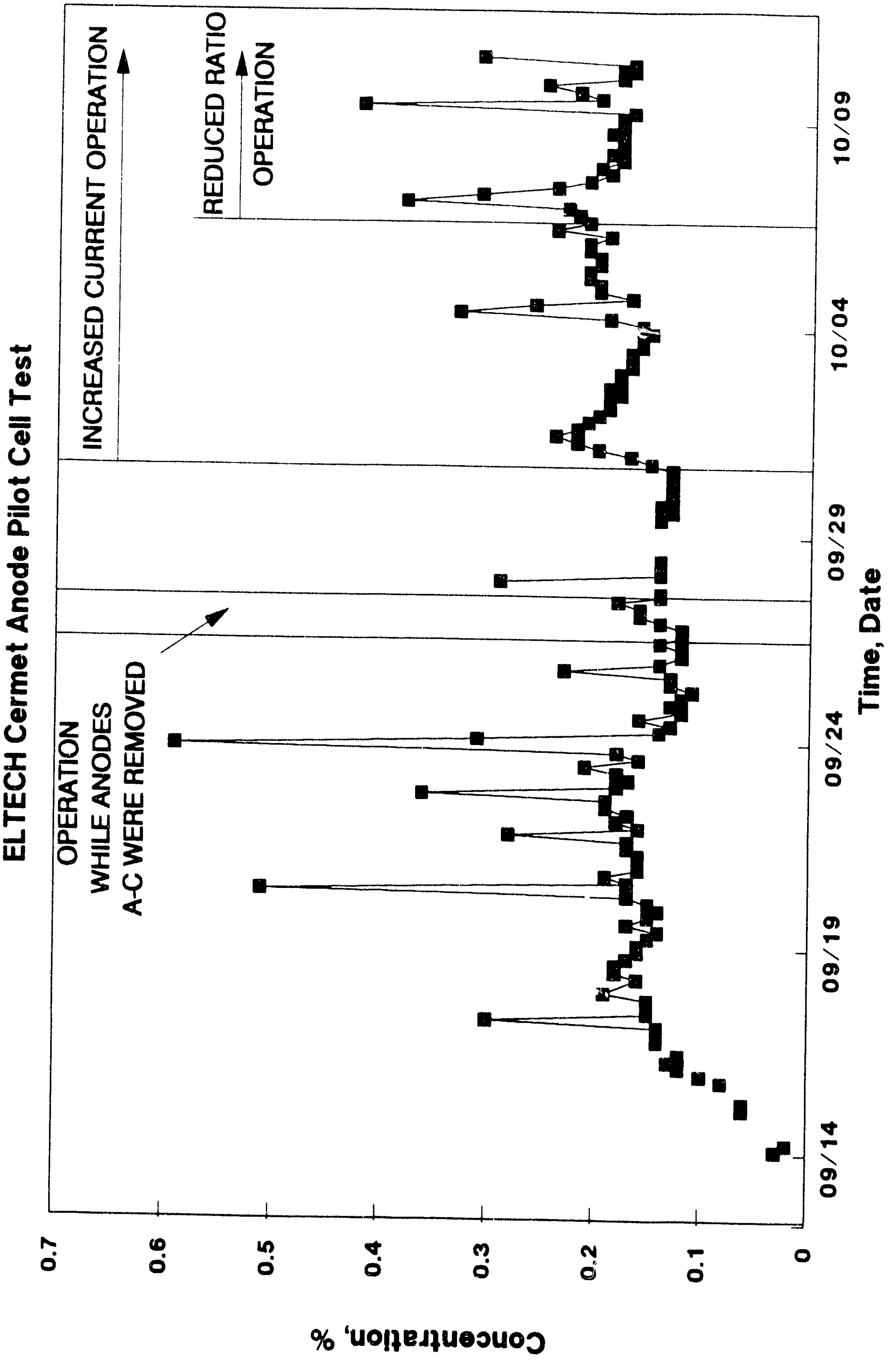

Figure 40

Fe Content in Metal

ELTECH Cermet Anode Pilot Cell Test

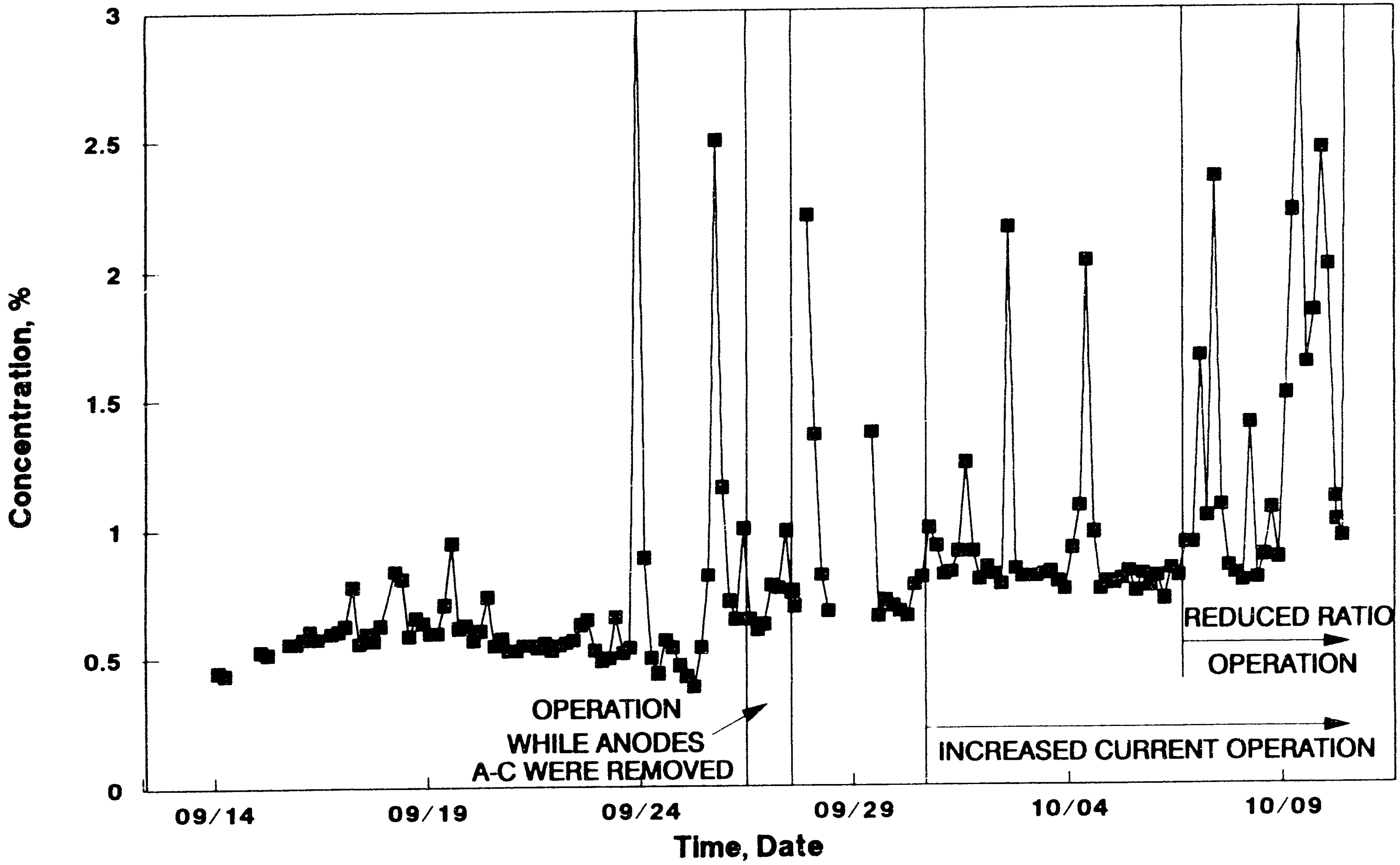

Figure 41

Ni CONTENT IN THE METAL

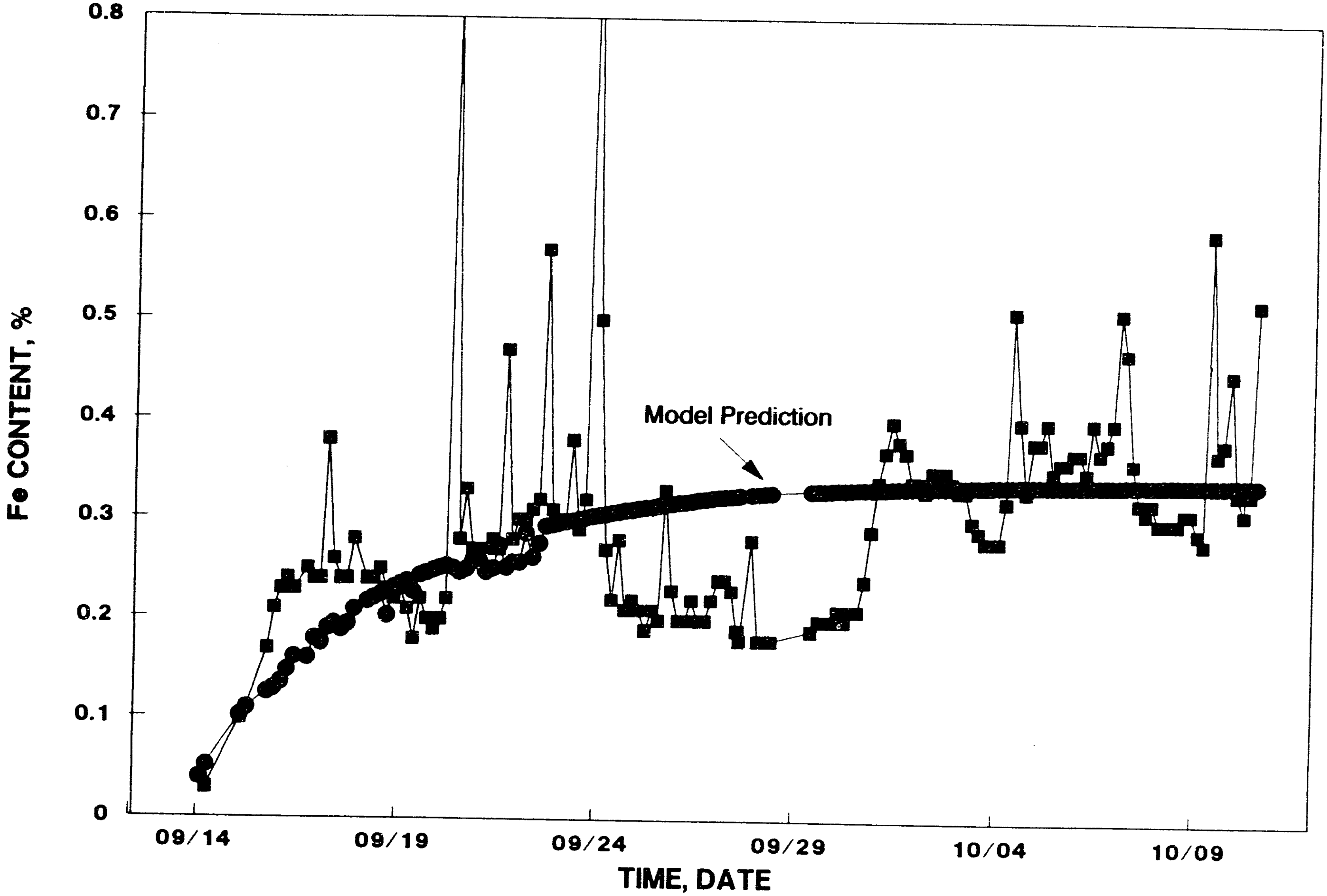

Figure 42

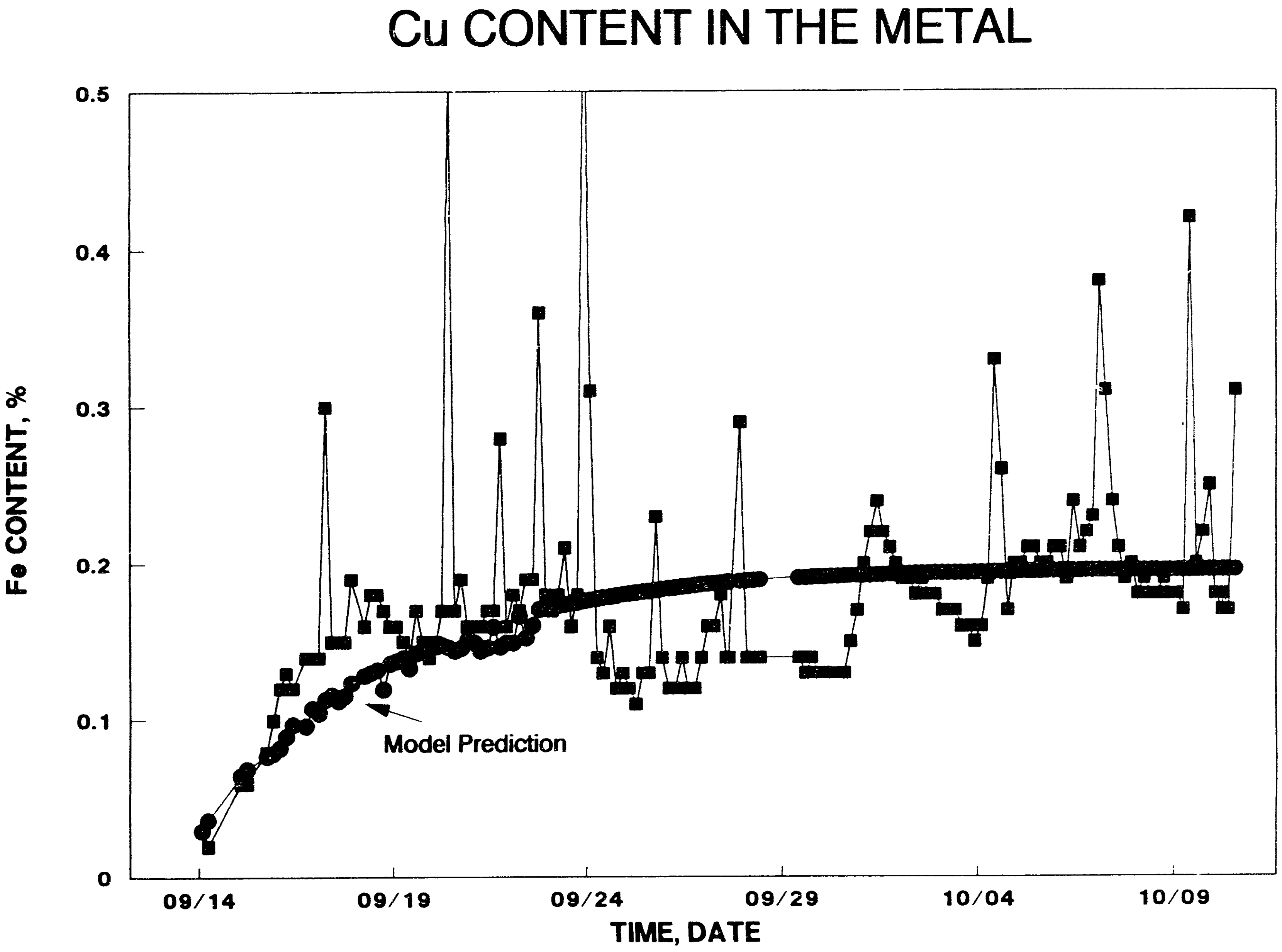
Cu CONTENT IN THE METAL
Fe CONTENT, %
0.5
0.4
0.3
0.2
0.1
0
Model Prediction
09/14
09/19
09/24
09/29
10/04
10/09
TIME, DATE

Figure 43

Fe CONTENT IN THE METAL

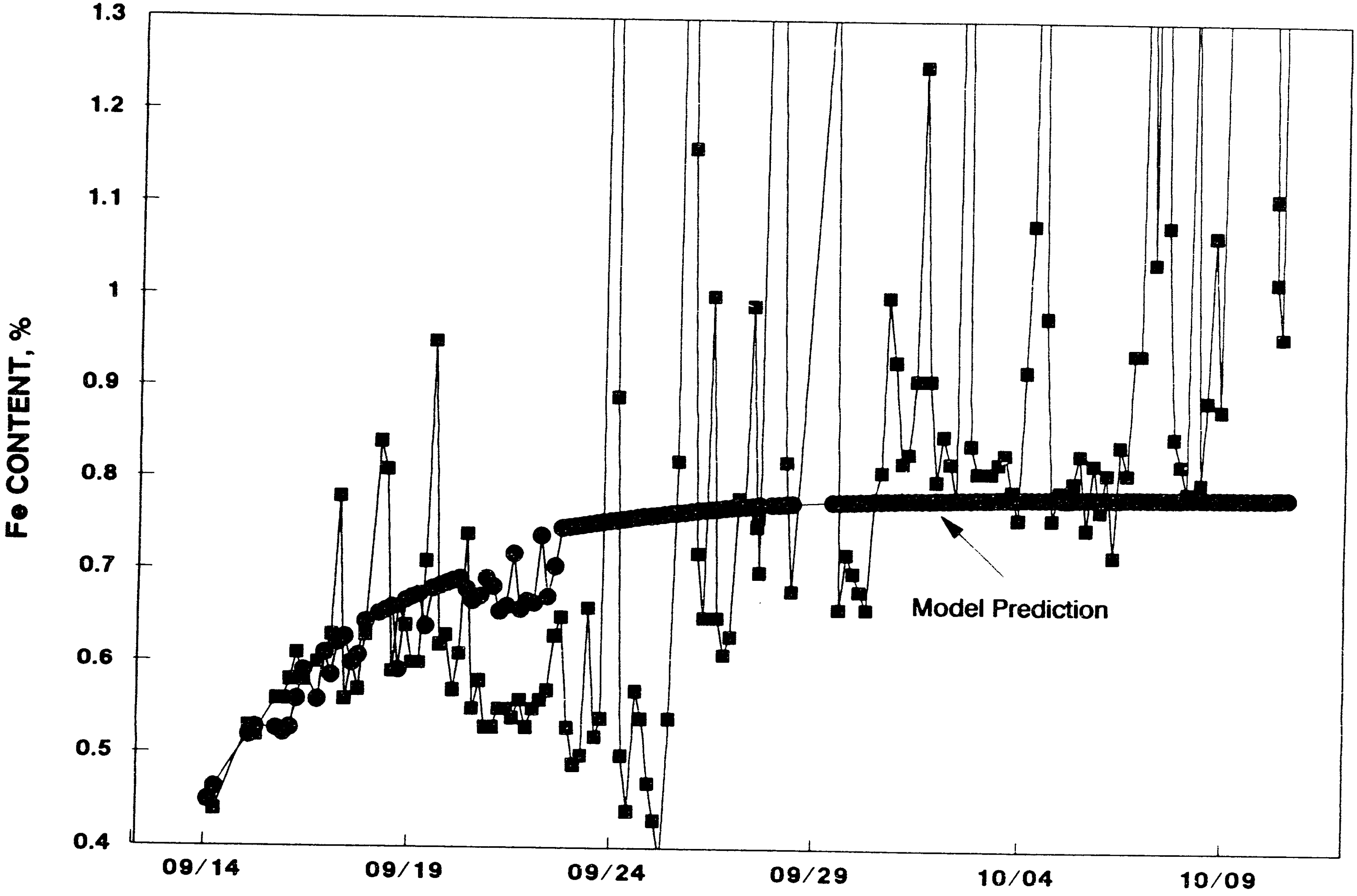

Figure 44

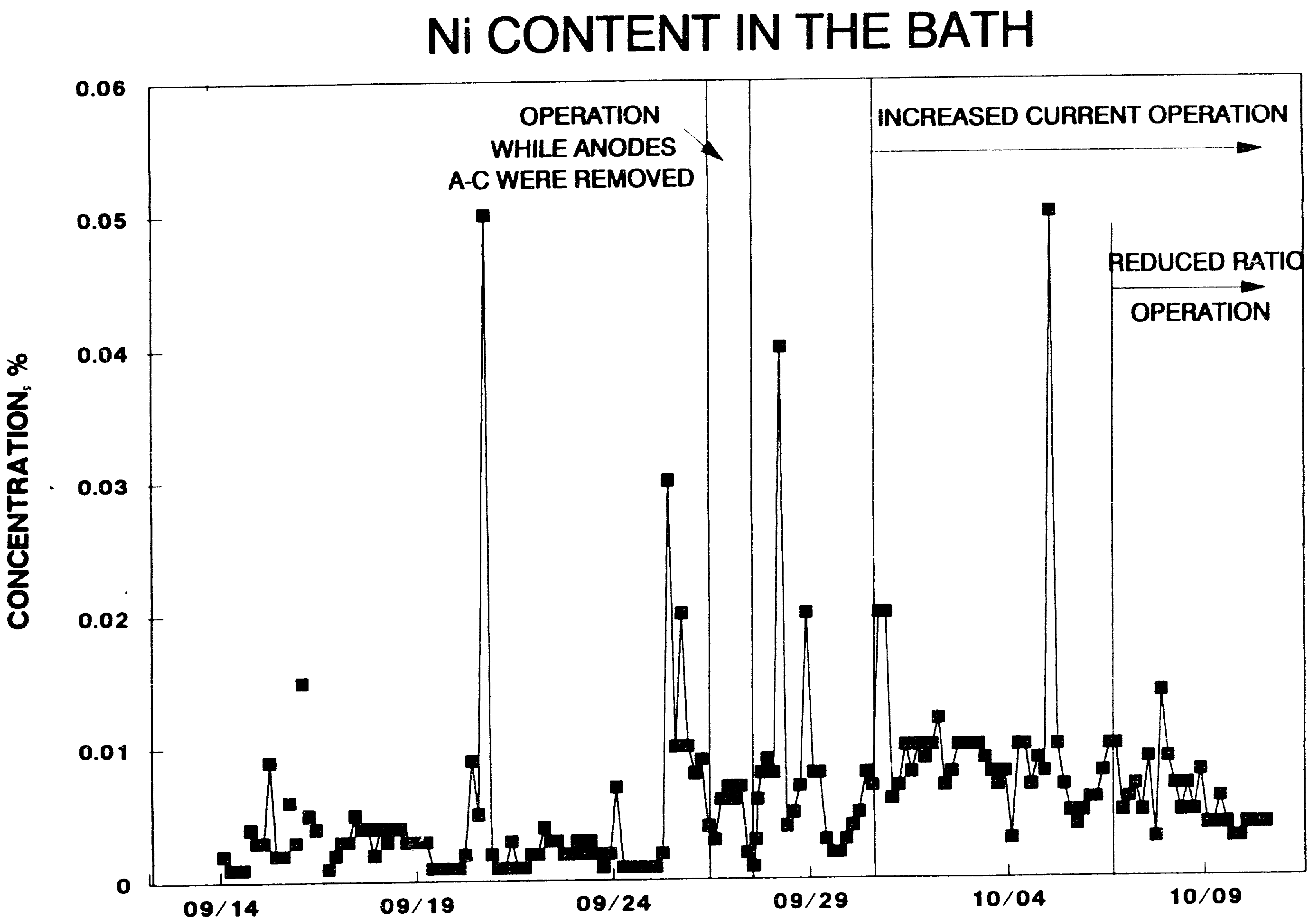
Ni CONTENT IN THE BATH
CONCENTRATION, %
0.06
0.05
0.04
0.03
0.02
0.01
0
09/14
09/19
09/24
09/29
10/04
10/09
TIME, DATE
OPERATION
WHILE ANODES
A-C WERE REMOVED
INCREASED CURRENT OPERATION
REDUCED RATIO
OPERATION

Figure 45

Cu CONTENT IN THE BATH

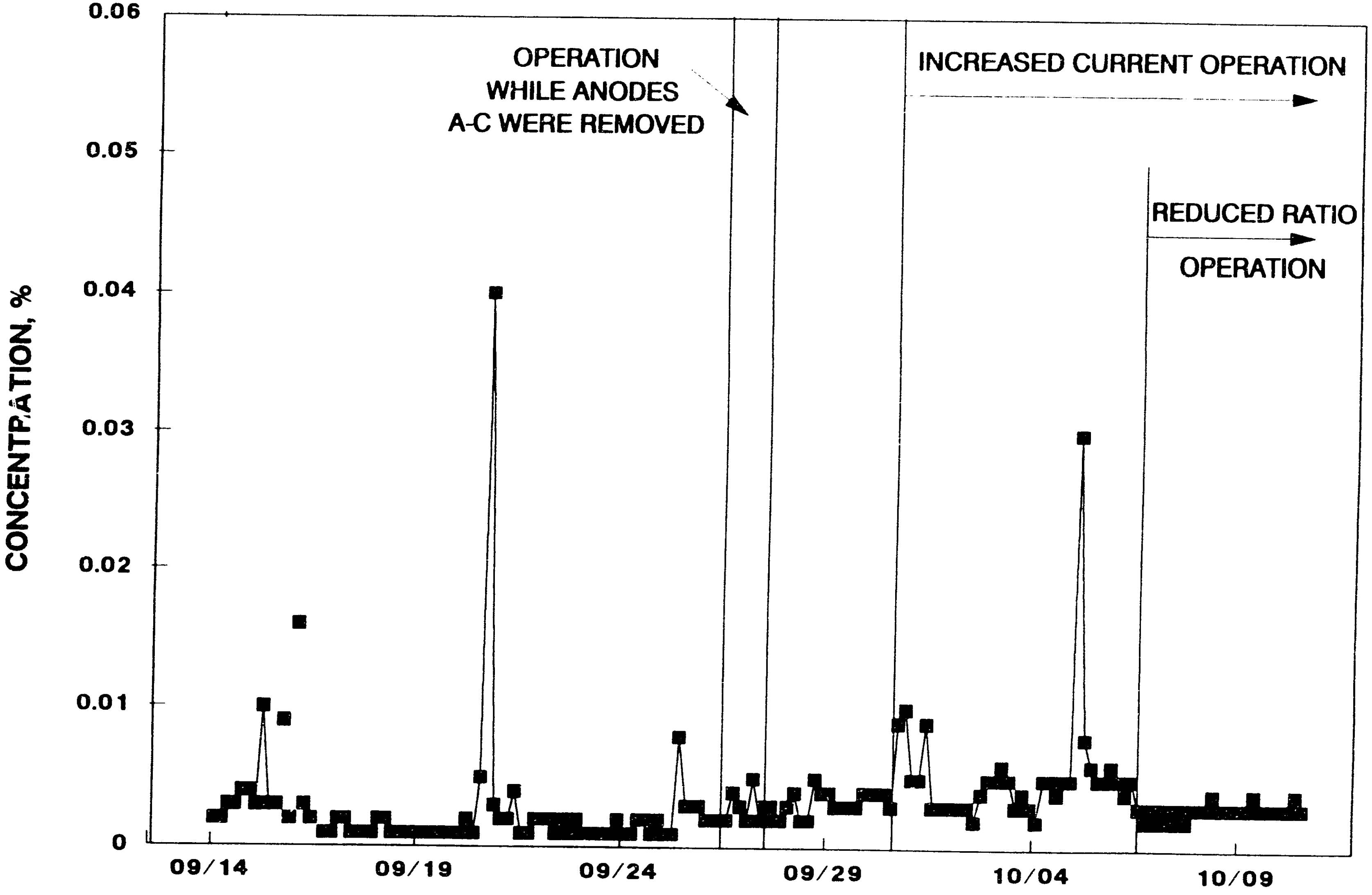

Figure 46

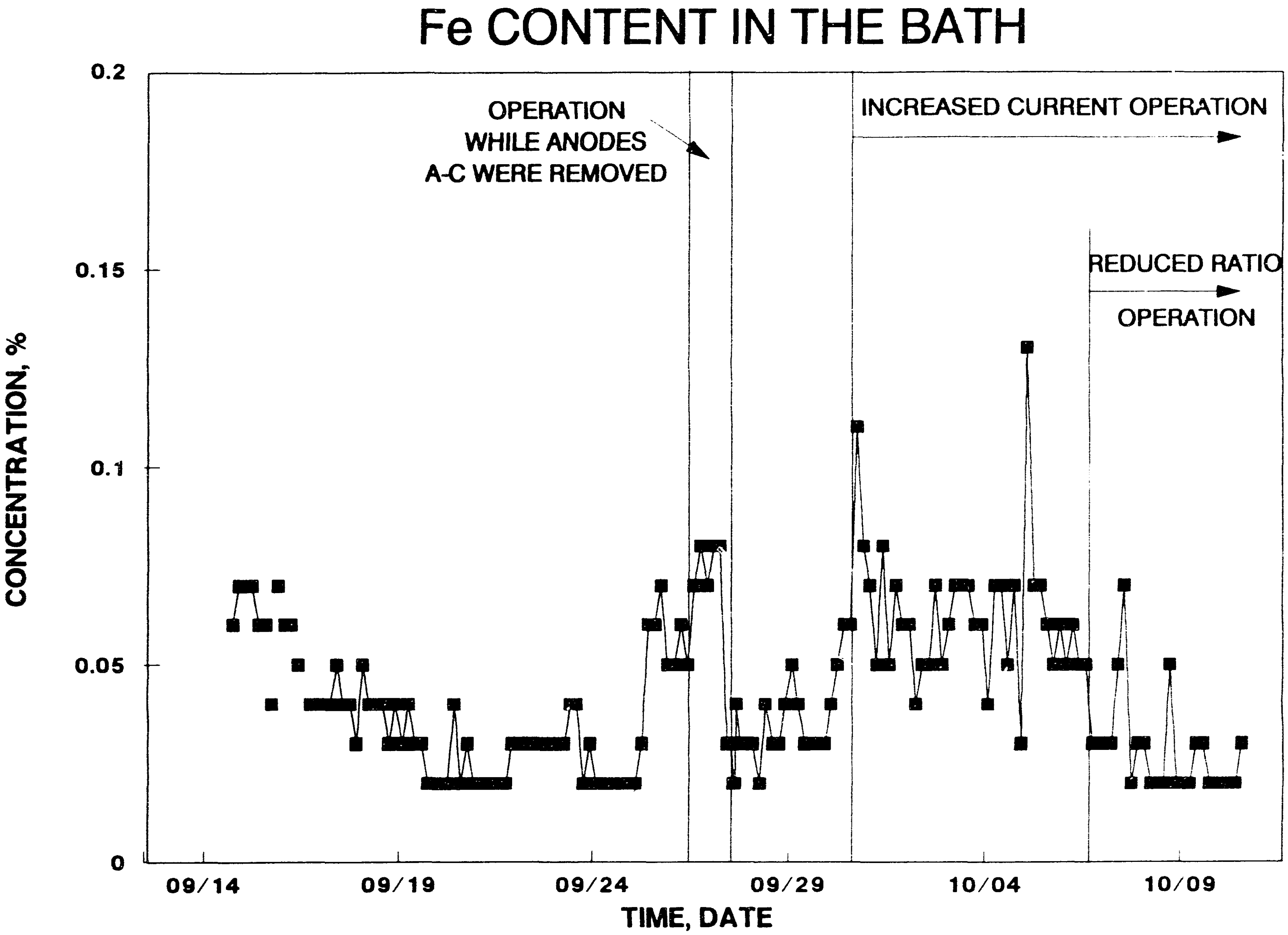

Fe CONTENT IN THE BATH

Figure 47

VI. DISCUSSION

The operation of the aluminum reduction pilot cell with cermet anodes using ELTECH's "Cerox" technology was successful in that individual anodes remained in continuous operation for as long as 600 hours and, upon removal, were basically intact. Corrosion rates, as determined from the metal impurities in the metal, were approximately half that experienced during operation of the cell with cermet anodes without the "Cerox" coating (PNL testing), but still higher than desired for an acceptable commercial operation.

Similar problems were encountered with cracking of the cermet anodes as was experienced during the previous PNL testing. A number of concerns about the cermet anode technology as well as with the "Cerox" coating technology were emphasized during this pilot reduction cell test.

These concerns about the cermet technology were basically the same seen during the PNL testing without the "Cerox" coating. These include:

a) Cermet Anode Cracking and Stem Breakage

While the anode conductor stem breakage did not occur in this testing as experienced during the PNL testing, due to a change in material, significant wear was observed on the stems, indicating that an improved connector material or protection of the stem is needed.

The thermal stress cracking of the cermet anodes still remained a significant problem with this particular design of the anode. Even though the pre-mature failure of anodes due to breakage was not a significant problem, as experienced during the PNL testing, it was still very much evident and requires further investigation.

b) Operation at Low Anode Current Density

The apparent need to operate cermet anodes at low anode current density indicates the need for a revised anode design, allowing significant increase in anode area with sufficient current conduction for 1) the thermal stability of the aluminum reduction cell and 2) maintaining the commercial cell productivity.

c) Operation at Alumina Saturation

It is essentially impossible to operate for long periods at saturated alumina conditions in a conventional reduction cell due to increasing muck build-up which results in increasing cathode drop and reduced availability of liquid volume in the cell cathode cavity.

The development of innovative anode and cell design is required to address these problems. Further development in cermet materials may still be required even with design changes, such that a suitable corrosion rate is achieved.

In addition to these general problems with the cermet anode technology, implementation of the "Cerox" coating adds some additional challenges.

a) Anode Current Distribution

To achieve uniform coating of the anode it is necessary to have a uniform current density on the anode. While this is a concern with any design, it is especially critical with the Cerox technology.

b) Replacement of Anodes

To achieve the initial coating on the cermet anode it is necessary to operate at elevated cerium fluoride concentrations in the electrolyte. It is unclear as to the effects this will have on anodes in the cell which already have a "Cerox" coating installed. It may be better to develop a procedure for pre-coating the anodes prior to actual installation in an operating cell. It is also not clear as to the dynamics of the coating when placed in the bath and not under electrolysis.

c) Liquid Level Control

As the coating is applied in the cell while elevated levels of cerium exist in the bath, it is necessary to be sure that the coating is applied while anode immersion is the maximum, otherwise uncoated areas of the anode will be exposed later in the operation.

d) Cerium Levels in the Metal

A major disadvantage to the "Cerox" technology is that the cerium concentrations in the metal are in the 3-4% range. An economical technology must be proven to reduce these concentrations to an acceptable level (< 1 ppm) before it would be accepted by industry.

VII. APPENDICES

APPENDIX A

Bath Composition

APPENDIX B

Metal Impurities

APPENDIX C

Bath Impurities

APPENDIX A

Bath Composition

ELTECH BATH ANALYSIS

SAMPLE ID	DATE	TIME	RATIO	CaF_2 %	Al_2O_3 %	EXCESS ALF_3 %	BATH TEMP DEG C	ALUMINA SAT %	CeF_3 %
2687-30A		1400		3.47					
2687-31C		1800		3.11					
2687-31A		2200		3.03					
2687-32B	AUG 31	1400		3.20					
2687-33A		2200		4.07					
2687-34B	SEPT 1	600		3.81					
2687-35A		1400		4.24					
2687-36B		2200	1.13	4.59					
2687-37B	SEPT 2	600	1.25	4.42					
2687-38C		1400	1.37	4.16					
2687-38D		2200	1.47	3.90					
2687-39B	SEPT 3	600	1.49	3.98					
2687-39D		1400		3.89					
2687-40A		2200		4.07					
2687-41B	SEPT 4	600	1.45	3.99					
2687-41D		1400	1.47	3.80					
2687-42B		2200	1.41	4.16					
2687-42D	SEPT 5	600	1.45	4.07					
2687-43B		1400	1.33	4.33					
2687-43D		2200	1.26	4.33					
2687-44B	SEPT 6	600	1.29	4.33					
2687-44D		1400	1.17	4.07					
2687-45B		2200	1.27	4.07					
2687-45D	SEPT 7	600	1.31	4.07					
2687-46B		1400	1.26	4.07					
2687-46D		2200	1.26	4.15					
2687-47B	SEPT 8	600	1.28	4.24					
2687-47D		1400	1.26	4.76					
2687-48B		2200	1.39	4.85					
2687-49B	SEPT 9	600	1.48	5.11					
2687-50A		1100							0.01
2687-50C		1300							1.17
2687-50E		1400	1.44	4.33					1.03
2687-51H		1800	1.45	4.33					0.71
2687-52A		2200	1.43	4.50					0.62
2687-52C	SEPT 10	200	1.44	4.58					0.52
2687-53A		600	1.43	4.59					0.48
2687-53C		1000	1.39	4.77					0.36
2687-53E		1400	1.36	4.68					0.22
2687-54E		1800	1.36	4.76					0.23
2687-54G		2200	1.37	4.76					0.24
2687-55B		200	1.39	4.76					0.49
2687-55D		600	1.41	4.68					0.48
2687-56A		1000							0.29
2687-56D		1400							0.34

ELTECH BATH ANALYSIS

SAMPLE ID	DATE	TIME	RATIO	CaF_2 %	Al_2O_3 %	EXCESS ALF_3 %	BATH TEMP DEG C	ALUMINA SAT %	CeF_3 %
2687–57E		1800	1.25	4.77					0.29
2687–57G		2200	1.22	4.51					0.26
2687–58B	SEPT 12	200	1.24	4.59					0.27
2687–58D		600	1.33	4.67					0.26
2687–59E		1000	1.36	4.77					0.30
2687–60A		1400	1.33	4.51					0.34
2687–60D		1800	1.34	4.41					0.34
2687–61B		2200	1.33	4.59					0.27
2687–61D	SEPT 13	200	1.35	4.51					0.34
2687–61F		600	1.37	4.59	3.76	3.33	973	43.2	0.54
2687–61H		1000	1.45	4.50	6.49	1.20	961	78.4	0.50
2687–62A		1400	1.50	3.98	4.37	0.00	971	49.1	0.39
2687–63B		1800	1.54	4.15	5.62	−0.94	974	62.2	0.35
2687–63D		2200	1.55	4.34	4.90	−1.18	973	54.8	0.36
2687–64B	SEPT 14	200	1.61	4.24	3.68	−2.57	973	40.8	0.32
2687–65B		600	1.60	4.34	4.45	−2.33	978	48.2	0.32
2687–65C		1000	1.61	3.58	2.72	−2.62	965	30.9	0.54
2687–65E		1200							0.52
2687–66A		1300							0.53
2687–66C		1330							0.50
2687–66C		1400	1.59	3.96	2.65	−2.15	970	29.7	0.48
2687–66E		1430							0.48
2687–67B		1500							0.46
2687–67D		1530							0.46
2687–67F		1600							0.45
2687–67H		1630							0.44
2687–68B		1730							0.41
2687–68D		1800	1.61	3.77	3.34	−2.60	972	36.7	0.38
2687–68F		2200	1.59	4.05	2.98	−2.14	972	33.1	0.33
2687–68H	SEPT 15	200	1.61	3.78	2.98	−2.61	975	32.2	0.31
2687–69B		600	1.62	4.15	3.02	−2.82	976	32.8	0.68
2687–69D		1000	1.60	3.48	2.73	−2.39	980	28.4	0.62
2687–69E		1200							0.87
2687–70B		1245							0.85
2687–70D		1330							[illegible]
2687–70F		1400	1.53	3.48	6.72	−0.71	969	74.8	0.77
2687–70H		1430							0.65
2687–70J		1500							0.66
2687–70L		1530							0.61
2687–70N		1600							0.62
2687–71B		1700							0.59
2687–71D		1800	1.51	3.39	5.73	−0.24	972	62.7	0.54
2687–71F		1900							0.51
2687–71H		2000							0.49
2687–71I		2100							0.47

ELTECH BATH ANALYSIS

SAMPLE ID	DATE	TIME	RATIO	CaF_2 %	Al_2O_3 %	EXCESS ALF_3 %	BATH TEMP DEG C	ALUMINA SAT %	CeF_3 %
2687−72B		2200	1.50	3.77	5.47	0.00	973	60.3	0.46
2687−72D	SEPT 16	0							0.43
2687−72F		200	1.48	3.78	4.87	0.49	973	53.8	0.42
2687−73B		400							0.38
2687−73D		600	1.47	4.24	5.96	0.72	973	66.9	0.36
2687−73F		800							0.37
2687−73H		1000	1.45	4.05	4.88	1.23	968	56.0	0.34
2687−73J		1400	1.46	3.77	5.14	0.98	975	56.3	0.40
2687−74B		1800	1.45	4.15	6.95	1.20	972	78.4	0.36
2687−74D		2200	1.43	4.34	5.38	1.72	978	59.3	0.39
2687−75B	SEPT 17	200	1.47	4.34	5.41	0.73	970	61.9	0.39
2687−75D		600	1.47	4.53	4.71	0.73	970	54.2	0.39
2687−75E		1000	1.48	4.43	4.97	0.48	970	57.0	0.40
2687−75G		1400	1.48	4.34	4.99	0.48	969	57.4	0.39
2689−1A		1800	1.49	4.34	4.29	0.24	971	48.8	0.38
2689−2A		2200	1.50	4.24	6.29	0.00	976	69.3	0.36
2689−2C	SEPT 18	200	1.49	4.34	6.71	0.24	974	75.1	0.38
2689−2D		600	1.49	4.24	6.82	0.24	981	73.3	0.37
2689−2G		1000	1.48	4.41	4.40	0.49	972	49.9	0.40
2689−3B		1400	1.48	4.28	5.00	0.49	971	56.8	0.36
2689−3D		1800	1.46	4.28	5.43	0.97	977	59.9	0.35
2689−4B		2200	1.44	4.34	5.11	1.48	966	59.9	0.34
2689−4D	SEPT 19	200	1.43	3.96	5.10	1.74	971	57.6	0.33
2689−4F		600	1.40	4.80	4.74	2.50	971	55.1	0.33
2689−4H		1000	1.38	4.40	5.64	3.01	965	66.9	0.31
2689−5B		1400	1.34	4.49	5.07	4.10	965	60.5	0.32
2689−5D		1800	1.31	4.58	5.45	4.91	969	64.2	0.31
2689−5F		2200	1.27	4.49	7.07	5.94	970	83.1	0.30
2689−6B	SEPT 20	200	1.25	4.41	7.33	6.50	966	87.7	0.35
2689−6D		600	1.28	4.40	6.59	5.69	976	75.0	0.38
2689−6E		1000	1.16	4.23	6.49	9.32	969	77.5	0.36
2689−6H		1400	1.10	3.78	7.05	11.26	987	78.3	0.41
2689−7B		1800	1.12	3.68	7.13	10.60	974	82.7	0.34
2689−7D		2200	1.21	3.77	7.79	7.69	990	82.8	0.35
2689−8B	SEPT 21	200	1.22	3.68	7.75	7.41	995	80.2	0.43
2689−8D		600	1.41	3.60	7.65	2.20	993	76.7	0.37
2689−8E		1000	1.27	3.96	7.49	5.95	985	80.8	0.35
2689−9A		1400	1.32	4.89	7.35	4.51	960	91.2	0.31
2689−9D		1800	1.37	4.68	6.48	3.23	985	70.4	0.30
2689−9F		2200	1.45	4.95	8.83	1.17	997	90.1	0.45
2689−10B	SEPT 22	200	1.53	5.31	7.64	−0.68	1002	75.9	0.42
2689−10D		600	1.52	5.29	8.08	−0.46	998	82.0	0.38
2689−11B		1000	1.51	5.39	7.60	−0.23	998	77.5	0.42
2689−11D		1400	1.47	5.20	9.79	0.68	1004	96.9	0.41
2689−11F		1800	1.49	5.22	7.83	0.23	1001	78.5	0.37

ELTECH BATH ANALYSIS

SAMPLE ID	DATE	TIME	RATIO	CaF_2 %	Al_2O_3 %	EXCESS ALF_3 %	BATH TEMP DEG C	ALUMINA SAT %	CeF_3 %
2689–11H		2200	1.51	5.21	8.26	−0.23	996	84.6	0.38
2689–12B	SEPT 23	200	1.52	5.22	7.34	−0.46	990	77.4	0.37
2689–12D		600	1.50	5.21	7.46	0.00	993	77.7	0.39
2689–12F		1000	1.50	5.10	2.38	0.00	975	27.1	0.40
2689–13B		1400	1.34	5.10	4.49	4.10	984	49.9	0.32
2689–13D		1800	1.33	5.11	6.65	4.27	983	74.3	0.31
2689–14B		2200	1.34	4.91	4.10	4.12	980	46.2	0.32
2689–14D	SEPT 24	200	1.34	4.84	7.76	3.96	979	87.5	0.28
2689–14F		600	1.34	4.54	7.05	4.01	983	77.3	0.28
2689–15B		1000	1.32	4.65	7.32	4.53	993	77.1	0.41
2689–15D		1400	1.30	4.58	7.23	5.08	991	77.0	0.50
2689–16B		1800	1.33	4.65	8.37	4.21	997	86.4	0.47
2689–16D		2200	1.32	4.84	7.36	4.52	993	78.0	0.40
2689–16F	SEPT 25	200	1.32	4.83	6.43	4.56	980	72.4	0.40
2689–17B		600	1.33	5.11	7.36	4.23	992	78.9	0.36
2689–17C		1000	1.41	4.94	7.90	2.16	1015	74.5	0.49
2689–17F		1400	1.43	4.39	10.28	1.63	1046	82.3	0.68
2689–18B		1800	1.42	4.12	11.08	1.86	1038	91.4	0.79
2689–18D		2200		4.49	11.05				0.89
2689–19B	SEPT 26	200	1.60	4.39	7.41	−2.25	1006	69.2	0.63
2689–19D		600	1.50	4.75	6.19	0.00	999	61.6	0.65
2689–19F		1000	1.41	4.66	9.23	2.13	1029	80.9	0.56
2689–20B		1400	1.48	4.37	6.42	0.48	1030	54.6	0.48
2689–20D		1800	1.49	4.12	10.13	0.23	1047	78.8	0.47
2689–21B		2200	1.47	3.66	10.33	0.69	1036	83.7	0.42
2689–21D	SEPT 27	200	1.47	3.77	6.69	0.72	1012	60.9	0.41
2689–22B		600	1.47	3.76	8.91	0.70	1020	78.0	0.39
2689–22C		1000	1.34	3.41	6.81	4.07	979	73.4	0.34
2689–22F		1300	1.33	3.12	7.22	4.34	984	75.4	0.67
2689–23B		1400	1.32	3.22	6.75	4.63	967	76.8	0.52
2689–23C		1500							0.46
2689–23E		1600							0.47
2689–24B		1800	1.23	3.40	7.94	7.12	1016	74.4	0.50
2689–24D		2200	1.23	3.59	7.35	7.15	995	75.7	0.49
2689–25B	SEPT 28	200	1.26	3.68	7.66	6.24	1008	74.2	0.53
2689–25D		600	1.39	3.67	7.90	2.70	1021	69.9	0.55
2689–26A		1000	1.43	4.03	5.64	1.73	990	58.0	1.07
2689–27A		1400	1.50	6.10	6.44	0.00	978	74.6	0.64
2689–27D		1800	1.67	6.03	5.98	−3.71	980	67.1	0.66
2689–28B		2200	1.62	4.94	6.37	−2.69	989	66.1	0.55
2689–28D	SEPT 29	200	1.59	6.55	5.60	−2.02	1013	54.2	0.57
2689–28F		600	1.72	6.63	5.26	−4.72	1003	52.6	0.50
2689–29B		1000	1.72	6.74	5.14	−4.72	1016	48.1	0.59
2689–29D1		1400	1.76	6.28	6.45	−5.45	1019	58.1	0.55
2689–29D2		1800	1.71	6.19	6.69	−4.47	1015	61.9	0.55

ELTECH BATH ANALYSIS

SAMPLE ID	DATE	TIME	RATIO	CaF_2 %	Al_2O_3 %	EXCESS ALF_3 %	BATH TEMP DEG C	ALUMINA SAT %	CeF_3 %
2689–30B		2200	1.71	5.90	10.26	−4.31	1033	85.8	0.59
2689–30D	SEPT 30	200	1.73	5.12	11.10	−4.68	1061	78.3	0.60
2689–30F		600	1.77	5.20	9.71	−5.50	1052	71.0	0.60
2689–31B		1000	1.78	5.04	7.44	−5.84	1037	58.3	0.63
2689–31D		1400	1.48	4.66	7.07	0.47	1004	68.7	0.57
2689–32B		1800	1.46	4.12	9.51	0.93	1043	75.9	0.66
2689–32D		2200	1.53	4.04	11.55	−0.66	1024	98.8	0.69
2689–33B	OCT 1	200	1.59	4.03	10.43	−1.97	1059	74.4	0.64
2689–33D		600	1.61	4.12	10.29	−2.39	1058	73.6	0.61
2689–34A		1000	1.54	4.29	11.25	−0.88	1016	100.7	0.56
2689–34C		1400	1.53	4.39	9.97	−0.67	1024	86.3	0.53
2689–35B		1800	1.47	4.21	9.86	0.69	1012	91.0	0.58
2689–35D		2200	1.45	4.12	10.17	1.16	1018	91.3	0.59
2689–36B	OCT 2	200	1.36	4.11	8.57	3.43	1006	82.9	0.47
2689–36D		600	1.35	4.39	9.06	3.66	1006	88.6	0.49
2689–36E		1000	1.37	4.39	12.31	3.03	1018	113.4	
2689–36H		1400	1.39	4.22	10.70	2.60	1016	98.5	0.43
2689–37B		1800	1.41	4.57	11.59	2.07	1041	96.0	0.51
2689–37D		2200	1.44	4.86	12.07	1.35	1035	102.8	0.46
2689–38B	OCT 3	200	1.50	5.30	12.49	0.00	1038	104.8	0.49
2689–38D		600	1.49	5.56	12.33	0.22	1043	102.2	0.46
2689–38F		1000	1.49	5.38	8.80	0.23	1031	76.7	0.51
2689–38H		1400	1.48	5.29	10.30	0.45	1020	94.5	0.42
2689–39B		1800	1.48	5.12	12.52	0.44	1038	105.0	0.50
2689–39D		2200	1.47	5.13	12.31	0.66	1011	117.5	0.53
2689–39F	OCT 4	200	1.41	0.12	0.98	2.45	979	9.4	0.60
2689–40B		600	1.41	4.86	9.45	2.12	993	98.6	0.60
2689–40C		1000	1.43	5.02	6.62	1.69	1023	60.1	0.55
2689–40F		1400	1.50	4.76	12.26	0.00	1039	100.7	0.42
2689–41B		1800	1.59	4.67	10.79	−1.95	1031	89.9	0.40
2689–41D		2200	1.69	4.77	12.28	−3.88	1044	94.2	0.35
2689–42B	OCT 5	200	1.73	4.40	14.70	−4.52	1072	96.3	0.35
2689–43B		600	1.63	4.39	13.05	−2.70	1073	87.4	0.35
2689–43D		1000	1.69	4.21	11.31	−3.95	1034	89.5	0.44
2689–43F		1400	1.64	4.31	9.44	−3.03	1041	73.1	0.39
2689–44A		1800	1.61	4.93	10.68	−2.36	1021	93.9	0.39
2689–44D		2200	1.63	4.75	9.83	−2.80	1019	86.5	0.34
2689–45B	OCT 6	200	1.61	4.94	10.75	−2.35	1026	92.2	0.41
2689–45D		600	1.68	4.83	8.98	−3.84	1024	76.4	0.41
2689–45F		1000	1.64	6.10	7.31	−3.04	1021	66.3	0.61
2689–45H		1400	1.61	5.48	8.82	−2.39	1017	80.5	0.55
2689–46B		1800	1.28	4.49	9.14	5.52	1024	84.3	0.57
2689–46D		2200	1.11	4.50	9.07	10.59	1025	88.5	0.62
2689–47B	OCT 7	200	1.17	4.32	9.10	8.73	1018	88.6	0.56
2689–47D		600	1.19	4.59	9.61	8.05	1034	88.0	0.61

ELTECH BATH ANALYSIS

SAMPLE ID	DATE	TIME	RATIO	CaF_2 %	Al_2O_3 %	EXCESS ALF_3 %	BATH TEMP DEG C	ALUMINA SAT %	CeF_3 %
2689-47F		1000	1.26	4.40	7.51	6.20	1015	72.3	0.65
2689-48B		1400	1.29	4.30	8.69	5.29	1029	77.8	0.69
2689-48D		1800	1.17	4.05	10.59	8.60	1033	96.3	0.51
2689-48F		2200	1.11	4.21	9.71	10.55	1019	95.9	0.52
2689-49B	OCT 8	200	1.07	4.30	9.89	11.81	1044	91.1	0.49
2689-49D		600	1.14	4.04	10.68	9.51	1046	93.6	0.51
2689-49E		1000	1.10	4.23	11.45	10.64	1031	108.4	0.34
2689-49G		1400	1.11	4.49	11.25	10.32	1052	99.1	0.37
2689-50B		1800	1.16	3.77	10.79	8.91	1036	96.5	0.38
2689-50D		2200	1.17	4.04	11.03	8.56	1039	97.9	0.45
2689-50F	OCT 9	200	1.18	4.22	11.26	8.22	1046	97.5	0.44
2689-51B		600	1.17	4.49	10.93	8.52	1032	101.1	0.44
2689-51D		1000	1.22	4.75	10.77	7.06	1046	93.4	0.46
2689-51F		1400	1.23	4.05	12.02	6.73	1035	106.0	0.49
2689-51H		1800	1.21	4.22	12.72	7.22	1042	110.4	0.38
2689-51J		2200	1.23	4.31	12.57	6.67	1051	104.8	0.40
2689-52B	OCT 10	200	1.14	4.05	11.86	9.37	1043	104.9	0.42
2689-52D		600	1.14	4.49	10.55	9.47	1044	94.5	0.42
2689-52G		1000	1.02	3.77	10.09	13.57	1029	98.9	0.45
2689-53B		1400	1.06	4.04	11.40	11.97	1000	122.4	0.55

APPENDIX B

Metal Impurities

METAL ANALYSIS

Sample ID	Date	Time	Ni, %	Fe, %	Cu, %	Ce, %
2687-30B		1400	0.58	0.76	0.48	
2687-31B		2200	0.90	1.14	0.79	
2687-31D	AUG 31	600	0.74	1.12	0.63	
2687-33B		2200	0.75	1.18	0.65	
2687-34A	SEPT 1	600	0.75	1.25	0.64	
2687-35B		1400	0.78	1.29	0.67	
2687-36A		2200	0.75	1.24	0.64	
2687-37A	SEPT 2	600	0.75	1.25	0.63	
2687-38A		1400	0.80	1.38	0.67	
2687-38D		2200	0.81	1.44	0.68	
2687-39A	SEPT 3	600	0.82	1.53	0.69	
2687-39C		1400	0.83	1.53	0.64	
2687-40B		2200	0.81	1.57	0.62	
2687-41A	SEPT 4	600	0.81	1.59	0.63	
2687-41C		1400	0.78	1.54	0.61	
2687-42A		2200	0.75	1.54	0.56	
2687-42D	SEPT 5	600	0.72	1.50	0.55	
2687-43A		1400	0.69	1.53	0.47	
2687-43C		2200	0.64	1.55	0.43	
2687-44A	SEPT 6	600	0.58	1.55	0.38	
2687-44C		1400	0.57	1.94	0.37	
2687-45A		2200	0.46	1.33	0.29	
2687-45C	SEPT 7	600	0.42	1.24	0.26	
2687-46A		1400	0.30	1.04	0.19	
2687-46C		2200	0.26	0.94	0.17	
2687-47A	SEPT 8	600	0.23	0.85	0.14	
2687-47C		1400	0.20	0.75	0.11	
2687-48A		2200	0.16	0.71	0.09	
2687-49A	SEPT 9	600	0.13	0.60	0.07	
2687-50B		1100	0.13	0.59	0.07	1.15
2687-50F		1400	0.12	0.57	0.06	1.62
2687-51G		1800	0.12	0.89	0.06	2.20
2687-52B		2200	0.12	0.58	0.06	2.21
2687-52D	SEPT 10	200	0.12	0.60	0.06	2.28
2687-53B		600	0.10	0.56	0.05	2.17
2687-53D		1000	0.10	0.58	0.06	2.18
2687-53F		1400	0.08	0.52	0.05	2.06
2687-54F		1800	0.08	0.50	0.05	2.13
2687-54H		2200	0.08	0.47	0.04	2.25
2687-55A	SEPT 11	200	0.06	0.47	0.04	2.09
2687-55C		600	0.06	0.46	0.04	2.02
2687-56B		1000	0.07	0.46	0.03	1.84
2687-56C		1400	0.07	0.46	0.03	2.20
2687-57F		1800	0.05	0.47	0.04	1.71
2687-57H		2200	0.06	0.44	0.04	2.55
2687-58A	SEPT 12	200	0.05	0.46	0.04	2.57

METAL ANALYSIS

Sample ID	Date	Time	Ni, %	Fe, %	Cu, %	Ce, %
2687-58C		600	0.05	0.44	0.04	2.93
2687-59A		1000	0.04	0.41	0.04	2.89
2687-60B		1400	0.04	0.40	0.03	2.93
2687-60C		1800	0.04	0.43	0.03	2.81
2687-61A		2200	0.04	0.44	0.03	2.82
2687-61C	SEPT 13	200	0.03	0.48	0.03	2.49
2687-61E		600	0.03	0.43	0.02	2.56
2687-61G		1000				2.77
2687-62B		1400				2.80
2687-63A		1800				2.82
2687-63C		2200				2.85
2687-64A	SEPT 14	200	0.04	0.45	0.03	2.84
2687-65A		600	0.03	0.44	0.02	2.65
2687-65D		1000				2.52
2687-65F		1200				2.62
2687-66B		1300				2.70
2687-66D		1330				2.52
2687-66D1		1400				2.75
2687-66F		1430				2.73
2687-67A		1500				2.50
2687-67C		1530				2.86
2687-67E		1600				2.67
2687-67G		1630				2.55
2687-67I		1640				2.72
2687-67J		1640				2.74
2687-67K		1640				2.76
2687-67L		1640				2.76
2687-68A		1730				2.81
2687-68C		1800				2.77
2687-68E		2200				2.64
2687-68G	SEPT 15	200	0.10	0.53	0.06	2.61
2687-69A		600	0.11	0.52	0.06	2.90
2687-69C		1000				3.04
2687-69F		1200				3.31
2687-70A		1245				3.36
2687-70C		1330				3.41
2687-70E		1400				3.36
2687-70G		1430				3.56
2687-70I		1500				3.61
2687-70K		1530				3.63
2687-70M		1600				3.33
2687-71A		1700				3.69
2687-71C		1800	0.17	0.56	0.08	3.68
2687-71E		1900				3.71
2687-71G		2000				3.80
2687-71J		2100				3.75

METAL ANALYSIS

Sample ID	Date	Time	Ni, %	Fe, %	Cu, %	Ce, %
2687-72A		2200	0.21	0.56	0.10	3.70
2687-72C	SEPT 16	0				3.61
2687-72E		200	0.23	0.58	0.12	3.72
2687-73A		400				3.65
2687-73C		600	0.24	0.61	0.13	3.73
2687-73E		800				3.68
2687-73G		1000	0.23	0.58	0.12	3.56
2687-73I		1400				3.35
2687-74A		1800	0.25	0.60	0.14	3.40
2687-74C		2200	0.24	0.61	0.14	3.14
2687-75A	SEPT 17	200	0.24	0.63	0.14	3.28
2687-75C		600	0.38	0.78	0.30	2.42
2687-75F		1000	0.26	0.56	0.15	3.24
2687-75H		1400	0.24	0.60	0.15	2.80
2689-1B		1800	0.24	0.57	0.15	3.00
2689-2B		2200	0.28	0.63	0.19	2.79
2689-2E	SEPT 18	600	0.24	0.84	0.16	2.80
2689-2F		1000	0.24	0.81	0.18	2.73
2689-3A		1400	0.25	0.59	0.18	2.42
2689-3C		1800	0.23	0.66	0.17	2.26
2689-4A		2200	0.22	0.64	0.16	2.54
2689-4C	SEPT 19	200	0.23	0.60	0.16	3.03
2689-4E		600	0.21	0.60	0.15	2.93
2689-4G		1000	0.18	0.71	0.14	2.18
2689-5A		1400	0.22	0.95	0.17	2.00
2689-5C		1800	0.20	0.62	0.15	2.94
2689-5E		2200	0.19	0.63	0.14	2.96
2689-6A	SEPT 20	200	0.20	0.57	0.15	2.92
2689-6C		600	0.22	0.61	0.17	2.86
2689-6F		1000	0.85	0.74	0.51	2.82
2689-6G		1400	0.28	0.55	0.17	2.91
2689-7A		1800	0.33	0.58	0.19	2.96
2689-7C		2200	0.27	0.53	0.16	2.97
2689-8A	SEPT 21	200	0.26	0.53	0.16	2.97
2689-8C		600	0.27	0.55	0.16	3.04
2689-8F		1000	0.28	0.55	0.17	2.97
2689-9B		1400	0.27	0.54	0.17	2.90
2689-9C		1800	0.47	0.56	0.28	2.87
2689-9E		2200	0.28	0.53	0.16	2.99
2689-10A	SEPT 22	200	0.30	0.55	0.18	2.89
2689-10C		600	0.30	0.56	0.17	2.91
2689-11A		1000	0.31	0.57	0.19	2.71
2689-11C		1400	0.32	0.63	0.19	2.44
2689-11E		1800	0.57	0.65	0.36	2.60
2689-11G		2200	0.31	0.53	0.18	2.71
2689-12A	SEPT 23	200	0.30	0.49	0.17	2.66

METAL ANALYSIS

Sample ID	Date	Time	Ni, %	Fe, %	Cu, %	Ce, %
2689–12C		600	0.30	0.50	0.18	2.60
2689–12E		1000	0.38	0.66	0.21	2.40
2689–13A		1400	0.29	0.52	0.16	2.36
2689–13C		1800	0.32	0.54	0.18	2.27
2689–14A		2200	0.97	3.23	0.59	1.60
2689–14C	SEPT 24	200	0.50	0.89	0.31	2.28
2689–14E		600	0.27	0.50	0.14	2.52
2689–15A		1000	0.22	0.44	0.13	3.31
2689–15C		1400	0.28	0.57	0.16	3.85
2689–16A		1800	0.21	0.54	0.12	3.49
2689–16C		2200	0.22	0.47	0.13	3.53
2689–16E	SEPT 25	200	0.21	0.43	0.12	3.55
2689–17A		600	0.19	0.39	0.11	3.75
2689–17D		1000	0.21	0.54	0.13	3.37
2689–17E		1400	0.20	0.82	0.13	3.63
2689–18A		1800	0.33	2.50	0.23	3.26
2689–18C		2200	0.23	1.16	0.14	3.73
2689–19A	SEPT 26	200	0.20	0.72	0.12	5.46
2689–19C		600	0.20	0.65	0.12	5.22
2689–19E		1000	0.22	1.00	0.14	3.58
2689–20A		1400	0.20	0.65	0.12	4.18
2689–20C		1800	0.20	0.61	0.12	3.81
2689–21A		2200	0.22	0.63	0.14	3.77
2689–21C	SEPT 27	200	0.24	0.78	0.16	3.48
2689–22A		600	0.24	0.77	0.16	3.26
2689–22D		1000	0.23	0.99	0.18	2.34
2689–22E		1300	0.19	0.75	0.14	4.61
2689–23A		1400	0.19	0.76	0.14	5.33
2689–23D		1500	0.18	0.70	0.14	4.18
2689–23F		1600				3.74
2689–24A		1800				3.21
2689–24C		2200	0.28	2.21	0.29	2.30
2689–25A	SEPT 28	200	0.18	1.36	0.14	2.78
2689–25C		600	0.18	0.82	0.14	3.90
2689–26A		1000	0.18	0.68	0.14	4.23
2689–28A		2200				2.75
2689–28C	SEPT 29	200				3.08
2689–28F		600				2.96
2689–29A		1000	0.19	1.37	0.14	3.75
2689–29C		1400	0.20	0.66	0.13	3.87
2689–29D		1800	0.20	0.72	0.14	3.95
2689–30A		2200	0.20	0.70	0.13	4.12
2689–30C	SEPT 30	200	0.21	0.68	0.13	4.08
2689–30E		600	0.20	0.66	0.13	4.28
2689–31A		1000	0.21	0.78	0.13	3.69
2689–31C		1400	0.21	0.81	0.13	4.43

METAL ANALYSIS

Sample ID	Date	Time	Ni, %	Fe, %	Cu, %	Ce, %
2689-32A		1800	0.24	1.00	0.15	4.39
2689-32C		2200	0.29	0.93	0.17	4.63
2689-33A	OCT 1	200	0.34	0.82	0.20	4.59
2689-33C		600	0.37	0.83	0.22	5.17
2689-34B		1000	0.40	0.91	0.24	
2689-34D		1400	0.38	1.25	0.22	
2689-35A		1800	0.37	0.91	0.21	4.41
2689-35C		2200	0.34	0.80	0.20	4.72
2689-36A	OCT 2	200	0.34	0.85	0.19	4.68
2689-36C		600	0.33	0.82	0.19	5.08
2689-36F		1000	0.35	0.78	0.18	4.15
2689-36G		1400	0.35	2.16	0.19	3.88
2689-37A		1800	0.35	0.84	0.18	4.64
2689-37C		2200	0.34	0.81	0.18	4.31
2689-38A	OCT 3	200	0.33	0.81	0.17	4.39
2689-38C		600	0.33	0.81	0.17	4.29
2689-38E		1000	0.30	0.82	0.17	3.80
2689-38G		1400	0.29	0.83	0.16	3.86
2689-39A		1800	0.28	0.79	0.16	3.88
2689-39C		2200	0.28	0.76	0.15	4.01
2689-39E	OCT 4	200	0.28	0.92	0.16	3.74
2689-40A		600	0.32	1.08	0.19	3.33
2689-40D		1000	0.51	2.03	0.33	2.15
2689-40E		1400	0.40	0.98	0.26	2.86
2689-41A		1800	0.33	0.76	0.17	3.14
2689-41C		2200	0.38	0.79	0.20	3.11
2689-42A	OCT 5	200	0.38	0.78	0.20	3.10
2689-43A		600	0.40	0.80	0.21	3.14
2689-43C		1000	0.35	0.83	0.21	3.09
2689-43E		1400	0.36	0.75	0.20	3.09
2689-44B		1800	0.36	0.82	0.20	3.10
2689-44C		2200	0.37	0.77	0.21	3.20
2689-45A	OCT 6	200	0.37	0.81	0.21	3.18
2689-45C		600	0.35	0.72	0.19	3.49
2689-45E		1000	0.40	0.84	0.24	4.01
2689-45G		1400	0.37	0.81	0.21	4.00
2689-46A		1800	0.38	0.94	0.22	4.07
2689-46C		2200	0.40	0.94	0.23	4.06
2689-47A	OCT 7	200	0.51	1.66	0.38	2.86
2689-47C		600	0.47	1.04	0.31	3.23
2689-47E		1000	0.36	2.35	0.24	2.78
2689-48A		1400	0.32	1.08	0.21	3.17
2689-48C		1800	0.31	0.85	0.19	3.49
2689-48E		2200	0.32	0.82	0.20	4.13
2689-49A	OCT 8	200	0.30	0.79	0.18	4.14
2689-49C		600	0.30	1.40	0.19	3.89

METAL ANALYSIS

Sample ID	Date	Time	Ni, %	Fe, %	Cu, %	Ce, %
2689-49F		1000	0.30	0.80	0.18	4.25
2689-49H		1400	0.30	0.89	0.18	4.34
2689-50A		1800	0.31	1.07	0.19	4.68
2689-50C		2200	0.31	0.88	0.18	4.84
2689-50E	OCT 9	200	0.29	1.51	0.18	4.16
2689-51A		600	0.28	2.22	0.17	4.68
2689-51C		1000	0.59	3.02	0.42	3.16
2689-51E		1400	0.37	1.63	0.20	3.72
2689-51G		1800	0.38	1.83	0.22	3.24
2689-51I		2200	0.45	2.46	0.25	2.51
2689-52A	OCT 10	200	0.33	2.01	0.18	3.52
2689-52C		600	0.31	1.11	0.17	3.81
2689-52E		700	0.33	1.02	0.18	
2689-52F		1000	0.33	0.96	0.17	
2689-53A		1400	0.52	5.36	0.31	2.92

APPENDIX C

Bath Impurities

BATH IMPURITIES

Sample ID	Date	Time	Cu, %	Ni, %	Fe, %
2687-30A		1400	0.005	0.017	0.060
2687-31C		1800	0.011	0.032	0.047
2687-31A		2200	0.002	0.009	0.025
2687-32B	AUG 31	1400	0.006	0.015	0.034
2687-33A		2200	0.003	0.008	0.048
2687-34B	SEPT 1	600	0.002	0.007	0.029
2687-35A		1400	0.002	0.007	0.029
2687-36B		2200	0.002	0.004	0.032
2687-37B	SEPT 2	600	0.002	0.007	0.029
2687-38C		1400	0.001	0.006	0.015
2687-38D		2200	0.001	0.007	0.019
2687-39B	SEPT 3	600	0.001	0.006	0.036
2687-39D		1400			
2687-40A		2200			
2687-41B	SEPT 4	600	0.001	0.005	0.016
2687-41D		1400			
2687-42B		2200			
2687-42D	SEPT 5	600	0.001	0.006	0.028
2687-43B		1400			
2687-43D		2200			
2687-44B	SEPT 6	600	0.001	0.005	0.031
2687-44D		1400			
2687-45B		2200			
2687-45D	SEPT 7	600	0.001	0.006	0.032
2687-46B		1400			
2687-46D		2200			
2687-47B	SEPT 8	600	0.001	0.020	0.130
2687-47D		1400			
2687-48B		2200			
2687-49B	SEPT 9	600	0.001	0.005	0.023
2687-50A		1100			
2687-50C		1300			
2687-50E		1400			
2687-51H		1800			
2687-52A		2200			
2687-52C	SEPT 10	200			
2687-53A		600			
2687-53C		1000			
2687-53E		1400			
2687-54E		1800			
2687-54G		2200			
2687-55B		200			
2687-55D		600			
2687-56A		1000			
2687-56D		1400			
2687-57E		1800			

BATH IMPURITIES

Sample ID	Date	Time	Cu, %	Ni, %	Fe, %
2687–57G		2200			
2687–58B	SEPT 12	200			
2687–58D		600			
2687–59E		1000			
2687–60A		1400			
2687–60D		1800			
2687–61B		2200			
2687–61D	SEPT 13	200			
2687–61F		600			
2687–61H		1000			
2687–62A		1400			
2687–63B		1800	0.002	0.001	0.210
2687–63D		2200	0.002	0.001	0.210
2687–64B	SEPT 14	200	0.002	0.002	0.420
2687–65B		600	0.002	0.001	0.290
2687–65C		1000	0.003	0.001	0.210
2687–65E		1200			
2687–66A		1300			
2687–66C		1330			
2687–66C		1400	0.003	0.001	0.210
2687–66E		1430			
2687–67B		1500			
2687–67D		1530			
2687–67F		1600			
2687–67H		1630			
2687–68B		1730			
2687–68D		1800	0.004	0.004	0.060
2687–68F		2200	0.004	0.003	0.070
2687–68H	SEPT 15	200	0.003	0.003	0.070
2687–69B		600	0.010	0.009	0.070
2687–69D		1000	0.003	0.002	0.060
2687–69E		1200			
2687–70B		1245			
2687–70D		1330			
2687–70F		1400	0.003	0.002	0.060
2687–70H		1430			
2687–70J		1500			
2687–70L		1530			
2687–70N		1600			
2687–71B		1700			
2687–71D		1800	0.009	0.006	0.040
2687–71F		1900			
2687–71H		2000			
2687–71I		2100			
2687–72B		2200	0.002	0.003	0.070
2687–72D	SEPT 16	0			

BATH IMPURITIES

Sample ID	Date	Time	Cu, %	Ni, %	Fe, %
2687-72F		200	0.016	0.015	0.060
2687-73B		400			
2687-73D		600	0.003	0.005	0.060
2687-73F		800			
2687-73H		1000	0.002	0.004	0.050
2687-73J		1400			
2687-74B		1800	0.001	0.001	0.040
2687-74D		2200	0.001	0.002	0.040
2687-75B	SEPT 17	200	0.002	0.003	0.040
2687-75D		600	0.002	0.003	0.040
2687-75E		1000	0.001	0.005	0.050
2687-75G		1400	0.001	0.004	0.040
2689-1A		1800	0.001	0.004	0.040
2689-2A		2200	0.001	0.002	0.030
2689-2C	SEPT 18	200	0.002	0.004	0.050
2689-2D		600	0.002	0.003	0.040
2689-2G		1000	0.001	0.004	0.040
2689-3B		1400	0.001	0.004	0.040
2689-3D		1800	0.001	0.003	0.030
2689-4B		2200	0.001	0.003	0.040
2689-4D	SEPT 19	200	0.001	0.003	0.030
2689-4F		600	0.001	0.003	0.040
2689-4H		1000	0.001	0.001	0.030
2689-5B		1400	0.001	0.001	0.030
2689-5D		1800	0.001	0.001	0.020
2689-5F		2200	0.001	0.001	0.020
2689-6B	SEPT 20	200	0.001	0.001	0.020
2689-6D		600	0.002	0.002	0.020
2689-6E		1000	0.001	0.009	0.040
2689-6H		1400	0.005	0.005	0.020
2689-7B		1800	0.040	0.050	0.030
2689-7D		2200	0.003	0.002	0.020
2689-8B	SEPT 21	200	0.002	0.001	0.020
2689-8D		600	0.002	0.001	0.020
2689-8E		1000	0.004	0.003	0.020
2689-9A		1400	0.001	0.001	0.020
2689-9D		1800	0.001	0.001	0.020
2689-9F		2200	0.002	0.002	0.030
2689-10B	SEPT 22	200	0.002	0.002	0.030
2689-10D		600	0.002	0.004	0.030
2689-11B		1000	0.001	0.003	0.030
2689-11D		1400	0.002	0.003	0.030
2689-11F		1800	0.001	0.002	0.030
2689-11H		2200	0.002	0.002	0.030
2689-12B	SEPT 23	200	0.001	0.003	0.030
2689-12D		600	0.001	0.002	0.030

BATH IMPURITIES

Sample ID	Date	Time	Cu, %	Ni, %	Fe, %
2689-12F		1000	0.001	0.003	0.040
2689-13B		1400	0.001	0.002	0.040
2689-13D		1800	0.001	0.001	0.020
2689-14B		2200	0.002	0.002	0.030
2689-14D	SEPT 24	200	0.001	0.007	0.020
2689-14F		600	0.001	0.001	0.020
2689-15B		1000	0.002	0.001	0.020
2689-15D		1400	0.002	0.001	0.020
2689-16B		1800	0.001	0.001	0.020
2689-16D		2200	0.002	0.001	0.020
2689-16F	SEPT 25	200	0.001	0.001	0.020
2689-17B		600	0.001	0.002	0.030
2689-17C		1000	0.008	0.030	0.060
2689-17F		1400	0.003	0.010	0.060
2689-18B		1800	0.003	0.020	0.070
2689-18D		2200	0.003	0.010	0.050
2689-19B	SEPT 26	200	0.002	0.008	0.050
2689-19D		600	0.002	0.009	0.060
2689-19F		1000	0.002	0.004	0.050
2689-20B		1400	0.002	0.003	0.070
2689-20D		1800	0.004	0.006	0.080
2689-21B		2200	0.003	0.007	0.070
2689-21D	SEPT 27	200	0.002	0.006	0.080
2689-22B		600	0.005	0.007	0.080
2689-22C		1000	0.002	0.002	0.030
2689-22F		1300	0.003	0.001	0.030
2689-23B		1400	0.003	0.001	0.020
2689-23C		1500	0.002	0.003	0.020
2689-23E		1600	0.003	0.006	0.040
2689-24B		1800	0.002	0.008	0.030
2689-24D		2200	0.002	0.009	0.030
2689-25B	SEPT 28	200	0.003	0.008	0.030
2689-25D		600	0.004	0.040	0.020
2689-26A		1000	0.002	0.004	0.040
2689-27A		1400	0.002	0.005	0.030
2689-27D		1800	0.005	0.007	0.030
2689-28B		2200	0.004	0.020	0.040
2689-28D	SEPT 29	200	0.004	0.008	0.050
2689-28F		600	0.003	0.008	0.040
2689-29B		1000	0.003	0.003	0.030
2689-29D1		1400	0.003	0.002	0.030
2689-29D2		1800	0.003	0.002	0.030
2689-30B		2200	0.004	0.003	0.030
2689-30D	SEPT 30	200	0.004	0.004	0.040
2689-30F		600	0.004	0.005	0.050
2689-31B		1000	0.004	0.008	0.060

BATH IMPURITIES

Sample ID	Date	Time	Cu, %	Ni, %	Fe, %
2689–31D		1400	0.003	0.007	0.060
2689–32B		1800	0.009	0.020	0.110
2689–32D		2200	0.010	0.020	0.080
2689–33B	OCT 1	200	0.005	0.006	0.070
2689–33D		600	0.005	0.007	0.050
2689–34A		1000	0.009	0.010	0.080
2689–34C		1400	0.003	0.008	0.050
2689–35B		1800	0.003	0.010	0.070
2689–35D		2200	0.003	0.009	0.060
2689–36B	OCT 2	200	0.003	0.010	0.060
2689–36D		600	0.003	0.012	0.040
2689–36E		1000	0.003	0.007	0.050
2689–36H		1400	0.002	0.008	0.050
2689–37B		1800	0.004	0.010	0.070
2689–37D		2200	0.005	0.010	0.050
2689–38B	OCT 3	200	0.005	0.010	0.060
2689–38D		600	0.006	0.010	0.070
2689–38F		1000	0.005	0.009	0.070
2689–38H		1400	0.003	0.008	0.070
2689–39B		1800	0.004	0.007	0.060
2689–39D		2200	0.003	0.008	0.060
2689–39F	OCT 4	200	0.002	0.003	0.040
2689–40B		600	0.005	0.010	0.070
2689–40C		1000	0.005	0.010	0.070
2689–40F		1400	0.004	0.007	0.050
2689–41B		1800	0.005	0.009	0.070
2689–41D		2200	0.005	0.008	0.030
2689–42B	OCT 5	200	0.030	0.050	0.130
2689–43B		600	0.008	0.010	0.070
2689–43D		1000	0.006	0.007	0.070
2689–43F		1400	0.005	0.005	0.060
2689–44A		1800	0.005	0.004	0.050
2689–44D		2200	0.006	0.005	0.060
2689–45B	OCT 6	200	0.005	0.006	0.050
2689–45D		600	0.004	0.006	0.060
2689–45F		1000	0.005	0.008	0.050
2689–45H		1400	0.003	0.010	0.050
2689–46B		1800	0.002	0.010	0.030
2689–46D		2200	0.003	0.005	0.030
2689–47B	OCT 7	200	0.002	0.006	0.030
2689–47D		600	0.003	0.007	0.030
2689–47F		1000	0.002	0.005	0.050
2689–48B		1400	0.003	0.009	0.070
2689–48D		1800	0.002	0.003	0.020
2689–48F		2200	0.003	0.014	0.030
2689–49B	OCT 8	200	0.003	0.009	0.030

BATH IMPURITIES

Sample ID	Date	Time	Cu, %	Ni, %	Fe, %
2689-49D		600	0.003	0.007	0.020
2689-49E		1000	0.004	0.005	0.020
2689-49G		1400	0.003	0.007	0.020
2689-50B		1800	0.003	0.005	0.050
2689-50D		2200	0.003	0.008	0.020
2689-50F	OCT 9	200	0.003	0.004	0.020
2689-51B		600	0.003	0.004	0.020
2689-51D		1000	0.004	0.006	0.030
2689-51F		1400	0.003	0.004	0.030
2689-51H		1800	0.003	0.003	0.020
2689-51J		2200	0.003	0.003	0.020
2689-52B	OCT 10	200	0.003	0.004	0.020
2689-52D		600	0.003	0.004	0.020
2689-52G		1000	0.004	0.004	0.020
2689-53B		1400	0.003	0.004	0.030

END

DATE FILMED

2 / 19 / 93